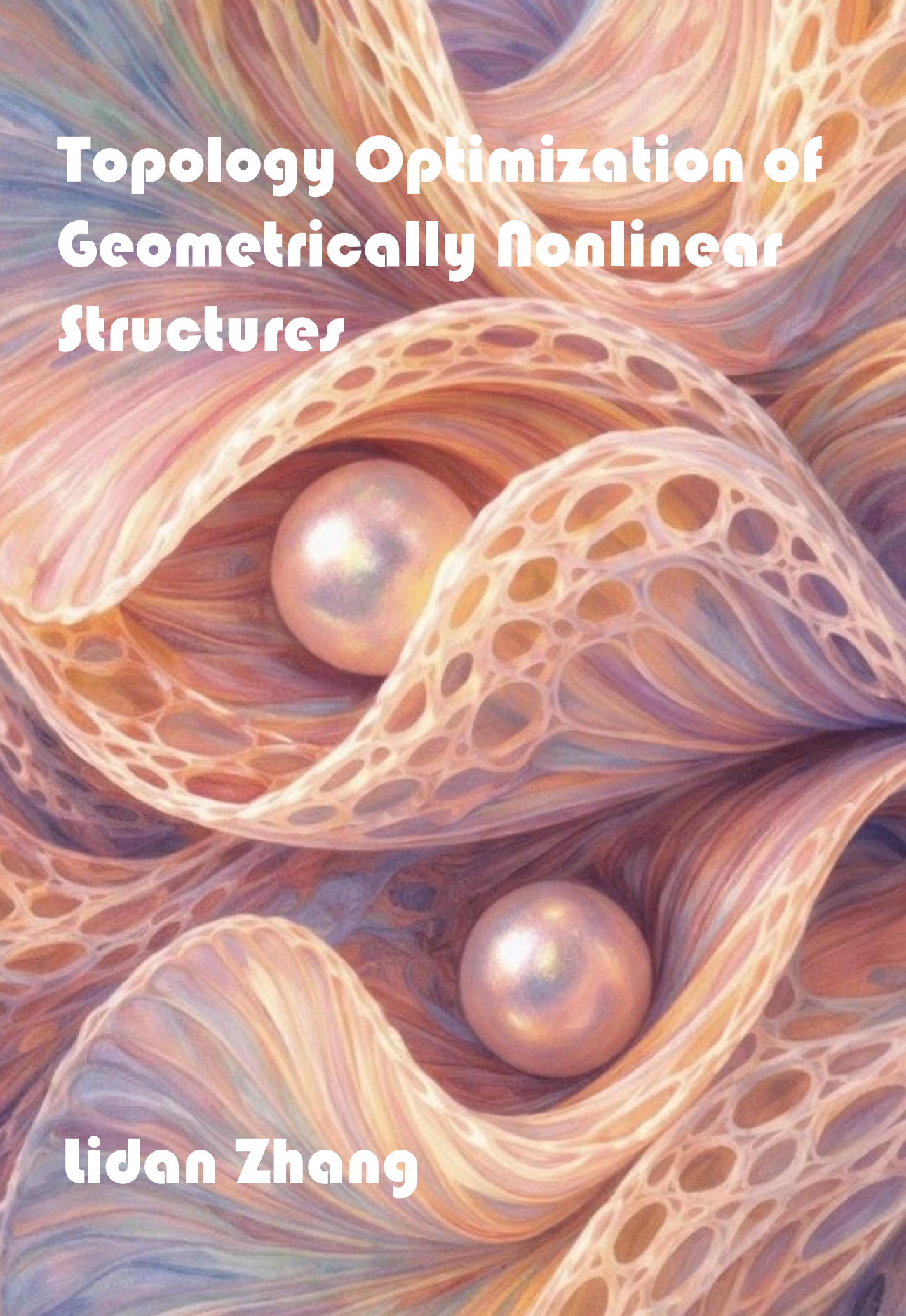
Topology Optimization of Geometrically Nonlinear Structures
lidan Zhang

# TOPOLOGY OPTIMIZATION OF GEOMETRICALLY NONLINEAR STRUCTURES

# TOPOLOGY OPTIMIZATION OF GEOMETRICALLY NONLINEAR STRUCTURES

## Dissertation

for the purpose of obtaining the degree of doctor
at Delft University of Technology,
by the authority of the Rector Magnificus, Prof. dr. ir. H. Bijl,
chair of the Board for Doctorates,
to be defended publicly on
Tuesday 24 February 2026 at 17:30 o'clock

by

**Lidan ZHANG**

This dissertation has been approved by the promotor

Composition of the doctoral committee:

| | |
|---|---|
| Rector Magnificus, | chairperson |
| Prof. dr. ir. A. van Keulen, | Delft University of Technology, *promotor* |
| | |
| *Independent members:* | |
| Dr. A. M. Aragón, | Delft University of Technology |
| Prof. dr. ir. J. L. Herder | Delft University of Technology |
| Prof. dr. K. Bertoldi | Harvard University, USA |
| Prof. dr. ir. M. Langelaar | Delft University of Technology |
| Prof. dr. O. Sigmund | Technical University of Denmark, Denmark |



The work presented in this dissertation was carried out in the Computational Design and Mechanics (CDM) group at Delft University of Technology. This research was funded by China Scholarship Council (CSC).

*Keywords:* Topology optimization, Geometrical nonlinearity, Reduced-order models, Low-density elements, Path-generation compliant mechanisms, Shells.

*Printed by:* Ipskamp Printing.

*Cover Design:* Lidan Zhang & AI.



ISBN 978-94-6536-032-4

An electronic version of this dissertation is available at
http://repository.tudelft.nl/.

*To my dearest parents and my loving husband, for their endless love, unwavering support, and constant encouragement.*

# CONTENTS

# SUMMARY

Incorporating geometric nonlinearity into topology optimization arises two main challenges: (1) high computational costs of solving the nonlinear governing equations, and (2) convergence difficulties in the analysis due to “low-density areas" compressed by neighboring stiffer regions. These challenges are addressed in this thesis, which then, focuses on applying topology optimization of geometrically nonlinear structures to design compliant mechanisms tracing user-defined motion paths.

First of all, Chapter 2 addresses the challenge of high computational cost by introducing reduced-order models (ROMs). The proposed method targets ROM bases consisting of a small set of base vectors, while maintaining accuracy. To this end, several fully automated techniques are developed and integrated for updating and maintaining the ROM basis, with path derivatives incorporated to better capture the behavior of highly flexible structures. In parallel, approximate sensitivity analysis methods are introduced to simplify computations and improve the efficiency of the optimization process. The effectiveness of the ROMs is demonstrated by numerical examples, which show substantial reductions in computational effort.

However, the efficiency of the proposed ROMs can deteriorate when faced with the second challenge, i.e., convergence difficulties arise from the compression of low-density regions. Such compression typically leads to “inside-out" elements in 2D structures or spurious local buckling in shells and plates. The former, i.e., “inside-out" elements, often causes computational divergence, while the latter, i.e., spurious local buckling, though not always divergent, can significantly increase the number of iterations required for convergence. These spurious instability modes are inevitably incorporated into the proposed ROM basis, which can render ROM analyses even less efficient than full-order ones. To mitigate this problem, two strategies are investigated in Chapter 3: (1) removing spurious instability modes from the ROM basis, and (2) eliminating them directly from the underlying physics. The latter approach is also applicable to standard FOM analyses. Their effectiveness is demonstrated through shell model examples, which provide detailed insights into the benefits and limitations of each approach.

To move beyond algorithmic developments, Chapters 4 and 5 apply geometrically nonlinear topology optimization to the practical design of path-generation compliant mechanisms. A main challenge in this context is ensuring material connectivity among the input, output, and support fixtures within the design domain. This challenge is addressed in Chapter 4 using a simple yet effective formulation that combines compliance and volume constraints. Here, compliance upper bounds are specified according to engineering requirements, while volume constraints are enforced through a proposed three-phase scheme. Building on this foundation, Chapter 5 applies the formulation to design path-generation mechanisms capable of tracing long-distance motion paths. In particular, shells and plates are explored because their compactness and flexible nature make them especially effective for achieving such motions. Finally, experiments on 3D-

printed prototypes validate the effectiveness of the proposed formulations in producing functional designs.

# SAMENVATTING

Het opnemen van geometrische non-lineariteit in topologie-optimalisatie brengt twee belangrijke uitdagingen met zich mee: (1) hoge rekenkosten voor het oplossen van de niet-lineaire vergelijkingen, en (2) convergentieproblemen in de analyse die worden veroorzaakt door "lage-dichtheidsgebieden" die worden samengedrukt door omliggende stijvere regio's. Deze uitdagingen worden in dit proefschrift behandeld, dat bovendien de nadruk legt op de toepassing van topologie-optimalisatie van geometrisch niet-lineaire structuren voor het ontwerpen van compliant mechanisms die vooraf gedefinieerde paden kunnen volgen.

Allereerst behandelt Hoofdstuk 2 de uitdaging van hoge rekenkosten door de introductie van gereduceerde ordemodellen (ROMs). De voorgestelde methode richt zich op ROM-bases die bestaan uit een kleine set basisvectoren, met behoud van nauwkeurigheid. Daartoe zijn verschillende volledig geautomatiseerde technieken ontwikkeld en geïntegreerd voor het bijwerken en onderhouden van de ROM-basis, waarbij padafgeleiden zijn opgenomen om het gedrag van zeer flexibele structuren beter vast te leggen. Parallel hieraan worden benaderende gevoeligheidsanalysemethoden geïntroduceerd om de berekeningen te vereenvoudigen en de efficiëntie van het optimalisatieproces te verbeteren. De effectiviteit van de ROMs wordt aangetoond met numerieke voorbeelden, die aanzienlijke reducties in rekeninspanning laten zien.

De efficiëntie van de voorgestelde ROMs kan echter verslechteren bij de tweede uitdaging, namelijk de convergentieproblemen die ontstaan door de compressie van lagedichtheidsgebieden. Dit manifesteert zich doorgaans als "binnenstebuitenëlementen in 2D structuren of als kunstmatige lokale knik in schalen en platen binnen de onderliggende fysica. De eerste situatie veroorzaakt vaak numerieke divergentie, terwijl de tweede, hoewel niet altijd divergent, het aantal iteraties dat nodig is voor convergentie aanzienlijk kan verhogen. Deze kunstmatige instabiliteitsmodi worden onvermijdelijk opgenomen in de voorgestelde ROM-basis, wat ertoe kan leiden dat ROM-analyses zelfs minder efficiënt zijn dan volledige-ordemodellen (FOMs). Om dit probleem te verhelpen, worden in Hoofdstuk 3 twee strategieën onderzocht: (1) het verwijderen van kunstmatige instabiliteitsmodi uit de ROM-basis, en (2) het rechtstreeks elimineren ervan uit de onderliggende fysica. Deze laatste aanpak is ook toepasbaar op standaard FOM-analyses. De effectiviteit van beide methoden wordt aangetoond met schaalmodelvoorbeelden, die gedetailleerde inzichten geven in de voordelen en beperkingen van elke aanpak.

Om verder te gaan dan louter algoritmische ontwikkelingen, passen Hoofdstukken 4 en 5 geometrisch niet-lineaire topologie-optimalisatie toe op het praktische ontwerp van conforme padgenererende mechanismen. Een belangrijke uitdaging in deze context is het waarborgen van materiaalsamenhang tussen de invoer-, uitvoer- en ondersteuningsbevestigingen binnen het ontwerpdomein. Deze uitdaging wordt in Hoofdstuk 4 aangepakt met een eenvoudige maar effectieve formulering die nalevings- en volume-

beperkingen combineert. Hierbij worden bovengrenzen voor de naleving vastgelegd op basis van technische vereisten, terwijl volumebeperkingen worden afgedwongen via een voorgesteld driefasenschema. Voortbouwend op deze basis past Hoofdstuk 5 de formulering toe voor het ontwerpen van padgenererende mechanismen die in staat zijn lange-afstandsbewegingspaden te volgen. In het bijzonder worden schalen en platen onderzocht, omdat hun compacte vorm en flexibele aard hen bijzonder geschikt maken voor het realiseren van dergelijke bewegingen. Tot slot valideren experimenten met 3D-geprinte prototypes de effectiviteit van de voorgestelde formuleringen bij het produceren van functionele ontwerpen.

# 1

# INTRODUCTION

1

In the early 20th century, due to the lack of efficient computing tools and complete theories, structural design and optimization depended on the experience of engineers. Consequently, the work was paced, in a sense, by trial and error. As reported by Vanderplaats [1], the first computer-based structural optimization appeared in 1960 [2], which ushered in a new era of structural design. Since then, with the evolution of electronic computing techniques, the development of finite element analysis (FEA) [3], and the maturity of mathematical programming theories [4], people have been gaining more powerful structural analysis tools, and gradually building up systematic structural design and optimization methods. Nowadays, optimization strategies are prospering in various engineering fields.

Structural optimization [5] is adjusting design variables, e.g., thickness, to achieve an objective, e.g. minimizing compliance. According to design variables, the main three categories of structural optimization are size, shape, and topology optimization (TO). As is shown in Fig. 1.1(a), a size optimization starts from a prescribed structure, and the geometry parameters, for example, cross-sectional areas of trusses, are modified to satisfy user-defined requirements. As for shape optimization shown in Fig. 1.1(b), the outline of the structure can be modified, but the layout inside cannot be changed. Concerning TO (see Fig. 1.1(c)), it can remove material inside the design domain and could also change the outline. Given that TO has the most design freedom, in this work, we focus on TO and target a simple shaped design domain, for example, a rectangle, but achieve a complex and innovative topology exhibiting geometrical nonlinearity.

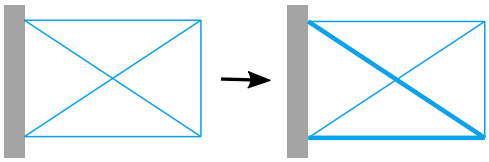

(a) Size optimization

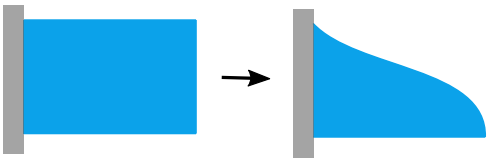

(b) Shape optimization

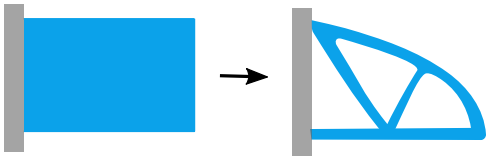

(c) Topology optimization

Figure 1.1: Three categories of optimization, which minimizes compliance with volume constraints.

## 1.1. TOPOLOGY OPTIMIZATION

Topology optimization [6] achieves optimized structural performance by designing material distribution in a prescribed design domain. This method has gained widespread use since it was introduced in the article by Bendsøe and Kikuchi in 1988 [7]. Now, the method is developing in a variety of directions such as solid isotropic material with penalization method (SIMP) [8], level set-based TO [9], moving morphable component-based TO (MMC) [10], moving morphable void approach (MMV) [11], evolutionary structural optimization (ESO) and bi-direction evolutionary structural optimization (BESO) [12]. Among these methods, the most common and classical one is SIMP, the basic idea of which is to scale element stiffness using a penalized pseudo-density. This method is used throughout this thesis.

Early applications of TO were on minimizing compliance and lightening weight [13]. With design requirements becoming more and more ambitious, TO is gradually adopted in various structural design problems, including designing compliant mechanisms [14], considering additive manufacturing (AM) constraints [15], optimizing AM process [16], involving fracture toughness [17], etc. The majority of these studies assume linear elastic material behavior and geometric linearity. Indeed, these simplifications are suitable for a large class of problems. However, when structures perform beyond the linear scope, for example, designing snap-through [18, 19] and path-generation mechanisms [20, 21], accounting for geometric nonlinearity is necessary.

As reported in [22], geometric nonlinearity can largely influence final designs. One of the examples, minimizing structural compliance, is shown in Fig. 1.2. The left one is the TO result for a small displacement FEA-modelling, whereas the right one is for a large displacement FEA-modelling. It can be seen that the final topology in the nonlinear setting is drastically different from the linear one. As is illustrated in [22], if the design obtained in the linear setting undergoes large deflections, its performance is much poorer compared to the design created in the nonlinear setting. Thus, it is essential to take geometric nonlinearity into consideration when deflections and rotations get finite.

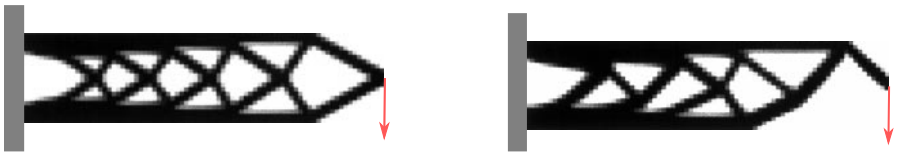

(a) Linear design (b) Nonlinear design

Figure 1.2: Topology optimization results for a cantilever beam that minimize compliance with volume constraints. The structure is fully clamped on the left side and a force $f$ acts at the right tip. $f = 12$ for the linear design and $f = 240$ for the nonlinear design. The pictures are taken from [22]. Used with permission of Springer Nature, from Structural and Multidisciplinary Optimization, Stiffness design of geometrically nonlinear structures using topology optimization, T. Buhl, C.B. Pedersen, and O. Sigmund, Feb 1, 2014.

## 1.2. GEOMETRIC NONLINEARITY

Geometrical nonlinearity (GNL) in this work is restricted to large deflection and finite rotations but small strain. Under this situation, the relationship between load and dis-

placement is nonlinear. More specifically, the stiffness of the structure is a function of displacements. One important characteristic of nonlinearity is that the load in one direction can influence the stiffness in another direction. To illustrate this coupling, consider the slender beam shown in Fig. 1.3. If the beam is subjected to stretching in the horizontal direction, the beam can support a vertical load with a relatively small deflection. However, if the beam is subjected to compression, although no vertical load is applied, the structure can suffer large vertical deflections resulting from buckling behavior. Consequently, overlooking the GNL would result in an incorrect evaluation of the structural stiffness. When introducing GNL to FEA, due to complicated couplings in geometrically nonlinear settings, intensive use has to be made of incremental-iterative finite element simulations, which typically results in high computational costs.

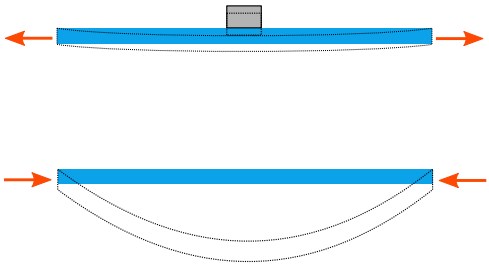

Figure 1.3: A slender beam model, which can support a vertical load when stretched and suffers from buckling when compressed.

### 1.2.1. COMPUTATIONAL EFFICIENCY

In TO, structural responses, e.g. displacements, required in optimization are typically obtained by finite element analysis (FEA). For nonlinear structural responses, the solutions are obtained in an iterative way, where the incremental-iterative method is usually adopted [23]. The latter, for a one-degree-of-freedom structure, is illustrated in Fig. 1.4, where an external load on the structure is incremented step by step. Within every load step, classical Newton iterations are conducted for obtaining the solution. In each Newton iteration, the most time-consuming step is the factorization of the tangent stiffness matrix, which has dimensions corresponding to the number of nodal degrees of freedom (DOFs). When the number of DOFs gets large, the computational efficiency is overwhelmingly decreased. One possibility to circumvent this, is introducing reduced-order modellings (ROMs) [24] to reduce the dimension of tangent stiffness matrices.

In ROMs, a basis $\mathbf{R}$ is utilized to reduce the structural stiffness matrix $\mathbf{K}$ to a smaller matrix $\overline{\mathbf{K}}$. The dimension of the latter depends on the number of base vectors in $\mathbf{R}$. Since the dimension of $\overline{\mathbf{K}}$ is usually much smaller than $\mathbf{K}$, factorization of $\overline{\mathbf{K}}$ can be very efficient. ROMs have already been explored in TO for linear structures [25–28]. Given the promising results in these publications, in the present work, we extend ROMs for the nonlinear setting, which target a relatively small set of base vectors while accuracy is still guaranteed.

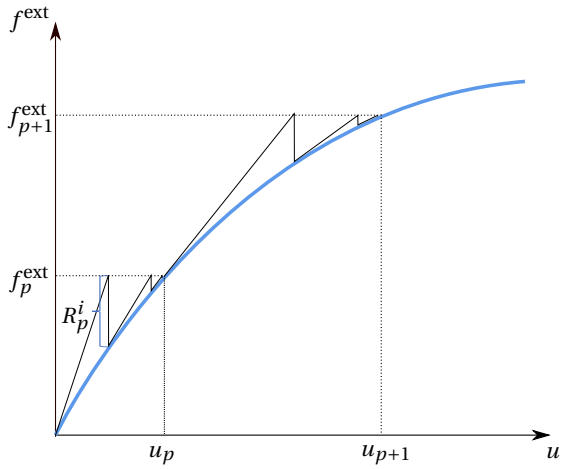


Figure 1.4: Incremental load control combined with Newton iterations. $f_p^{\text{ext}}$ represents the external load at the $p$th incremental step, $R_p^i$ the residual between internal and external load at the $i$th Newton iteration within in the $p$th incremental step, and $u_p$ the displacement corresponding to $f_p^{\text{ext}}$.

### 1.2.2. SPURIOUS MODES

In the geometrically nonlinear setting, stiffness reduction, i.e., instabilities could occur when the structure is subjected to compression. This is typically encountered in low-density areas in TO. Since TO tends to generate areas with large density differences. Relatively low-density areas, i.e., very compliant regions, are usually surrounded by solid areas, i.e., very stiff regions. The former can be compressed by the latter and encounter spurious instabilities, consequently resulting in indefinite and/or ill-conditioned tangent stiffness matrices. Such behavior is fatal in 2D structures since elements could easily reverse, i.e., become “inside-out", resulting in complete failure of the analysis (see the example shown in Fig. 1.5(a)). Concerning shells, as shown in Fig. 1.5(b), spurious instability often appears as local buckling. Although it may not always cause divergence, it can greatly increase the number of analysis iterations needed for convergence.

In ROMs, previously defined nonlinear solutions are typically used as basis vectors, inherently incorporating local buckling into the ROM basis and thereby spoiling the convergence and efficiency of ROMs. To effectively utilize ROMs, the analysis convergence difficulties caused by low-density areas must be addressed. Various methods have already been explored in full-order modellings (FOMs) and tested on 2D structures [29–33]; however, not all of them can be tailored for ROMs, and conveniently extended to shells. Given this, in the present work, we investigate several techniques, which can be easily adapted to the proposed ROMs and applied to shell structures.

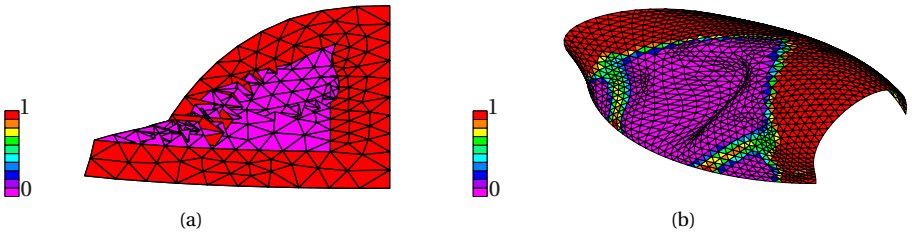


(a) (b)

Figure 1.5: Low-density elements causing “inside-out" elements in 2D structures shown in (a) and local buckling in shells shown in (b).

## 1.3. DESIGN OF PATH-GENERATION COMPLIANT MECHANISMS

Nowadays, topology optimization for geometrically nonlinear structures, has been applied in various creative design tasks, for example, development of compliant metamaterials [34, 35] and mechanisms (CMs) [36–39]. In particular, compliant mechanisms can be designed such that their output ports follow a user-defined trajectory in response to applied displacements or forces at input ports. Such mechanisms are known as path-generation compliant mechanisms (PGCMs), which are the focus of this work.

PGCMs are widely used in high-precision systems, such as micro-scale manipulators [40, 41] and positioning stages for scanning probe microscopy [42]. The latter serves as a representative example to illustrate the role of PGCMs in precision systems. A simplified depiction of the microscope and a potential stage design is shown in Fig. 1.6(a). Since the scanning range of the microscope is small, a positioning stage is required to acquire surface information from larger specimens. This stage must follow a prescribed path, e.g., a horizontal line, when a specific actuation is applied, as shown in Fig. 1.6(b).

Because the mechanism must fit within a limited workspace while delivering a relatively large output displacement, compliant mechanisms with a high displacement-to-size ratio are preferred. Traditionally, such mechanisms are designed through experience, analytical modeling, and assembly of existing components. However, due to the complexity of the models and limited design intuition, developing large-stroke PGCMs often involves extensive trial and error. To facilitate this process, topology optimization methods could be used [43–45].

As mentioned earlier, TO offers the most design freedom among the three optimization methods, making it highly promising for generating complex and innovative PGCM designs. A key challenge in applying TO to PGCMs lies in establishing material connectivity within the design domain. Various sophisticated techniques have been proposed to address this issue [46–50], but most are limited to specific optimization algorithms or structure types. For example, as shown in Fig. 1.7, connectivity can be enforced by mapping a set of Bézier curves onto a fixed finite element mesh [46]. While effective, such methods are difficult to extend to other element types, such as shell and plate elements, which are particularly suitable for achieving large displacement-to-size ratios due to their flexible and compact nature. Given these limitations, it is worthwhile to develop a simple and general formulation, with a particular focus on exploring shell and

plate mechanisms.

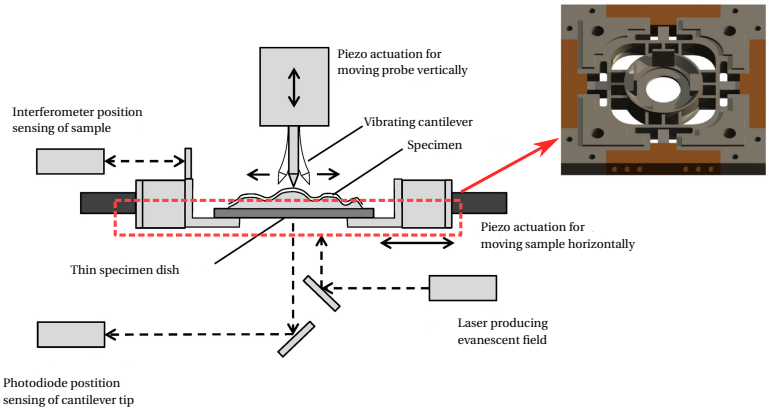


(a) A model of a scanning probe microscopy and its positioning stage.

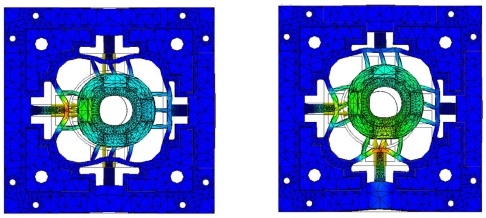

(b) Positioning stage deformations of single axis actuation (left) and dual axis actuation (right).

Figure 1.6: A scanning probe microscopy and the design of its positioning stages where the positioning stage is necessary to acquire surface information of a large specimen, and desired motions are illustrated in Fig. 1.6(b) [42]. This is an open access article distributed under the terms of the Creative Commons CC-BY license.

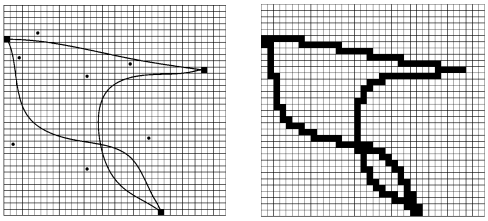

Figure 1.7: Material connectivity in PGCM design described by mapping a set of Bezier curve onto a fixed finite element mesh. The Bezier curve is on the left and the mapped topology is on the right [46]. Used with permission of American Society of Mechanical Engineers (ASME), from Design Synthesis of Path Generating Compliant Mechanisms by Evolutionary Optimization of Topology and Shape, Tai Kang, Cui Guang Yu, Ray Tapabrata, 124, 3, 2002-01-01.

## 1.4. THE AIM OF THIS RESEARCH

As mentioned in the preceding sections, although topology optimization has been introduced in various applications, the majority of work is restricted to a linear setting. This is mainly due to high computational costs and spurious modes. Thus, **exploring techniques to enhance efficiency and alleviate spurious instabilities is one of the aims of this work**. Furthermore, TO for geometrically nonlinear structures is also desired to assist real-life design practice. One typical application that requires geometrical nonlinear is path-generation mechanisms (PGCM). However, available formulations are quite complicated, and most of them are restricted to specific optimization algorithms and structure types. Consequently, TO-based PGCMs are usually restricted in 2D designs. In this work, **we aim to propose a simple and general formulation for path-generation mechanism design, and explore mechanisms based on plates and shells, which are very suitable to exhibit large deflections and rotations.**

## 1.5. OUTLINE

In this thesis, the research problems mentioned above are addressed in the following chapters. Most chapters in this thesis are based on publications. Thus, while there is some inevitable redundancy, the benefit is that each chapter is self-contained.

First of all, to enhance the computational efficiency of TO for structures with GNL, ROMs are explored in Chapter 2. The proposed ROMs target a small number of base vectors while accuracy is still guaranteed. For this, several fully automated update and maintenance techniques for the ROM basis are investigated and combined. Next, in Chapter 3, several techniques are explored to alleviate spurious instabilities, with a particular focus on those that can be easily adapted to ROMs. Proposed techniques can be divided into two types. One focuses on refining the ROM bases and the other targets the physics represented by full-order models.

Next, from an application perspective, Chapter 4 proposes a simple and general formulation for path-generation mechanism design, which can be easily implemented and applied to any type of structure. The formulation is extended to several large-stroke PGCM designs in Chapter 5, and validations on the basis of 3D printed specimens are also conducted.

## REFERENCES

[1] G. N. Vanderplaats, *Structural optimization for statics, dynamics and beyond,* Journal of the Brazilian Society of Mechanical Sciences and Engineering **28**, 316 (2006).

[2] L. A. Schmit, *Structural design by systematic synthesis,* in *Proceedings of the 2nd National Conference on Electronic Computation* (ASCE, New York, NY, 1960) pp. 105–132.

[3] T. J. R. Hughes, *The Finite Element Method: Linear Static and Dynamic Finite Element Analysis* (Prentice-Hall, 1987).

[4] H. P. Williams, *Model building in mathematical programming* (John Wiley & Sons, 2013).

[5] R. T. Haftka and Z. Gürdal, *Elements of structural optimization* (Springer Science & Business Media, 2012).

[6] O. Sigmund and K. Maute, *Topology optimization approaches,* Structural and Multidisciplinary Optimization **48**, 1031 (2013).

[7] M. P. Bendsøe and N. Kikuchi, *Generating optimal topologies in structural design using a homogenization method,* Computer methods in applied mechanics and engineering **71**, 197 (1988).

[8] M. P. Bendsøe and O. Sigmund, *Material interpolation schemes in topology optimization,* Archive of applied mechanics **69**, 635 (1999).

[9] N. P. Van Dijk, K. Maute, M. Langelaar, and F. Van Keulen, *Level-set methods for structural topology optimization: a review,* Structural and Multidisciplinary Optimization **48**, 437 (2013).

[10] X. Guo, W. Zhang, and W. Zhong, *Doing topology optimization explicitly and geometrically—a new moving morphable components based framework,* Journal of Applied Mechanics **81**, 081009 (2014).

[11] W. Zhang, J. Chen, X. Zhu, J. Zhou, D. Xue, X. Lei, and X. Guo, *Explicit three dimensional topology optimization via moving morphable void (mmv) approach,* Computer Methods in Applied Mechanics and Engineering **322**, 590 (2017).

[12] X. Huang and M. Xie, *Evolutionary topology optimization of continuum structures: methods and applications* (John Wiley & Sons, 2010).

[13] M. P. Bendsoe and O. Sigmund, *Topology optimization: theory, methods, and applications* (Springer Science & Business Media, 2003).

[14] O. Sigmund, *On the design of compliant mechanisms using topology optimization,* Journal of Structural Mechanics **25**, 493 (1997).

[15] E. van de Ven, R. Maas, C. Ayas, M. Langelaar, and F. van Keulen, *Overhang control based on front propagation in 3d topology optimization for additive manufacturing,* Computer Methods in Applied Mechanics and Engineering **369**, 113169 (2020).

[16] W. Wang, D. Munro, C. C. Wang, F. van Keulen, and J. Wu, *Space-time topology optimization for additive manufacturing,* Structural and Multidisciplinary Optimization **61**, 1 (2020).

[17] J. Zhang, F. van Keulen, and A. M. Aragón, *On tailoring fracture resistance of brittle structures: A level set interface-enriched topology optimization approach,* Computer Methods in Applied Mechanics and Engineering **388**, 114189 (2022).

[18] T. Bruns, O. Sigmund, and D. A. Tortorelli, *Numerical methods for the topology optimization of structures that exhibit snap-through,* International Journal for Numerical Methods in Engineering **55**, 1215 (2002).

[19] H. Deng, L. Cheng, X. Liang, D. Hayduke, and A. C. To, *Topology optimization for energy dissipation design of lattice structures through snap-through behavior,* Computer Methods in Applied Mechanics and Engineering **358**, 112641 (2020).

[20] A. K. Mallik and S. G. Dhande, *Analysis and synthesis of mechanical error in path-generating linkages using a stochastic approach,* Mechanism and Machine Theory **22**, 115 (1987).

[21] J. R. McGARVA, *Rapid search and selection of path generating mechanisms from a library,* Mechanism and machine theory **29**, 223 (1994).

[22] T. Buhl, C. B. Pedersen, and O. Sigmund, *Stiffness design of geometrically nonlinear structures using topology optimization,* Structural and Multidisciplinary Optimization **19**, 93 (2000).

[23] R. De Borst, M. A. Crisfield, J. J. Remmers, and C. V. Verhoosel, *Nonlinear finite element analysis of solids and structures* (John Wiley & Sons, 2012).

[24] D. J. Lucia, P. S. Beran, and W. A. Silva, *Reduced-order modeling: new approaches for computational physics,* Progress in aerospace sciences **40**, 51 (2004).

[25] C. Gogu, *Improving the efficiency of large scale topology optimization through on-the-fly reduced order model construction,* International Journal for Numerical Methods in Engineering **101**, 281 (2015).

[26] O. Amir, M. P. Bendsøe, and O. Sigmund, *Approximate reanalysis in topology optimization,* International Journal for Numerical Methods in Engineering **78**, 1474 (2009).

[27] E. C. Hooijkamp and F. v. Keulen, *Topology optimization for linear thermo-mechanical transient problems: modal reduction and adjoint sensitivities,* International Journal for Numerical Methods in Engineering **113**, 1230 (2018).

[28] S. Wang, E. de Sturler, and G. Paulino, *Large-scale topology optimization using preconditioned krylov subspace methods with recycling,* International journal for numerical methods in engineering **69**, 2441 (2007).

[29] T. E. Bruns and D. A. Tortorelli, *An element removal and reintroduction strategy for the topology optimization of structures and compliant mechanisms,* International journal for numerical methods in engineering **57**, 1413 (2003).

[30] R. D. Lahuerta, E. T. Simões, E. Campello, P. M. Pimenta, and E. C. Silva, *Towards the stabilization of the low density elements in topology optimization with large deformation,* Computational Mechanics **52**, 779 (2013).

[31] G. H. Yoon and Y. Y. Kim, *Element connectivity parameterization for topology optimization of geometrically nonlinear structures,* International journal of solids and structures **42**, 1983 (2005).

[32] N. P. van Dijk, M. Langelaar, and F. Van Keulen, *Element deformation scaling for robust geometrically nonlinear analyses in topology optimization,* Structural and Multidisciplinary Optimization **50**, 537 (2014).

[33] F. Wang, B. S. Lazarov, O. Sigmund, and J. S. Jensen, *Interpolation scheme for fictitious domain techniques and topology optimization of finite strain elastic problems,* Computer Methods in Applied Mechanics and Engineering **276**, 453 (2014).

[34] Y. Lu, Q. Luo, and L. Tong, *Topology optimization for metastructures with quasi-zero stiffness and snap-through features,* Computer Methods in Applied Mechanics and Engineering **434**, 117587 (2025).

[35] Y. Tang, A. Zhang, Q. Zhou, M. He, and L. Xia, *Data-driven design of topologically optimized auxetic metamaterials for tailored stress–strain and poisson's ratio-strain behaviors,* Materials & Design **256**, 114290 (2025).

[36] V. Shobeiri and Y. M. Xie, *Topology optimization for creating nonreciprocal compliant mechanisms: Numerical and experimental investigations,* Extreme Mechanics Letters **77**, 102345 (2025).

[37] L. R. Alacoque, A. Bhattacharyya, and K. A. James, *Compliant mechanism synthesis using nonlinear elastic topology optimization with variable boundary conditions,* International Journal for Numerical Methods in Engineering **126**, e7613 (2025).

[38] Y. Lu, Q. Luo, and L. Tong, *Multi-objective and multi-constraint topology optimization of nonlinear compliant mechanisms,* Thin-Walled Structures **208**, 112761 (2025).

[39] G. Granlund and M. Wallin, *Designing compliant self-locking structures using topology optimization,* Structural and Multidisciplinary Optimization **68**, 77 (2025).

[40] S. Xiao and Y. Li, *Visual servo feedback control of a novel large working range micro manipulation system for microassembly,* Journal of Microelectromechanical Systems **23**, 181 (2013).

[41] J. Shen, X. Fang, J. Liu, L. Liu, H. Lu, and J. Lou, *Design, manufacture, and two-step calibration of a piezoelectric parallel microrobot at the millimeter scale for micromanipulation,* Mechanism and Machine Theory **206**, 105928 (2025).

[42] G. De Silva, S. Burgess, T. Hatano, S. Khan, K. Zhang, T. Nguyen, G. Herrmann, C. Edwards, and M. Miles, *Optimisation of a nano-positioning stage for a transverse dynamic force microscope,* Precision Engineering **50**, 183 (2017).

[43] M. Naves, R. Aarts, and D. Brouwer, *Large stroke high off-axis stiffness three degree of freedom spherical flexure joint,* Precision engineering **56**, 422 (2019).

[44] S.-C. Huang and T.-P. Dao, *Design and computational optimization of a flexure-based xy positioning platform using fea-based response surface methodology,* International Journal of Precision Engineering and Manufacturing **17**, 1035 (2016).

[45] Y.-C. Chen, B.-K. Huang, Z.-T. You, C.-Y. Chan, and T.-M. Huang, *Optimization of lightweight structure and supporting bipod flexure for a space mirror,* Applied optics **55**, 10382 (2016).

[46] K. Tai, G. Y. Cui, and T. Ray, *Design synthesis of path generating compliant mechanisms by evolutionary optimization of topology and shape,* J. Mech. Des. **124**, 492 (2002).

[47] K.-J. Lu and S. Kota, *Topology and Dimensional Synthesis of Compliant Mechanisms Using Discrete Optimization,* Journal of Mechanical Design **128**, 1080 (2005).

[48] A. Saxena, *A Material-Mask Overlay Strategy for Continuum Topology Optimization of Compliant Mechanisms Using Honeycomb Discretization,* Journal of Mechanical Design **130**, 082304 (2008).

[49] A. Saxena, *Topology design with negative masks using gradient search,* Structural and Multidisciplinary Optimization **44**, 629 (2011).

[50] A. Saxena, *Synthesis of Compliant Mechanisms for Path Generation using Genetic Algorithm,* Journal of Mechanical Design **127**, 745 (2004).

# 2

# TOPOLOGY OPTIMIZATION OF GEOMETRICALLY NONLINEAR STRUCTURES USING REDUCED-ORDER MODELING

*High computational costs are encountered in topology optimization problems of geometrically nonlinear structures since intensive use has to be made of incremental-iterative finite element simulations. To alleviate this computational intensity, reduced-order models (ROMs) are explored in this chapter. The proposed method targets ROM bases consisting of a relatively small set of base vectors while accuracy is still guaranteed. For this, several fully automated update and maintenance techniques for the ROM basis are investigated and combined. In order to remain effective for flexible structures, path derivatives are added to the ROM basis. The corresponding sensitivity analysis (SA) strategies are presented and the accuracy and efficiency are examined. Various geometrically nonlinear examples involving both solid and shell elements are studied to test the proposed ROM techniques. Test cases demonstrate that the set of degrees of freedom appearing in the nonlinear equilibrium equation typically reduces to several tens. Test cases show a reduction of up to 6 times fewer full system updates.*

This chapter has been published in Computer Methods in Applied Mechanics and Engineering **416**, 116371 (2023)

## 2.1. INTRODUCTION

Topology optimization methods are highly-efficient structural design techniques which can assist in the development of new design principles in innovative sectors of industry. Mainstream topology optimization methods include SIMP [1], level set-based methods [2], ESO methods [3], BESO methods [4], and MMC [5]. In the present work, we mainly focus on topology optimization using the SIMP method.

The majority of studies on topology optimization of mechanical structures assumes linear elastic material behavior and geometric linearity. Indeed, these simplifications are suitable for a large class of problems. However, for specific classes, it is necessary to account for geometric nonlinearity in the analysis. Typical examples are thin-walled structures [6, 7], compliant mechanisms [8, 9], and multi-stable structures with snap-through behavior [10]. Consequently, seeking efficient and effective methods to carry out topology optimization for structures exhibiting geometric nonlinearity is of great practical relevance.

Several aspects cause topology optimization of geometrically nonlinear structures to be challenging. Compared with their linear counterparts, nonlinear structural optimization problems are computationally expensive since intensive use has to be made of incremental-iterative finite element simulations [11]. Besides, when deflections and rotations become finite, although deformations may still be small, void elements in the design space may get severely distorted and even "inverted", causing the tangent stiffness matrices to be indefinite and/or ill-conditioned, which may easily spoil the convergence of the nonlinear finite element analysis. This leads to catastrophic failure of the overarching optimization process [12–14]. Furthermore, like topology optimization of eigenfrequencies or buckling loads, spurious modes will occur in low-density areas. Low-density areas are very flexible as compared to areas with full densities, and may therefore control the lowest eigenmodes of the whole structure [15, 16]. In the present work, we primarily focus on the reduction of the computational burden associated with topology optimization when geometrical nonlinearity is considered. Potentially, reduced-order models (ROMs) are powerful strategies to deal with such problems.

ROMs attempt to use a small number of generalized variables to approximate the behavior governed by a large number of degrees of freedom (DOFs) associated with the full-order model (FOM). Each generalized variable corresponds to a base vector which can be a natural frequency mode, buckling mode, a static displacement field, among others [17–19]. The computational costs of a ROM depend heavily on the number of base vectors and effort to create the basis. ROMs are potentially valuable for the incremental-iterative solution of large-scale problems, as encountered in structural nonlinear analysis. Chan and Hsiao [19] used the solution vectors and correction vectors generated during a modified Newton process as base vectors for nonlinear static analysis. Safjan [20] not only used correction vectors but also the lowest eigenvectors of updated tangent stiffness matrices. Kim *et al.* [21] constructed ROMs for nonlinear structural dynamic analysis of isotropic and functionally graded plates. They combined linear FOM solutions with additional nonlinear FOM static solutions, so-called "dual modes", which were generated by applying a series of representative static loads on the structure.

In topology optimization, various applications of ROMs have been reported for linear settings. Amir *et al.* [22] applied a ROM for approximate reanalysis in topology optimiza-

tion of linear structures. They demonstrated that relatively rough approximations were acceptable in analysis since a consistent ROM-based sensitivity evaluation was applied, in which the errors caused by the ROM are taken into account. Gogu [23] applied ROMs for topology optimization of linear structures and enriched the ROM basis with previously calculated solutions. Hooijkamp and van Keulen [24] focused on topology optimization for linear transient thermomechanical problems. A reduced thermal modal basis augmented with static correction was used to replace the tedious backward transient integration by analytical convolutions in the adjoint sensitivity analysis. Wang *et al.* [25] investigated large-scale three-dimensional linear topology optimization problems. They used the Krylov subspace method combined with preconditioning techniques to solve the optimization problems and reduce the computing burden by recycling selected search spaces from previously analyzed linear systems.

For ROM-based topology optimization in nonlinear settings, a few publications related to material nonlinearity can be found. For instance, Xia and Breitkopf [26] presented a reduced multiscale model for macroscopic structural design considering material nonlinear microstructures. The ROM model uses Proper Orthogonal Decomposition (POD) and diffuse approximation to replace the detailed microscopic finite element analysis. However, for geometric nonlinearity, publications can only be found in size and shape optimization problems, but not for topology optimization. For example, for size optimization, Orozco and Ghattas [27] used ROMs to reduce the SQP-based simultaneous analysis and design (SAND) problem taking into account geometric nonlinearity. The resulting reduced problem has the same size as the nested analysis and design (NAND) problem but achieves higher efficiency. Given the promising results obtained in previous work, it is concluded that ROMs have great potential in topology optimization for geometrically nonlinear structures. Nevertheless, ROMs have never been introduced in this field.

In this chapter, ROMs are applied to topology optimization problems for geometrically nonlinear structures aiming at enhancing the computational efficiency of the associated incremental-iterative finite element simulations and the corresponding sensitivity analysis. The proposed ROMs target a relatively small set of base vectors while the accuracy can still be guaranteed. For this, several fully automated update and maintenance strategies for the ROM basis are investigated and combined. Besides, approximated ROM-based sensitivity analysis strategy (ARSA) is presented and the accuracy of the SA strategies are examined and compared to consistent FOM-based sensitivity analysis (CFSA). In addition, a formulation of consistent ROM-based sensitivity analysis (CRSA) is presented in the chapter. However, no numerical tests are conducted for CRSA, since this sensitivity is rather unpractical for the updating techniques presented in this work. Finally, various geometrically nonlinear examples involving solid or shell elements are studied to test the proposed ROM-based topology optimization techniques.

## 2.2. GEOMETRICALLY NONLINEAR TOPOLOGY OPTIMIZATION

Topology optimization formulations associated with an objective function $J$, inequality constraints $\mathbf{h}$, design variables (pseudo densities) $\boldsymbol{\rho}$ and their corresponding lower

bounds $\boldsymbol{\rho}_{\min}$ can be expressed by

$$\begin{aligned} &\min_{\boldsymbol{\rho}} J\left[\mathbf{d}\left[\boldsymbol{\rho}\right],\boldsymbol{\rho}\right], \\ &\text{s.t.}: \mathbf{h}\left[\mathbf{d}\left[\boldsymbol{\rho}\right],\boldsymbol{\rho}\right] \leq \mathbf{0}, \\ &\qquad \mathbf{0} < \boldsymbol{\rho}_{\min} \leq \boldsymbol{\rho} \leq \mathbf{1}. \end{aligned} \tag{2.1}$$

Here "$[*]$" denotes the function of "$*$", $\mathbf{d}$ represents mechanical responses, i.e., nodal degrees of freedom. Lower bounds $\boldsymbol{\rho}_{\min}$ are typically set to avoid singularity caused by removing material.

In many cases, simplifying topology optimization to a linear setting is sufficient to achieve a good and reasonable design. However, the linearity assumption is too restrictive for designs involving flexible structures exposed to finite rotations and/or for which geometric stiffness plays a crucial role. These structures often exhibit finite deflections and rotations, although the deformations remain small. Thus, it is paramount to consider geometric nonlinearity to ensure the final design functions correctly.

The geometrically nonlinear equilibrium equations are formulated using the virtual work principle

$$\delta W^{\text{int}} = \delta W^{\text{ext}}. \tag{2.2}$$

Here, $\delta W^{\text{ext}}$ is the external virtual work and $\delta W^{\text{int}}$ represents the internal virtual work. In a discrete setting, the external virtual work can be expressed by

$$\delta W^{\text{ext}} = \mathbf{f}^{\text{T}} \delta \mathbf{d}, \tag{2.3}$$

where $\mathbf{f}$ represents the external nodal loads. In order to avoid all finite element details, we shall introduce generalized deformations and stresses. Their precise definition depends on the finite elements at hand and their implementation. The internal virtual work in a discrete form can be expressed by

$$\delta W^{\text{int}} = \boldsymbol{\sigma}^{\text{T}} \delta \boldsymbol{\epsilon}, \tag{2.4}$$

where $\boldsymbol{\sigma}$ represents the generalized stresses and $\boldsymbol{\epsilon}$ the generalized deformations, with $\boldsymbol{\epsilon}[\mathbf{d}]$. Given the geometrically nonlinear setting, $\boldsymbol{\epsilon}[\mathbf{d}]$ is nonlinear in $\mathbf{d}$. For the variations of $\boldsymbol{\epsilon}$ it follows

$$\delta \boldsymbol{\epsilon} = \mathbf{D}\left[\mathbf{d}\right] \delta \mathbf{d}, \tag{2.5}$$

where the components of $\mathbf{D}$ are determined by

$$D_{ij} = \frac{\partial \epsilon_i}{\partial d_j}. \tag{2.6}$$

A generalized constitutive relation can be used to express the generalized stresses in terms of the generalized deformations. Since a linear elastic material model is assumed, this general expression can be formulated as

$$\boldsymbol{\sigma} = \mathbf{S}\boldsymbol{\epsilon}, \tag{2.7}$$

where $\mathbf{S}$ is the generalized constitutive matrix. At element level, the matrices corresponding to $\mathbf{D}$ and $\mathbf{S}$ are denoted by $\mathbf{D}_e$ and $\mathbf{S}_e$.

In the SIMP method [1], the constitutive matrix is scaled at element level with element density $\rho_e$:

$$\mathbf{S}_e \rightarrow \rho_e^p \mathbf{S}_e. \tag{2.8}$$

Here parameter $p$ is used to penalize intermediate densities. A low value of $p$ results in more intermediate density elements, while a high value of $p$ results in a less convex optimization problem but more crisp designs. Usually, $p = 3$ is adopted [1].



Starting from Eq. (2.2), the equilibrium equation can be expressed as

$$\mathbf{D}^{\mathrm{T}}[\mathbf{d}]\,\boldsymbol{\sigma} - \mathbf{f} = \mathbf{q}[\mathbf{d}] - \mathbf{f} = \mathbf{0}, \tag{2.9}$$

where $\mathbf{q} = \mathbf{D}^{\mathrm{T}}\boldsymbol{\sigma}$ represents the so-called “internal" load.

To solve the governing equations, an incremental-iterative method is applied in the present work. For this, a load factor $\lambda$ is introduced. Thus, the external load $\mathbf{f}$ is written as a function of $\lambda$. Then, the equilibrium equation reads

$$\mathbf{q}[\mathbf{d}] - \mathbf{f}[\lambda] = \mathbf{0}. \tag{2.10}$$

Next, the corresponding rate equations follow as

$$\mathbf{K}_{\mathrm{T}}[\mathbf{d}]\,\frac{\mathrm{d}\mathbf{d}}{\mathrm{d}\lambda} - \frac{\mathrm{d}\mathbf{f}}{\mathrm{d}\lambda} = \mathbf{0}, \tag{2.11}$$

with the $l \times l$ tangent stiffness matrix $\mathbf{K}_{\mathrm{T}}$ being defined as

$$\mathbf{K}_{\mathrm{T}} = \frac{\partial \mathbf{q}[\mathbf{d}]}{\partial \mathbf{d}}, \tag{2.12}$$

where $l$ is the number of structural DOFs. Then, the incremental technique starting from load step $i$ to $i+1$ can be formulated as

$$\mathbf{d}^{i+1} = \mathbf{d}^i + \left(\mathbf{K}_{\mathrm{T}}\left[\mathbf{d}^i\right]\right)^{-1}\left(\mathbf{f}\left[\lambda^{i+1}\right] - \mathbf{q}\left[\mathbf{d}^i\right]\right). \tag{2.13}$$

After the load increment has been applied, classical Newton iterations are carried out to obtain the corresponding nonlinear solution. For a specific load level $\lambda^{i+1} = \lambda^c$, the Newton iterations follow as

$$\mathbf{d}_{j+1} = \mathbf{d}_j + \left(\mathbf{K}_{\mathrm{T}}\left[\mathbf{d}_j\right]\right)^{-1}\left(\mathbf{f}\left[\lambda^c\right] - \mathbf{q}\left[\mathbf{d}_j\right]\right). \tag{2.14}$$

Here superscripts are used to identify the different load levels, whereas subscripts are used to indicate Newton iterations at a constant load level. The Newton iterations are continued until the convergence criterion is satisfied. The latter is defined by the norm of the residual:

$$e_f = \frac{\|\mathbf{f}[\lambda^c] - \mathbf{q}\left[\mathbf{d}_{j+1}\right]\|}{\|\mathbf{f}[\lambda^c]\|} \leq \epsilon_f. \tag{2.15}$$

Here $e_f$ denotes the imbalance error, $\epsilon_f$ a user-defined tolerance, and $\|*\|$ represents a norm. The latter for a vector $\mathbf{x} = [x_1, x_2, ...., x_l]$, in this work, is denoted by $\|\mathbf{x}\| = \sqrt{x_1^2 + x_2^2 + .... + x_l^2}$. Here $l$ stands for the dimension, which is the number of structural nodal DOFs in Eq. (2.15).

If the convergence criterion Eq. (2.15) is satisfied, the Newton iterations are converged. After convergence for a particular load level, we move to the next load step and the corresponding nonlinear solution is obtained again iteratively. As observed, since intensive use has to be made of incremental-iterative finite element simulations, the solution may be very expensive, particularly when the number of DOFs gets large. Especially in optimization, this become problematic because a large number of nonlinear problems has to be solved during the design process. In order to enhance efficiency, reduced-order modeling is introduced in the next section.

## 2.3. ROM-BASED FINITE ELEMENT ANALYSIS

Ritz' method is used to reduce the kinematic DOFs. For this, the nodal degrees of freedom are approximated by

$$\bar{\mathbf{d}} = \mathbf{R}\mathbf{y}, \tag{2.16}$$

where $\bar{\mathbf{d}}$ denotes the approximate nodal degrees of freedom for the full-order model and $\mathbf{y}$ are generalized coordinates. The matrix $\mathbf{R}$ represents the ROM basis

$$\mathbf{R} = [\boldsymbol{\phi}_1, \boldsymbol{\phi}_2, ..., \boldsymbol{\phi}_m], \tag{2.17}$$

where $m$ is the number of base vectors and $\boldsymbol{\phi}_i$ denotes an individual base vector. In order to obtain an efficient ROM, it is essential that the number of base vectors ($m$) is significantly smaller than the number of nodal degrees of freedom ($l$). Using Ritz' method, the ROM-based governing equation can be expressed as

$$\mathbf{R}^{\mathrm{T}}(\mathbf{q}\left[\bar{\mathbf{d}}\right] - \mathbf{f}) = \mathbf{0}. \tag{2.18}$$

Here,

$$\mathbf{q}\left[\bar{\mathbf{d}}\right] = \mathbf{D}^{\mathrm{T}}\left[\bar{\mathbf{d}}\right]\boldsymbol{\sigma}\left[\bar{\mathbf{d}}\right] = \mathbf{D}^{\mathrm{T}}\left[\mathbf{R}\mathbf{y}\right]\left(\mathbf{S}\boldsymbol{\epsilon}\left[\mathbf{R}\mathbf{y}\right]\right). \tag{2.19}$$

The corresponding rate equations follow as

$$\left(\bar{\mathbf{K}}_{\mathrm{T}}\left[\mathbf{y}\right]\right)^{-1}\frac{\mathrm{d}\mathbf{y}}{\mathrm{d}\lambda} - \frac{\mathbf{R}^{\mathrm{T}}\mathbf{f}}{\mathrm{d}\lambda} = \mathbf{0}, \tag{2.20}$$

with $\bar{\mathbf{K}}_{\mathrm{T}}$ representing the $m \times m$ reduced tangent stiffness matrix, which is expressed by full tangent stiffness matrix $\mathbf{K}_{\mathrm{T}}\left[\bar{\mathbf{d}}\right]$, i.e., $\mathbf{K}_{\mathrm{T}}\left[\mathbf{R}\mathbf{y}\right]$, and ROM basis $\mathbf{R}$ :

$$\bar{\mathbf{K}}_{\mathrm{T}}\left[\mathbf{y}\right] = \mathbf{R}^{\mathrm{T}}\mathbf{K}_{\mathrm{T}}\left[\mathbf{R}\mathbf{y}\right]\mathbf{R}. \tag{2.21}$$

Here, the right-hand term can be assembled element-by-element:

$$\mathbf{R}^{\mathrm{T}}\mathbf{K}_{\mathrm{T}}\left[\mathbf{R}\mathbf{y}\right]\mathbf{R} = \bigwedge_{e}\mathbf{R}_e^{\mathrm{T}}\mathbf{K}_{\mathrm{T}}^{e}\left[\mathbf{R}\mathbf{y}\right]\mathbf{R}_e. \tag{2.22}$$

Here, $\mathbf{R}_e$ and $\mathbf{K}_{\mathrm{T}}^{e}$ are corresponding matrices at element level.

As in the FOM setting, an incremental-iterative method can be applied to solve the nonlinear reduced governing equations. For a specific load step $\lambda^{i+1} = \lambda^{\mathrm{c}}$, the ROM-based Newton iterations can be expressed as

$$\mathbf{y}_{j+1} = \mathbf{y}_j + \triangle\mathbf{y}_{j+1}, \tag{2.23}$$

with

$$\Delta \mathbf{y}_{j+1} = \left(\overline{\mathbf{K}}_{\mathrm{T}}\left[\mathbf{y}_j\right]\right)^{-1} \mathbf{R}^{\mathrm{T}}\left(\mathbf{f}[\lambda^c] - \mathbf{q}\left[\mathbf{R}\mathbf{y}_j\right]\right). \tag{2.24}$$

As can be seen from Eq. (2.23) and Eq. (2.24) , Newton iterations are based on the reduced tangent stiffness matrix. This contributes to the computational efficiency since the dimensions of the latter depends on the number of base vectors, which is much smaller than the number of structural DOFs. The ROM-based Newton iterations for a specific load step are continued until a ROM-based convergence criterion is met. The latter is defined by using the norm of the reduced residual:

$$e_r = \frac{\|\mathbf{R}^{\mathrm{T}}\left(\mathbf{f}[\lambda^c] - \mathbf{q}\left[\mathbf{R}\mathbf{y}_{j+1}\right]\right)\|}{\|\mathbf{R}^{\mathrm{T}}\mathbf{f}[\lambda^c]\|} \leq \epsilon_r. \tag{2.25}$$

Here, $e_r$ denotes the imbalance error and $\epsilon_r$ a user-defined tolerance. The dimensions of $\mathbf{R}^{\mathrm{T}}\left(\mathbf{f}[\lambda^c] - \mathbf{q}\left[\mathbf{R}\mathbf{y}_{j+1}\right]\right)$ and $\mathbf{R}^{\mathrm{T}}\mathbf{f}[\lambda^c]$ equal the number of base vectors.

After the ROM-based Newton iterations have converged, we get $\mathbf{y}^{\mathrm{c}}$ corresponding to $\lambda^c$. Next, we project $\mathbf{y}^{\mathrm{c}}$ to get the ROM-based solution $\overline{\mathbf{d}}^{\mathrm{c}}$ for the nodal degrees of freedom by Eq. (2.16) , and then assess its accuracy. If the solution $\overline{\mathbf{d}}^{\mathrm{c}}$ is accurate, then it should also satisfy the full system equilibrium equation. This implies that the norm of the full-system based residual, $\|\mathbf{f}[\lambda^c] - \mathbf{q}\left[\overline{\mathbf{d}}^{\mathrm{c}}\right]\|$, should be sufficiently small. Hence, an error measure based on the full-system residual is proposed as

$$\eta = \frac{\|\mathbf{f}[\lambda^c] - \mathbf{q}\left[\overline{\mathbf{d}}^{\mathrm{c}}\right]\|}{\|\mathbf{f}[\lambda^c]|}. \tag{2.26}$$

Here, the dimensions of $\mathbf{f}[\lambda^c] - \mathbf{q}\left[\overline{\mathbf{d}}^{\mathrm{c}}\right]$ and $\mathbf{f}[\lambda^c]$ equal the number of structural nodal DOFs.

If $\eta$ is smaller than a user defined tolerance $\delta_s$, then the ROM-based solution is considered accurate. Otherwise, the ROM-based solution, though well converged, is considered inaccurate and needs to be improved. For this, correction strategies and techniques to construct, update, and maintain the ROM basis are introduced in the next section.

## 2.4. ROM BASIS

One of the most critical ingredients of the ROM is the choice of an appropriate set of base vectors. Effectively, the required set may depend on both the current load level ($\lambda^{\mathrm{c}}$), as well as on the structure, i.e., the design at hand. An ideal set of base vectors should be linearly independent, requiring low computational cost for its generation, and sufficiently complete to capture the nonlinear response of the structure. In addition, the number of base vectors should be limited to ensure a small ROM basis. To meet the aforementioned requirements, firstly, orthogonalization is applied to ensure linear independence (details are provided in Appendix A.1). Secondly, the ROM basis is initiated using FOM-based solutions. Thirdly, to ensure accuracy, a FOM-based correction technique is adopted. The initialization and the correction are provided in Section 2.4.1. Next, the ROM basis is augmented on the basis of FOM-based solutions evaluated for previous designs. The details of this augmentation are described in Section 2.4.2. In order to ensure the ROM basis remains compact, maintenance strategies are presented in Section 2.4.3.

### 2.4.1. INITIALIZATION AND ERROR CONTROL

At the very beginning of the optimization, i.e., at the first load step of the first optimization step, the ROM basis is empty. Hence, the optimization is initiated using the full-order model. As reported in [19], including the converged nonlinear solution and correction solutions obtained during Newton iterations constitute good ingredients for a ROM-based nonlinear static analysis. In our experience, correction solutions of iterations do not effectively contribute to the accuracy of ROMs, but increase the number of base vectors. Hence, in the proposed scheme, we exclusively add the first converged nonlinear FOM solution, but also consider the first predictor solution, i.e., the FOM solution to the linearized governing equation in the undeformed configuration. Following that, a ROM basis with these two vectors can be used to generate a ROM-based solution for the next load step.

After convergence of a ROM-based analysis, the accuracy of the solution is evaluated using Eq. (2.26), which is the full-order residual, but evaluated for the ROM-based solution. If the solution is accurate enough, i.e., $\eta \leqslant \delta_s$, then no correction is required and the current ROM solution will be accepted. If the error is too large, i.e., $\eta > \delta_s$, a correction is applied to eliminate the error. For this, starting from the present ROM-based solution, FOM-based Newton iterations are conducted. Subsequently, the resulting converged FOM-based solution is regarded as the final result for the current load step. It is obvious that the correction based on the full system is relatively time-consuming. Thus, improving the accuracy of ROMs to reduce computing time for FOM-based corrections is essential for efficiency. Consequently, before proceeding to the next load step, the resulting FOM-based nonlinear solution is added to the ROM basis. Hence, the next load step will be based on the updated ROM basis. The extension of the ROM basis is restricted by a maximum number of base vectors. If the ROM basis has reached the maximum number of base vectors, then specific base vectors will be removed from the basis. The details are provided in Section 2.4.3.

#### PATH DERIVATIVES FOR FLEXIBLE STRUCTURES

A ROM basis, as described in the previous subsection, is accurate for most cases except for very flexible structures like structures exhibiting nearly inextensional bending. In these cases, the flexible bending mode is typically badly represented by the existing basis, leading to ROM-based responses which are far too stiff. To grasp this concept more easily, consider a cantilever beam subjected to pure bending. When the deformation is correctly captured in a nonlinear manner, we observe that the beam can bend into a circle. This circular shape indicates that the beam's tip experiences both out-of-plane and in-plane deflections. In contrast, a poorly represented flexible bending mode would exhibit insufficient in-plane deflection, i.e., excessive in-plane stiffness. One extreme case of the latter is a linear mode where no in-plane deflection appears. One solution for the issue is to introduce curvature information on the load-deflection path, i.e., 2nd-order path derivatives. Such derivatives add information on the flexible bending modes. More explanations can be found in Appendix A.2. In this section, the method of adding curvature information is presented.

The 2nd-order path derivatives can be approximated by forward finite-differences:

$$\frac{\mathrm{d}^2\mathbf{d}}{\mathrm{d}\lambda^2} = \frac{\mathbf{d}^* - 2\mathbf{d}^*_{\Delta\lambda^*} + \mathbf{d}^*_{2\Delta\lambda^*}}{(\Delta\lambda^*)^2}. \tag{2.27}$$



Here, $\mathbf{d}^*$ denotes a FOM-based solution corresponding to the current load level $\lambda^*$, $\Delta\lambda^*$ a small perturbation of the load factor $\lambda^*$, $\mathbf{d}^*_{\Delta\lambda^*}$ and $\mathbf{d}^*_{2\Delta\lambda^*}$ are FOM-based perturbation solutions corresponding to perturbed load levels $(\lambda^*+\Delta\lambda^*)$ and $(\lambda^*+2\Delta\lambda^*)$, respectively. Given the introduced orthonormalization (see Appendix A.1), a practical approach to include the information on the 2nd-order path derivative is by simply adding $\mathbf{d}^*$, $\mathbf{d}^*_{\Delta\lambda^*}$, and $\mathbf{d}^*_{2\Delta\lambda^*}$ as new base vectors. Note, the FOM-based solution $\mathbf{d}^*$ has already been added to the basis. Starting from $\lambda^*$, the load factor is perturbed twice to get $\mathbf{d}^*_{\Delta\lambda^*}$ and $\mathbf{d}^*_{2\Delta\lambda^*}$. It is deserved to mention that including only $\mathbf{d}^*_{\Delta\lambda^*}$ is equivalent to adding current tangent information of the path. This can also contribute the accuracy to some extend. But for very flexible structures, the curvature information is highly desired to ensure the accuracy, which can be roughly achieved by adding $\mathbf{d}^*_{2\Delta\lambda^*}$. Here, we use the perturbation step $\Delta\lambda^* = \Delta\lambda \times 10^{-3}$, i.e., $\Delta\lambda^*$ is selected as a small fraction of the applied load step $\Delta\lambda$, which, based on our test cases, is effective. Since $\Delta\lambda^*$ is very small, modified Newton iterations can be employed to keep the updating computationally efficient, where the tangent stiffness matrix corresponding to $\lambda^*$ is used for both steps. By adding $\mathbf{d}^*_{\Delta\lambda^*}$ and $\mathbf{d}^*_{2\Delta\lambda^*}$, we efficiently add information on the curvature of the loading path, thus improving the accuracy of the corresponding ROM-based solutions. For one optimization step, the strategy is schematically illustrated in the Fig. 2.1, where $\mathbf{R}_i$ represents the ROM basis of load step $i$ .

### 2.4.2. AUGMENTATION TECHNIQUE

In the previous sections, we described the ROM updating strategy for the first step in the optimization. Such a method, in which we construct the ROM basis from scratch, can also be applied to subsequent optimization steps. However, this would disregard the potential benefits of FOM-based solutions evaluated for previous designs. The FOM-based solutions can be stored and could provide an accurate prediction of a slightly adapted design. To maximize the use of previous FOM-based solutions, i.e., previous ROM bases, we propose an augmentation technique in this section.

As an illustration, Fig. 2.2 depicts the first and second step of an optimization. Here $\mathbf{R}_i^k$ denotes the ROM basis of load step $i$ at optimization iteration $k$. When $k = 1$, the strategy as described in Section 2.4.1 applies. For $k > 1$ and $i = 1$, instead of using FOMs for initialization, we directly take $\mathbf{R}_1^{k-1}$ as the current ROM basis to enhance the efficiency. After convergence, error control, as described in Section 2.4.1, is applied and the ROM basis is updated if too large an error is encountered. When $k > 1$ and $i > 1$, we check the base vectors of load level $i$ and $i+1$ from the previous optimization iteration $k-1$. We add these base vectors if they are not included in the current ROM basis. Then, the augmented ROM basis is applied to generate the ROM-based solution for the next load level. Similarly, after convergence, the error control is applied and the ROM basis is updated if necessary.

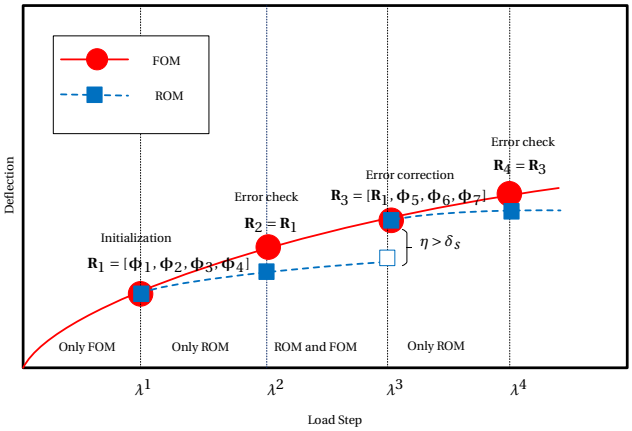


Figure 2.1: Initialization and accuracy control for ROMs. The red line represents schematically the FOM-based solutions, the blue line the ROM-based solution, $\mathbf{R}_i$ denotes the ROM basis corresponding to load level $\lambda^i$, $\boldsymbol{\Phi}_m$ are base vectors, and $\delta_s$ is a user-defined error tolerance. Initialization is applied at the first load level $(\lambda^1)$ where $\boldsymbol{\Phi}_1$ denotes the linear FOM solution, $\boldsymbol{\Phi}_2$ the FOM-based nonlinear solution, $\boldsymbol{\Phi}_3$ and $\boldsymbol{\Phi}_4$ perturbation solutions. Error checking is performed for each ROM-based solution. In the above illustration, for load level $(\lambda^2)$, the error is acceptable and, thus, no FOM-based correction is applied. Consequently, $\mathbf{R}^2$ is used for load level $(\lambda^3)$. However, for load level $(\lambda^3)$, too large an error is detected and a FOM-based correction is conducted and the ROM basis is extended by $\boldsymbol{\Phi}_5$, the FOM-based nonlinear solution, as well as by $\boldsymbol{\Phi}_6$ and $\boldsymbol{\Phi}_7$. The latter follows from the corresponding perturbations. Subsequently, the same logic as for $(\lambda^2)$ is applied for $(\lambda^4)$.

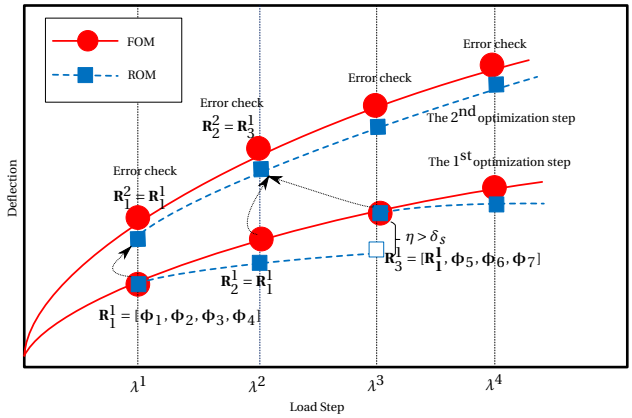


Figure 2.2: Augmentation of ROM basis where the red lines represent the FOM-based solutions, the blue lines the ROM-based solutions, $\mathbf{R}_i^k$ denotes the ROM basis corresponding to load level $\lambda^i$ in optimization step $k$, $\boldsymbol{\Phi}_m$ are base vectors, and $\delta_s$ is a user-defined error tolerance. When $k = 1$, the same logic as described in Section 2.4.1 applies. For $(k = 2, i = 1)$, instead of initializing the ROM basis with FOMs, we take $\mathbf{R}_1^1$ as the current ROM basis. Then, similar to the first optimization iteration, error checking is applied to the ROM-based solution. Since the error in this example is acceptable, no FOM-based correction is applied. Hence, at $(k = 2, \lambda^1)$, we have $\mathbf{R}_1^2 = \mathbf{R}_1^1$. Next, before $\mathbf{R}_1^2$ is used for the second load level, it is augmented by previous design's ROM bases $\mathbf{R}_2^1$ and $\mathbf{R}_3^1$. After convergence, the error checking is performed. Since no error correction is applied, at $(k = 2, \lambda^2)$, we have $\mathbf{R}_2^2 = \mathbf{R}_3^1$. Subsequently, the same strategy is applied to the subsequent load levels and optimization steps.

### 2.4.3. MAINTENANCE STRATEGIES

As shown, it is advantageous to include new base vectors throughout the optimization. The ROM basis is updated on the one hand to maintain accuracy for different load levels. On the other hand, the ROM basis is adapted to new designs when topology designs change. Given this, it is necessary to limit the maximum number of base vectors in order to maintain compactness of the ROM basis. If the number of base vectors reaches the maximum, old base vectors must be removed from the ROM basis to make room for new vectors. The corresponding strategy is described in this section.

For a ROM basis $\mathbf{R} = [\boldsymbol{\phi}_1, \boldsymbol{\phi}_2, \cdots, \boldsymbol{\phi}_m]$, base vectors from $\boldsymbol{\phi}_1$ to $\boldsymbol{\phi}_m$ are sequentially added to $\mathbf{R}$ following the strategy described in previous subsections. After adding each new vector, we apply the orthogonalization (see Appendix A.1) to all vectors in the basis. This implies that the base vector added at last, i.e., $\boldsymbol{\phi}_m$, could make very large contributions to the ROM-based solution, whereas, the vector added at first, i.e., $\boldsymbol{\phi}_1$, could make very small contributions. Consequently, when the basis is full and a new vector need to be added, we simply remove the first base vector, i.e., $\boldsymbol{\phi}_1$, from the ROM basis.

Furthermore, if the ROM basis is not full yet, it is possible to reduce the size even further without sacrificing accuracy. This can be done by removing the base vector with the smallest contribution. The contribution $c_i$ of base vector $\boldsymbol{\phi}_i$ can be expressed by

$$c_i = \left| \frac{y_i}{y_{\max}} \right|, \tag{2.28}$$

where $y_i$ denotes generalized coordinates, " $|*|$ " means an absolute value, and

$$y_{\max} = \max(y_1, y_2, .., y_m). \tag{2.29}$$

If $c_{\min} = \min\{c_i\} < \delta_{\text{rej}}$, we then remove the base vector corresponding to $c_{\min}$. Here $\delta_{\text{rej}}$ denotes a user-defined small value and we use $1 \times 10^{-8}$ in this work. This method is known as "rejection", which will be applied to all ROM-based load levels where the ROM-based solution is deemed accurate. So far, we have explained all related strategies for initializing, updating, and maintaining the ROM basis. In order to use ROMs for optimization, we still need to deduce the ROM-based sensitivities. More details are given in the next section.

## 2.5. DESIGN SENSITIVITY ANALYSIS

For topology optimization, sensitivity analysis (SA) is essential. The adjoint method is frequently used since the number of design variables is typically much larger than the number of constraints. The adjoint formulation for FOMs is already well-known in the field. Hence, we just summarize it in Section 2.5.1 and refer to it as consistent FOM sensitivity analysis (CFSA). CFSA will be used when a FOM-based solution is available, e.g., after initialization and error correction. In fact, one could use CFSA for a ROM-based solution, but this would be expensive and, effectively, the resulting sensitivities are not consistent. Consequently, we derive the consistent ROM-based sensitivity analysis (CRSA) in Section 2.5.2, which requires derivatives of all base vectors. However, owing to our augmentation technique, which involves previous FOM solutions, such derivatives are rather impractical to be considered. Therefore, an approximation is created for

the CRSA, and the modified formulation is referred to as the approximate ROM-based sensitivity analysis (ARSA).

### 2.5.1. CONSISTENT FOM SENSITIVITY ANALYSIS (CFSA)



To deduce the adjoint formulations for the consistent FOM sensitivity, we introduce the equilibrium equation Eq. (2.10) to the response function $J$ by adjoint variables $\theta$, where the augmented response function $\bar{J}$ is

$$\bar{J}\left[\mathbf{d}\left[\rho\right],\rho\right] = J\left[\mathbf{d}\left[\rho\right],\rho\right] + \theta^{\mathrm{T}}\left(\mathbf{f} - \mathbf{q}\left[\mathbf{d}\left[\rho\right],\rho\right]\right). \tag{2.30}$$

To improve readability, $\mathbf{d}\left[\rho\right]$ is shortly represented by $\mathbf{d}$.

The derivative of $\bar{J}$ with respect to $\boldsymbol{\rho}$ is

$$\frac{\mathrm{d}\bar{J}\left[\mathbf{d},\rho\right]}{\mathrm{d}\rho} = J_{,\mathbf{d}}\left[\mathbf{d},\rho\right]\frac{\mathrm{d}\mathbf{d}}{\mathrm{d}\rho} - \theta^{\mathrm{T}}\left(\mathbf{q}_{,\mathbf{d}}\left[\mathbf{d},\rho\right]\frac{\mathrm{d}\mathbf{d}}{\mathrm{d}\rho} + \mathbf{q}_{,\rho}\left[\mathbf{d},\rho\right]\right) + J_{,\rho}\left[\mathbf{d},\rho\right], \tag{2.31}$$

Here the comma represents partial derivatives. From Eq. (2.31), the computation of the expensive derivatives $\frac{\mathrm{d}\mathbf{d}}{\mathrm{d}\rho}$ can be avoided if the adjoint variables $\theta$ are selected as the solution of

$$\mathbf{K}_{\mathrm{T}}\left[\mathbf{d},\rho\right]\,\theta = J_{,\mathbf{d}}\left[\mathbf{d},\rho\right]. \tag{2.32}$$

Here, one linear solution step need to be conducted. When $\mathbf{K}_{\mathrm{T}}$ is large, its decomposition could be expensive if it is not available. After obtaining $\theta$, the design sensitivity can be calculated by

$$\frac{\mathrm{d}J\left[\mathbf{d},\rho\right]}{\mathrm{d}\rho} = \frac{\mathrm{d}\bar{J}\left[\mathbf{d},\rho\right]}{\mathrm{d}\rho} = -\theta^{\mathrm{T}}\mathbf{q}_{,\rho}\left[\mathbf{d},\rho\right] + J_{,\rho}\left[\mathbf{d},\rho\right]. \tag{2.33}$$

Given that $\mathbf{q}_{,\rho}$ is easy to evaluate, the only time-consuming term could be the solution of Eq. (2.32). In fact, one could use CFSA for a ROM-based solution, but this would be expensive and, effectively, the resulting sensitivities are still not consistent. Consequently, we derive (approximate) ROM-based sensitivity analysis in the next section.

### 2.5.2. CONSISTENT ROM-BASED SENSITIVITY ANALYSIS (CRSA) AND ITS APPROXIMATION (ARSA)

At first, the consistent reduced-order sensitivity analysis (CRSA) is derived. We introduce the ROM-based equilibrium function related to $\bar{\mathbf{d}}$ (see Eq. (2.18)) to the response function $J$ by adjoint variables $\boldsymbol{\mu}$. Meanwhile, we also introduce the FOM-based equilibrium function related to base vectors $\boldsymbol{\Phi}_j$ (see Eq. (2.9)) to $J$ by adjoint variables $\theta_j$. Then, the augmented objective function can be defined as

$$\bar{J}\left[\bar{\mathbf{d}}\left[\rho\right],\rho\right] = J\left[\bar{\mathbf{d}}\left[\rho\right],\rho\right] + \boldsymbol{\mu}^{\mathrm{T}}\mathbf{R}^{\mathrm{T}}\left(\mathbf{f} - \mathbf{q}\left[\bar{\mathbf{d}}\left[\rho\right],\rho\right]\right) + \sum_{j=1}^{m}\theta_j^{\mathrm{T}}\left(\mathbf{f}_{\boldsymbol{\Phi}} - \mathbf{q}_{\boldsymbol{\Phi}}\left[\boldsymbol{\Phi}_j\left[\rho\right],\rho\right]\right), \tag{2.34}$$

where $m$ is the number of base vectors. Next, to improve readability, $\bar{\mathbf{d}}\left[\rho\right]$ is compactly denoted by $\bar{\mathbf{d}}$ and $\boldsymbol{\Phi}_j\left[\rho\right]$ by $\boldsymbol{\Phi}_j$.

Taking derivatives of Eq. (2.34) to design variables $\boldsymbol{\rho}$, we get

$$\begin{aligned}\frac{\mathrm{d}\bar{J}\left[\bar{\mathbf{d}},\boldsymbol{\rho}\right]}{\mathrm{d}\boldsymbol{\rho}} &= J_{,\bar{\mathbf{d}}}\left[\bar{\mathbf{d}},\boldsymbol{\rho}\right]\frac{\mathrm{d}\bar{\mathbf{d}}}{\mathrm{d}\boldsymbol{\rho}} + J_{,\boldsymbol{\rho}}\left[\bar{\mathbf{d}},\boldsymbol{\rho}\right] + \boldsymbol{\mu}^{\mathrm{T}}\frac{\mathrm{d}\mathbf{R}^{\mathrm{T}}}{\mathrm{d}\boldsymbol{\rho}}\left(\mathbf{f}-\mathbf{q}\left[\bar{\mathbf{d}},\boldsymbol{\rho}\right]\right)\\ &\quad -\boldsymbol{\mu}^{\mathrm{T}}\mathbf{R}^{\mathrm{T}}\left(\mathbf{q}_{,\bar{\mathbf{d}}}\left[\bar{\mathbf{d}},\boldsymbol{\rho}\right]\frac{\mathrm{d}\bar{\mathbf{d}}}{\mathrm{d}\boldsymbol{\rho}} + \mathbf{q}_{,\boldsymbol{\rho}}\left[\bar{\mathbf{d}},\boldsymbol{\rho}\right]\right)\\ &\quad -\sum_{j=1}^{m}\theta_j^{\mathrm{T}}\left(\mathbf{q}_{\boldsymbol{\Phi},\bar{\mathbf{d}}}\left[\boldsymbol{\Phi}_j,\boldsymbol{\rho}\right]\frac{\mathrm{d}\boldsymbol{\Phi}_j}{\mathrm{d}\boldsymbol{\rho}} + \mathbf{q}_{\boldsymbol{\Phi},\boldsymbol{\rho}}\left[\boldsymbol{\Phi}_j,\boldsymbol{\rho}\right]\right),\end{aligned} \tag{2.35}$$

where

$$\boldsymbol{\mu}^{\mathrm{T}}\frac{\mathrm{d}\mathbf{R}^{\mathrm{T}}}{\mathrm{d}\boldsymbol{\rho}} = \sum_{j=1}^{m}\mu_j\left(\frac{\mathrm{d}\boldsymbol{\Phi}_j}{\mathrm{d}\boldsymbol{\rho}}\right)^{\mathrm{T}}. \tag{2.36}$$

and

$$\frac{\mathrm{d}\bar{\mathbf{d}}}{\mathrm{d}\boldsymbol{\rho}} = \frac{\mathrm{d}\mathbf{R}}{\mathrm{d}\boldsymbol{\rho}}\mathbf{y} + \mathbf{R}\frac{\mathrm{d}\mathbf{y}}{\mathrm{d}\boldsymbol{\rho}}, \tag{2.37}$$

$$\frac{\mathrm{d}\mathbf{R}}{\mathrm{d}\boldsymbol{\rho}}\mathbf{y} = \sum_{j=1}^{m} y_j\frac{\mathrm{d}\boldsymbol{\Phi}_j}{\mathrm{d}\boldsymbol{\rho}}. \tag{2.38}$$

Then, the derivatives Eq. (2.35) can be expressed as

$$\begin{aligned}\frac{\mathrm{d}\bar{J}\left[\bar{\mathbf{d}},\boldsymbol{\rho}\right]}{\mathrm{d}\boldsymbol{\rho}} =& J_{,\boldsymbol{\rho}}\left[\bar{\mathbf{d}},\boldsymbol{\rho}\right] - \boldsymbol{\mu}^{\mathrm{T}}\mathbf{R}^{\mathrm{T}}\mathbf{q}_{,\boldsymbol{\rho}}\left[\bar{\mathbf{d}},\boldsymbol{\rho}\right] - \sum_{j=1}^{m}\theta_j^{T}\mathbf{q}_{\boldsymbol{\Phi},\boldsymbol{\rho}}\left[\boldsymbol{\Phi}_j,\boldsymbol{\rho}\right]\\ &+\sum_{j=1}^{m}\left\{y_j\left(J_{,\bar{\mathbf{d}}}\left[\bar{\mathbf{d}},\boldsymbol{\rho}\right] - \boldsymbol{\mu}^{\mathrm{T}}\mathbf{R}^{\mathrm{T}}\mathbf{q}_{,\bar{\mathbf{d}}}\left[\bar{\mathbf{d}},\boldsymbol{\rho}\right]\right) + \mu_j\left(\mathbf{f}-\mathbf{q}\left[\bar{\mathbf{d}},\boldsymbol{\rho}\right]\right)^{\mathrm{T}} - \theta_j^{\mathrm{T}}\mathbf{q}_{\boldsymbol{\Phi},\bar{\mathbf{d}}}\left[\boldsymbol{\Phi}_j,\boldsymbol{\rho}\right]\right\}\frac{\mathrm{d}\boldsymbol{\Phi}_j}{\mathrm{d}\boldsymbol{\rho}}\\ &+\left(J_{,\bar{\mathbf{d}}}\left[\bar{\mathbf{d}},\boldsymbol{\rho}\right]\mathbf{R} - \boldsymbol{\mu}^{\mathrm{T}}\mathbf{R}^{\mathrm{T}}\mathbf{q}_{,\bar{\mathbf{d}}}\left[\bar{\mathbf{d}},\boldsymbol{\rho}\right]\mathbf{R}\right)\frac{\mathrm{d}\mathbf{y}}{\mathrm{d}\boldsymbol{\rho}}.\end{aligned} \tag{2.39}$$

The derivatives $\frac{\mathrm{d}\mathbf{y}}{\mathrm{d}\rho}$ are avoided if the adjoint variables $\boldsymbol{\mu}$ satisfy

$$\mathbf{R}^{\mathrm{T}}\mathbf{K}_{\mathrm{T}}\left[\bar{\mathbf{d}},\boldsymbol{\rho}\right]\mathbf{R}\boldsymbol{\mu} = \bar{\mathbf{K}}_{\mathrm{T}}\left[\bar{\mathbf{d}},\boldsymbol{\rho}\right]\boldsymbol{\mu} = \mathbf{R}^{\mathrm{T}}J_{,\bar{\mathbf{d}}}^{\mathrm{T}}\left[\bar{\mathbf{d}},\boldsymbol{\rho}\right]. \tag{2.40}$$

Here $\bar{\mathbf{K}}_{\mathrm{T}}\left[\bar{\mathbf{d}},\boldsymbol{\rho}\right]$ denotes the reduced tangent stiffness matrix. Since $\bar{\mathbf{K}}_{\mathrm{T}}\left[\bar{\mathbf{d}},\boldsymbol{\rho}\right]$ is only associated with a few reduced DOFs, the solution of Eq. (2.40) is conveniently obtained and will be evaluated in the final configuration. The tedious part is to eliminate the derivatives of the base vectors $\frac{\mathrm{d}\boldsymbol{\Phi}_j}{\mathrm{d}\boldsymbol{\rho}}$. For this, the corresponding adjoint variables $\theta_j$, for $j = 1,2,\ldots,m$, have to satisfy

$$\mathbf{q}_{\boldsymbol{\Phi},\bar{\mathbf{d}}}^{\mathrm{T}}\left[\boldsymbol{\Phi}_j,\boldsymbol{\rho}\right]\theta_j = \mathbf{K}_{\mathrm{T}}\left[\boldsymbol{\Phi}_j,\boldsymbol{\rho}\right]\theta_j = y_j\left(J_{,\bar{\mathbf{d}}}\left[\bar{\mathbf{d}},\boldsymbol{\rho}\right] - \boldsymbol{\mu}^{\mathrm{T}}\mathbf{R}^{\mathrm{T}}\mathbf{K}\left[\bar{\mathbf{d}},\boldsymbol{\rho}\right]\right)^{\mathrm{T}} + \mu_j\left(\mathbf{f}-\mathbf{q}\left[\bar{\mathbf{d}},\boldsymbol{\rho}\right]\right). \tag{2.41}$$

Note, the tangent stiffness matrix $\mathbf{K}_{\mathrm{T}}\left[\boldsymbol{\phi}_j, \rho\right]$ is related to FOMs. More specifically, it will be related to FOMs for previous designs and/or different load levels due to the proposed updating scheme. Hence, this adjoint formulation would call for availability of tangent stiffness matrices corresponding to other load levels and/or different designs. Thus, it is not efficient to calculate these terms in the ROM-based sensitivities. Therefore, an approximated method is proposed, which ignores the derivatives of $\boldsymbol{\phi}_j$. This means that it is assumed that the dependency of $\boldsymbol{\phi}_j$ on $\boldsymbol{\rho}$ has a relative minor effect on the resulting sensitivities. Following this strategy, the approximated formulation is expressed as

$$\frac{\mathrm{d}J\left[\bar{\mathbf{d}}, \boldsymbol{\rho}\right]}{\mathrm{d}\boldsymbol{\rho}} \approx -\boldsymbol{\mu}^{\mathrm{T}}\mathbf{R}^{\mathrm{T}}\mathbf{q}_{,\boldsymbol{\rho}}\left[\bar{\mathbf{d}}, \boldsymbol{\rho}\right] + J_{,\boldsymbol{\rho}}\left[\bar{\mathbf{d}}, \boldsymbol{\rho}\right]. \tag{2.42}$$

In Eq. (2.42), the adjoint variable $\boldsymbol{\mu}$ is computed using Eq. (2.40). This implies that we do not need previous tangent operators. Compared to CFSA, this strategy only needs a reduced-order linear analysis, which leads to computational efficiency.

## 2.6. NUMERICAL EXAMPLES

Several numerical examples involving shell elements and solid elements are studied in this section to evaluate the proposed ROM-based techniques. The shell elements applied in this paper are 6-node, 12-DOF triangle elements, which can describe finite rotations by a co-rotation formulation. More detail are provided in the work of Van Keulen and Booij [28]. The solid elements are standard 6-node, 12-DOF tetrahedral elements with one integration point.

For the efficiency illustration, note that in each Newton iteration the main cost could come from two operations: (1) multiplying the ROM basis with the tangent stiffness matrix, and (2) the decomposition of the tangent stiffness matrix.1) For ROMs, from the Eq. (2.21), the operation count for the multiplication is $(2l-1)\times 2ml = 4ml^2 - 2ml$, where $l$ is the number of DOFs and $m$ is the number of ROM basis. Since matrix decomposition scales cubically with matrix dimension, the decomposition cost is $O(m^3)$. Given $m << l$, the overall cost of one ROM Newton iteration is $O(l^2)$. For FOMs, the decomposition of an $l \times l$ tangent stiffness matrix scales as $O(l^3)$. Approximately, one FOM-based iteration is roughly as expensive as $l$ ROM-based iterations. Therefore, comparing the number of FOM and ROM Newton iterations provides a fair means of evaluating efficiency.

In the numerical tests, the efficiency of ROMs is measured by counting the number of ROM-based Newton iterations (ROM-based updates) and FOM-based correction iterations (FOM-based correction updates) for each topology optimization step. These numbers are compared with the number of FOM-based Newton iterations (FOM-based updates) of an exclusively FOM-based strategy. To keep illustrations compact, several terms are defined in the Tab. 2.1. Here, the exclusively FOM-based strategy does not reuse solutions from previous FOM analyses, even though such reuse could be proposed as a potential way to improve FOM efficiency. However, in nonlinear FEA, reusing previous FOM solutions can in fact be less efficient than the standard FOM approach (i.e.„ without reuse). This is because, for each load step, the deformation fields from previous designs would need to be stored and then reloaded for the current design. Both storing and retrieving these large datasets are time-consuming and memory-intensive, making

the procedure comparable in cost to simply restarting the incremental–iterative analysis from scratch.

Table 2.1: Definition of terms used in the numerical examples

| Name | Meaning |
|---|---|
| ONLY FOM | Exclusively FOM-based method |
| ROM* | ROMs without path derivatives and augmentation |
| $(\text{ROM}^*)_\text{f}$ | The number of FOM-based correction updates in ROM* for each optimization step |
| $(\text{ROM}^*)_\text{r}$ | The number of ROM-based updates in ROM* for each optimization step |
| ROM+A | ROMs with augmentation without path derivatives |
| $(\text{ROM}+\text{A})_\text{f}$ | The number of FOM-based correction updates in ROM+A for each optimization step |
| $(\text{ROM}+\text{A})_\text{r}$ | The number of ROM-based updates in ROM+A for each optimization step |
| ROM+A+P | ROMs with augmentation and path derivatives |
| $(\text{ROM}+\text{A}+\text{P})_\text{f}$ | The number of FOM-based correction updates in ROM+A+P for each optimization step |
| $(\text{ROM}+\text{A}+\text{P})_\text{r}$ | The number of ROM-based updates in ROM+A+P for each optimization step |

### 2.6.1. CYLINDRICAL SHELL

We embark on testing with a mildly nonlinear case to assess the effectiveness of the proposed ROMs. A cylindrical shell is shown in Fig. 2.3, where all details of the problem have been provided and the quantities involved have consistent units. We consider four different strategies for topology optimization, including ROM+A+P, ROM+A, ROM*, and "ONLY FOM".

A comparison of their efficiency is provided in Fig. 2.4. As observed in Fig. 2.4(a), "ONLY FOM" requires around 40 FOM-based updates every optimization step, whereas, per optimization step, ROM* only requires 20 FOM-based updates and 60 ROM-based updates. Here, 60 ROM-based updates have negligible effect on efficiency since each ROM-based update only requires factorization of a small matrix of $10 \times 10$ size. For further efficiency improvement, augmentation is included (see the result for ROM+A shown in Fig. 2.4(a)). Here, we can typically reduce the number of FOM-based updates to less than 20 per optimization step and logically, the number of ROM-based updates increases a bit to 60. Next, the impact of path derivatives is studied in Fig. 2.4(b). From the result, no obvious difference is obtained. It makes sense since path derivatives are mainly for inextensional bending structures, but it is not the case in this example.

Corresponding convergence curves of the four strategies are compared in Fig. 2.5. Evidently, all strategies underwent nearly the same optimization progress and converge to the same final result. This implies that the approximation we made in ROM-based sensitivity analysis, i.e., ARSA, has negligible impacts on the optimization progress and final result for this case. For details, we zoom in at an intermediate design of ROM+A+P, shown in Fig. 2.5, and look at its sensitivity of the constraint $u_x^\text{A} - 2.5\ le0$. The sensitivity value was obtained automatically by ARSA since the analysis ended with a ROM-based solution. As a comparison, we used FOMs to rerun the analysis for the same intermediate design and extracted CFSA values as shown in Fig. 2.5. According to the results, ARSA and CFSA provide a consistent sign but differing magnitudes. These differences did not obviously lead ROM-based optimization progress diverge from the FOM-based one. It indicates that there are possibilities for optimization to ignore the errors existing in sensitivity values.

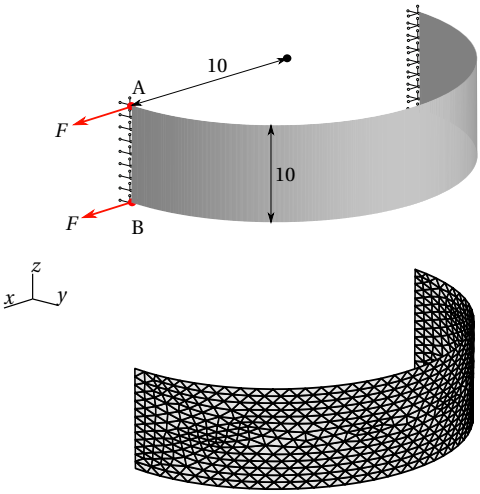


$E$=100 × 10^6 $t$ = 0.1
$\nu$=0.3 $\epsilon_r = 10 \times 10^{-9}$
$F$=300 $\epsilon_f = 10 \times 10^{-6}$
$\lambda$=0.15 $\delta_{\text{rej}} = 10 \times 10^{-9}$
$\Delta\lambda$=0.015 $\delta_s = 0.5$

Objective : Min $V$
s.t.: $u_x^{\text{A}} \leq 2.5$, $u_x^{\text{B}} \leq 2.5$
Number of base vectors : 10
Number of shell elements : 1178

Figure 2.3: Cylindrical shell. All quantities have consistent units. Here, $F$ denotes nodal forces applied at points A and B, $t$ thickness, $E$ Young's modulus, $\lambda$ load factor, $\Delta\lambda$ increment of $\lambda$, $\epsilon_f$ the convergence tolerance for FOMs (see Eq. (2.15)), $\epsilon_r$ the convergence tolerance for ROMs (see Eq. (2.25)), $\delta_{\text{rej}}$ the rejection tolerance (see Section 2.4.3), $\delta_s$ the error tolerance for ROM-based results (see Section 2.4.1), $V$ volume, $u_x^{\text{A}}$ displacement of point A in x direction, and $u_x^{\text{B}}$ displacement of point B in x direction.

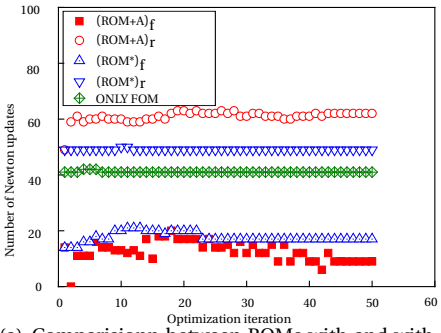


(a) Comparisionn between ROMs with and without augmentation

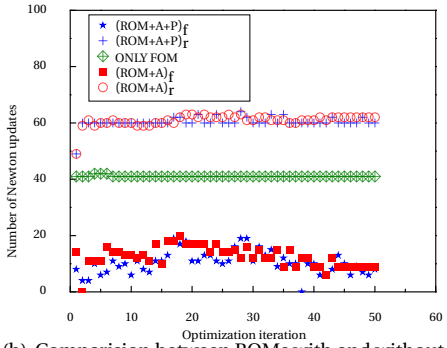


(b) Comparision between ROMs with and without path derivatives

Figure 2.4: Efficiency test for the cylindrical model. The efficiency of ROMs is measured by counting the number of ROM-based updates and FOM-based correction updates for each topology optimization step. In the left picture, blue shapes denote ROMs without path derivatives and augmentation, where the up-pointing triangles are the number of ROM-based updates and the down-pointing triangles are corresponding FOM-based correction updates. The red shapes denote ROMs with augmentation without path derivatives, where the circles are ROM-based updates and the squares are FOM-based. In the right picture, the blue shapes represent ROMs with augmentation and path derivatives, where the stars are the number of ROM-based updates and the crosses are the corresponding FOM-based updates. The red shapes here are the same as the left picture. These numbers are compared with the number of FOM-based updates of exclusively FOM strategy, which are shown by the green points in both the left and right pictures. From the distribution of the points, we can see that ROMs with augmentation have better performance than ROMs without augmentation. The differences between ROMs with and without path derivatives are not distinct for this example.

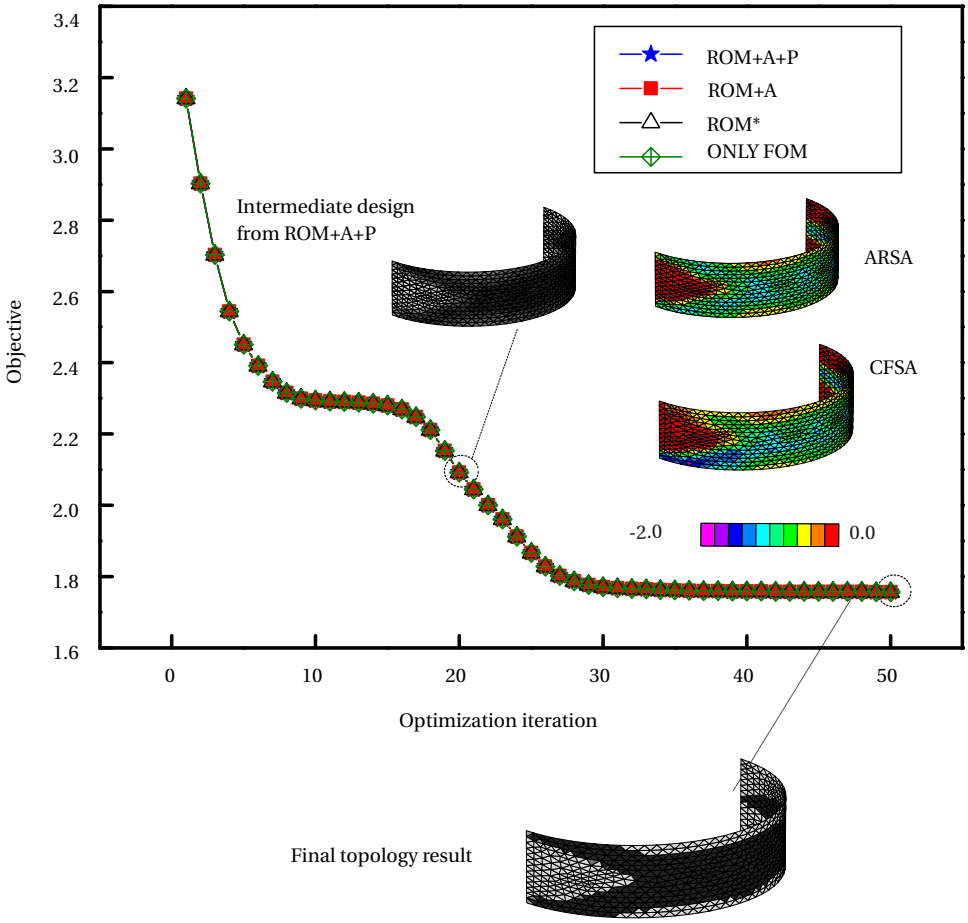


Figure 2.5: Histories of objective values for the cylindrical model. For sensitivity evaluations, an intermediate design is selected from the optimization progress involving ROM+A+P method shown by the middle black-white figure. Focusing on this intermediate design, both ARSA and CFSA are used to calculate the sensitivity values of $u_x^{\mathrm{A}}$ with regard to all element pseudo densities. Different colors in ARSA and CFSA results represent sensitivity values. As observed, ARSA and CFSA provide consistent signs but differing magnitudes at some parts. These differences did not cause a big influence on the optimization progress and topology results. Both convergence and final design are similar. The final topology results for FOMs and ROMs are identically shown in the black-white figure on the right.

### 2.6.2. CANTILEVER SOLID BEAM

A cantilever beam is depicted in Fig. 2.6. In this figure, all details of the problem have been provided and quantities involved have consistent units. Given that the structure exhibits nearly inextensional bending behavior, it can highlight the importance of introducing path derivatives.

We consider four strategies including ROM*, ROM+A, ROM+A+P, and "ONLY FOM" for topology optimization. A comparison of their efficiency is shown in Fig. 2.7. First of all, we investigate the influences of augmentation; the results can be found in Fig. 2.7(a).

As observed, the "ONLY FOM" method requires around 40 FOM-based updates, whereas ROM* only needs 10 FOM-based correction updates per optimization step. When augmentation is included, analyses are purely done by ROMs for 33 optimization steps and for the remaining 17 steps, no more than 10 correction updates are needed. Logically, decreasing the number of FOM-based correction updates results in a slight increase in ROM-based updates for ROM+A method. The increase hardly influences efficiency since in each ROM-based update, only a small matrix of size $10 \times 10$ is factorized. After the introduction of path derivatives, as shown in Fig. 2.7(b), analyses are purely done by ROMs for 45 optimization steps and only 5 FOM-based correction updates are required in the remaining 5 optimization steps.

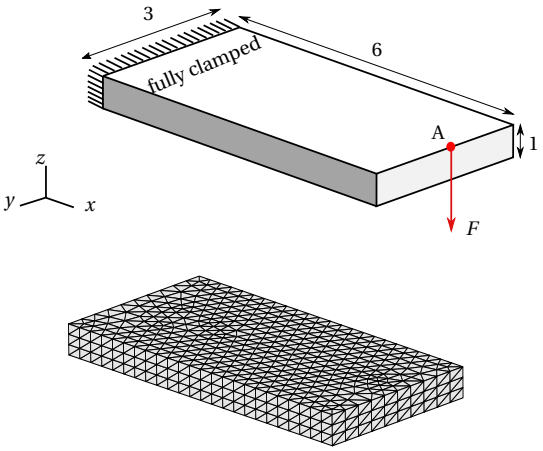


$E$=100 × 10^6
$\nu$=0.3
$F$=60 × 10^6
$\lambda$=1
$\Delta\lambda$=0.1

$\epsilon_r = 10 \times 10^{-9}$
$\epsilon_f = 10 \times 10^{-6}$
$\delta_{\text{rej}} = 10 \times 10^{-9}$
$\delta_s = 0.5$

Objective : Min $V$
s.t.: $-u_z^{\text{A}} \le 1.4$, $u_x^{\text{A}} \le 0.2$
Number of base vectors : 10
Number of solid elements : 5976

Figure 2.6: Cantilever solid beam. All quantities have consistent units. Here, $F$ denotes a concentrate force applied to Point A, $E$ Young's modulus, $\lambda$ load factor, $\Delta\lambda$ load increment, $\epsilon_f$ the convergence tolerance for FOMs (see Eq. (2.15)), $\epsilon_r$ the convergence tolerance for ROMs (see Eq. (2.25)), $\delta_{\text{rej}}$ the rejection tolerance (see Section 2.4.3), $\delta_s$ the error tolerance for ROM-based results (see Section 2.4.1), $V$ Volume, $u_z^{\text{A}}$ displacement of Point A in z direction, and $u_x^{\text{A}}$ displacement of Point A in x direction.

Corresponding convergence curves of the four strategies are compared in Fig. 2.8. In the figure, we zoom in at an intermediate design of ROM+A+P and look at its sensitivities for the constraint $-u_x^{\text{A}} - 1.4 \le 0$. Here the sensitivity was automatically obtained by ARSA since the analysis ended with a ROM-based solution. As a comparison, we then used FOMs to rerun the analysis for the same intermediate design and extracted CFSA values. According to the results, nearly identical SA values are obtained by ARSA and CFSA, and obviously lead to nearly the same optimization progress and topology result of the four strategies. The corresponding topology results can be found in Fig. 2.8.

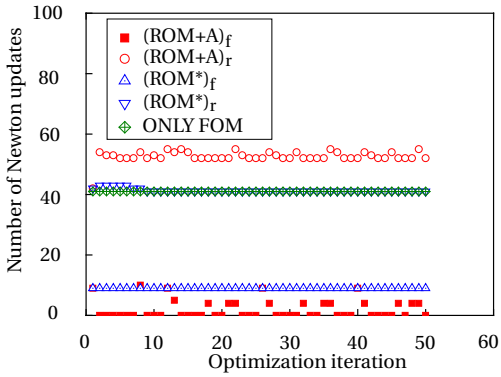


(a) Comparision between ROMs with and without augmentation

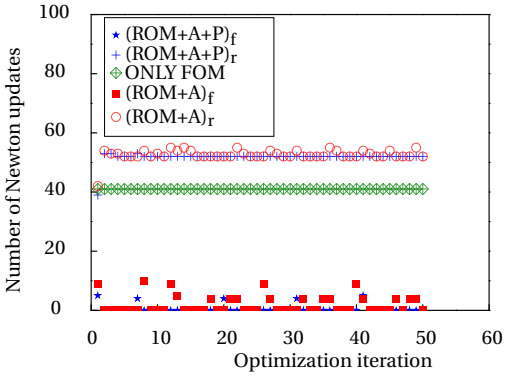


(b) Comparision between ROMs with and without path derivatives

Figure 2.7: Efficiency test for the cantilever beam model. The efficiency of ROMs is measured by counting the number of ROM-based updates and FOM-based correction updates for each topology optimization step. In the left picture, blue shapes denote ROMs without path derivatives and augmentation, where the up-pointing triangles are the number of ROM-based updates and the down-pointing triangles are corresponding FOM-based correction updates. The red shapes denote ROMs with augmentation without path derivatives, where the circles are ROM-based updates and the squares are FOM-based. In the right picture, the blue shapes represent ROMs with augmentation and path derivatives, where the starts are the number of ROM-based updates and the crosses are the corresponding FOM-based updates. The red shapes here are the same as the left picture. These numbers are compared with the number of FOM-based updates of exclusively FOM strategy, which are shown by the green points in both the left and right pictures. From the comparison, ROM+A performs better than ROM*, and ROM+A+P further improves the efficiency compared to ROM+A.

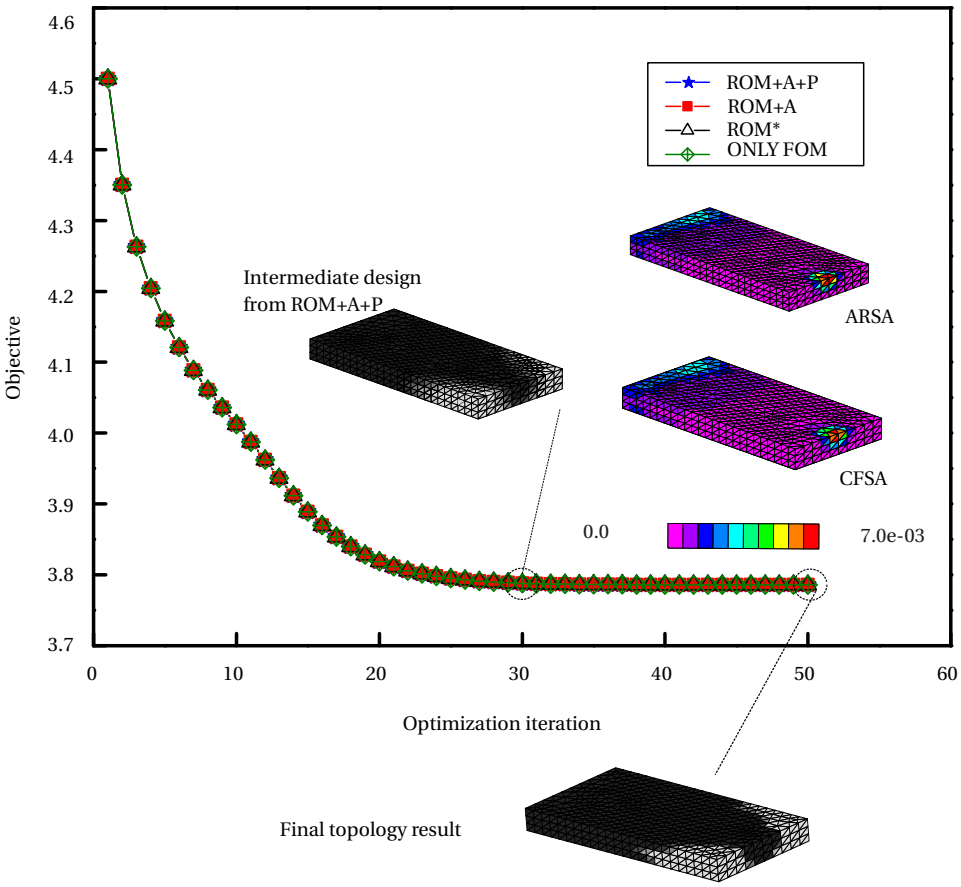


Figure 2.8: Histories of objective values for the cantilever beam model. For sensitivity evaluations, an intermediate design is selected from the optimization progress involving ROM+A+P method shown by the middle black-white figure. Focusing on this intermediate design, both ARSA and CFSA are used to calculate the sensitivity values of $-u_z^{\mathrm{A}}$ with regard to all element pseudo densities. Different colors in ARSA and CFSA results represent sensitivity values, where ARSA and CFSA provide nearly identical results and lead to the same result shown in the black-white figure on the right.

### 2.6.3. THIN PLATE MODEL

A thin plate model is described in Fig. 2.9. In this figure, all details of the problem have been provided and quantities have consistent units. In this example, we expect a very slender topology result where displacements can increase largely between two neighboring load steps. In this way, the advantage of augmentation technique can be clearly illustrated. We use four strategies including ROM*, ROM+A, ROM+A+P, and "ONLY FOM" for topology optimization. The efficiency is compared in Fig. 2.10. First of all, we investigate the influences of augmentation and the results can be found in Fig. 2.10(a). As observed, the "ONLY FOM" method requires roughly 40 updates until the 20th optimization step. Thereafter, it increases to approximately 70 when the structure has become more slender. Similarly, after the 20th optimization step, ROM* intensively involves FOM-based

correction updates.

This inaccuracy is mainly due to large displacement changes between neighboring load steps. The situation can be improved by application of the augmentation technique. With augmentation from higher load levels of previous designs, ROM+A needs fewer than 20 correction updates for the whole optimization progress. After involving path derivative, as shown in Fig. 2.10(b), although slightly, the efficiency can be further improved compared with ROM+A.

Corresponding convergence curves are compared in Fig. 2.11. In the figure, we zoom in at an intermediate design of ROM+A+P and look at its sensitivity of the constraint $u_z^{\mathrm{A}} - 0.15 \leq 0$. Here the sensitivity was automatically obtained by ARSA since the analysis ended with a ROM-based solution. As a comparison, we used FOMs to rerun the analysis for the same intermediate design and got CFSA values. According to the results, identical SA values are obtained by ARSA and CFSA, and obviously lead to the same optimization progress and topology result of the four strategies. The corresponding final topology is also shown in Fig. 2.11.

In alignment with the nonlinear case, for the linear case, we minimize the volume while considering displacement constraints, but here the upper limit is established to be 100 times smaller than the nonlinear case. As illustrated in Fig. 2.12, with large displacement requirements, the solution found in nonlinear scope distributes the material uniformly along the symmetrical boundary, attempting to move away from the simply supported boundary to form a flexible strip, which can exhibit large deflections and rotations. With small displacement requirements, the material is concentrated more towards the applied force, resulting in a design that is closely linked to the simply supported boundary. The results demonstrated that topologies in nonlinear and linear scope can be distinct, consequently, linear design is not a fair replacement of the nonlinear one.

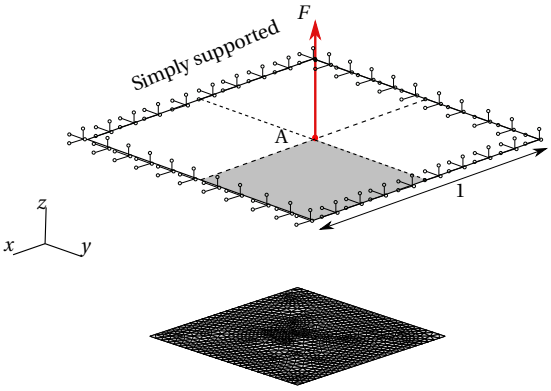


$E$=300 × 10$^9$ $t$=0.01
$\nu$=0.3 $\epsilon_r = 10 \times 10^{-9}$
$F$=30 × 10$^6$ $\epsilon_f = 10 \times 10^{-6}$
$\lambda$=0.15 $\delta_{\mathrm{rej}} = 10 \times 10^{-9}$
$\Delta\lambda$=0.015 $\delta_s = 0.5$

Objective : Min $V$
s.t.: $u_z^{\mathrm{A}} \leq 0.15$
Number of base vectors : 10
Number of elements : 1496

Figure 2.9: Square thin plate. All quantities have consistent units. Here, $F$ denotes a concentrated force applied to Point A, $t$ thickness, $E$ Young's modulus, $\lambda$ load factor, $\Delta\lambda$ increment of $\lambda$, $\epsilon_f$ the convergence tolerance for FOMs (see Eq. (2.15)), $\epsilon_r$ the convergence tolerance for ROMs (see Eq. (2.25)), $\delta_{\mathrm{rej}}$ the rejection tolerance (see Section 2.4.3), $\delta_s$ the error tolerance for ROM-based results (see Section 2.4.1), $V$ volume, and $u_z^{\mathrm{A}}$ displacement of Point A in z-direction. Due to symmetry, a quarter of the plate is selected for optimization.

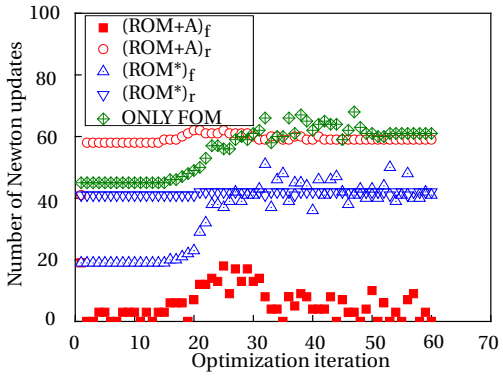


(a) comparision between ROMs with and without augmentation

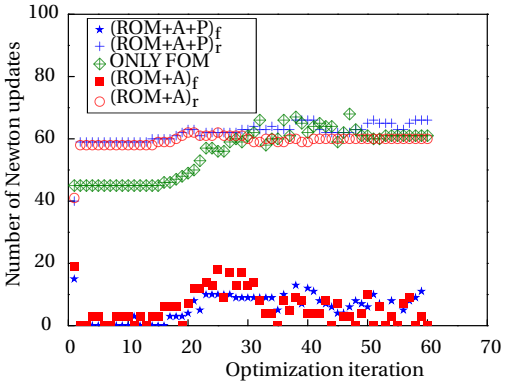


(b) Comparison between ROMs with and without path derivatives

Figure 2.10: Efficiency test for the thin plate. The efficiency of ROMs is measured by counting the number of ROM-based updates and FOM-based correction updates for each topology optimization step. In the left picture, blue shapes denote ROMs without path derivatives and augmentation, where the up-pointing triangles are the number of ROM-based updates and the down-pointing triangles are corresponding FOM-based correction updates. The red shapes denote ROMs with augmentation without path derivatives, where the circles are ROM-based updates and the squares are FOM-based. In the right picture, the blue shapes represent ROMs with augmentation and path derivatives, where the starts are the number of ROM-based updates and the crosses are the corresponding FOM-based updates. The red shapes here are the same as the left picture. These numbers are compared with the number of FOM-based updates of exclusively FOM strategy, which are shown by the green points in both the left and right pictures. From the comparison, ROM+A is obviously superior to ROM*. ROM+A+P performs slightly better than ROM+A.

As is commonly understood, when a design exhibits mild nonlinearity, the differences between linear and nonlinear topologies may not be distinct. Thus, neglecting nonlinearity in the analysis may only lead to displacement errors but not an ineffective design. For relative high nonlinear cases, the differences between linear and nonlinear topologies could be obvious. Normally, a design optimized in the linear regime cannot generally satisfy the requirements of the nonlinear problem. For this thin plate case, we can observe a noticeable difference between the topologies under small and large dis-

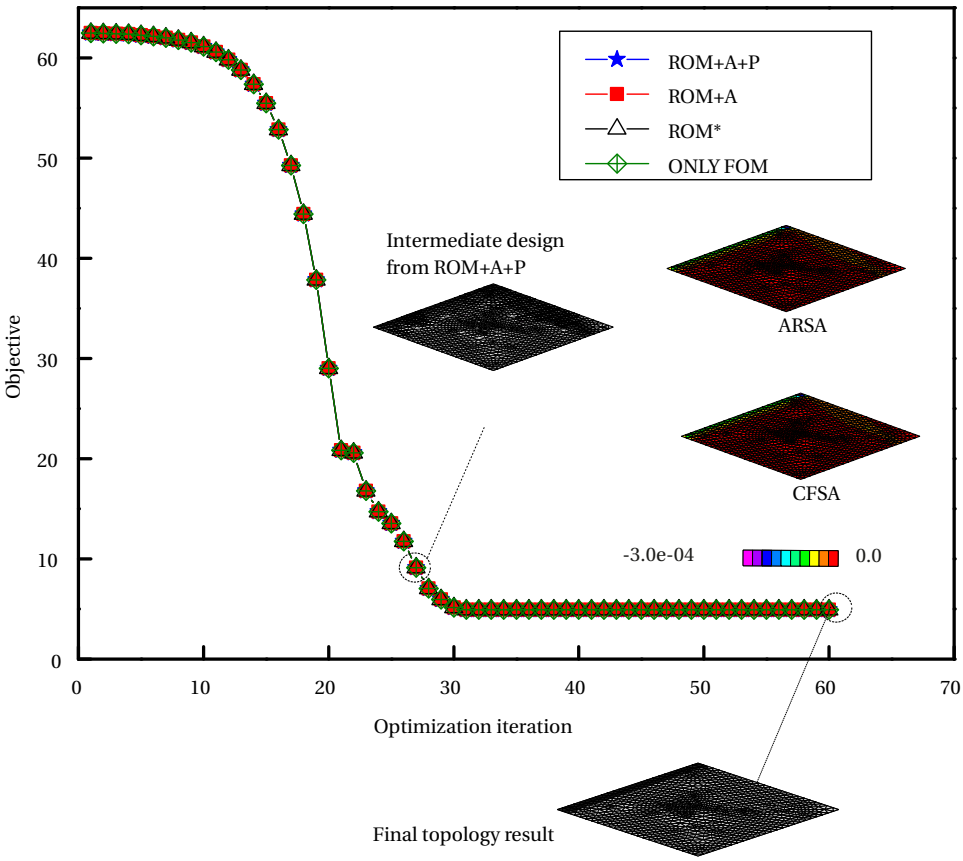


Figure 2.11: Histories of objective values for the square thin plate model. For sensitivity evaluations, an intermediate design is selected from the optimization progress involving ROM+A+P method shown by the middle black-white figure. Focusing on this intermediate design, both ARSA and CFSA are used to calculate the sensitivity values of $u_x^{\mathrm{A}}$ with regard to all element pseudo densities. Different colors in ARSA and CFSA results represent sensitivity values, where ARSA and CFSA provide nearly identical results and lead to the same result shown in the black-white figure on the right.

placement requirements shown in Fig. 2.12.

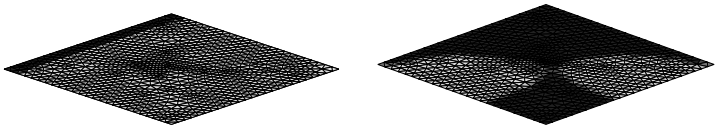

(a) Nonlinear result (b) Linear result

Figure 2.12: Comparison between linear and nonlinear topology results for the thin plate model. For both cases, we minimize volume with displacement constraints. For the linear case, the upper limit of displacement constraint is 0.0015 but for the nonlinear case, it is 0.15. At convergence, both displacement constraints are active.

### 2.6.4. SPHERICAL STRUCTURE

A spherical structure is illustrated in Fig. 2.13. In this figure, all details of the problem have been provided and all quantities have consistent units. The structure is separately discretized with shell elements and solid elements. We conducted topology optimization for both cases using the four strategies, and their efficiency and convergence results will be compared in the following subsections. Given that the structure exhibits nearly inextensional bending behavior, it can demonstrate the necessity of introducing path derivatives.

#### SPHERICAL THIN SHELL

For the structure meshed with shell elements shown in Fig. 2.13(c), we compare the efficiency of the four strategies in Fig. 2.14. First, we look into the effects of augmentation excluding path derivatives. The results can be found in Fig. 2.14(a). The "ONLY FOM" method performs stably, which requires roughly 70 updates per optimization step. For ROMs without augmentation, i.e., ROM*, it needs around 40 FOM-based and 80 ROM-based updates until the 20th optimization iteration. Thereafter, the number of both FOM-based and ROM-based updates becomes unstable. Especially, more than 80 FOM-based correction updates are required in the majority of optimization steps. After introducing the augmentation (see results of ROM+A), the number of ROM-based updates becomes much smaller compared to ROM*, but is still around and even exceeds 80. The efficiency can be improved further by introducing path derivatives. As shown in Fig. 2.14(b), ROMs with path derivatives and augmentation, i.e., ROM+A+P, can reduce the number of FOM-based correction updates to fewer than 40 for most optimization steps. However, the number of FOM-based corrections and ROM-based updates is still unstable. Particularly, at the 28th optimization step, we observe more than 100 FOM-based updates.

In order to understand the reasons behind the large number of FOM-based updates, we zoom in on the intermediate design at the 28th optimization step. Then, the ROM-based and the corrected FOM-based deformations at the last load incremental step are shown in Fig. 2.14(b). As observed, a local buckling mode is clearly visible in the middle low-density area of the ROM-based deformation figure. When looking at the corresponding FOM-based deformations, we observe a completely different local buckling mode. Given the differences, FOMs are intensively used to transfer the ROM-based one to the FOM-based one. To address this, in future work, techniques for refining ROMs need to be explored.

Corresponding convergence curves for the four strategies are shown in Fig. 2.15. As observed, ROM+A+P and ROM+A converge to the same objective value, which is slightly larger than the "ONLY FOM" result. The differences related to final topologies can be found in Fig. 2.15, which could result from the differences between ROM-based and FOM-based solutions, as well as the approximation introduced by the ROM-based sensitivity analysis method ARSA. The ARSA value of the constraint $-u_z^{\mathrm{A}}-4 \leq 0$ for an intermediate design can be observed in Fig. 2.15. As a comparison, we reran the analysis using FOMs for the same intermediate design and got CFSA. Here CFSA and ARSA have the same sign but different magnitudes. These errors could lead to different results when structures become flexible. As for ROM*, it converges to nearly the same result as the "ONLY FOM" method. This would not be surprising after looking at the efficiency test

(see Fig. 2.14(a)). Since the inaccuracy of ROM*, nearly all of the load incremental steps ended with FOM-based solutions, and consequently, the optimization is led by CFSA instead of ARSA.



### SPHERICAL SOLID SHELL

For the structure meshed with solid elements in Fig. 2.13(b), we compare the efficiency of the four strategies shown in Fig. 2.16. We start by examining the effects of augmentation and the results are shown in Fig. 2.16(a). Here, the "ONLY FOM" method requires roughly 50 updates for most optimization steps, however, increasing to more than 100 between the 20th and the 40th optimization step. We then zoom in on one of the intermediate designs and look at the deformation, see Fig. 2.16(a). As observed, the elements on the left bottom corner of the design are inside-out due to compression, which leads to convergence difficulties in the FOM-based analysis. The convergence difficulties in FOMs also have big influence on ROM*, since it intensively uses FOMs for both error correction and initialization at every optimization step. For ROM+A, the influence becomes less severe since the augmentation technique reduces the times of switching back to FOMs and avoids FOM-based initialization at every optimization step. Here only for three of the optimization steps, ROM+A requires more than 20 correction updates and the maximum number is about 40. If path derivatives are used (see Fig. 2.16(b)), a better result is obtained, though not distinctly. Here, the largest number of FOM-based correction updates is roughly 30.

The corresponding convergence curves are compared in Fig. 2.17. Although the four strategies went through different optimization processes, they ultimately achieve similar objective values. ROM+A and ROM+A+P converge to nearly the same objective value, which is a bit larger than the one of "ONLY FOM". The differences in topology can be seen on the right of Fig. 2.17, where more material appears in the middle of the ROM+A+P and ROM+A results. These variations could result from the differences between ROM-based and FOM-based solutions ($\delta_s = 0.5$), as well as ARSA. The ARSA value of the constraint $-u_z^{\mathrm{A}} - 4 \leq 0$ for an intermediate design from ROM+A+P can be seen in Fig. 2.17. As a comparison, we then used FOMs to rerun the analysis for the same intermediate design and got CFSA values. According to the results, ARSA and CFSA provide a consistent sign but differing magnitudes. These errors could lead to differences in results when the structure is flexible. As for ROM*, since CFSA is frequently used due to its inaccurate ROM-based solutions, it converges to nearly the same result as the "ONLY FOM" method.

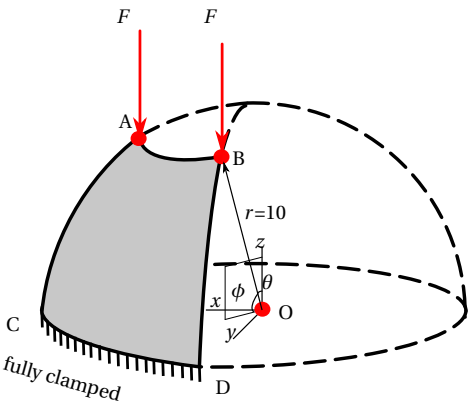


| Shell structure | |
|---|---|
| $E$=100 × $10^6$ | $t$=0.1 |
| $\nu$=0.3 | $\epsilon_r = 10 \times 10^{-9}$ |
| $F$=6 × $10^3$ | $\epsilon_f = 10 \times 10^{-6}$ |
| $\lambda$=0.15 | $\delta_{\text{rej}} = 10 \times 10^{-9}$ |
| $\Delta\lambda$=0.015 | $\delta_s = 0.5$ |

Objective : Min $V$
s.t.: $-u_z^{\text{A}} \le 4$, $-u_z^{\text{B}} \le 4$,
$-u_x^{\text{A}} \le -1$, $-u_y^{\text{B}} \le -1$
Number of base vectors : 20

| Solid structure | |
|---|---|
| $E$=100 × $10^6$ | $t$=1 |
| $\nu$=0.3 | $\epsilon_r = 10 \times 10^{-9}$ |
| $F$=6 × $10^3$ | $\epsilon_f = 10 \times 10^{-6}$ |
| $\lambda$=1 | $\delta_{\text{rej}} = 10 \times 10^{-9}$ |
| $\Delta\lambda$=0.1 | $\delta_s = 0.5$ |

Objective : Min $V$
s.t.: $-u_z^{\text{A}} \le 4$, $-u_z^{\text{B}} \le 4$,
$-u_x^{\text{A}} \le -1$, $-u_y^{\text{B}} \le -1$
Number of base vectors : 20

(a)

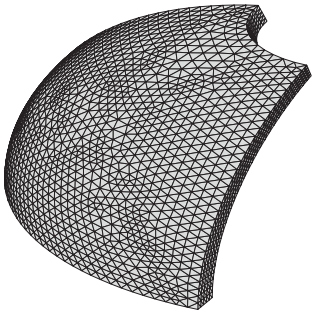

(b)

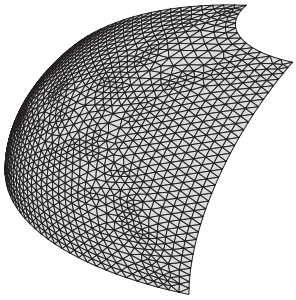

(c)

Figure 2.13: Spherical structure and its meshes. (a) is the geometry. All quantities have consistent units. Coordinates of Point A is $(r,\theta,\phi) = (10, \frac{2\pi}{5}, 0)$, Point B $(r,\theta,\phi) = (10, \frac{2\pi}{5}, \frac{\pi}{2})$, Point C $(r,\theta,\phi) = (10, \frac{\pi}{2}, 0)$, and Point D $(r,\theta,\phi) = (10, \frac{\pi}{2}, \frac{\pi}{2})$. Here, $F$ denotes nodal forces applied to Point A and B, $t$ thickness, $E$ Young's modulus, $\lambda$ load factor, $\Delta\lambda$ increment of $\lambda$,$\epsilon_f$ the convergence tolerance for FOMs (see Eq. (2.15)), $\epsilon_r$ the convergence tolerance for ROMs (see Eq. (2.25)), $\delta_{\text{rej}}$ the rejection tolerance (see Section 2.4.3), $\delta_s$ the error tolerance for ROM-based results (see Section 2.4.1), $V$ Volume, $u_z^{\text{A}}$ displacement of Point A in z direction, $u_x^{\text{A}}$ displacement of Point A in x direction, $u_z^{\text{B}}$ displacement of Point B in z direction, and $u_x^{\text{B}}$ displacement of Point B in x direction. The model meshed with solid elements is shown in (b). The number of solid elements is 34740. The model meshed with shell elements is shown in (c). The number of shell elements is 2316

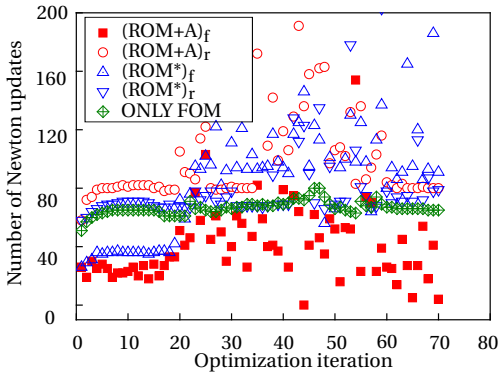


(a) Comparision between ROMs with and without augmentation

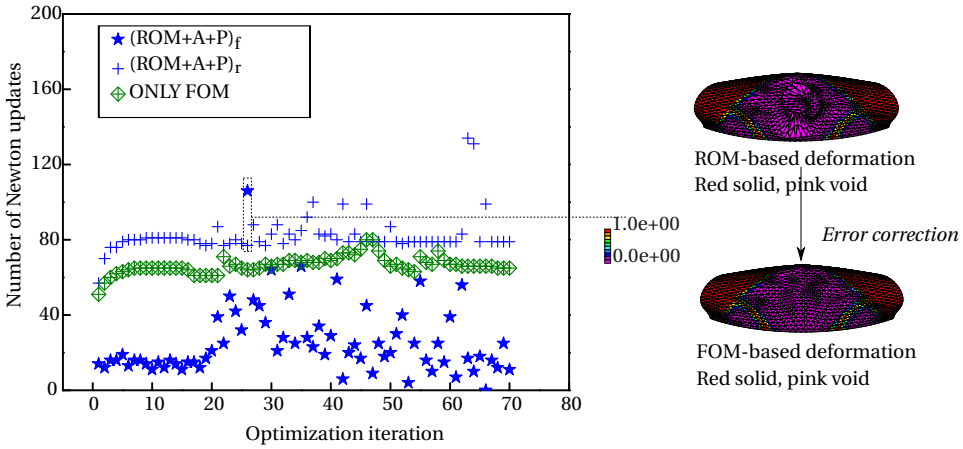


(b) Comparison between ROMs with and without path derivatives

Figure 2.14: Efficiency test for the spherical thin shell. The efficiency of ROMs is measured by counting the number of ROM-based updates and FOM-based correction updates for each topology optimization step. In (a), blue shapes denote ROMs without path derivatives and augmentation, where the up-pointing triangles are the number of ROM-based updates and the down-pointing triangles are corresponding FOM-based correction updates. The red shapes denote ROMs with augmentation without path derivatives, where the circles are ROM-based updates and the squares are FOM-based. In (b), the blue shapes represent ROMs with augmentation and path derivatives, where the starts are the number of ROM-based updates and the crosses are the corresponding FOM-based updates. The red shapes here are the same as the left picture. These numbers are compared with the number of FOM-based updates of exclusively FOM strategy, which are shown by the green points in both (a) and (b). From the results, ROM+A performs better than ROM*, though both of them show extremely unstable update numbers. ROM+A+P has the best performance among the three ROM strategies. However, a large number of correction iterations are still observed. To understand this, an intermediate design is selected and ROM-based analysis is performed. Concerning the final load incremental step, corresponding ROM-based and the corrected FOM-based deformations are shown on the right. As observed, the ROM-based and FOM-based results show different local buckling modes. Thus, FOMs are intensively involved to transfer the ROM-based one to the FOM-based one.

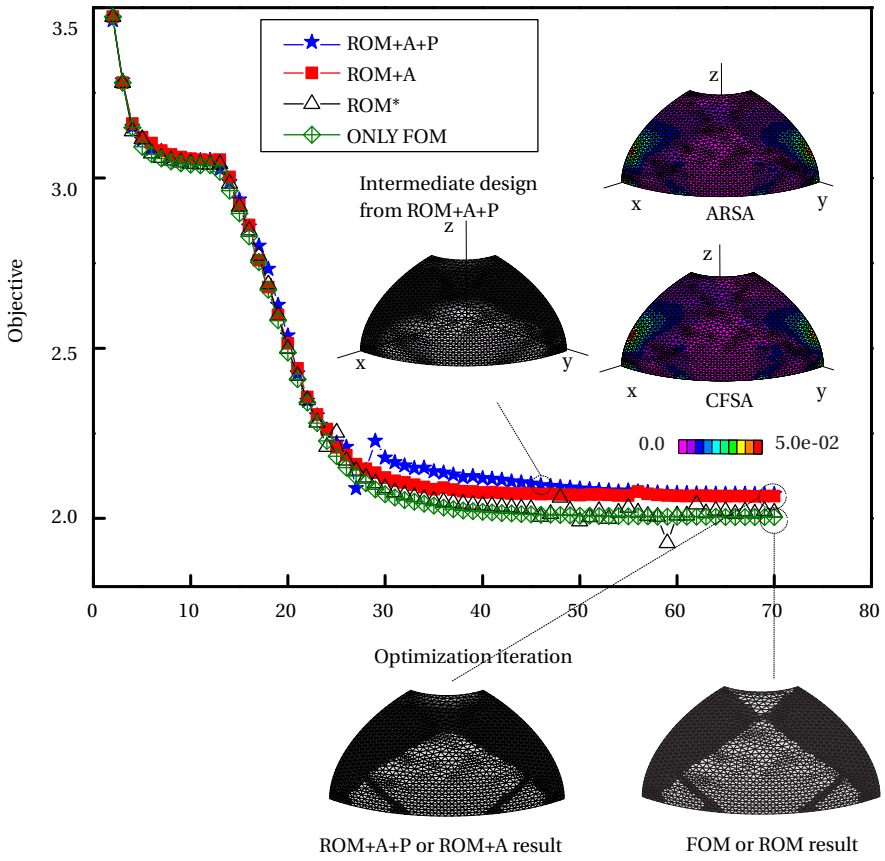


Figure 2.15: Histories of objective values for the spherical thin shell model. An intermediate design is selected from the optimization progress involving ROM+A+P method shown by the middle black-white figure. Focusing on this intermediate design, both ARSA and CFSA are used to calculate the sensitivity values of $-u_z^{\mathrm{A}}$ with regard to all element pseudo densities. Different colors in ARSA and CFSA represent sensitivity values. Here ARSA and CFSA provide a consistent sign with differing magnitudes. These errors lead to slightly different results when the structure is flexible, which are illustrated by the black-white topology results shown on the right. Here, designs, at the 70th optimization steps, of ROM+A+P and ROM+A have a bit more material than the design of "ONLY FOM". For ROM*, since its inaccuracy, nearly all of the load incremental steps ended with FOM-based solutions, and consequently, the optimization is led by CFSA instead of ARSA. Then, it converges to the same result as the "ONLY FOM" method.

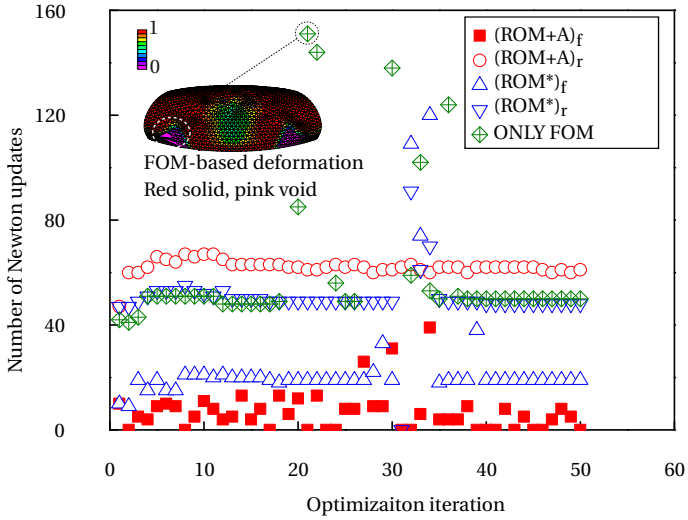


(a) Comparision between ROMs with and without augmentation

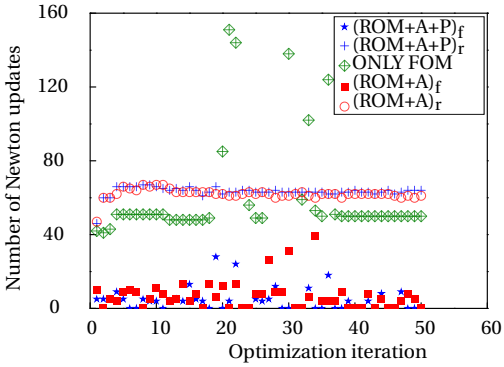


(b) ROMs with and without path derivatives

Figure 2.16: Efficiency test for the spherical solid shell. The efficiency of ROMs is measured by counting the number of ROM-based updates and FOM-based correction updates for each topology optimization step. In (a), blue shapes denote ROMs without path derivatives and augmentation, where the up-pointing triangles are the number of ROM-based updates and the down-pointing triangles are corresponding FOM-based correction updates. The red shapes denote ROMs with augmentation without path derivatives, where the circles are ROM-based updates and the squares are FOM-based. In (b), the blue shapes represent ROMs with augmentation and path derivatives, where the starts are the number of ROM-based updates and the crosses are the corresponding FOM-based updates. The red shapes here are the same as the left picture. These numbers are compared with the number of FOM-based updates of exclusively FOM strategy, which are shown by the green points in both (a) and (b). From the results, the ONLY FOM method encounters divergence difficulties between the 20th and the 40th optimization steps. The reason is the instability of low-density elements as shown in the deformation figure. The convergence difficulties in FOMs have big influence on ROM* since it intensively uses FOMs for both error correction and initialization at every optimization step. For ROM+A, the influence becomes less severe since the augmentation technique improves accuracy and avoids FOM-based initialization at every optimization step. Then, if path derivatives are used, a better result than ROM+A is obtained, though the differences are not distinct.

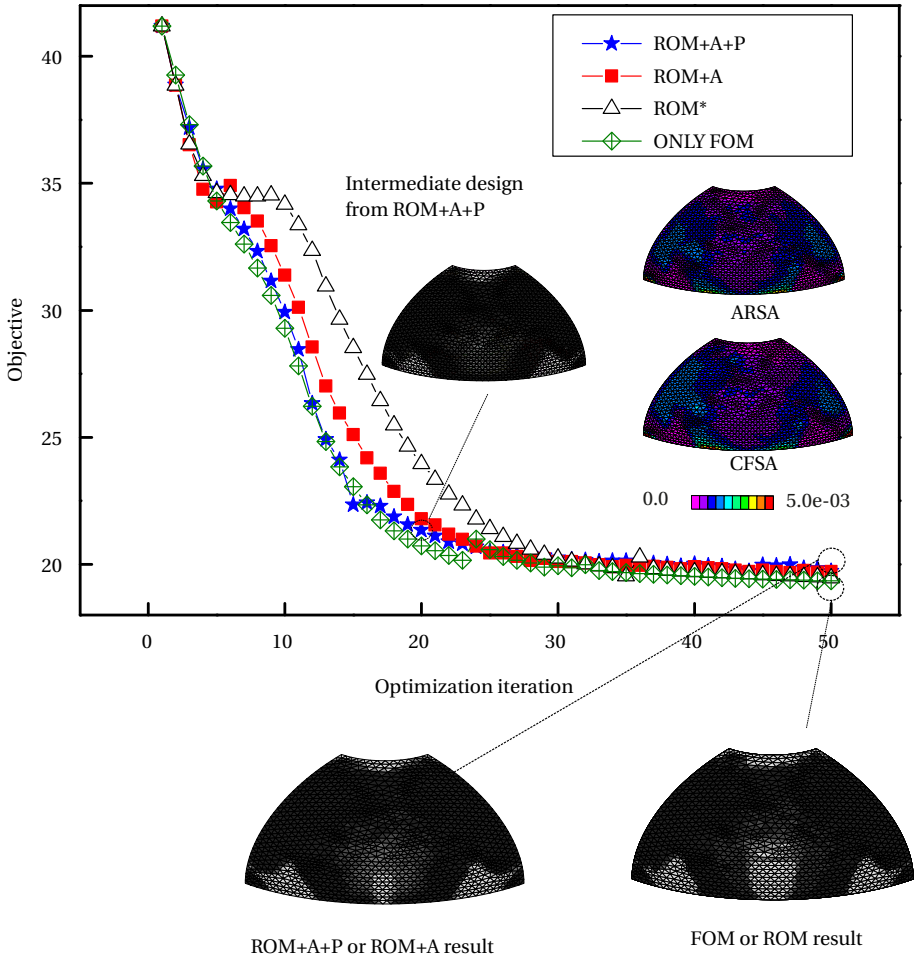


Figure 2.17: Histories of objective values for the spherical solid shell. An intermediate design is selected from the optimization progress involving ROM+A+P method shown by the middle black-white figure. Focusing on this intermediate design, both ARSA and CFSA are used to calculate the sensitivity values of $-u_z^{\mathrm{A}}$ with regard to all element pseudo densities. Different colors in ARSA and CFSA represent sensitivity values, where ARSA and CFSA provide a consistent sign with differing magnitudes. These errors lead to slightly different results when the structure is flexible, which are illustrated by the black-white topology results shown on the right. Here, designs, at the 50th optimization step, of ROM+A+P and ROM+A have a bit more material than the design of "ONLY FOM". As for ROM*, since CFSA is frequently used due to its inaccurate ROM-based solutions, it converges to nearly the same result as the "ONLY FOM" methods.

## 2.7. SUMMARY AND CONCLUSIONS

This study introduces ROMs to improve the computing efficiency of incremental-iterative, geometrically nonlinear finite element simulations and the corresponding sensitivity analysis for topology optimization problems. We have explained the initialization, update, error control, and augmentation techniques for the proposed ROMs. Besides, we have proposed approximated ROM-based sensitivity analysis strategies (ARSA) for prac-

tical and efficient use. Finally, the performance of the mentioned techniques has been examined by various geometrically nonlinear examples involving both solid as well as shell elements, and the results have been benchmarked against normal FOM-based ones.

Based on the findings, the proposed ROMs can effectively improve computing efficiency with a base vector number of no more than 20. Especially, with the augmentation from previous designs, the ROMs' efficiency can be greatly improved. Importantly, path derivatives are necessary for flexible structures; otherwise, ROM-based analysis lacks an effective description of flexible modes.



It is noticed that the ROM base also includes information from the void areas. As we use a Newton process, the displacements and rotations may be less accurate in void areas than in the solid domain. Given the fact that we need a basis which includes all nodal degrees of freedom, only selectively including nodal degrees of freedom is not an option. Moreover, it would increase complexity of the method significantly. Finally, the examples demonstrate that including all nodal degrees of freedom in the basis does not lead to complications. One issue caused by void areas could be spurious local buckling behavior shown in the spherical shell example. To address the issue, additional methodologies need to be employed, which is beyond the scope of the current study.

With regard to sensitivities, we proposed an approximate ROM-based sensitivity analysis method (ARSA). Here, we ignore the gradients of base vectors from previous designs with regard to design variables and consequently, exclude previous tangent operators. In this way, we improve the efficiency of ROM-based sensitivity analysis. The suggested ARSA can successfully guide most cases to the same solution as obtained using a FOM-based formulation. However, for flexible structures, we observe slight differences between ROM-based and FOM-based topology results. The differences could result from the errors introduced by ROM-based solutions as well as the approximation brought in by ARSA.

## REFERENCES

[1] M. P. Bendsøe and O. Sigmund, *Material interpolation schemes in topology optimization,* Archive of applied mechanics **69**, 635 (1999).

[2] N. P. van Dijk, K. Maute, M. Langelaar, and F. Van Keulen, *Level-set methods for structural topology optimization: a review,* Structural and Multidisciplinary Optimization **48**, 437 (2013).

[3] Y. M. Xie and G. P. Steven, *A simple evolutionary procedure for structural optimization,* Computers & structures **49**, 885 (1993).

[4] O. Querin, V. Young, G. Steven, and Y. Xie, *Computational efficiency and validation of bi-directional evolutionary structural optimisation,* Computer Methods in Applied Mechanics and Engineering **189**, 559 (2000).

[5] X. Guo, W. Zhang, and W. Zhong, *Doing topology optimization explicitly and geometrically—a new moving morphable components based framework,* Journal of Applied Mechanics **81**, 081009 (2014).

[6] A. Polynkin, F. Van Keulen, and V. Toropov, *Optimization of geometrically nonlinear thin-walled structures using the multipoint approximation method,* Structural optimization **9**, 105 (1995).

[7] H. Altenbach, O. Morachkovsky, K. Naumenko, and A. Sychov, *Geometrically nonlinear bending of thin-walled shells and plates under creep-damage conditions,* Archive of Applied Mechanics **67**, 339 (1997).

[8] Z. Luo and L. Tong, *A level set method for shape and topology optimization of large-displacement compliant mechanisms,* International journal for numerical methods in engineering **76**, 862 (2008).

[9] B. S. Lazarov, M. Schevenels, and O. Sigmund, *Robust design of large-displacement compliant mechanisms,* Mechanical sciences **2**, 175 (2011).

[10] T. Bruns, O. Sigmund, and D. A. Tortorelli, *Numerical methods for the topology optimization of structures that exhibit snap-through,* International Journal for Numerical Methods in Engineering **55**, 1215 (2002).

[11] K. Bathe, *Finite Element Procedures* (Prentice Hall, 2006).

[12] N. P. van Dijk, M. Langelaar, and F. van Keulen, *Element deformation scaling for robust geometrically nonlinear analyses in topology optimization,* Structural and Multidisciplinary Optimization **50**, 537 (2014).

[13] R. D. Lahuerta, E. T. Simões, E. M. Campello, P. M. Pimenta, and E. C. Silva, *Towards the stabilization of the low density elements in topology optimization with large deformation,* Computational Mechanics **52**, 779 (2013).

[14] T. E. Bruns and D. A. Tortorelli, *An element removal and reintroduction strategy for the topology optimization of structures and compliant mechanisms,* International Journal for Numerical Methods in Engineering **57**, 1413 (2003).

[15] G. Xingjun and M. Haitao, *Topology optimization of continuum structures under buckling constraints,* Computers and Structures **157**, 142 (2015).

[16] N. Pedersen, *Maximization of eigenvalues using topology optimization,* Structural and Multidisciplinary Optimization **20**, 2 (2000).

[17] J. Zhao and W. Chunjie, *Geometrically nonlinear finite element behaviour using buckling mode superposition,* Computer Methods in Applied Mechanics and Engineering **53**, 101 (2016).

[18] D. Nagy and M. König, *Geometrically nonlinear finite element behaviour using buckling mode superposition,* Computer Methods in Applied Mechanics and Engineering **19**, 447 (1979).

[19] A. S. L. Chan and K. M. Hsiao, *Nonlinear analysis using a reduced number of variables,* Computer Methods in Applied Mechanics and Engineering **52**, 899 (1985).

[20] A. Safjan, *Nonlinear structural analysis via reduced basis technique,* Computers and Structures **29**, 1055 (1988).

[21] K. Kim, A. G. Radu, X. Q. Wang, and M. P. Mignolet, *Nonlinear reduced order modeling of isotropic and functionally graded plates,* International Journal of Non-Linear Mechanics **49**, 100 (2013).

[22] O. Amir, M. P. Bendsøe, and O. Sigmund, *Approximate reanalysis in topology optimization,* International Journal for Numerical Methods in Engineering **78**, 1474 (2009).

[23] C. Gogu, *Improving the efficiency of large scale topology optimization through on-the-fly reduced order model construction,* International Journal for Numerical Methods in Engineering **101**, 281 (2015).

[24] E. Hooijkamp and F. v. Keulen, *Topology optimization for linear thermo-mechanical transient problems: Modal reduction and adjoint sensitivities,* International Journal for Numerical Methods in Engineering **113**, 1230 (2018).

[25] S. Wang, E. de Sturler, and G. Paulino, *Large-scale topology optimization using preconditioned krylov subspace methods with recycling,* International journal for numerical methods in engineering **69**, 2441 (2007).

[26] L. Xia and P. Breitkopf, *A reduced multiscale model for nonlinear structural topology optimization,* Computer Methods in Applied Mechanics and Engineering **280**, 117 (2014).

[27] C. E. Orozco and O. N. Ghattas, *A reduced sand method for optimal design of nonlinear structures,* International Journal for Numerical Methods in Engineering **40**, 2759 (1997).

[28] F. Van Keulen and J. Booij, *Refined consistent formulation of a curved triangular finite rotation shell element,* International journal for numerical methods in engineering **39**, 2803 (1996).

# 3

# ELIMINATION OF SPURIOUS MODES IN ROM-BASED TOPOLOGY OPTIMIZATION OF GEOMETRICALLY NONLINEAR STRUCTURES

*In geometrically nonlinear topology optimization, “low-density areas", subjected to compression from neighboring stiffer regions, can lead to complications, such as “inside-out" elements in 2D structures or spurious local buckling in shells and plates. The former typically causes computational divergence, while the latter, though not always divergent, could significantly increase the analysis iterations required for convergence, resulting in significant higher computational costs. To enhance efficiency, reduced-order modeling (ROM) could be used, as it employs a small number of generalized variables to approximate the behavior governed by the numerous degrees of freedom (DOFs) in the full-order model (FOM). However, the presence of spurious buckling can severely compromise ROM efficiency, even requiring more analysis iterations compared to methods relying on full-order models.*

*To address the analysis convergence difficulties caused by spurious buckling in ROMs, two approaches are investigated. The first and simplest approach involves removing spurious modes from the ROM basis. The second approach focuses on eliminating spurious modes directly from the underlying physics, which can be extended to standard FOM-based analyses. The above strategies are primarily evaluated using shell models, providing a detailed analysis of their effectiveness.*

This chapter will be submitted to a journal

## 3.1. INTRODUCTION

Topology optimization (TO) [1] is a highly efficient tool which can assist in creating designs in innovative and competitive sectors of industry. The basic idea is to achieve designs satisfying specific engineering requirements by optimizing material distribution in a prescribed design domain. The method is broadly used in various fields [2–5]. Most of the applications are restricted to linear settings. However, if structures must perform at or beyond the limits of conventional design envelopes, considering only linearity in structural design can limit their reliability and performance. For example, accounting for geometrically nonlinearity is essential when designing thin-walled structures exhibiting finite deflections and rotations [6–8], flexures delivering high-precision motions [9, 10], and snap-through mechanisms [11–13]. Thus, exploring methods for TO involving geometrically nonlinearity is critical. However, considering geometrically nonlinear structures in TO is particularly challenging because (i) the computational burden associated with resolving the nonlinear governing equations [14, 15] and (ii) analysis convergence difficulties caused by low-density areas [16].

The first challenge, the computational burden, is due to intensive use of incremental-iterative finite element simulations. Reduced-order models (ROMs) are potentially powerful strategies to deal with such problems. ROMs use a small number of generalized variables to approximate the behavior governed by a large number of degrees of freedom (DOFs) associated with the full-order model (FOM). Each generalized variable corresponds to a base vector, which can be a buckling mode, a static displacement field, a natural frequency mode, among others [17–19]. In topology optimization, ROMs have been widely applied in linear settings [20–23], with a few studies addressing material nonlinearity [24, 25]. Building on their promising results, we extended the use of ROMs to geometrically nonlinear topology optimization as formulated in our previous work [15]. The proposed ROMs are based on Ritz' method. They target a relatively small set of carefully adapted base vectors, while at the same time, the accuracy of the ROM-based solutions can be guaranteed. The ROM basis is constructed adaptively and may include FOM-based linear solutions, nonlinear solutions, and approximate path derivatives. To adapt to the optimization process, the ROM basis may be augmented using base vectors generated from previous design iterations. Numerical tests confirmed the efficiency of ROM-based topology optimization (TO) [15]. However, when there are analysis convergence difficulties caused by low-density areas, ROMs are unable to effectively reduce the computational burden.

The analysis convergence difficulties arise from low-density areas being compressed by neighboring stiffer regions. This leads to ill-conditioned tangent stiffness matrices, typically causing “inside-out" elements in 2D structures and local buckling in shells and plates. The former often results in computational divergence, while the latter, although not always divergent, could significantly increase the number of analysis iterations needed for convergence. In ROMs, nonlinear solutions are typically used as basis vectors, inherently incorporating local buckling into the ROM basis and thereby spoiling the convergence of ROMs. To effectively utilize ROMs, the analysis convergence difficulties caused by low-density areas must be addressed.

Several studies have proposed methods to address instabilities in FOM settings. One of them is the element removal and reintroduction method proposed by Bruns and Tor-

torelli [16]. This method systematically removes low-density elements from the finite element mesh during the incremental-iterative solution process and reintroduces them for sensitivity evaluations. However, careful handling of boundary conditions is crucial after element removal to avoid encountering singular structures. Additionally, intermediate density elements may still remain in the design domain, potentially leading to instabilities despite the application of this method. More importantly, this method is not easily compatible with the proposed ROMs since element removal will lead to inconsistencies between different base vectors which are generated from different intermediate designs. For another method, Lahuerta *et al.* [26] suggest using hyperelastic neo-hooken material models instead of linear Saint Venant material models for geometrically nonlinear TO. Hyperelastic materials are designed to exhibit hardening behavior under compression, which can help mitigate computational divergence caused by low-density areas. However, for shells, owing to their 3D nature, spurious buckling can still occur when the load exceeds a certain threshold, even if the elements are incompressible. A related approach that also uses hyperelastic neo-Hookean materials is the third medium contact (TMC) method [27–30], which inserts a layer of neo-Hookean elements between two potential contact bodies; these elements stiffen under compression, preventing penetration when contact occurs. However, TMC elements can undergo severe distortion under large compression, causing divergence in nonlinear finite element analysis. To reduce such distortions, Bluhm *et al.* [29] proposed the “HuHu" method, which augments the strain energy density with an additional term based on Hessian displacement field to penalize higher-order deformations and thereby regularizes the element shape during deformation. Nonetheless, the “HuHu" method undesirably penalizes bending and quadratic compression more than necessary. As proposed in [30], this excessive penalization can be reduced by subtracting a “LuLu" term constructed from the Laplacian of the displacement field, and consequently facilitating a greater degree of bending while maintaining stability. In general, TMC elements combined with regularization techniques focusing primarily on controlling large element deformations.As discussed earlier when introducing the work of [26], shell elements can behave almost rigidly during local buckling, with their shape remaining nearly unchanged. Therefore, the TMC method may not be a suitable option for resolving spurious local buckling in shells. Similarly, restricting deformations while allowing large rigid body motions, two typical methods have been proposed. The first is Element Connectivity Parameterization (ECP) method presented by Yoon and Kim [31], where modified finite elements are used. Each of them consists of a regular finite element and corresponding elastic truss connections, with the pseudo densities of the trusses, rather than the elements, used as design variables [32]. Instabilities in ECP formulations, as reported in [33], occur when truss densities become low. In such cases, even though the element strains remain small, the corresponding patch may reverse due to rigid body motions of the element. The second method is Element Deformation Scaling (EDS), proposed by van Dijk *et al.* [34]. This method separates the element displacement field into rigid body motions and pure deformations, scaling the pure deformation component. However, similar to the ECP method, instabilities can arise in EDS due to rigid body motions, even when the element itself undergoes only linear deformation. As constraining deformations alone is not sufficiently effective, Wang *et al.* [35] proposed a strain energy interpolation method that

also limits rigid-body motions for low-density elements. This method introduces a scaling parameter between 0 and 1 into the displacement field. The strain energy is interpolated between a linear and a nonlinear model. For low-density elements, this scaling reduces the geometric stiffness matrices, allowing the elements to behave linearly and avoid instabilities. This approach is simple to integrate with the proposed ROMs and will be one of the strategies explored in this work.

Since ROMs were recently introduced to topology optimization (TO) for geometrically nonlinear structures in our previous work [15], methods to address convergence difficulties have not yet been extended to ROMs. Additionally, the existing approaches primarily focus on 2D structures, while their behavior for shells remains unexplored. Therefore, this chapter focuses on flexible shells modeled using a co-rotation formulation [32] and develops tailored methods to address convergence issues caused by low-density elements in ROMs. The first and simplest approach involves removing spurious modes from the ROM basis: One strategy eliminates specific directions from the ROM basis, guided by the eigenvalues and eigenvectors of reduced matrices; another strategy directly removes spurious contributions associated with low-density areas from the basis. The second approach focuses on eliminating spurious modes directly from the underlying physics. Inspired by [35], we apply strain interpolation to low-density elements. The interpolation, for shells, is applied only to the membrane strains, since they are the main causes of spurious instabilities. Then, to explore more innovative and robust solutions for shells and ROMs, the chapter also introduces a new approach involving normal and complementary structures. The complementary structure acts as a flexible support, stabilizing distortions in low-density areas. These second type of methods can be extended to standard FOM-based analyses. The chapter aims to thoroughly investigate the performance of the above strategies and provide deeper insights into the underlying challenges.

This chapter is structured as follows: Section 2 introduces geometrically nonlinear topology optimization and the previously proposed Reduced-Order Models (ROMs) [15]. Section 3 demonstrates the convergence difficulties in ROMs caused by spurious buckling, using shell models. Section 4 presents two strategies for removing spurious modes from the ROM basis, with their effectiveness evaluated using the shell models from Section 3. Section 5 presents two methods to remove spurious modes from FOM-based solutions. Their effectiveness is first tested on a 2D C-shaped structure and on the shell models from Section 3. Finally, Section 6 gives the conclusions.

## 3.2. ROM-BASED GEOMETRICALLY NONLINEAR TOPOLOGY OPTIMIZATION

Topology optimization formulations with an objective function $J$, inequality constraints $\mathbf{h}$, design variables (pseudo densities) $\boldsymbol{\rho}$ and their corresponding lower bounds $\boldsymbol{\rho}_{\min}$ can be expressed by

$$\begin{aligned} &\min_{\boldsymbol{\rho}} J\left[\mathbf{d}\left[\boldsymbol{\rho}\right], \boldsymbol{\rho}\right], \\ &\text{s.t.}: \mathbf{h}\left[\mathbf{d}\left[\boldsymbol{\rho}\right], \boldsymbol{\rho}\right] \leq \mathbf{0}, \\ &\qquad \mathbf{0} < \boldsymbol{\rho}_{\min} \leq \boldsymbol{\rho} \leq \mathbf{1}. \end{aligned} \tag{3.1}$$

Here, lower bounds $\boldsymbol{\rho}_{\min}$ are typically set to avoid singularities caused by removing material. Mechanical responses $\mathbf{d}$, i.e. nodal degrees of freedom are usually obtained by solving equilibrium governing equations, which for geometrically nonlinear cases, can be expressed by

$$\mathbf{D}^{\mathrm{T}}[\mathbf{d}]\,\boldsymbol{\sigma} - \mathbf{f} = \mathbf{q}[\mathbf{d}] - \mathbf{f} = \mathbf{0}, \tag{3.2}$$

where $\mathbf{f}$ represents the external nodal load, $\boldsymbol{\sigma}$ generalized stresses, and $\mathbf{q} = \mathbf{D}^{\mathrm{T}}\boldsymbol{\sigma}$ the so-called "internal" load, with

$$D_{ij} = \frac{\partial \epsilon_i}{\partial d_j}. \tag{3.3}$$

Here, $\epsilon_i$ represents generalized deformations. Given that we mainly focus on shells prone to large deflections and rotations but with small deformations, linear material model is used, shown by

$$\boldsymbol{\sigma} = \mathbf{S}\boldsymbol{\epsilon}, \tag{3.4}$$

where $\mathbf{S}$ is the generalized constitutive matrix. At element level, the matrices corresponding to $\mathbf{D}$ and $\mathbf{S}$ are denoted by $\mathbf{D}_e$ and $\mathbf{S}_e$.

In the SIMP method [1], the constitutive matrix is scaled at element level with element density $\rho_e$:

$$\mathbf{S}_e \rightarrow \rho_e^p \mathbf{S}_e, \tag{3.5}$$

where parameter $p$ is used to penalize intermediate densities and usually, $p = 3$ is adopted [1].

To solve the governing equations, incremental-iterative methods are typically used. Here, a load factor $\lambda$ is introduced, and consequently, the external load $\mathbf{f}$ is written as a function of $\lambda$. Then, the equilibrium equation reads

$$\mathbf{q}[\mathbf{d}] - \mathbf{f}[\lambda] = \mathbf{0}, \tag{3.6}$$

with "$[\cdots]$" denoting a function of "$\cdots$". Next, the corresponding rate equations follow as

$$\mathbf{K}_{\mathrm{T}}[\mathbf{d}]\,\frac{\mathrm{d}\mathbf{d}}{\mathrm{d}\lambda} - \frac{\mathrm{d}\mathbf{f}}{\mathrm{d}\lambda} = \mathbf{0}, \tag{3.7}$$

with the $l \times l$ tangent stiffness matrix $\mathbf{K}_{\mathrm{T}}$ being defined as

$$\mathbf{K}_{\mathrm{T}} = \frac{\partial \mathbf{q}[\mathbf{d}]}{\partial \mathbf{d}}, \tag{3.8}$$

where $l$ is the number of structural DOFs. In these simulations, the external load $\mathbf{f}$ is divided into several load steps. Each load level involves an initial linear prediction, followed by several Newton iterations. During these iterations, the tangent stiffness matrix $\mathbf{K}_{\mathrm{T}}$ must be updated and a set of linear equations need to be solved. Then, the solution may be very expensive, particularly when the number of nodal degrees of freedom gets large.

The computational burden can increase further due to the scaling in Eq. (3.5), where a low pseudo-density makes elements highly compliant. These compliant elements are easily deformed by neighboring stiffer elements undergoing large displacements. This

leads to ill-conditioned tangent stiffness matrices, typically causing “inside-out" elements in 2D structures and local buckling in shells and plates. The former often results in computational divergence, while the latter, although not always divergent, could significantly increase the number of analysis iterations and may call for smaller load steps to ensure convergence.

To improve efficiency, reduced-order modeling (ROMs) was introduced in [15]. A brief explanation of the proposed ROMs is outlined here, with more detailed information available in [15]. In the proposed ROMs, the nodal degrees of freedom are approximated by:



$$\overline{\mathbf{d}} = \mathbf{R}\mathbf{y}, \tag{3.9}$$

where $\overline{\mathbf{d}}$ denotes the approximate nodal degrees of freedom for the full-order model and $\mathbf{y}$ are generalized coordinates. The matrix $\mathbf{R}$ represents the ROM basis

$$\mathbf{R} = [\boldsymbol{\phi}_1, \boldsymbol{\phi}_2, ..., \boldsymbol{\phi}_m], \tag{3.10}$$

where $\boldsymbol{\phi}_m$ denotes an individual base vector, $m$ represents the number of base vectors and for efficiency, one targets a relatively small number of base vectors, i.e., $m \ll l$. In the proposed ROMs, base vectors could be FOM-based linear solutions, nonlinear solutions, and (approximate) path derivatives. To ensure the formation of a well-defined orthonormal basis, these vectors are orthonormalized using the Gram-Schmidt process, starting from $\boldsymbol{\phi}_m$ and progressing to $\boldsymbol{\phi}_1$. Details on the orthonormalization process are provided in Appendix A.1.

Using Ritz' method, the ROM-based governing equation can be expressed as

$$\mathbf{R}^{\mathrm{T}}(\mathbf{q}\left[\overline{\mathbf{d}}\right] - \mathbf{f}) = \mathbf{0}. \tag{3.11}$$

Here,

$$\mathbf{q}\left[\overline{\mathbf{d}}\right] = \mathbf{D}^{\mathrm{T}}\left[\overline{\mathbf{d}}\right]\boldsymbol{\sigma}\left[\overline{\mathbf{d}}\right] = \mathbf{D}^{\mathrm{T}}\left[\mathbf{R}\mathbf{y}\right]\mathbf{S}\boldsymbol{\epsilon}\left[\mathbf{R}\mathbf{y}\right]. \tag{3.12}$$

The corresponding rate equations follow as

$$\left(\overline{\mathbf{K}}_{\mathrm{T}}\left[\mathbf{y}\right]\right)^{-1}\frac{\mathrm{d}\mathbf{y}}{\mathrm{d}\lambda} - \frac{\mathbf{R}^{\mathrm{T}}\mathbf{f}}{\mathrm{d}\lambda} = \mathbf{0}, \tag{3.13}$$

with $\overline{\mathbf{K}}_{\mathrm{T}}$ representing the $m \times m$ reduced tangent stiffness matrix shown as

$$\overline{\mathbf{K}}_{\mathrm{T}}\left[\mathbf{y}\right] = \mathbf{R}^{\mathrm{T}}\mathbf{K}_{\mathrm{T}}\left[\mathbf{R}\mathbf{y}\right]\mathbf{R}. \tag{3.14}$$

Here, the right-hand term can be assembled element-by-element:

$$\mathbf{R}^{\mathrm{T}}\mathbf{K}_{\mathrm{T}}\left[\mathbf{R}\mathbf{y}\right]\mathbf{R} = \bigwedge_{e}\mathbf{R}_e^{\mathrm{T}}\mathbf{K}_{\mathrm{T}}^{e}\left[\mathbf{R}\mathbf{y}\right]\mathbf{R}_e, \tag{3.15}$$

where $\mathbf{R}_e$ and $\mathbf{K}_{\mathrm{T}}^{e}$ are corresponding matrices at element level.

As in the FOM setting, an incremental-iterative method can be applied to solve the nonlinear reduced governing equations. Here, Newton iterations are based on the reduced tangent stiffness matrix Eq. (3.15). This significantly improves the computational

efficiency since the dimensions of the latter depend on the number of base vectors used, which is much smaller than the number of structural DOFs.

For a load level $\lambda^c$, after the ROM-based Newton iterations have converged, we have obtained the corresponding generalized coordinates $\mathbf{y}^c$. Next, the ROM-based solution $\overline{\mathbf{d}}^c$ follows using Eq. (3.9), and its accuracy is assessed. If the solution $\overline{\mathbf{d}}^c$ is accurate, then it should also satisfy the full system equilibrium equation. This implies that the norm of the full-system based residual, i.e. $\|\mathbf{f}[\lambda^c] - \mathbf{q}\left[\overline{\mathbf{d}}^c\right]\|$ should be sufficiently small. Here, $\|\cdots\|$ denotes the $l_2$ norm. Throughout the chapter, the norm is based on the standard inner-product. Hence, an error measure based on the full-system residual is proposed as

$$\eta = \frac{\|\mathbf{f}[\lambda^c] - \mathbf{q}\left[\overline{\mathbf{d}}^c\right]\|}{|\mathbf{f}[\lambda^c]\|}. \tag{3.16}$$

Here, the dimensions of $\mathbf{f}[\lambda^c] - \mathbf{q}\left[\overline{\mathbf{d}}^c\right]$ and $\mathbf{f}[\lambda^c]$ equal the number of structural nodal DOFs.

If $\eta$ is smaller than a user-defined tolerance $\delta_s$, then the ROM-based solution is considered accurate. Otherwise, a correction needs to be applied to further reduce the error. For correcting the error, starting from the present ROM-based solution, FOM-based Newton iterations are conducted. Then, the resulting converged FOM-based solution is regarded as the final result for the current load level. This FOM-based solution, along with its corresponding (approximate) path derivatives (see Chapter 2.4.1), is incorporated into the ROM basis for completeness. The updated ROM basis is then used for the next load level. For more details see Chapter 2. In practice, the presence of spurious buckling causes $\eta$, as defined in Eq. (3.16), to increase significantly, leading to many FOM-based correction iterations. The effect of spurious modes on ROM-based solutions are detailed in the next section using a shell example.

## 3.3. THE EFFECT OF SPURIOUS MODES ON ROM-BASED SOLUTIONS

A typical optimization example illustrating the influence of spurious modes on ROMs is shown in Fig. 3.1. The optimization problem involves minimizing the volume $V$, subject to displacement constraints, as expressed by

$$\begin{aligned} &\min V, \\ &\text{s.t. } d_z^A \geq -4, d_z^B \geq -4, \\ &\quad d_x^A \leq -1, d_y^B \leq -1, \end{aligned} \tag{3.17}$$

where $d_x^A$ and $d_y^B$ represent the displacement components of Point A and B in $x$ and $y$ directions separately, and $d_z^A$ and $d_z^B$ in $z$-direction . The displacements are determined by solving the nonlinear equilibrium equations using the incremental-iterative method, where load control is applied. The final load level is $\lambda = 0.15$, with an incremental step size of $\Delta\lambda = 0.015$, resulting in a total of 10 incremental steps. The maximum number of Newton iterations per incremental load step is set to 50, which serves as an indicator

of divergence in the numerical results: If an incremental step reaches 50 iterations, it indicates that convergence was not achieved at that step.

The outcome of the optimization process is shown in Fig. 3.2(a), while the efficiency evaluation is presented in Fig. 3.2(b). The efficiency of ROMs is assessed by counting the number of ROM-based Newton iterations and FOM-based error correction iterations. These counts are compared to the number of Newton iterations required by the standard FOM method (ONLY_FOM).

Observations reveal that after 20 optimization steps, FOM-based error corrections become more frequent, with their numbers in most steps being comparable to those in the ONLY_FOM method. Notably, at the 28th optimization step, the total number of FOM-based corrections across all incremental load steps exceeds 100, significantly surpassing the count in the ONLY_FOM method, which is 64.

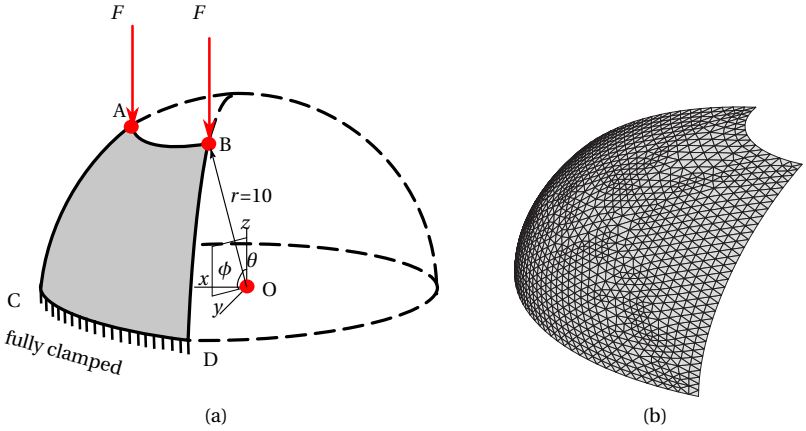


Figure 3.1: Spherical structure and its finite element mesh. (a) is geometry. All quantities have consistent units. Coordinates of Point A are $(r,\theta,\phi) = (10, \frac{2\pi}{5}, 0)$, Point B $(r,\theta,\phi) = (10, \frac{2\pi}{5}, \frac{\pi}{2})$, Point C $(r,\theta,\phi) = (10, \frac{\pi}{2}, 0)$, and Point D $(r,\theta,\phi) = (10, \frac{\pi}{2}, \frac{\pi}{2})$. Here, $F = 6 \times 10^3$ denotes nodal forces applied to Point A and B. Thickness is 0.1. Young's modulus $E = 100 \times 10^6$, and Poisson's ratio $\nu = 0.3$. In the incremental-iterative method, the maximum load level $\lambda$ is 0.15, with an incremental step size of $\Delta\lambda = 0.015$, resulting in a total of 10 incremental steps.The maximum number of Newton iterations per incremental step is set to 50. (b) shows the finite element mesh, where 6-node 12-DOF shell elements are utilized as documented in [32].

To understand why FOM-based corrections are heavily involved, we analyze an intermediate design shown in Fig. 3.3 by conducting both ROM-based and FOM-based analyses and summarizing the number of Newton iterations in Tab. 3.1. As observed, at the 7th and 10th incremental steps, nearly 30 correction iterations are required in the ROM-based analysis.

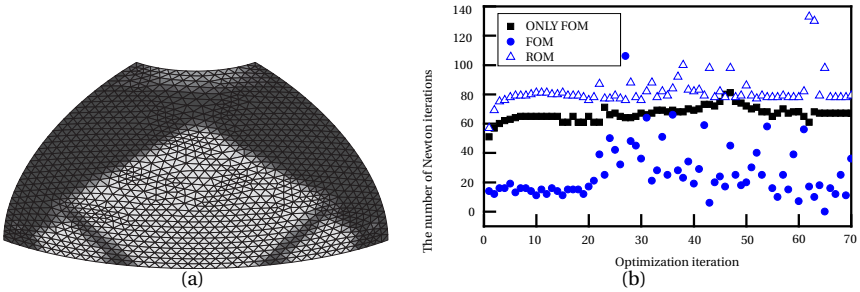


(a) (b)



Figure 3.2: Final topology and efficiency test: (a) The final topology, with an objective value of 2.06. (b) Efficiency test results. The efficiency of the ROMs is evaluated by comparing the number of ROM-based updates (represented by blue triangles) with the number of FOM-based correction iterations (represented by blue circular markers) for each optimization step. These results are compared to the number of FOM-based updates in the purely FOM strategy, indicated by the black markers.

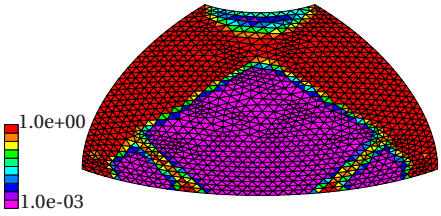


Figure 3.3: An intermediate topology optimization design obtained using ONLY_FOM method. Here, red represents a pseudo-density of $\rho_e = 1$, while pink corresponds to $\rho_e = 1\times10^{-3}$, i.e., the lower bound for $\rho_e$. The other colors indicate intermediate values between these two limits.

To investigate further, we focus on these two incremental load steps and illustrate the final ROM-based and FOM-based deformed configurations in Fig. 3.4 and Fig. 3.5, respectively. As seen, while FOM-based deformations exhibit slight spurious buckling in the middle of the low-density area, ROM-based deformations show severe spurious buckling in the same region. This significant difference leads to the intensive use of FOM-based correction iterations. The severe buckling in ROM-based deformations can be explained by analyzing the corresponding ROM basis. For this, the ROM basis at the 7th load step is shown in Fig. 3.6. Here, the entire basis consist of orthonormalized FOM-based solutions. Since FOM-based solutions contain spurious buckling modes, these modes are simultaneously orthonormalized and incorporated into the basis. As a result, when these vectors are combined to construct the ROM-based solutions, the orthonormalized spurious modes are also combined, creating a spurious buckling mode in the middle low-density area that differs from the FOM-based one. Due to these differences, many correction iterations are required, reducing the efficiency of ROMs. To address this, one potential solution is to remove the spurious modes from the ROM basis, which is further investigated in the next section.

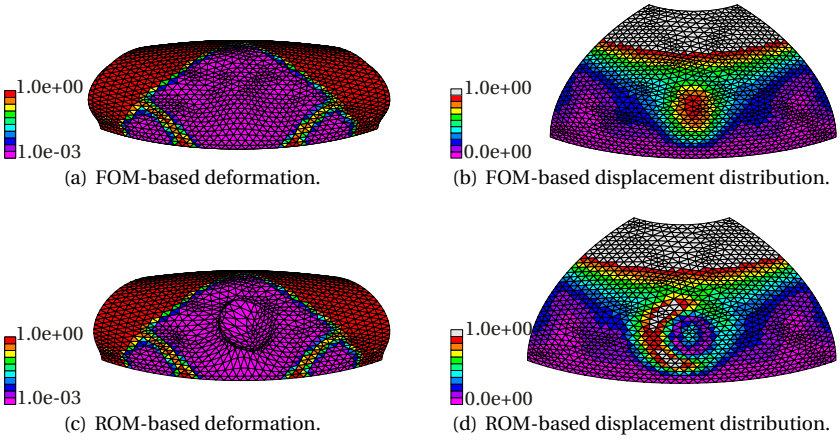


(a) FOM-based deformation. (b) FOM-based displacement distribution.

(c) ROM-based deformation. (d) ROM-based displacement distribution.

Figure 3.4: The deformed configuration of the design shown in Fig. 3.3 at the 7th load step. On the left, the topology and the deformations are illustrated, while on the right, displacement distributions for further illustrating the deformations.

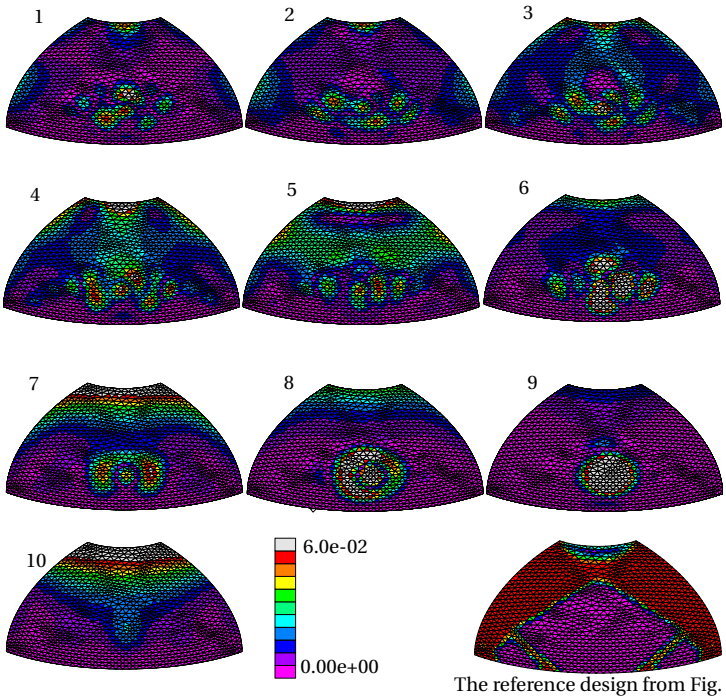


The reference design from Fig. 3.3

Figure 3.6: Base vectors at the 7th load step for the design shown in Fig. 3.3. The latter is copied and pasted as the last small figure for clarification. The current ROM basis contains 10 orthonormalized base vectors. orthogonalization follows Gram-Schmidt in Appendix A.1 proceeding from vector 10 to vector 1. Specifically, vector 10 shown here represents the FOM-based solution at the current incremental load step, while vector 1 is obtained by taking the FOM-based solution from a previous incremental load step, subtracting its projections onto vectors 10 through 2.

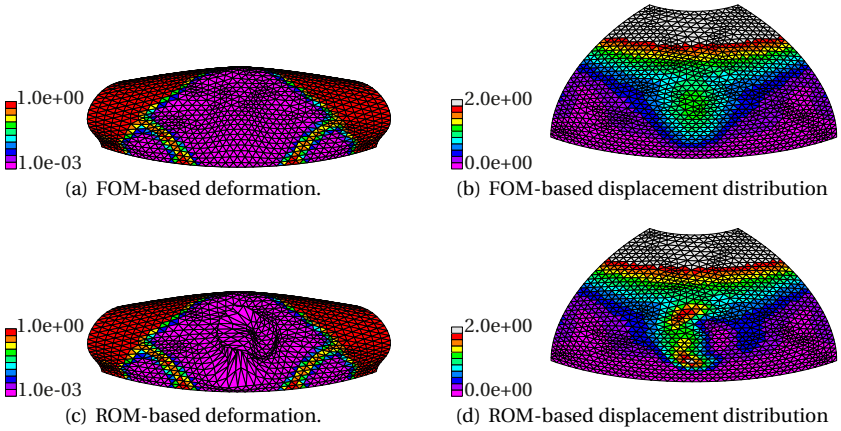


(a) FOM-based deformation. (b) FOM-based displacement distribution

(c) ROM-based deformation. (d) ROM-based displacement distribution

Figure 3.5: The deformed configuration of the design shown in Fig. 3.3 at the 10th load step. On the left, the topology and the deformations are illustrated, while on the right, displacement distributions are depicted for further illustrating deformations

## 3.4. SPURIOUS MODE ELIMINATION FROM ROM BASIS

As shown in the previous section, spurious modes are inseparable from each base vector. As a result, combining base vectors also combines spurious modes, leading to significant errors in the ROM-based solution. A potential solution is to reduce or eliminate spurious modes in low density areas from the ROM basis without affecting the modes in non-low-density areas. This section explores two techniques. One involves the elimination of specific directions from the ROM basis, where eigenvalues and eigenvectors of reduced matrices, i.e. $\overline{\mathbf{K}}_{\mathrm{T}}$ in Eq. (3.14), guide the elimination process. The other targets adaptation of the ROM basis, which attempts to directly removes all spurious mode contributions from the base vectors.

### 3.4.1. EIGENVALUE-BASED REMOVAL METHOD

The first technique removes specific directions from a ROM basis by using eigenvalues and eigenvectors from reduced system matrices, i.e., the reduced tangent stiffness. Here, the selected eigenvectors to be removed should predominantly contain spurious modes, identified by their relatively small eigenvalues compared to other eigenvalues. Continuing the investigation of the ROM basis shown in Fig. 3.6, we calculate the eigenvalues of the associated reduced matrix and display them in Fig. 3.7. Here, we define eigenvalue ratios as $-\log_{10}\left|\frac{\text{eigenvalue}}{\text{maximum eigenvalue}}\right|$ and a higher ratio indicates a relatively smaller eigenvalue.

As observed from Fig. 3.7, ratios 6 and 9 are significantly higher compared to the others, and their corresponding eigenvectors, which consist solely of spurious modes, are shown in Fig. 3.8. These eigenvectors can be eliminated from the ROM basis (see Fig. 3.6) by orthogonalizing all base vectors with respect to them, using the orthonormalization process described in Appendix A.1. Applying this approach, the resulting ROM basis is

Table 3.1: Iteration history of the FOM-based and ROM-based analysis. $\lambda$ is the load level, $n_{\mathrm{f}}$ the number of FOM updates in ONLY_FOM method, $n_{\mathrm{rr}}$ the number of ROM-based iterations, and $n_{\mathrm{rf}}$ the number of related FOM-based correction iterations. Comments refer to the ROM-based analysis. The number of incremental steps is 10 and for each incremental step, the maximum number of Newton iterations is 50. As seen, the ONLY_FOM method converges in 70 iterations, while ROM-based method encounters convergence difficulties at the 7th and the 10th incremental load steps, leading to a total of 74 FOM-based corrections.

| $i$ | $\lambda$ | $n_{\mathbf{f}}$ | $n_{\mathbf{rf}}$ | $n_{\mathbf{rr}}$ | Comments |
|---|---|---|---|---|---|
| 1 | 0.015 | 7 | 7 | 0 | only FOM |
| 2 | 0.03 | 15 | 7 | 8 | no FOM |
| 3 | 0.045 | 19 | 11 | 15 | 4 FOM |
| 4 | 0.06 | 25 | 11 | 23 | no FOM |
| 5 | 0.075 | 37 | 22 | 31 | 11 FOM |
| 6 | 0.09 | 45 | 22 | 42 | no FOM |
| 7 | 0.105 | 51 | 49 | 49 | 27 FOM |
| 8 | 0.12 | 57 | 49 | 56 | no FOM |
| 9 | 0.135 | 63 | 49 | 63 | no FOM |
| 10 | 0.15 | 70 | 74 | 71 | 25 FOM |

shown in Fig. 3.9. As observed, the spurious modes in vector 10 vanishes completely. Although some spurious modes remain in other base vectors, they are significantly weakened.

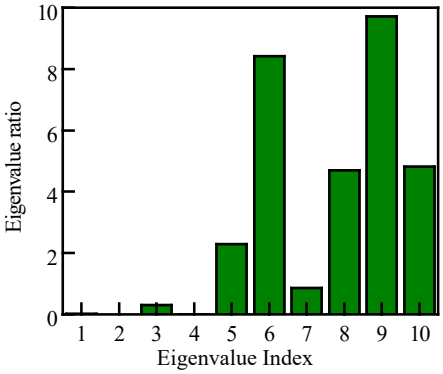


Figure 3.7: The eigenvalue ratios are calculated using the formula $-\log_{10}\left|\frac{\text{eigenvalue}}{\text{maximum eigenvalue}}\right|$. In this context, the eigenvalues refer to those of the reduced tangent stiffness matrix associated with the base vectors shown in Fig. 3.6. A larger ratio corresponds to a relatively smaller eigenvalue.

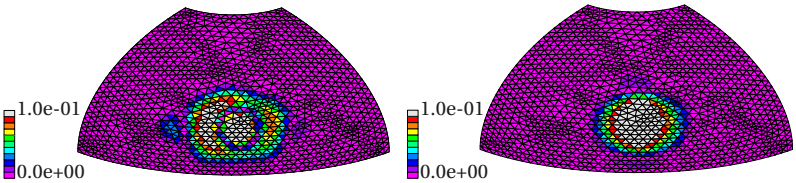


(a) No.6 eigenmode (b) No.9 eigenmode

Figure 3.8: Eigenvectors of the reduced stiffness matrix corresponding to eigenvalues 6 and 9, where white means displacements exceed 0.1, red large displacements, and pink small displacements. As observed, displacements exclusively concentrate to the middle low-density area.

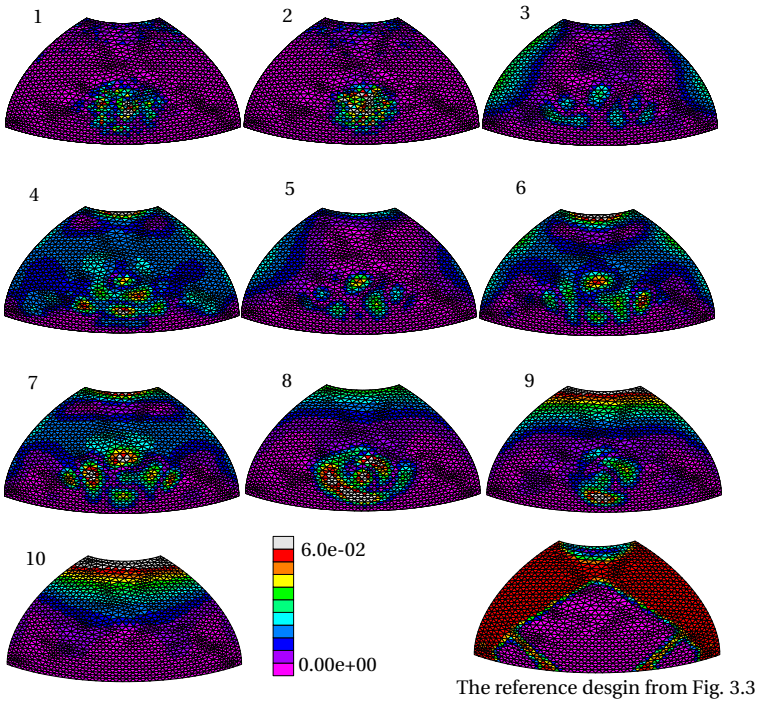


Figure 3.9: The base vectors shown here correspond to those depicted in Fig. 3.6, but with eigenvalue-based removal applied. The colors of base vectors show the displacement field.

To investigate the feasibility of the method, we incorporate it into the ROM-based analysis for the intermediate design shown in Fig. 3.3: (1) At any load level, as long as the ROM basis is updated, eigenvalue analysis is performed on the reduced tangent stiffness matrix; (2) if eigenvalue ratios for any eigenvalues are obviously significant (with a ratio above 8 as a test threshold), the corresponding eigenvectors are subtracted from the basis; (3) the refined ROM basis will be used in the next load level.

For the above introduced method, the number of Newton iterations for each load level is documented in Tab. 3.2. Here, the total number of FOM-based correction iterations is reduced as compared to Tab. 3.1, where no eigenvector elimination is applied. However, the 7th and 9th load steps still require many FOM-based corrections. To investigate the reasons, the corresponding final deformed configurations are illustrated in Fig. 3.10 and Fig. 3.11. According to Fig. 3.10, error corrections are required at the 7th load step because the ROM-based deformation in the low-density areas (Fig. 3.10(a)) noticeably differs from the FOM-based result (Fig. 3.4(a)). Although the distortions are less severe than in the case without eigenvector removal shown in Fig. 3.4(c), the remaining differences are still large enough to require a significant number of corrections. Given this phenomenon, the issue may lie in the incomplete removal of spurious modes from the ROM basis. However, even with complete removal, a large number of FOM-based corrections may still be required. The latter can be deducted by looking at the 9th incremental load step.

At the 9th incremental step, the ROM-based deformations in Fig. 3.11(c) and (d) exhibit far less spurious buckling in the central low-density area than the FOM-based result in Fig. 3.11(a). Because this spurious buckling should be present in the FOM-based solution but is nearly absent in the ROM-based one, the error measurement detects a discrepancy. As a result, additional FOM-based corrections are required to reproduce the missing buckling, shifting the ROM-based deformation from the state in Fig. 3.11(c) toward that in Fig. 3.11(a).

These observations indicate that complete removal of spurious buckling modes from the ROM basis does not effectively improve the efficiency of ROMs. Since spurious buckling is inherent in FOMs, the ROM basis should be able to accurately capture it to reduce FOM-based error corrections. However, eigenvalue-based removal may leave either too many or too few spurious modes in low-density areas, making the ROM unable to reproduce the spurious buckling observed in the FOM solution. To address this limitation, the next section presents a more direct and effective approach.

Table 3.2: Iteration history with eigenvalue-based removal method. $\lambda$ represents load levels, $n_{rf}$ is the number of FOM-based correction iterations, $n_{rr}$ is the number of ROM-based iterations. The number of incremental steps is 10 and for each incremental step, the maximum number of Newton iterations is 50. As observed, fewer FOM-based corrections are needed to be compared to Tab. 3.1, although the improvement is only slight.

| $i$ | $\lambda$ | $n_{rf}$ | $n_{rr}$ | Comments |
|---|---|---|---|---|
| 1 | 0.015 | 7 | 0 | only FOM |
| 2 | 0.03 | 7 | 8 | no FOM |
| 3 | 0.045 | 11 | 15 | 4 FOM |
| 4 | 0.06 | 11 | 23 | no FOM |
| 5 | 0.075 | 22 | 30 | 11 FOM |
| 6 | 0.09 | 22 | 41 | no FOM |
| 7 | 0.105 | 40 | 48 | 18 FOM |
| 8 | 0.12 | 40 | 55 | no FOM |
| 9 | 0.135 | 57 | 61 | 17 FOM |
| 10 | 0.15 | 57 | 70 | no FOM |

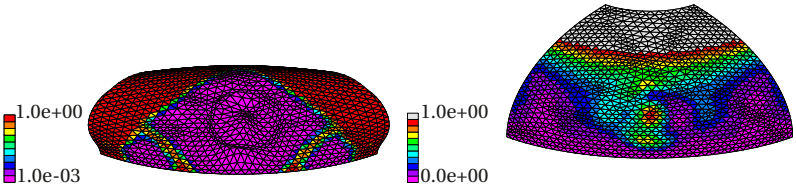


(a) ROM-based deformation. (b) ROM-based displacement distribution.

Figure 3.10: With the eigenvalue-based removal method, ROM-based deformation at the 7th load step related to the design shown in Fig. 3.3. The left shows the topology and the deformations and the right describes displacement field. Compared to Fig. 3.4(c) and Fig. 3.4(d), distortions in the middle low-density area are less severe.

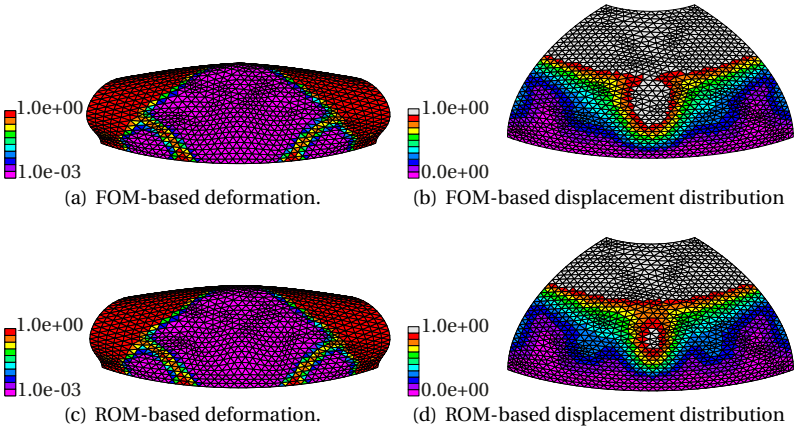


(a) FOM-based deformation. (b) FOM-based displacement distribution

(c) ROM-based deformation. (d) ROM-based displacement distribution

Figure 3.11: Deformations and displacement distributions of the design shown in Fig. 3.3 at the 9th load step. The ROM-based result exhibits much smaller distortions in the middle low-density area than the FOM-based one. Because this spurious buckling should be present in the FOM-based solution but is nearly absent in the ROM-based one, the error measurement detects a discrepancy. As a result, additional FOM-based corrections are required to reproduce the missing buckling, shifting the ROM-based deformation from the state in (c) toward that in (a).



### 3.4.2. ROM BASIS ADAPTATION TECHNIQUE

This section explores a simple and direct adaptation method to effectively reduce the number of FOM-based corrections. The method attempts to eliminate spurious modes from all base vectors except the newly added one, meaning that spurious buckling in the FOM solution is represented solely by the newest base vector, rather than as a combination of orthogonal components from multiple vectors. The above is achieved by directly setting the nodal displacements (both deflections and rotations) in low-density areas to zero. To determine whether a node belongs to a low-density area, we first calculate an average pseudo-density $\overline{\rho}^k$ for each node $k$ using

$$\overline{\rho}^k = \frac{1}{m} \sum_{n=1}^{m} \rho_n^i. \tag{3.18}$$

Here, $m$ denotes the number of elements connected to the node $k$, and $\rho_n^k$ represents the pseudo density of element $n$ linked to node $k$. If $\overline{\rho}^k$ is below a threshold (0.01 is used in this test), then it is considered to belong to a low-density area and all displacements including deflections and rotations at this node are set to zero. Applying the above to the ROM basis shown in Fig. 3.6, we obtain Fig. 3.12. As seen, only the last vector contains spurious buckling modes in the middle low-density area.

Next, we incorporate the above adaptation method to ROM-based analysis for the intermediate design given in Fig. 3.3: At any load level, as long as the ROM basis is updated, the adaptation is applied. Following this scheme, the iteration history is shown in Tab. 3.3. It is observed that the total number of FOM-based correction iterations is significantly reduced. Given these promising results, the method is then applied to a complete optimization problem. We use the optimization formulation described in Eq. (3.17), and

show the final results in Fig. 3.13.

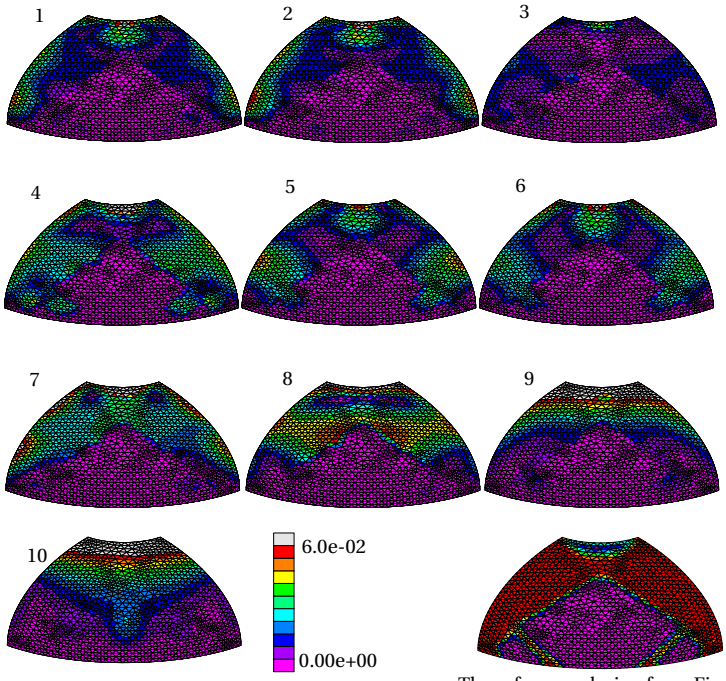


The reference design from Fig. 3.3

Figure 3.12: The base vectors shown here correspond to those depicted in Fig. 3.6, but with ROM basis adaptation method applied. As shown, the spurious buckling in FOMs will be captured exclusively by the newest base vector, i.e., vector 10.

Table 3.3: Iteration history using ROMs with ROM basis adaptation method. $\lambda$ represents load levels, $n_{\mathrm{rf}}$ the number of FOM-based correction iterations in ROM method, $n_{\mathrm{rr}}$ is the number of ROM-based iterations. The number of incremental steps is 10 and for each incremental step, the maximum number of Newton iterations per load step is 50. The number of FOM-based correction is largely reduced due to ROM basis adaptation.

| $i$ | $\lambda$ | $n_{\mathbf{rf}}$ | $n_{\mathbf{rr}}$ | Comments |
|---|---|---|---|---|
| 1 | 0.015 | 7 | 0 | only FOM |
| 2 | 0.03 | 7 | 8 | no FOM |
| 3 | 0.045 | 11 | 15 | 4 FOM |
| 4 | 0.06 | 11 | 23 | no FOM |
| 5 | 0.075 | 22 | 30 | 11 FOM |
| 6 | 0.09 | 22 | 38 | no FOM |
| 7 | 0.105 | 22 | 45 | no FOM |
| 8 | 0.12 | 34 | 45 | 12 FOM |
| 9 | 0.135 | 34 | 60 | no FOM |
| 10 | 0.15 | 34 | 66 | no FOM |

As shown, compared to the results without ROM adaptation in Fig. 3.2, a smaller objective value is achieved, and the efficiency is improved. Notably, as depicted in Fig. 3.13(b), ROMs with the adaptation consistently require fewer FOM-based iterations than the ONLY_FOM method throughout the optimization process. However, the number of FOM-based correction iterations temporarily increases around the 21st and 53rd optimization steps. To investigate this, the final deformed configurations at the 20th, 21st, and 53rd steps are shown in Fig. 3.14, Fig. 3.15, and Fig. 3.16, respectively.

As shown in Fig. 3.14, no spurious buckling appears in FOM-based solutions up to the 20th optimization step. Since the ROM basis is constructed from these FOM-based solutions, it also does not yet contain any spurious modes. At the 21st step, as shown in Fig. 3.15, spurious buckling appears in the FOM-based solution. However, since the current ROM basis still originates from the 20th step, when no spurious modes were present, it is unable to capture this newly introduced buckling, requiring several FOM-based correction iterations to produce the spurious buckling in the ROM-based solution. Similarly, at the 53rd step shown in Fig. 3.16, a new type of spurious buckling appears in the FOM-based solution. This spurious buckling may not be accurately captured by the spurious mode in the newest ROM base vector, resulting in many FOM-based corrections.

In summary, the ROM adaptation approach captures spurious buckling in the FOM solution by the spurious mode in the newest base vector, rather than a combination of orthonormalized spurious modes. This helps avoid excessive distortion in the ROM-based solution. However, since spurious buckling in the FOM can continue to evolve throughout the optimization process, the newest base vector may sometimes not represent the spurious buckling accurately, leading to a temporary increase of FOM-based correction iterations.

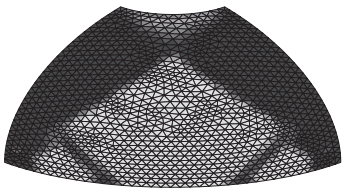

(a)

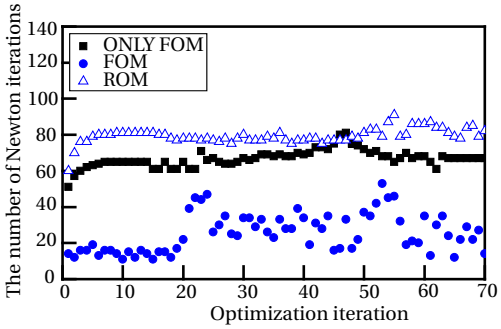


(b)

Figure 3.13: Final topology and efficiency test with ROM basis adaptation method. (a) Final topology, with objective value 2.055. (b) Efficiency test result. The efficiency of ROMs is assessed by measuring the number of ROM-based updates, shown by triangle blue points, and FOM-based correction iterations, shown by round blue points, at each optimization step. These numbers are compared with the number of FOM-based updates of exclusively FOM strategy, which are the black points. The number of incremental load steps is 10, and the maximum number of Newton iterations per analysis incremental load step 50, i.e., per optimization step 500.

To better capture spurious buckling, an additional ROM basis could be introduced specifically to represent the spurious buckling in the FOM solution. However, this would

increase the complexity of the ROM-based method and is not the focus of this chapter. To further improve the efficiency of ROMs, an alternative approach is to eliminate spurious buckling directly from the FOM solutions. Two related methods, which can be integrated with ROMs, are explored in the following sections.



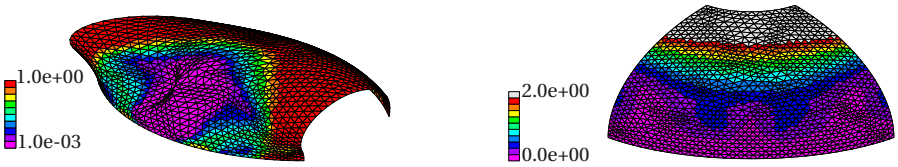


(a) Deformation (b) Displacement distribution

Figure 3.14: Final (FOM-based) deformations and displacement field at the 20th optimization step. Here, spurious local buckling has not yet appeared in the middle low-density areas.

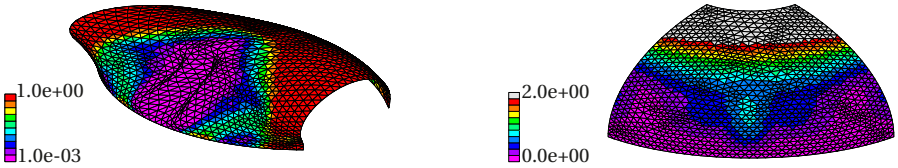


(a) Deformation. (b) Displacement distribution

Figure 3.15: Final (FOM-based) deformations and displacement field at the 21st optimization step. Here, spurious buckling start appearing in the middle low-density area.

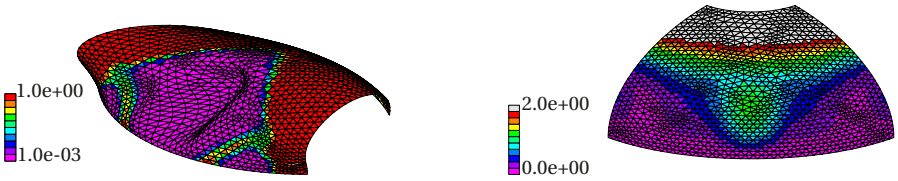


(a) Deformation (b) Displacement distribution

Figure 3.16: Final (FOM-based) deformations and displacement field at the 53rd optimization step Here, a new spurious buckling appears in the middle low-density area, distinct from the one shown in Fig. 3.15.

## 3.5. PHYSICS-BASED REMOVAL

To further improve efficiency, this section explores methods to eliminate spurious buckling using physics-based approaches. Two approaches are investigated: the first is a strain interpolation technique, and the second uses a complementary structure.

### 3.5.1. STRAIN INTERPOLATION

The strain interpolation method presented in this section is inspired by the strain energy interpolation approach proposed by Wang *et al.* [35]. In their formulation, the strain energy of an element, $\phi_e$, is interpolated between the nonlinear strain energy, $\phi_{NL}$, and the linear strain energy, $\phi_L$. The nonlinear component, $\phi_{NL}$, accounts for geometric and potentially material nonlinearity, while the linear component, $\phi_L$, assumes both geometric and material linearity. The interpolated strain energy, $\phi_e$, is then expressed as:

$$\phi_e(\mathbf{d}_e) = \left[\phi_{NL}(\gamma_e \mathbf{d}_e) - \phi_L(\gamma_e \mathbf{d}_e) + \phi_L(\mathbf{d}_e)\right] E_e, \tag{3.19}$$

where $\mathbf{d}_e$ is nodal degrees of freedom, $E_e$ Young's modulus, and $\gamma_e$ an element displacement scaling factor between 0 and 1 defined by the heaviside function

$$\gamma_e = \frac{\tanh(\beta\eta) + \tanh(\beta(\rho_e^p - \eta))}{\tanh(\beta\eta) + \tanh(\beta(1-\eta))}. \tag{3.20}$$

Here, $\rho_e$ represents an element pseudo density, $p$ the penalization parameter in the SIMP method, $\eta$ a threshold, and $\beta$ the changing speed of $\gamma_e$ near the threshold $\eta$. If $\rho_e^p < \eta$, then $\gamma_e$ would approach 0, and $\phi_e(\mathbf{d}_e) = \phi_L(\mathbf{d}_e)E_e$, meaning void elements exhibit linear behavior. If $\rho_e^p > \eta$, then $\gamma_e$ would approach 1, and $\phi_e(\mathbf{d}_e) = \phi_{NL}(\mathbf{d}_e)E_e$, indicating that solid elements exhibit nonlinear behavior. When $\rho_e^p$ is close to $\eta$, then $\gamma_e$ takes a value between 0 and 1, causing intermediate-density elements to partially lose their nonlinearity.

For shell structures, we introduce a simplified version of the above approach by interpolating the strains instead of the strain energies. Given that membrane strain is the primary contributor to local buckling behavior in shells, the interpolation is applied directly to the membrane strains only. This is expressed as:

$$\boldsymbol{\epsilon}_e[\gamma_e \mathbf{d}_e] = \boldsymbol{\epsilon}^{NL}[\gamma_e \mathbf{d}_e] - \boldsymbol{\epsilon}^{L}[\gamma_e \mathbf{d}_e] + \boldsymbol{\epsilon}^{L}[\mathbf{d}_e], \tag{3.21}$$

where $\boldsymbol{\epsilon}^L$ is element linear strain, and $\boldsymbol{\epsilon}^{NL}$ element nonlinear strain. Since $\boldsymbol{\epsilon}^{NL}$ and $\boldsymbol{\epsilon}^L$ can be expressed by

$$\epsilon_{ij}^{NL} = \frac{1}{2}(d_{i,j} + d_{j,i} + d_{k,i}\, d_{k,j}) \tag{3.22}$$

and

$$\epsilon_{ij}^{L} = \frac{1}{2}(d_{i,j} + d_{j,i}), \tag{3.23}$$

where Einstein convention is applied, the membrane strain interpolation can be expressed by

$$\epsilon_{ij} = \frac{1}{2}(d_{i,j} + d_{j,i}) + \frac{1}{2}\gamma_e^2(d_{k,i}\, d_{k,j}), \tag{3.24}$$

where the nonlinear term on the right would be scaled down when an element's pseudo density is close or smaller than the threshold $\eta$ prescribed in Eq. (3.20).

To validate the strain interpolation method, we use a 2D C-shaped example shown in Fig. 3.17. First, the structure is directly meshed with solid elements, and standard FOMs are used to calculate the number of Newton iterations and the displacements $u_y$ of $(x, y) = (1, 1)$. Next, low-density elements are added to the middle of the C-shaped

structure, and the analysis is repeated using ROMs, as well as standard FOMs with and without strain interpolation. For the parameters in the heaviside function, $\eta = 0.01$ and $\beta = 500$ are selected according to the recommendation in [35].

The deformed configurations from the aforementioned analysis are shown in Fig. 3.18, while the number of Newton iterations and displacement results are compared in Tab. 3.4. As illustrated, without strain interpolation, the low-density elements in the middle exhibit severe instabilities, leading to divergence in the FOM-based analysis. In contrast, when strain interpolation is applied, the FOM-based analysis converges smoothly within 48 iterations. The interpolation technique is also effective for ROMs, allowing the ROM-based analysis to converge smoothly with only 15 FOM-based correction iterations. Importantly, all the analyses produce nearly identical displacement results. In summary, for 2D structures, the strain interpolation method successfully stabilizes low-density areas while maintaining displacement accuracy.



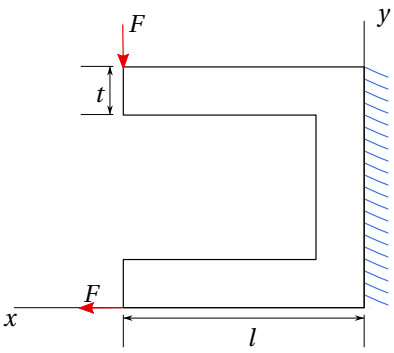


Figure 3.17: A 2D C-shape structure fixed on the right side. All quantities have consistent units. Here $l = 1$, $t = 0.2$, Young's modulus is $E = 3 \times 10^{11}$, Poisson's ratio $\nu = 0.3$, and $F = 1 \times 10^{6}$.

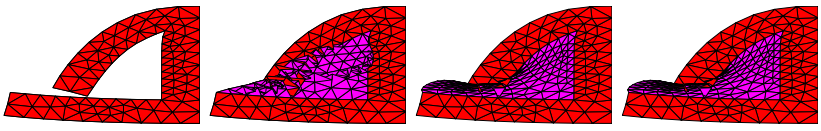


Figure 3.18: Final deformed configuration of the c-shape structure. The red means $\rho_e = 0.999$ and the pink means $\rho_e = 1 \times 10^{-3}$. (a) FOM-based deformations with exclusively solid elements. (b) FOM-based deformations including void elements in the middle. (c) With strain interpolation, FOM-based deformations including void elements in the middle. (d) With strain interpolation, ROM-based deformations including void elements in the middle.

Table 3.4: Analysis results of the C-shape structure using exclusively FOMs without strain interpolation (Normal FOM), FOMs with interpolation (scaled FOM), and ROMs with interpolation (scaled ROM method). Here, $n_{\mathrm{f}}$ and $n_{\mathrm{r}}$ represent the number of FOM-based and ROM-based iterations separately, and $u_y$ the displacement in y-direction of the point located at $(x, y) = (1, 1)$ in Fig. 3.17. Besides, $n^{\mathrm{ref}}$ and $u_y^{\mathrm{ref}}$ represent those of the reference structure shown in Fig. 3.18(a). The number of incremental steps is 10 and for each incremental step, the maximum number of Newton iterations is 50.

| **methods** | $n_{\mathbf{f}}(n^{\mathbf{ref}} = 48)$ | $n_{\mathrm{rf}}$ | $n_{\mathrm{rr}}$ | $u_y(u_y^{\mathbf{ref}} = 0.69574)$ |
|---|---|---|---|---|
| Normal FOM | 202 | | | 0.69574 |
| Scaled FOM | 48 | | | 0.69574 |
| Scaled ROM | | 15 | 47 | 0.69570 |



### STRAIN INTERPOLATION FOR SHELLS

Given the promising 2D results, the strain interpolation method is tested on the flexible shell shown in Fig. 3.19, which is an intermediate design from the optimization process in Fig. 3.13(b). With standard FOM-based analysis and strain interpolation where $\eta = 0.01$, the final deformed configuration is illustrated in Fig. 3.20. As can be observed, strain interpolation effectively eliminates spurious modes in the middle low-density areas.

Displacement results at the final incremental step with and without strain interpolation are compared for different $\eta$ values in Tab. 3.5. As can be observed, when $\eta$ is relatively large, strain interpolation significantly reduces the displacement. As $\eta$ decreases, the reduction gradually alleviated.

This displacement reduction happens because the scaling parameter $\gamma$ affects the nonlinear strain term, especially when rigid body rotations dominate the configuration change. To illustrate this, a simple example of pure rigid body rotation is shown in Fig. 3.21, where a rigid bar rotates by 90 degrees. When using a nonlinear strain model, strain in x-direction, i.e., $\epsilon_{xx}$ can be expressed by

$$\epsilon_{xx} = u_{,x} + 0.5(u_{,x}^2 + v_{,x}^2) = -1 + 0.5((-1)^2 + 1^2) = 0, \tag{3.25}$$

where $u$ represents the displacement in x-direction and $v$ in y-direction. Here, the strain is exactly zero as expected. However, if ignoring the nonlinear term of the strain, i.e. using a linear model, we obtain

$$\epsilon_{xx} = u_{,x} = -1, \tag{3.26}$$

which shows that scaling down and even eliminating the nonlinear strain term introduces artificial in-plane stiffness, preventing the structure from properly exhibiting rigid body rotations. As a result, for nearly inextensional shell structures, where rigid body rotation is relatively dominant, scaling down the nonlinear term adds extra stiffness, leading to displacement reduction. This behavior is further analyzed through a pure-bending shell example with displacement scaling, as detailed in Appendix A.3.

Here, we have discussed only the interpolation between linear and nonlinear strains by introducing the scaling parameter $\gamma$ into the displacement field. However, the same issue can also arise when interpolating between linear and nonlinear strain energies, as

well as between the linear stiffness matrix and the nonlinear tangent stiffness matrix. For strain-energy interpolation (Eq. (3.19)), consider the rigid-body rotation example shown in Fig. 3.21, the interpolation between the linear and nonlinear strain energies can be expressed as $\phi_{xx} = 0.5\left(\gamma u_{,x} + 0.5\gamma^2\left(u_{,x}^2 + v_{,x}^2\right)\right)^2 - 0.5\gamma^2 u_{,x}^2 + 0.5u_{,x}^2$. Similar to strain interpolation, $\gamma \to 0$ will result in $\phi_{xx} = 0.5$, i.e., artificial stretching energy. For stiffness matrix interpolation, nonlinear tangent stiffness matrix can be expressed by $\mathbf{G}[\mathbf{d}] + \mathbf{K}[\mathbf{d}]$, where $\mathbf{d}$ represents displacement field, $\mathbf{K}[\mathbf{d}]$ elastic stiffness matrix, and $\mathbf{G}$ geometric stiffness matrix. The former can be expressed by $\mathbf{K}[\mathbf{d}] = \mathbf{D}[\mathbf{d}]^T\mathbf{S}\mathbf{D}[\mathbf{d}]$. The latter can be expressed by $\mathbf{S}\epsilon[\mathbf{d}]\frac{\partial \mathbf{D}[\mathbf{d}]}{\partial \mathbf{d}}$. Here $\epsilon$ represents strain. The definition of $\mathbf{D}$ and $\mathbf{S}$ can be found in section 3.2. As seen, if a scaling parameter $\gamma$ is introduced to $\mathbf{d}$, the $\mathbf{G}$ matrix will be largely impacted by scaling the nonlinear term in the strain, which dominantly describing rigid body rotations.

Therefore, scaling the nonlinearity may not be the best approach for flexible shells. In the next section, we explore an alternative methodology that avoids nonlinearity scaling.

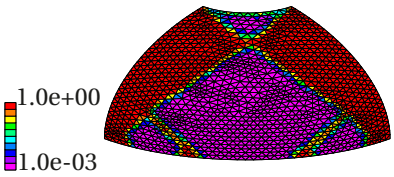


Figure 3.19: An intermediate topology optimization design obtained using ONLY_FOM method. Here, red means pseudo density $\rho_e = 1$, pink $\rho_e = 1 \times 10^{-3}$, i.e., the lower bound of $\rho_e$, and other colors values in-between.

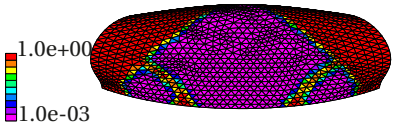


(a) FOM-based deformations with strain interpolation.

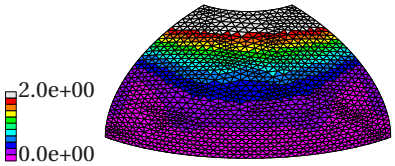


(b) Displacement distributions of (a).

Figure 3.20: FOM-based final deformed configuration and displacement distributions with the strain interpolation. On the left, red means solid ($\rho_e = 1$) and pink void ($\rho_e = 1 \times 10^{-3}$). On the right, white means displacements exceed 2.0, red large displacements, and pink small displacements. Here, no local buckling appear in the middle low-density area. The threshold of the heaviside function is $\eta = 0.01$.

Table 3.5: Displacement comparison with and without the strain interpolation method. Here, $\eta$ represents the threshold of the Heaviside function, $n_f$ denotes the number of FOM-based iterations, and $u_z$ is the displacement in z-direction of Point A, as indicated in Fig. 3.1(a). Additionally, $n^{\text{ref}}$ and $u^{\text{ref}}$ correspond to the reference values obtained using FOMs without strain interpolation. The analysis consists of 10 incremental steps, with a maximum of 50 Newton iterations per step.

| $\log_{10}\eta$ | $n_f$ ($n^{\text{ref}} = 70$) | $u_z$ ($u_z^{\text{ref}} = -3.9997$) |
|---|---|---|
| -2 | 55 | -3.1989 |
| -3 | 56 | -3.4321 |
| -5 | 58 | -3.8040 |
| -9 | 59 | -3.8043 |

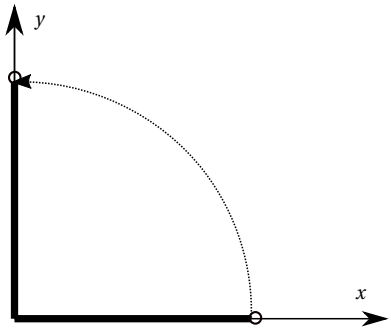


Figure 3.21: A rigid bar rotates by 90 degrees.



### 3.5.2. COMPLEMENTARY STRUCTURE

To explore a novel way for addressing spurious instabilities and resolving the problem of artificial stiffness, in this section, we study a strategy involving complementary structures. The latter refers to structures with element pseudo density $\rho_e^c = 1 - \rho_e$ where $\rho_e$ is the pseudo density of the original structures. The complementary structure can serve as a flexible support for the low-density areas in the original structure to ensure positive definite stiffness matrices. To explain the approach in a straightforward manner, Fig. 3.22 depicts a 1D truss and its complementary structure, where the original structure is shown on the left and the complementary one on the right.

The original structure consists of Elements 1 and 2 with stiffness values $k_1$ and $k_2$, respectively. The complementary structure contains Elements 3 and 4 with stiffness values $k_3 = 1 - k_1$ and $k_4 = 1 - k_2$. The degrees of freedom between the two structures are interconnected via spring elements, indicated by the yellow lines, which have a stiffness of $c$. The structures are illustrated separately for clarity, but in actual analysis, they overlap. Boundary conditions are applied solely to the original structure.

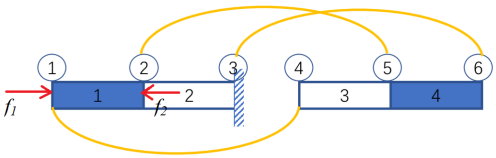


Figure 3.22: An one-dimension truss and its complementary structure. The truss with two elements, three nodes, and two horizontal DOFs is shown on the left, while its complementary is shown on the right. Here, we assume the stiffness of Element 1 is $k_1$ and of Element 2 is $k_2$ , $k_1, k_2 \in [0, 1]$. Then, in the complementary structure, the stiffness of Element 3 is $1 - k_1$ and of Element 4 is $1 - k_2$. The DOFs between the two structures are coupled by spring elements with stiffness $c$ shown by the yellow lines. The two structures are drawn from a distance to convey the concept effectively. In real analysis, they overlap with each other. Boundary conditions are only applied to the original structure.

We assume $k_1 > 0$, then the stiffness matrix $\mathbf{K}$ of the original structure is

$$k_1 \begin{bmatrix} 1 & -1 \\ -1 & 1+\frac{k_2}{k_1} \end{bmatrix}. \tag{3.27}$$

Involving the complementary structure, the stiffness matrix of the whole system can be expressed by

$$k_1 \begin{bmatrix} 1+\frac{c}{k_1} & -1 & -\frac{c}{k_1} & 0 & 0 \\ -1 & 1+\frac{k_2}{k_1}+\frac{c}{k_1} & 0 & -\frac{c}{k_1} & 0 \\ -\frac{c}{k_1} & 0 & \frac{1-k_1}{k_1}+\frac{c}{k_1} & -\frac{1-k_1}{k_1} & 0 \\ 0 & -\frac{c}{k_1} & -\frac{1-k_1}{k_1} & \frac{1-k_1}{k_1}+\frac{1-k_2}{k_1}+\frac{c}{k_1} & -1 \\ 0 & 0 & 0 & -1 & \frac{1-k_2}{k_1}+\frac{c}{k_1}. \end{bmatrix} \tag{3.28}$$

To demonstrate how the complementary structure stabilizes the original one, we set $k_2 = 0$ and $k_1 = 1$, which leads to a singular matrix of the original structure shown by

$$\begin{bmatrix} 1 & -1 \\ -1 & 1 \end{bmatrix}. \tag{3.29}$$

However, concerning the matrix involving the complementary structure, when $k_2 = 0$ and $k_1 = 1$, the stiffness matrix

$$\begin{bmatrix} 1+c & -1 & -c & 0 & 0 \\ -1 & 1+c & 0 & -c & 0 \\ -c & 0 & c & 0 & 0 \\ 0 & -c & 0 & 1+c & -1 \\ 0 & 0 & 0 & -1 & 1+c \end{bmatrix}, \tag{3.30}$$

can still be positive definite if a proper spring stiffness $c$ is chosen.

An appropriate spring stiffness $c$ can prevent low-density regions from turning "inside-out" or exhibiting spurious local buckling, without restricting displacements in solid areas. One possible choice for $c$ is based on the maximum diagonal term of the element's linear stiffness matrices. While it is possible to define a unique spring stiffness for each element and update it during optimization, this would complicate the method. To simplify, the same $c$ is used for all elements and is fixed throughout the optimization process. This value is determined based on the maximum diagonal term among all elements obtained from the initial solid design, represented by $k_{\mathrm{m}}$.

In practice, the spring stiffness $c$ can be defined as follows: if the membrane stiffness $k_{\mathrm{m}}$ is on the order of $10^{\zeta}$, then $c$ can be selected within the range of $1 \times 10^{\zeta-8}$ to $1 \times 10^{\zeta-7}$. For practical cases involving multiple degrees of freedom, each DOF of the original structure is coupled to the corresponding DOF of the complementary structure via a linear spring element with the same stiffness. Further details and examples illustrating this approach are provided in the following sections.

### C-SHAPE STRUCTURE

In this section, the C-shape example shown in Fig. 3.17 is investigated. With a complementary structure on top, the updated C-shape model is shown in Fig. 3.23(a). Each

DOF of the original structure is coupled to the corresponding DOF of the complementary structure via a linear spring element shown by red lines. While the two structures should ideally overlap, they are drawn with a separation for clarity. The boundary conditions for the analysis remain identical to those in Fig. 3.17, but they are applied only to the original structure at the bottom.

Firstly, we apply FOMs to the entire system to evaluate the ability of the complementary structure to stabilize low-density areas and examine the effect of different spring stiffness values. In Tab. 3.6, the displacements in y-direction of the point located at $(x, y) = (1, 1)$ in Fig. 3.17 and the number of FOM updates are compared for different spring stiffness values.



Here, the maximum diagonal term among all elements, $k_{\mathrm{m}}$, is obtained by performing an additional linear analysis on the fully solid structure. With $k_{\mathrm{m}}$ having a magnitude of $10^8$, the most accurate results are expected when the spring stiffness falls within the range $c = [1, 10]$.

As anticipated, the results show that with the complementary structure, when $c = 1$ or $c = 10$, the displacement at the point $(x, y) = (1, 1)$ in Fig. 3.17 closely matches the reference value from the fully solid C-shape model shown in Fig. 3.18(a). Additionally, there are no convergence issues during the analysis process, as indicated by the number of Newton iterations.

From the deformed configuration shown in Fig. 3.23(b), the middle void area of the original structure is effectively stabilized by the solid region in the complementary structure. Although significant deformations are observed at the interface between the solid and void areas, the convergence of the analysis remains unaffected.

Secondly, the method is applied to the ROM setting, with $c = 10$ selected as the spring stiffness. The number of Newton iterations and the corresponding displacement results are presented in Tab. 3.6. It is observed that only 15 correction iterations are required, and the displacements obtained from ROM-based and FOM-based analyses are identical.

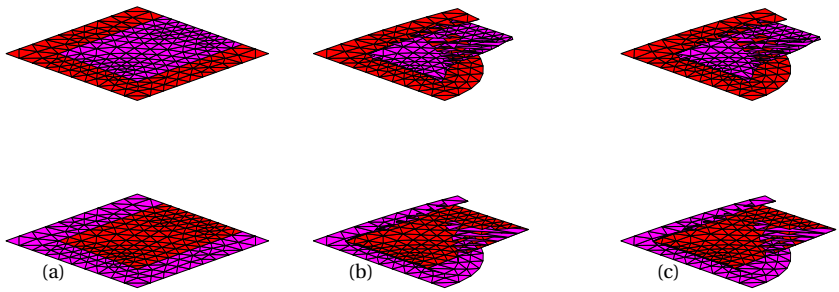


Figure 3.23: A c-shape model and its deformed configurations with complementary structures. The bottom structures are original structures, and the top structures are complementary structures. Here, red elements are with $\rho_{\mathrm{e}} = 0.999$ and pink $\rho_{\mathrm{e}} = 1 \times 10^{-3}$. (a)Undeformed system; (b) FOM-based final deformed configuration; and (c) ROM-based final deformed deformed configuration.

The ROM-based deformation, shown in Fig. 3.23(c), is indistinguishable from the FOM-based deformation. The significant deformations at the interface between solid

and void have no impact on the accuracy or efficiency of the ROMs. These results confirm that the complementary structure can effectively integrate with ROMs to eliminate spurious modes.

Table 3.6: Analysis result of the c-shape complementary system with different spring stiffness $c$. Here, $k_{\mathrm{m}}$ is the maximum diagonal term of linear element stiffness matrices, $n_{\mathrm{f}}$ is the number of FOM-based Newton iterations, $n_{\mathrm{rr}}$ number of ROM iterations, $n_{\mathrm{rf}}$ number of correction iterations in ROMs, $u_y$ the displacement in y-direction of the point located at $(x, y) = (1, 1)$ in Fig. 3.17, $n^{\mathrm{ref}}$ and $u_y^{\mathrm{ref}}$ are those of the reference structure depicted in Fig. 3.18(a). The number of incremental steps is 10 and for each incremental step, the maximum number of Newton iterations is 50.

| $k_{\mathbf{m}}(\rho = 1)$ | method | $c$ | $n_{\mathbf{f}}(n^{\mathbf{ref}} = 47)$ | $n_{\mathrm{rf}}$ | $n_{\mathrm{rr}}$ | $u_z(u_y^{\mathbf{ref}} = 0.69574)$ |
|---|---|---|---|---|---|---|
| 2.8142e8 | FOM | 1 | 60 | | | 0.69574 |
| | | 10 | 57 | | | 0.69573 |
| | | 100 | 52 | | | 0.69567 |
| | | 1000 | 48 | | | 0.69507 |
| | ROM | 10 | | 15 | 47 | 0.69572 |

### SPHERICAL SHELL

Given the promising results from the 2D case, the complementary structure is applied to the flexible spherical shell structure shown in Fig. 3.19. Since membrane strain is the primary cause of spurious modes, only the translational DOFs are coupled using springs between the original and complementary structures. Boundary conditions are applied exclusively to the original structure.

Firstly, we apply FOMs to the entire system to evaluate the ability of the complementary structure to stabilize low-density areas and examine the effect of different spring stiffness values. In Tab. 3.7, the displacements in z-direction at the top corner of the structure and the number of FOM updates are compared for different spring stiffness values.

Here, $k_{\mathrm{m}}$ is determined through a separate linear analysis of a fully solid design, with a magnitude of $1 \times 10^7$. Based on this, $c$ can be chosen between 0.1 and 1. As observed, when $c = 0.1$ or $c = 1$, the FOM-based displacements with the complementary structures are comparable to those without them.

The deformed configuration is shown in Fig. 3.24(b). As observed, no spurious modes are present in the low-density areas. Although significant stretching deformations occur at the interface between solid and void areas, they do not affect convergence.

Secondly, the method is applied to the ROM setting, with $c = 0.1$ chosen as the spring stiffness. The number of Newton iterations and the corresponding displacement results are shown in Tab. 3.7. As observed, only 22 correction iterations are required, and the displacement matches exactly with the FOM-based result. The ROM-based deformation is illustrated in Fig. 3.24(c), where it is evident that, with the assistance of the complementary structures, no spurious modes appear in the ROM basis.

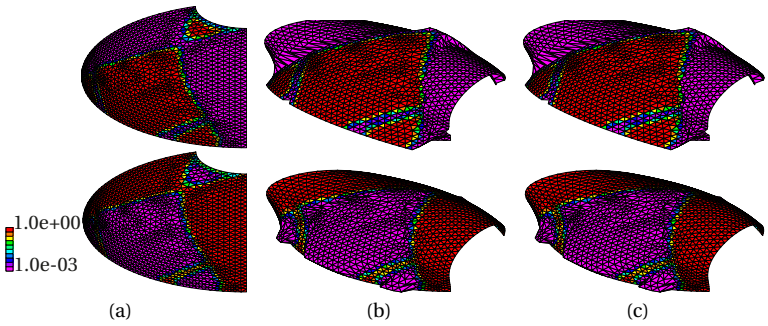


Figure 3.24: A spherical shell intermediate design and its deformed configurations with complementary structures. Here, red means $\rho_e = 1$ and pink $\rho_e = 1 \times 10^{-3}$. (a) undeformed system; (b) Fom-based deformation; and (c) ROM-based deformation. The connection springs in between are ignored for printing purpose.

Table 3.7: Analysis result of the shell complementary system with different spring stiffness $c$. Here, $k_m$ is the maximum diagonal term of linear element stiffness matrices, $n_f$ is the number of FOM-based Newton iterations, $u_x$ and $u_z$ are the displacements in x-direction at coordinate $(r,\theta,\phi) = (10, \frac{2}{5}\pi, 0)$, $n^{\text{ref}}$ and $u^{\text{ref}}$ are those of the reference, i.e., FOM-based results of the original structure. The number of incremental steps is 10 and for each incremental step, the maximum number of Newton iterations is 50.

| $k_{\mathbf{m}}(\rho = 1)$ | method | $c$ | $n_{\mathbf{f}}(n^{\mathbf{ref}} = 70)$ | $n_{\text{rf}}$ | $n_{\text{rr}}$ | $u_z(u_z^{\text{ref}} = -3.9997)$ |
|---|---|---|---|---|---|---|
| 1.1046e7 | FOM | 0.1 | 71 | | | -3.9963 |
| | | 1 | 63 | | | -3.9735 |
| | | 10 | 61 | | | -3.8339 |
| | ROM | 0.1 | | 22 | 68 | -3.9963 |

Given the promising results from the intermediate design analysis, complementary structures are now applied to a complete topology optimization process. Throughout the optimization, 1) spring stiffness $c = 0.1$ is used, and 2) the pseudo-densities of the original structure, $\rho_e$, are used as the design variables. Then, the pseudo-densities of the complementary structure, $\rho_e^c$, are calculated using the formula $\rho_e^c = 1 - \rho_e$ when $1 - \rho_e \geq \rho_0$; otherwise, $\rho_e^c = \rho_0$. Here, $\rho_0 = 1 \times 10^{-3}$ is chosen to prevent singularities.

With the introduction of the complementary structure, the response values $J$, such as objectives and constraints, depend on both $\rho_e$, the pseudo-densities of the original structure, and $1 - \rho_e$, the pseudo-densities of the complementary structure. As a result, the sensitivity evaluation can be expressed as

$$\frac{\mathrm{d}J}{\mathrm{d}\rho_e} = \frac{\partial J}{\partial \rho_e} - \frac{\partial J}{\partial (1-\rho_e)}, \tag{3.31}$$

which means the sensitivity values of the original structure are adjusted by subtracting the sensitivity values of the complementary structure. With the above settings, we conduct ROM-based topology optimization for the spherical shell model shown in Fig. 3.1, with the optimization formulations depicted in Eq. (3.17).

The final topology is shown in Fig. 3.25(a). Compared to the one shown in Fig. 3.2(a), where no complementary structure is used, the incorporation of the complementary structure results in a design with less material.

The efficiency test results are shown in Fig. 3.25(b). As seen, the use of the complementary structure ensures that both the number of ROM-based iterations and FOM-based correction iterations remain stable throughout the optimization process. The number of correction iterations stays below 20 and even approaches zero after 50 optimization steps.



As seen, with a fixed spring stiffness, the complementary structure can effectively stabilize the low-density areas throughout the optimization and prevents the introduction of spurious modes into the ROM basis. Although introducing the complementary structure doubles the degrees of freedom, the method can be combined with the proposed ROMs to achieve relatively high efficiency.

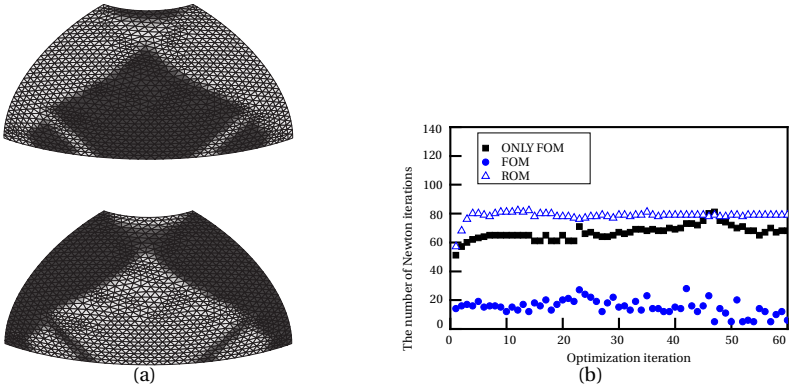


(a) (b)

Figure 3.25: Topology optimization results for spherical shell using ROMs with complementary structures. The connection springs in between are ignored for printing purpose. (a) Topology result where the objective value is 2.042. (b) Efficiency test in topology optimization with complementary structures. The efficiency of ROMs is assessed by measuring the number of ROM-based updates, shown by triangle blue points, and FOM-based correction iterations, shown by round blue points, at each optimization step. These numbers are compared with the number of FOM-based updates of exclusively FOM strategy, which are the black points. The number of incremental steps 10, maximum number of Newton iterations within one incremental step 50.

## 3.6. SUMMARY AND CONCLUSIONS

This chapter primarily focuses on flexible shells, investigating convergence difficulties in the ROM-based topology optimization method caused by low-density areas. Here, convergence difficulties refer to the need for numerous FOM-based correction iterations to reduce significant differences between FOM-based and ROM-based deformations in low-density areas. These differences arise because orthonormalized FOM-based solutions, which contain local buckling in low-density areas, i.e., spurious modes are used as ROM base vectors. The combination of these orthonormalized spurious modes ultimately produces a buckling mode in the ROM-based solutions that differ from those in the FOM-based solutions.

Based on findings, the solution to alleviate ROM convergence difficulties is to narrow

the gap between ROM- and FOM-based deformations in low-density areas or to eliminate spurious modes from the underlying physics. To narrow the differences, modifying the ROM basis can be an option. These methods are straightforward to implement and specifically tailored for ROMs. However, since spurious modes can develop and evolve during optimization, ROMs may fail to capture newly developed spurious modes at certain optimization steps, temporarily increasing the need for FOM-based corrections. Additionally, these methods are effective only when FOMs can converge; otherwise, removing spurious modes from the physics are necessary.

To eliminate spurious modes from the physics, a straightforward approach is to reduce the nonlinearity of low-density elements, as typically done in the strain interpolation method. However, by scaling the displacement field, rigid-body rotations in low-density elements are reduced, which introduces artificial in-plane stiffness in flexible shells structures. Similar issue can also arise when interpolating tangent stiffness matrices or structural energy, as long as these methods tend to scale the displacement field.

To avoid this artificial stiffness, we explored a method involving complementary structure connected to the original structure via spring elements. This complementary structure acts as a flexible support, stabilizing low-density regions and preventing spurious local buckling. Although large deformations are observed in the transition areas between solid and void elements, these do not appear to affect convergence. While introducing the complementary structure doubles the degrees of freedom, the method can be combined with the proposed ROMs to achieve relatively high efficiency. The current work considers coupling only translational DOFs. Extending the coupling to include all DOFs could be beneficial for achieving exact void regions in the optimized design.



## REFERENCES

[1] M. P. Bendsøe and O. Sigmund, *Material interpolation schemes in topology optimization,* Archive of applied mechanics **69**, 635 (1999).

[2] L. F. Sá, P. V. Yamabe, B. C. Souza, and E. C. Silva, *Topology optimization of turbulent rotating flows using spalart–allmaras model,* Computer Methods in Applied Mechanics and Engineering **373**, 113551 (2021).

[3] H.-K. Zhang, W.-J. Wu, Z. Kang, and X.-Q. Feng, *Topology optimization method for the design of bioinspired self-similar hierarchical microstructures,* Computer Methods in Applied Mechanics and Engineering **372**, 113399 (2020).

[4] L. Chen, C. Lu, H. Lian, Z. Liu, W. Zhao, S. Li, H. Chen, and S. P. Bordas, *Acoustic topology optimization of sound absorbing materials directly from subdivision surfaces with isogeometric boundary element methods,* Computer Methods in Applied Mechanics and Engineering **362**, 112806 (2020).

[5] J. Zhu and T. Gao, *Topology optimization in engineering structure design* (Elsevier, 2016).

[6] A. Polynkin, F. Van Keulen, and V. Toropov, *Optimization of geometrically nonlinear thin-walled structures using the multipoint approximation method,* Structural optimization **9**, 105 (1995).

[7] H. Altenbach, O. Morachkovsky, K. Naumenko, and A. Sychov, *Geometrically nonlinear bending of thin-walled shells and plates under creep-damage conditions,* Archive of Applied Mechanics **67**, 339 (1997).

[8] E. Rank, S. Kollmannsberger, C. Sorger, and A. Düster, *Shell finite cell method: A high order fictitious domain approach for thin-walled structures,* Computer Methods in Applied Mechanics and Engineering **200**, 3200 (2011).

[9] *A Large Range Spatial Linear Guide With Torsion Reinforcement Structures*, International Design Engineering Technical Conferences and Computers and Information in Engineering Conference, Vol. Volume 5A: 42nd Mechanisms and Robotics Conference (2018) v05AT07A025.

[10] M. Naves, R. Aarts, and D. Brouwer, *Large stroke high off-axis stiffness three degree of freedom spherical flexure joint,* Precision Engineering **56**, 422 (2019).

[11] T. Bruns, O. Sigmund, and D. A. Tortorelli, *Numerical methods for the topology optimization of structures that exhibit snap-through,* International Journal for Numerical Methods in Engineering **55**, 1215 (2002).

[12] H. Deng, L. Cheng, X. Liang, D. Hayduke, and A. C. To, *Topology optimization for energy dissipation design of lattice structures through snap-through behavior,* Computer Methods in Applied Mechanics and Engineering **358**, 112641 (2020).

[13] K. A. James and H. Waisman, *Layout design of a bi-stable cardiovascular stent using topology optimization,* Computer Methods in Applied Mechanics and Engineering **305**, 869 (2016).

[14] J. Marconi, P. Tiso, and F. Braghin, *A nonlinear reduced order model with parametrized shape defects,* Computer Methods in Applied Mechanics and Engineering **360**, 112785 (2020).

[15] L. Zhang, Y. Zhang, and F. van Keulen, *Topology optimization of geometrically nonlinear structures using reduced-order modeling,* Computer Methods in Applied Mechanics and Engineering **416**, 116371 (2023).

[16] T. E. Bruns and D. A. Tortorelli, *An element removal and reintroduction strategy for the topology optimization of structures and compliant mechanisms,* International journal for numerical methods in engineering **57**, 1413 (2003).

[17] J. Zhao and W. Chunjie, *Geometrically nonlinear finite element behaviour using buckling mode superposition,* Computer Methods in Applied Mechanics and Engineering **53**, 101 (2016).

[18] D. Nagy and M. König, *Geometrically nonlinear finite element behaviour using buckling mode superposition,* Computer Methods in Applied Mechanics and Engineering **19**, 447 (1979).

[19] A. S. L. Chan and K. M. Hsiao, *Nonlinear analysis using a reduced number of variables,* Computer Methods in Applied Mechanics and Engineering **52**, 899 (1985).

[20] O. Amir, M. P. Bendsøe, and O. Sigmund, *Approximate reanalysis in topology optimization,* International Journal for Numerical Methods in Engineering **78**, 1474 (2009).

[21] C. Gogu, *Improving the efficiency of large scale topology optimization through on-the-fly reduced order model construction,* International Journal for Numerical Methods in Engineering **101**, 281 (2015).

[22] E. Hooijkamp and F. v. Keulen, *Topology optimization for linear thermo-mechanical transient problems: Modal reduction and adjoint sensitivities,* International Journal for Numerical Methods in Engineering **113**, 1230 (2018).

[23] S. Wang, E. de Sturler, and G. Paulino, *Large-scale topology optimization using preconditioned krylov subspace methods with recycling,* International journal for numerical methods in engineering **69**, 2441 (2007).

[24] L. Xia and P. Breitkopf, *A reduced multiscale model for nonlinear structural topology optimization,* Computer Methods in Applied Mechanics and Engineering **280**, 117 (2014).

[25] C. E. Orozco and O. N. Ghattas, *A reduced sand method for optimal design of nonlinear structures,* International Journal for Numerical Methods in Engineering **40**, 2759 (1997).

[26] R. D. Lahuerta, E. T. Simões, E. M. Campello, P. M. Pimenta, and E. C. Silva, *Towards the stabilization of the low density elements in topology optimization with large deformation,* Comput. Mech. **52**, 779–797 (2013).

[27] P. Wriggers, J. Schröder, and A. Schwarz, *A finite element method for contact using a third medium,* Computational Mechanics **52**, 837–847 (2013).

[28] P. Wriggers, J. Korelc, and P. Junker, *A third medium approach for contact using first and second order finite elements,* Computer Methods in Applied Mechanics and Engineering **436**, 117740 (2025).

[29] G. Bluhm, O. Sigmund, and K. Poulios, *Internal contact modeling for finite strain topology optimization,* Computational Mechanics **67**, 1 (2021).

[30] A. H. Frederiksen, A. Dalklint, O. Sigmund, and K. Poulios, *Improved third medium formulation for 3d topology optimization with contact,* Computer Methods in Applied Mechanics and Engineering **436**, 117595 (2025).

[31] G. H. Yoon and Y. Y. Kim, *Element connectivity parameterization for topology optimization of geometrically nonlinear structures,* International Journal of Solids and Structures **42**, 1983 (2005).

[32] F. Van Keulen and J. Booij, *Refined consistent formulation of a curved triangular finite rotation shell element,* International journal for numerical methods in engineering **39**, 2803 (1996).

[33] M. Langelaar, K. Maute, N. van Dijk, and F. van Keulen, *Investigation of instabilities arising in internal element connectivity parameterization,* in *Proceedings of the 2nd International Conference on Engineering Optimization*, edited by Rodrigues, H., Herskovits, J., and Mota Soares, C. (s.n., 2010) pp. 1–10, 2nd International Conference on Engineering Optimization, Lisbon, Portugal ; Conference date: 06-09-2010 Through 09-09-2010.

[34] N. P. van Dijk, M. Langelaar, and F. van Keulen, *Element deformation scaling for robust geometrically nonlinear analyses in topology optimization,* Structural and Multidisciplinary Optimization **50**, 537 (2014).

[35] F. Wang, B. S. Lazarov, O. Sigmund, and J. S. Jensen, *Interpolation scheme for fictitious domain techniques and topology optimization of finite strain elastic problems,* Computer Methods in Applied Mechanics and Engineering **276**, 453 (2014).

# 4

# CONNECTIVITY-DRIVEN TOPOLOGY OPTIMIZATION FOR PATH-FOLLOWING COMPLIANT MECHANISM

*We propose a topology optimization (TO) formulation and related optimization scheme for designing compliant mechanisms following a user-defined trajectory. To ensure the broad applicability and achieve precisely control of the outputs, geometric nonlinearity with incremental solutions are considered. A challenge in the design optimization of these structures is the development of formulations with satisfactory balance between (i) precise trajectory control, and (ii) proper connectivity between the input/output ports and the support. Previously proposed density-based topology optimization formulations typically lack the promotion of the desired load-transferring connections, or usually complicate the design using mixed shape, size, and topology variables to enforce a minimum connectivity. To simplify design process using exclusive topology variables, i.e. purely density-based TO methods, we propose a relatively straightforward formulation involving commonly-used response functions, such as compliance and volume as constraints. For the constraints, the chapter provides a scheme for defining corresponding upper limits. Numerical examples of challenging shell and plate design optimization problems demonstrate the effectiveness of the proposed formulation and scheme in the generation of load-transferring connections while limiting the impact on the performance of the path-generation functionality.*

This chapter has been published in Structural and Multidisciplinary Optimization, **68(2)**, Article 36. (2025)

## 4.1. INTRODUCTION

Density-based topology optimization (TO) was initially mostly applied in linear stiffness design [1, 2]. Since then, the method is widely used for many other design purposes [3–6]. One of the prevalent applications is compliant mechanisms [7–9], for which, Density-based TO allows creating highly complex and sophisticated structures that would be challenging to design based on intuition. A class of typically complicated-to-design compliant mechanisms is known as path-generation compliant mechanisms (PGCMs). A PGCM's out ports can move following a user-defined trajectory, when, for example, displacements or forces are applied to the input ports. To achieve precise control of the output ports along the defined trajectory, nonlinear analysis with incremental solutions are prevalent adopted in topology optimization for PGCMs. Furthermore, even though practical applications may require linear relationships between inputs and outputs, the mechanism itself may exhibit finite deflections and rotations. Consequently, it is necessary to consider geometric nonlinearity in potential designs for ensuring broad applicability, for example decoupled X-Y stages [10–12] and linear guide actuators [13–15].

To design PGCMs using Density-based TO, it could be challenging to automatically promote connectivity between input, output ports, and supporting boundaries. A typical result exhibiting lack of connectivity is shown in Fig. 4.1, where the objective is to minimize the squared in-plane displacements of the center point at multiple pseudo-time points given a prescribed out-of-plane displacement. The optimizer opts here to converge to the obvious trivial solution of disconnecting the center point. Although this design can achieve the specified goal, it lacks physical meaning in the real world.

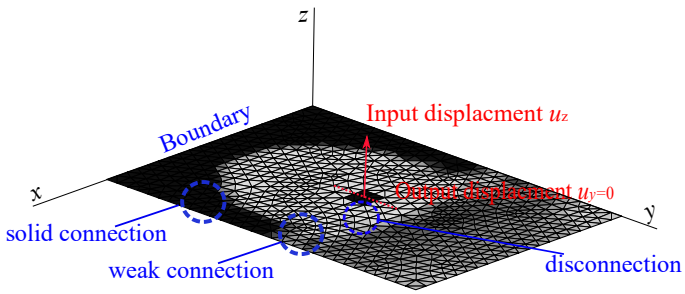


Figure 4.1: A topology optimization result without connectivity. The objective is to minimize the squared in-plane displacements $u_y$ of the center point at multiple pseudo-time points given a prescribed out-of-plane displacement $u_z$. Here, black represents solid material (pseudo density $\rho_e$=1), white void ($\rho_e$=0), and gray those in between ($0 < \rho_e < 1$). The middle black block represents a non-design area. The design shows both disconnections with void elements and weak connections with gray elements.

For the issue illustrated in Fig. 4.1, the reason, as stated in [7], is the lack of force transfer requirements among the input, output, and the support in purely density-based TO methods. To ensure connectivity, preferably with solid connections shown in Fig. 4.1, two methodologies are generally employed: one involves incorporating force transfer requirements into the density-based TO, while the other abandon purely density-based TO, proposing a different parameterization method, such as incorporating size and shape design variables. The latter approach has been extensively explored in previous works.

First, shape variables can ensure the connectivity. Tai *et al.* [16, 17] expressed structural topology by mapping a set of Bezier curves onto a fixed finite element mesh, which connected input to output ports. Along the Bezier curves, materials were allowed to grow on the finite element mesh to form a new structural topology. Due to the inherent continuity of Bezier curves, any topology mapped from these curves always maintains connectivity. Lu and Kota [18], as well as Zhou and Ting [19] segment the load path into multiple sections, where the length and position of each section were then designed. This, in turn, guarantees the structural connectivity among the input and output ports. For the above method, it is necessary to determine an initial shape guess, which often requires some level of domain knowledge, engineering intuition, or prior experience. Furthermore, given that shape design variables are involved in the methods mentioned above, related sensitivity calculations become relatively difficult. Thus, zero-gradient methods, e.g. genetic algorithms (GA) are prevalent choices adopted in the mentioned works instead of more efficient gradient-based methods. Second, connectivity can be ensured by size variables corresponding to ground structures' elements. Saxena [20], Rai *et al.* [21–25], Nagendra *et al.* [26], and Naik *et al.* [27], focusing on frame-element-based ground structures, designed PGCM by adjusting, for example, the length and height of frame elements. Given that an intermediate value of such design variable is manufacturable, no connectivity issues as in purely density-based TO are encountered. However, the size control method may be restricted to ground-structure-based designs and may not be easily applied to other types of elements, such as plates and shells, which can be manufactured more readily using laser cutting.



Another approach to enhance connectivity in path-generation mechanisms is through the use of hexagonal tessellated finite elements and negative masks [28–30]. Briefly, they discretize the design domain by Hexagonal elements, then, utilizing movable masks to define the topology, where material inside the mask is removed. By utilizing edge-connected Hexagonal elements and the proposed boundary smoothing techniques[31], they can form hinge-free designs. Besides, as is verified in their previous work, using masks with hexagonal elements helps ensure the minimum and maximum length scales in the topology, consequently obtaining readily manufacturable designs [32]. However, ensuring length scales or changing the design parameterization may not address all kinds of connection issues, such as the case study for which the result is shown in Fig. 1. Here the weak connections could be resolved, but the disconnections may not. Consequently, the hexagonal tessellation combined with negative mask method may also not solve the disconnections shown in Fig. 1. In previous work related to designs of contact-aided compliant mechanisms [33–36], indeed, no disconnection issue like the one shown in Fig.1 is encountered. This could be that the connectivity between their outputs/inputs and boundaries are implicitly indicated in complex path-generation requirements. In our cases, we explore relatively simple paths focusing on specific timing positions. In this context, disconnections like those depicted in Fig. 1 may be more easily encountered. Furthermore, the hexagonal tessellation combined with negative mask method may not be readily applied to shells and plates, which are light-weighted, easily manufactured, and potentially exhibiting large deflections compared to their footprint.

To explore methods that are easily implemented and versatile for various elements and structures—especially shells and plates, which are easily manufactured using tech-

niques like laser cutting—we will focus on density-based topology optimization (TO) methods. These methods are readily available, easy to apply to any type of element, and do not require domain knowledge for initial designs. When applying density-based TO, load transfer requirement is a possibility for promoting the connectivity. For considering load transfer requirement for PGCM designs, several related work can be found. Saxena and Anathasuresh [37] introduced springs to output ports during the optimization procedure. The springs can avoid forming disconnections, but the required stiffness of the spring is difficult to decide. Pedersen *et al.* [7] considered three load cases in the nonlinear analysis to ensure connectivity, which are: 1) without any force at the output port, 2) with a force at the output port aligned with the trajectory, and 3) with a force at the output port perpendicular to the trajectory. The design was mandated to follow the desired trajectory in all three load cases, which promotes the connectivity of a path-generation design. Although the formulation is general and effective, the solution process faces overwhelming computing efforts due to nonlinear matrix updating and refactorization. Furthermore, gray elements would still appear in the results. For the latter, Reinisch *et al.* [38] introduced stress constraints to the method in [7]. However, stress constraints could further increase computational time. Moreover, optimization formulations that involve stress constraints may encounter issues with singular optima, necessitating additional treatments [39]. Recognizing the intricacies of past methods, there is a compelling need to explore a streamlined, versatile, and effective approach. This aims to guarantee seamless connectivity and suppress undesired gray areas, paving the way for a more efficient and universally applicable design methodology.

To tackle the challenges mentioned above corresponding to density-based TO, we follow Koppen *et al.* [40], and introduce a straightforward optimization formulation aimed at promoting connectivity, whose parameter selection scheme is illustrated to suppress the gray elements. The proposed formulation, which is introduced in Section 4.2, involves commonly used compliance and volume functions as constraints and, consequently, is easily extended to any structure and optimization algorithm. The upper limits of mentioned constraints are defined by the proposed embedded parameter selection strategy, which is explored extensively in Section 4.3. Next, several numerical examples in Section 4.4 verify the effectiveness of the proposed formulation and solution scheme. We use shells and plates in our numerical examples because of their slender nature and coupling between stretching and bending, which make them ideal for designing relatively large-displacement compliant mechanisms and promising for achieving complex path-generation requirements. Moreover, many practical compliant mechanisms can be and are being manufactured from plates and thin-walled tubes, utilizing techniques such as laser cutting.

## 4.2. FORMULATIONS

To achieve connectivity and potentially further suppress gray elements in the design of PGCMs, one typical option is to include appropriate constraints in the optimization formulations. In this section, our primary focus is on identifying suitable and easily implemented constraints through mathematical analysis of the corresponding optimization formulations. Prior to delving into the optimization formulation for PGCMs, we introduce fundamental concepts of a general density-based topology optimization for-

mulation in Section 4.2.1. Here, the knowledge related to Lagrange multipliers and the reason of forming gray elements provide the basis for the proposed formulations in Section 4.2.2 and the optimization scheme in Section 4.3. Consequently, relatively elaborate introductions are given in this section.

### 4.2.1. DENSITY-BASED TOPOLOGY OPTIMIZATION FORMULATION

A density-based topology optimization problem can be generally expressed by

$$\min_{\boldsymbol{\rho}} \; f_0(\boldsymbol{\rho}), \tag{4.1}$$

$$\text{s.t.} \; g_l(\boldsymbol{\rho}) \leq 0, \;\; \forall l = \{1...q\} \tag{4.2}$$

$$\mathbf{0} < \boldsymbol{\rho}_0 \leq \boldsymbol{\rho} \leq \mathbf{1}, \tag{4.3}$$

Here, $f_0$ is an objective function, $g_l$ the $l$ constraint, $q$ the number of constraints, $\boldsymbol{\rho}$ pseudo-densities, $\boldsymbol{\rho}_0$ the lower limit of $\boldsymbol{\rho}$, and $\mathbf{1}$ the upper limit of $\boldsymbol{\rho}$ with all components equal to 1. Typically, to solve an optimization problem with inequality constraints, a Lagrange function involving $f_0$ and $g_l$ is defined as

$$L(\boldsymbol{\rho}, y_l) = f_0(\boldsymbol{\rho}) + \sum_{l=1}^{q} y_l g_l(\boldsymbol{\rho}), \tag{4.4}$$

where $y_l \geq 0$ represents a Lagrange multiplier expressed by

$$y_l = \frac{\partial L}{\partial g_l}, \tag{4.5}$$

which reflects the relationship between the Lagrange function and the constraint during the optimization process. From Eq. (4.4), it follows that the constraints contribute to the Lagrange function only when $y_l > 0$. This knowledge is used in the following sections to select the upper limits of the constraints.

Moreover, if we express a constraint $g_l$ by a variable term $w_l$ combined with a constant term (the upper limit) $\overline{w}_l$, i.e. $g_l(\boldsymbol{\rho}) = w_l(\boldsymbol{\rho}) - \overline{w}_l$, the Lagrange multiplier $y_l$ is then

$$y_l = -\frac{\partial L(\boldsymbol{\rho}, y_l, \overline{w}_l)}{\partial \overline{w}_l}. \tag{4.6}$$

Given the above, when optimization comes to a stationary point $(\boldsymbol{\rho}^*, y_l^*)$, according to the envelope theory, Eq. (4.6) is transformed to

$$y_l^* = -\frac{\partial f_0(\boldsymbol{\rho}^*, \overline{w}_l)}{\partial \overline{w}_l}, \tag{4.7}$$

which defines the relationship between the objective value $f_0$ and the upper limit $\overline{w}_l$. From Eq. (4.7), by analyzing the Lagrange multiplier at the converged point, we can predict how changes in the upper limit will impact the objective value. This understanding is central to our optimization scheme outlined in Section 4.3, where users can adjust the constraint upper limits to suppress gray elements further, according to the desired objective error tolerance.

After introducing the Lagrange multipliers, the original optimization problem can be transformed to

$$\min_{\boldsymbol{\rho}_0 \le \boldsymbol{\rho} \le \mathbf{1}} \max_{y_l \ge 0} L(\boldsymbol{\rho}, y_l). \tag{4.8}$$

By exploring the minimizing problem related to $\boldsymbol{\rho}$ shown in Eq. (4.8), we can understand why there are gray elements, based on the partial derivative of $L$ with respect to $\rho_k$:

$$\frac{\partial L}{\partial \rho_k} = \frac{\partial f_0}{\partial \rho_k} + \sum_{l=1}^{q} y_l \frac{\partial g_l}{\partial \rho_k}, \tag{4.9}$$

Here, if $\frac{\partial L}{\partial \rho_k} > 0$, reducing element $k$'s density would reduce $L$. Consequently, in the next iteration, the design variable value of element $k$ will lower. Conversely, if $\frac{\partial L}{\partial \rho_k} < 0$, in the next iteration, the element $k$'s density will increase. When $\frac{\partial L}{\partial \rho_k} = 0$, there is no need for the optimizer to increase or reduce $\rho_k$, potentially resulting in an intermediate density value between the upper and lower limits, i.e., a gray element. The latter is usually alleviated by introducing black-white projection schemes, such as Heaviside filter. However, only by pushing elements to become black-white possibly results in topologies consisting of disjoint solid areas. One possibility to effectively enhance the connectivity in density-based TO is to carefully selected constraints for PGCM designs. Details about how the constraints are selected from a mathematical aspect are illustrated in the next section.

### 4.2.2. FORMULATIONS FOR PATH-GENERATION COMPLIANT MECHANISMS

In this section, we present a simple optimization formulation for establishing connectivity in path-generation designs using density-based topology optimization (TO) methods. We first describe the objective function. Then, we propose two essential constraints, and explain their importance for establishing the connectivity from a mathematical aspect.

To meet a path-generation requirement when both shape and timing are important, usually, several precision points are used to represent a user-defined path followed by the mechanism. Each precision point is denoted by a pair of input and output values, i.e., $(u_{i,j}^{\text{in}}, u_{i,j}^{\text{out}})$ where $j$ and $i$ represents the indexes of precision points and degrees of freedom, respectively. The inputs here are closely tied to the incremental steps in the nonlinear analysis. For the outputs, in the desired (user-defined) path, they are predetermined. While in the realized path, it is calculated through nonlinear analysis. During the optimization process, efforts are made to minimize the disparity between the desired path and the realized path. Consequently, the objective function is expressed by

$$f_0 = \sum_{i=1}^{n} \sum_{j=1}^{m} \alpha_{i,j} \left( u_{i,j}^{\text{out}} - u_{i,j}^{*} \right)^2. \tag{4.10}$$

Here, $u_{i,j}^{\text{out}}$ and $u_{i,j}^{*}$ denote the outputs on the realized and desired paths, receptively. Besides, $m$ represents the number of precision points, $n$ the number of degrees of freedom (DOFs), and $\alpha_{i,j}$ represents a weight factor. The latter is set to 1 in the work but can be adjusted if different precision points have different levels of importance.

If we take the above objective function and conduct an unconstrained optimization, the Lagrange function is the objective function itself. Then the gradient of the Lagrange function, i.e. the objective function $f_0$, with respect to $\rho_k$ can be expressed by

$$\frac{\partial f_0}{\partial \rho_k} = \sum_{i=1}^{n} \sum_{j=1}^{m} 2\alpha_{i,j}(u_{i,j}^{\text{out}} - u_{i,j}^{*}) \frac{\partial u_{i,j}}{\partial \rho_k}. \tag{4.11}$$

When the unconstrained optimization problem reaches the optimum, it satisfies the condition $\frac{\partial f_0}{\partial \rho_k} = 0$. As defined in Section 4.2.1, $\frac{\partial f_0}{\partial \rho_k} = 0$ would lead to gray elements. Hence, it is highly probable that the connectivity is not established.

In order to establish connectivity, we consider constraints that can contribute non-zero sensitivities. Usually, a mechanism following user-defined paths is desired to maintain sufficient stiffness to support a load in its undeformed configuration, i.e. within the linear scope. For the latter, information can usually be found in stiffness specifications of a design. It defines the load a mechanism must carry in its undeformed configuration, and the allowed displacement given the load. By utilizing the information, we can set a linear compliance constraint expressed by

$$g_c = C_s - \overline{C_s} \quad \forall s = \{1...q\}, \tag{4.12}$$

Here, $C_s$ is the compliance calculated in a separate linear load case with a load $(\mathbf{F}_L)_s$ applied in $s$-direction, $q$ the number of directions where compliance constraints are required, and $\overline{C_s}$ the corresponding upper limit defined by the user, which can be determined as $(\mathbf{F}_L \overline{\mathbf{u}}_L)_s$. Here, $(\overline{\mathbf{u}}_L)_s$ is the allowable displacement given this load.

Next, for simplification, we assume that only one compliance constraint is involved. Then, the Lagrange function can be expressed by

$$L = f_0 + y_c(C - \overline{C}) \tag{4.13}$$

where $y_c$ denotes the multiplier for the compliance constraint. The gradient of $L$ with regard to $\rho_k$ is

$$\frac{\partial L}{\partial \rho_k} = \frac{\partial f_0}{\partial \rho_k} + y_c \frac{\partial C}{\partial \rho_k}. \tag{4.14}$$

If $\frac{\partial f_0}{\partial \rho_k}$ approaches 0, $\frac{\partial L}{\partial \rho_k}$ depends on $y_c \frac{\partial C}{\partial \rho_k}$. In this situation, regarding $y_c > 0$, if $y_c \frac{\partial C}{\partial \rho_k} < 0$ and not close to 0, then $\frac{\partial L}{\partial \rho_k} < 0$ and the pseudo density of element $k$ will increase. If $y_c \frac{\partial C}{\partial \rho_k}$ is close to 0, then $\frac{\partial C}{\partial \rho_k}$ is close to 0, which means the element $k$ currently has almost no influence on both the objective and the compliance constraint. In other words, element $k$ contributes to nothing but increase the volume. In this case, the element could be gray and floating in the design domain, which is defined as a useless element. To remove such an element, a volume constraint $g_v = V - \overline{V}$ can be introduced to the optimization formulation, where $V$ presents the design's volume and $\overline{V}$ the corresponding upper limit. With the volume constraint, the Lagrange formulation can be expressed by

$$L = f_0 + y_c(C - \overline{C}) + y_v(V - \overline{V}) \tag{4.15}$$

where $y_v$ denotes the multiplier for the volume constraint. The gradient of $L$ with regard to an element pseudo density $\rho_k$ is

$$\frac{\partial L}{\partial \rho_k} = \frac{\partial f_0}{\partial \rho_k} + y_c \frac{\partial C}{\partial \rho_k} + y_v \frac{\partial V}{\partial \rho_k}. \tag{4.16}$$

Here, we only discuss the situation when $y_v > 0$ and $y_c > 0$. If both $\frac{\partial f_0}{\partial \rho_k}$ and $\frac{\partial C}{\partial \rho_k}$ are near to zero, $\frac{\partial L}{\partial \rho_k}$ is completely dependent on the value of $y_v \frac{\partial V}{\partial \rho_k}$. Since the sensitivity of the volume constraint $\frac{\partial V}{\partial \rho_k}$ is always positive, we have $\frac{\partial L}{\partial \rho_k} > 0$ indicating that the element will be removed, and the issue related to useless elements (materials) is resolved. The only chance for Eq. (4.16) to render an intermediate element density is when $y_c \frac{\partial C}{\partial \rho_k} = -y_v \frac{\partial V}{\partial \rho_k}$, but this rarely happens in practice. If it happens, we can still disrupt the balance by adjusting the upper limits. Since stiffness is often specified as a design requirement, in this study we choose to adjust the upper limit of the volume constraint. By introducing the compliance and volume constraints, the proposed formulations can be finally summarized as

$$\begin{aligned} \min_{\boldsymbol{\rho}} \; & f_0(\boldsymbol{\rho}) = \sum_{i=1}^{n} \sum_{j=1}^{m} \alpha_{i,j} (u_{i,j}^{\text{out}}(\boldsymbol{\rho}) - u_{i,j}^{*})^2, \\ \text{s.t. } & C_s(\boldsymbol{\rho}) \le \overline{C_s}, \quad \forall s = 1...q \\ & V \le \overline{V}, \\ & \mathbf{0} < \boldsymbol{\rho}_0 \le \boldsymbol{\rho} \le \mathbf{1}. \end{aligned} \tag{4.17}$$

Overall, the resulting optimization formulation can be viewed as a simplified version of the three–load–case methodology proposed in [7]. Instead of introducing additional nonlinear load cases as [7], the proposed approach in this work relies on enforcing stiffness only in the undeformed configuration to achieve the required connectivity. In certain situations, considering stiffness solely in the undeformed configuration may indeed be adequate: when the stiffness to be constrained is expected to increase as deformation processes, in which case constraining the undeformed stiffness provides a conservative choice; and when the purpose of enforcing compliance is simply to ensure load transfer for establishing connectivity between the input/output and the support.

According to all the discussions in this section, we still have several questions to answer: 1) How we can ensure both $y_v > 0$ and $y_c > 0$; 2) How we can define the initial upper limits of volume constraints; and 3) When and how we can adjust the volume upper limits. These questions are important for promoting connectivity and suppressing gray elements. So in the next section, we will answer these questions by proposing a parameter selection scheme which is embedded in the optimization process.

## 4.3. OPTIMIZATION SCHEME

In this section, we propose an optimization scheme, involving the prediction and adjustment of $\overline{V}$ to obtain connectivity and suppressing gray elements for PGCM designs. A general scheme is shown in Fig. 4.2 and explanations are followed.

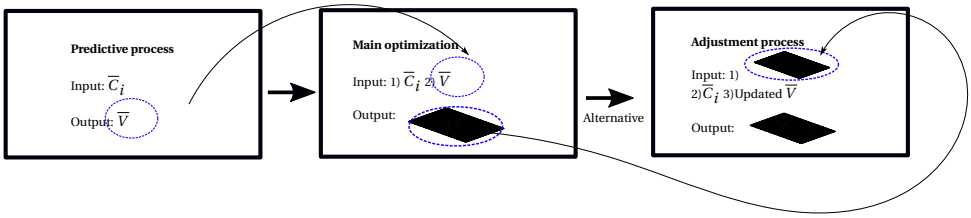


Figure 4.2: A general three-process optimization scheme to ensure a clear topology. Firstly, a known upper limit of compliance $\overline{C}_i$ is used to predict the upper limit of volume $\overline{V}$. With the predicted $\overline{V}$, the optimization starts with both volume and compliance constraints, and we call this process Main optimization. From the Main optimization, a topology with promoted connectivity will be obtained. Then, alternatively, we can further suppress the gray element by conducting an adjustment process, where the converged topology from the Main optimization will be taken as the start point, and volume will be adjusted according to objective error allowance. The adjustment process is alternative, the user can also consider using suitable post-processing method to deal with remained gray elements. But please notice that post-processing method could influence the performance of manufacturing prototypes.



- **Predictive process**. Initially, the upper limit of the volume constraint can be roughly estimated by aggregating the volume of beneficial elements at several optimization steps, where these elements exhibit negative objective sensitivities with respect to their pseudo densities, as described in Section 4.2.1. The prediction becomes more accurate when considering optimization steps with a positive compliance constraint Lagrange multiplier $y_c > 0$, as only then does the compliance constraint contribute to the objective and connectivity (see Section 4.2.2). Based on these considerations, we perform predictive optimization for 20 iterations, which is typically sufficient for a relatively accurate estimation. During the optimization, with compliance constraints (but not the volume constraint yet), we aggregate the volume of beneficial elements at each step where $y_c > 0$, and the average of these values across all steps is taken as the upper limit of the volume constraint $\overline{V}$. If $y_c$ remains zero throughout the prediction, the smallest recorded value is used. A pseudo-algorithm for this prediction process is shown in Algorithm 1.

- **Main optimization**. After the predictive process, we obtain the volume upper limit. Then with both the volume and compliance constraints, we can conduct the main optimization process. Here, we suggest starting the main optimization from scratch instead of from the end of the predictive process. Since in the topology of the latter, clusters of solid elements surrounded by void elements, referred to as "islands," can appear. The "islands" can eventually be removed with a latter applied volume constraint, but may require more optimization iterations than expected and could result in a sub-optimal local minimum. After convergence of the main optimization, the connectivity between input/output points and supporting boundaries can be promoted. Alternatively, we can proceed with the adjustment process to further suppress gray elements.

- **Adjustment process**. In the adjustment process, we start from the converged topology in the main optimization process and continue with a reduced $\overline{V}$. A decrease of $\overline{V}$ is usually followed by an increase of the objective value, that is, the squared error of paths. Thus, the decrease of $\overline{V}$ should be determined based on the error

tolerance specified in the design requirements. The error tolerance is related to how much performance the designer is willing to lose to make the product manufacturable. Allowing more error increases the chances of suppressing gray elements. Then, according to the error tolerance, we can define the change of $\overline{V}$ using Eq. (4.7). However, if the reduction in $\overline{V}$ is relatively substantial, the prediction by Eq. (4.7) may not be accurate since Eq. (4.7) is verified for a small region around the optimal point. To address this issue, we can readjust $\overline{V}$ after the optimization achieves a new equilibrium, and continue the optimization with the new $\overline{V}$. The adjustment strategy is outlined in Algorithm 2, which takes the converged topology from Main optimization as the start point. After each volume adjustment, the optimization just continues instead of restarting from the beginning. The adjustment process is optional. Users can also use post-processing methods to handle gray elements. However, post-processing methods might affect the performance of manufacturing prototypes, and the extent of this influence is unpredictable.

4

**Algorithm 1** Prediction process for defining the upper limit of the volume constraint $\overline{V}$ with a known compliance value $\overline{C}$. Here, $i$ represents the optimization step, $k$ element indexes, and $\frac{\partial f_0}{\partial \rho_k}$ the sensitivity of the objective function w.r.t the pseudo density of element $k$. According to our experience, $\beta_0 = 20$ iterations are enough for an initial guess of the volume upper limit.

$\beta_0 \leftarrow 20$ ▷ *Number of iterations in the prediction process
$\gamma \leftarrow 0$ ▷ *Number of optimization steps where $y_c > 0$
$V_{\text{total}} \leftarrow 0$ ▷ *Sum of volume
$V_{\text{min}} \leftarrow 10^5$ ▷ *Minimum of volume
**for** i = {1, ..., $\beta_0$} **do**
  Conduct optimization step $i$ with $\overline{C}$, then
  **for** k = {1, ..., number of elements} **do**
    **if** $\frac{\partial f_0}{\partial \rho_k} < 0$ **then**
      $V_i \leftarrow V_i + V_k$
    **end if**
  **end for**
  **if** $y_c > 0$ **then**
    $V_{\text{total}} \leftarrow V_{\text{total}} + V_i$
    $\gamma \leftarrow \gamma + 1$
  **end if**
  **if** $V_{\text{min}} > V_i$ **then**
    $V_{\text{min}} \leftarrow V_i$
  **end if**
**end for**
**if** $\gamma > 0$ **then**
  $\overline{V} \leftarrow \frac{V_{\text{total}}}{\gamma}$
**else**
  $\overline{V} \leftarrow V_{\text{min}}$
**end if**

**Algorithm 2** Adjustment process. The process is optional and conducted after the convergence of the main optimization process, only if gray elements appear in the convergence topology. Here $f_0$ represents the convergence objective value at the end of the main optimization process, $y_v$ the corresponding Lagrange multiplier at the end of the main optimization process, $f_0^{new}$ the objective value at the new stationary point after an adjustment of $\overline{V}$, and $y_v^{new}$ the corresponding Lagrange multiplier at the new stationary point. We set a threshold 0.1, if the difference between the expected and achieved objective is smaller than 0.1, we stop the process.

**Require:** $\Delta f_0$ ▷ *Allowable increase of objective if $\overline{V}$ is decreased
$f^{expected} \leftarrow f_0 + \Delta f_0$ ▷ *Expected objective after volume adjustment
$\Delta\overline{V} \leftarrow \Delta f_0 / y_v$
$\overline{V} \leftarrow \overline{V} - \Delta\overline{V}$
Next, continue optimization with $\overline{C}$ and $\overline{V}$, starting from the converged topology of Main optimization to a new convergence, then
$y_v \leftarrow y_v^{new}$
$\Delta f_0 \leftarrow f^{expected} - f^{new}$
**while** $\text{Abs}(\frac{\Delta f_0}{f^{expected}}) > 0.1$ **do**
    $\Delta\overline{V} \leftarrow \Delta f_0 / y_v$
    $\overline{V} \leftarrow \overline{V} - \Delta\overline{V}$
    Next, continue optimization with $\overline{C}$ and $\overline{V}$ to a new convergence, then
    $y_v \leftarrow y_v^{new}$
    $\Delta f_0 \leftarrow f^{expected} - f^{new}$
**end while**

## 4.4. NUMERICAL EXAMPLES

Four examples are given in this section to illustrate the effectiveness of the proposed formulation and solution scheme with the first two concerning plates and the last two shells. In the first example, we test the ability of the volume constraint to remove useless elements. For the second plate example, we explore how the objective value changes when the volume upper limits change. Then, in the third example, we demonstrate the ability of the formulation to design a mechanism exhibiting a complex path. Finally, we design a structure that has input and output ports in different locations. In the following examples, SIMP method [1] is used to generate the topology, which is typically solved by MMA method. Displacements required in SIMP are calculated by incremental-iterative methods [41], where only geometric nonlinearity is taken into account. 6-nodes-12-DOF shell elements are employed [42]. The method we proposed can be combined with any type of elements. We utilize irregular mesh due to it is readily available in our code. Furthermore, using irregular meshes could be benefit irregular design domain and boundary conditions in future work. The termination criteria in the following is: (1) the relative change of the objective value smaller than 0.01 for continuous 50 optimization steps (2) reach the maximum number of optimization iterations, which is 1000.

### 4.4.1. A PLATE-BASED COMPLIANT MECHANISM TRACING A SLANT LINE

The first illustration shows how a plate mechanism is developed. The cantilever plate in Fig. 4.3 serves as the design domain. The right sides' center node is intended to follow the user-defined path indicated by the blue line. Displacements in the x and y directions

are outputs involved in the objective function, whereas displacements in the z direction are prescribed as inputs. The related optimization parameters are listed in Tab. 4.1.

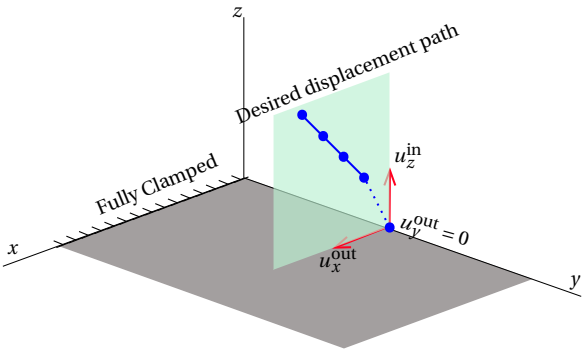


Figure 4.3: A cantilever plate model. The length is 3 cm, width 2 cm, and thickness 0.1 cm. The blue line, which has four precision points, represents the required displacement path. A part of the path is indicated by a dashed line since we are not concerned with moving from the beginning position to the first precision point. The red arrows represent the local coordinate system in which the locations of precision points are defined. Poisson's ratio is 0.3

| | |
|---|---|
| $u_{z,j}^{in}$ | 0.8, 1.2, 1.6, 2 cm |
| $\left(u_{x,j}^*, u_{y,j}^*\right)$ | (0.2, 0), (0.4, 0), (0.6, 0), (0.8, 0) cm |
| $E$ | 300 GPa |

The optimization results are displayed in Tab. 4.2. Here (a) shows the result ignoring the compliance constraint where the connectivity to the supporting boundary is not promoted. Whereas, a clear topology is obtained in (b) by incorporating both compliance and volume restrictions. Here, since no disconnected structures and gray areas appear, the adjustment step is not required. In (c), we only include the compliance constraint but exclude the volume. Here, the result contains more solid material than the one in (b), but the extra material is meaningless since it hardly affect the objective value. Furthermore, the extra material is eliminated from (c) by including the volume constraint. Starting optimization with (c) and include the volume constraint, we can get the result (d), which is nearly the same as (b). The transition from (c) to (d) also illustrates the volume constraint's ability to eliminate unnecessary material.

The deformed configurations and deflection curves for the results displayed in (b) of Tab. 4.2 are presented in Fig. 4.4. It is shown that the design is able to trace the user-defined path with relatively small errors. The optimization iteration history is shown in Fig.4.5. Oscillations are typically observed in the early stages, and peaks often appear when the compliance restriction is close to be activated, where an increase in objective is accompanied by a decrease in compliance. In other words, here optimization strikes a balance between two different intermediate designs, one that reduces objective and the other that reduce the compliance, i.e., increasing stiffness. After 150 optimization iterations, oscillations vanish, and after 200 iterations, the optimization reaches a convergence.

Table 4.1: The specification of constraints' upper bounds for the slant-line-tracing plate mechanism design. The upper limit for compliance constraint $\overline{C}$ is set by specific stiffness requirements, specifically by the prescribed load $F_z^{\mathrm{L}}$ and allowable maximum displacement $u_z^{\mathrm{L}}$. The upper limit for volume constraint $\overline{V}$ is defined by the prediction process shown in Algorithm 1 with 20 optimization iterations. For each iteration, in the figure of the 5th row, we record the Lagrange multiplier for the compliance constraint $y_c$ and the volume percentage $r_v$. The latter represents the volume of the beneficial elements w.r.t that of the design domain $V_{\mathrm{t}}$. The average value of $r_v$ is given in the row. Finally, $\overline{V}$ is calculated in the last row.

| Symbols | Values | Comments |
|---|---|---|
| $F_z^{\mathrm{L}}$ | 0.01 N | Prescribed |
| $u_z^{\mathrm{L}}$ | $0.25\times10^{-3}$ cm | Prescribed |
| $\overline{C}$ | $2.5\times10^{-6}$ Ncm | $F_z^{\mathrm{L}}\times u_z^{\mathrm{L}}$ |
| $\overline{r_v}$ | 0.57 | 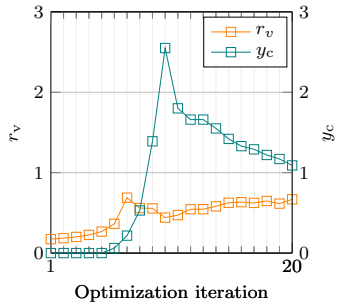  |
| $\overline{V}$ | $0.57V_{\mathrm{t}}$ | $\overline{r_v}\times V_{\mathrm{t}}$ |

Table 4.2: Topology results of the plate mechanism tracing a slant line.(a) acts as a comparison, illustrating the connectivity issue in the density-based TO if the proposed method is not applied. (b) is the output of main optimization starting from the scratch. (c) shows the results without volume constraints starting from the scratch. (d) shows the ability of volume constrains to remove extra elements starting from (c). Here $f_0$ represents the real objective value, $\overline{C}$ and $\overline{V}$ upper limits for compliance and volume constraints respectively whose definition is shown in Table 1. The relative objective error is then defined as $\mu_{\mathrm{error}}^{\mathrm{obj}}=\frac{\sqrt{f_0}}{|u_{\mathrm{max}}|}$ where $u_{\mathrm{max}}=2$ cm presents the maximum displacement.

| Index | Topology | $\overline{C}$ (Ncm) | $\overline{V}$ | $f_0$(cm × cm) | $\mu_{\mathrm{error}}^{\mathrm{obj}}$ |
|---|---|---|---|---|---|
| (a) | 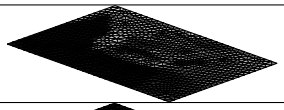 | None | $0.57V_t$ | $1.02\times10^{-5}$ | 0.16% |
| (b) | 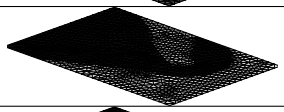 | $2.5\times10^{-6}$ | $0.57V_t$ | $9.90\times10^{-3}$ | 4.97% |
| (c) | 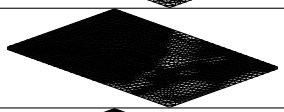 | $2.5\times10^{-6}$ | None | $9.82\times10^{-3}$ | 4.95% |
| (d) | 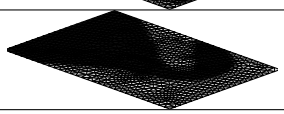 | $2.5\times10^{-6}$ | $0.57V_t$ | $9.91\times10^{-3}$ | 4.97% |

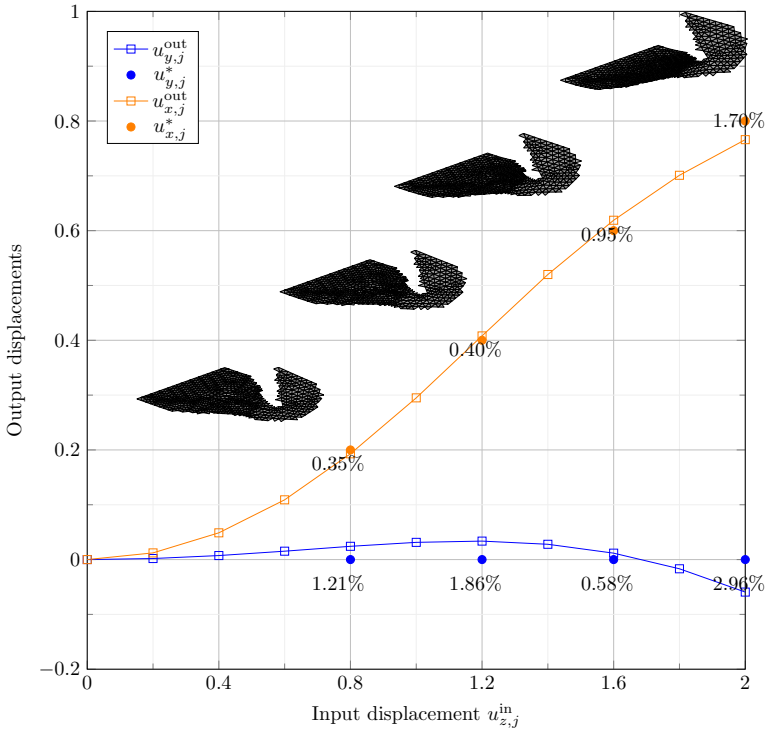


Figure 4.4: Deflection curves and deformed configurations for the topology shown in (a) of Tab. 4.2, the latter which are coupled to four precision points. The percentage values denotes the relative displacement error $\mu^{\text{d}}_{\text{error}} = \frac{|u^{\text{out}}_{l,j} - u^{*}_{l,j}|}{|u_{\text{max}}|}$.

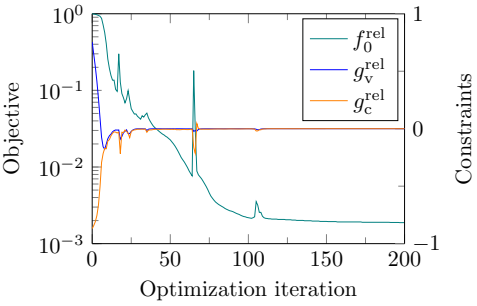


Figure 4.5: Optimization convergence of the slant-line-tracing plate mechanism. The objective shown here, is the value relative to that of the initial solid design. For the compliance constraint, which is relative to the upper limit, i.e., $g_c^{\text{rel}} = \frac{g_c}{C}$. For the volume constraint, which is relative to that of the design domain, i.e., $g_v^{\text{rel}} = \frac{g_v}{V_t}$. The upper limits of volume and compliance constraints are constant as depicted in Tab. 4.1.

### 4.4.2. A PLATE-BASED COMPLIANT MECHANISM TRACING A NORMAL LINE

This example produces a trajectory mechanism from the cantilever plate seen in Fig.4.6. The middle black block indicates a non-design domain. The structural central node is meant to follow the displacement path indicated by the blue line. As input, the displacement in the $z$-direction is specified. The displacement along the $y$-axis is considered as

the output.

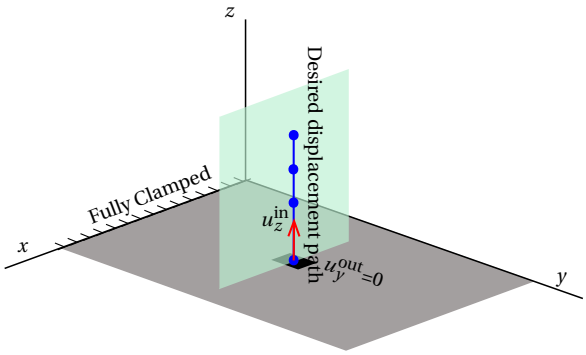


Figure 4.6: A plate model tracing a normal line. The length is 3 cm, width 2 cm, and thickness 0.08 cm. The desired displacement path is shown by the blue line, which is approximated by three precision points. A one-dimension local coordinate system shown by the red arrows is used to describe the points. Poisson's ratio is 0.3

| | |
|---|---|
| $u^{in}_{z,j}$ | 1, 1.5, 2 cm |
| $u^{*}_{y,j}$ | 0, 0, 0 cm |
| $E$ | 300 GPa |

To define the upper limit $\overline{C}$, we load the structure by $F_z^L$ at the structural central node in a separate linear load case. Assuming the allowable maximum displacement $u_z^L$ is prescribed, we can obtain $\overline{C}$. Next, with $\overline{C}$, we define $\overline{V}$. All the aforementioned parameters are listed in Tab. 4.3.

Topology results are depicted in Tab. 4.4. As illustrated in row (a), if the compliance constraint is ignored, we fail to generate the connection to the supporting boundary. If both compliance and volume constraints are applied, the connectivity is developed and shown in the (b). However, the design might be enhanced since gray areas are visible along the supported side. Therefore, the adjustment step is required for suppressing the gray elements. We allow a relative objective function error ($\mu^{obj}_{error} = \frac{\sqrt{f_0}}{|u_{max}|}$ ) up to 6.5%. The upper limit of the volume constraint is then modified according to Algorithm 2, and a better topology is ultimately produced shown in (c). The corresponding deformed configurations and deflection paths are illustrated in Fig. 4.7. It is observable that the structural central point can trace the normal line with displacement errors $\mu^{d}_{error}$ of less than 6%.

The convergence history in Fig. 4.8 provides information on how the volume upper limit $\overline{V}$ varies during the whole optimization. As seen in Fig.4.8(a), $\overline{V}$ remains constant in the main optimization process, and equal to the value specified in Tab. 4.3. The optimization converge around 200 iterations. Then, the adjustment process is shown in Fig.8(b), where the new $\overline{V} = 0.34V_t$ is set by Eq. (4.7), which involves the objective error 6.5% and the volume constraint's current Lagrange multiplier $y_v$. Starting with the new volume upper limit after another 100 iterations, the objective converges to a value larger than the predicted one shown by the dashed line. This is because Eq. (4.7) only works in a small region near the convergence point. With $\Delta\overline{V}$ getting larger, the objective values at new convergence points gradually deviate from the predicted value calculated by Eq. (4.7) (See Fig. 4.9). To attain the predicted objective, we can adjust $\overline{V}$ again. According to the new converged $y_v$ and the difference between current $f_0$ and the target $f_0$, the

volume upper limit is then adjusted to $0.37V_t$. The above adjustment is consistent with the Algorithm 2. As seen in Fig. 4.8(b), $\overline{V}$ is modified at 150 iteration and the objective converges to the predicted value after another 100 iterations.

Table 4.3: The specification of constraints' upper bounds for the plate mechanism tracing a normal line. Here, $\overline{C}$ is set by specific stiffness requirements. The upper limit for volume constraint $\overline{V}$ is defined by the prediction process shown in Algorithm 1 with 20 optimization iterations. For each iteration, in the figure of the 5th row, we record the Lagrange multiplier for the compliance constraint $y_c$ and the volume percentage $r_v$. The latter represents the volume of the beneficial elements w.r.t that of the design domain $V_t$. The average value of $r_v$ is given in the row. Finally, $\overline{V}$ is calculated in the last row.

| Symbols | Values | Comments |
|---|---|---|
| $F_z^L$ | 0.01 N | prescribed |
| $u_z^L$ | $0.4 \times 10^{-3}$ cm | prescribed |
| $\overline{C} = F_z^L \times u_z^L$ | $4 \times 10^{-6}$ N cm | |
| $\overline{r_v}$ | 0.45 | 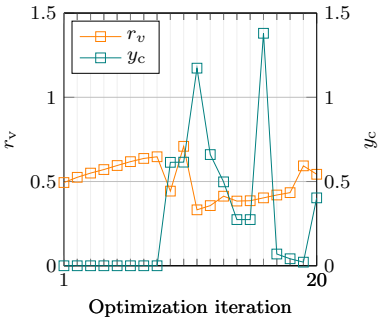  |
| $\overline{V}$ | $0.45V_t$ | $\overline{r_v} \times V_t$ |

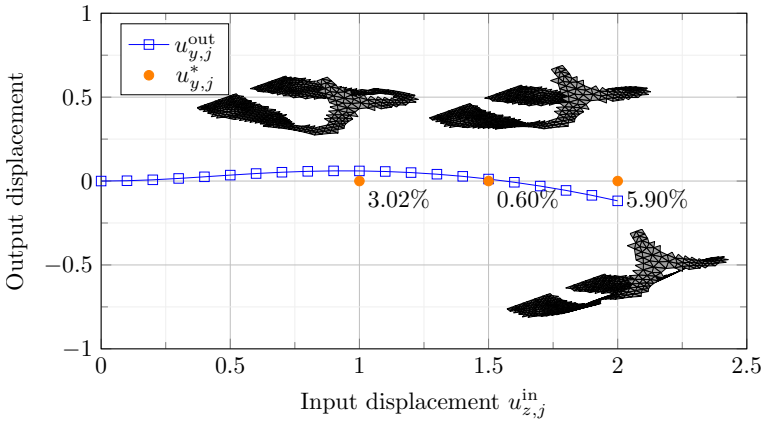


Figure 4.7: Deflection curves and deformed configurations for the topology shown in (c) of Tab. 4.4. The percentage values denote the relative displacement error $\mu_{error}^{d} = \frac{|u_{l,j}^{out} - u_{l,j}^{*}|}{|u_{max}|}$.

Table 4.4: Topology results of the plate mechanism tracing a normal line. (a) acts as a comparison, illustrating the connectivity issue in the density-based TO if the proposed method is not applied. The result is not an output from our proposed scheme. (b) is the output of main optimization starting from the scratch. (c) is the output of adjustment process starting from (b). Here, $\overline{C}$ and $\overline{V}$ are upper limits for compliance and volume constraints. For $\overline{V}$, specifically, $0.45V_t$ is from the predictive process (Algorithm 1), and $0.37V_t$ is the upper limit at the end of the adjustment process (Algorithm 2). $f_0$ is the real objective value. $\mu^{\text{obj}}_{\text{error}} = \frac{\sqrt{f_0}}{|u_{\max}|}$ denotes the relative objective error where $u_{\max}$ presents the maximum displacement.

| Index | Topology | $\overline{C}$ (N cm) | $\overline{V}$ | $f_0$ (cm × cm) | $\mu^{\text{obj}}_{\text{error}}$ |
|---|---|---|---|---|---|
| (a) | 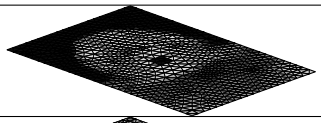 | None | $0.45V_t$ | $3.11\times10^{-6}$ | 0.09% |
| (b) | 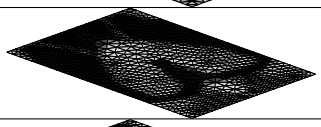 | $4\times10^{-6}$ | $0.45V_t$ | $5.88\times10^{-3}$ | 3.83% |
| (c) | 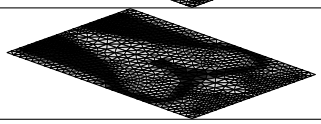 | $4\times10^{-6}$ | $0.37V_t$ | $1.71\times10^{-2}$ | 6.54% |

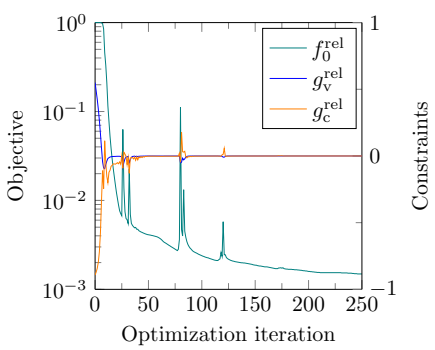


(a) Main optimization process

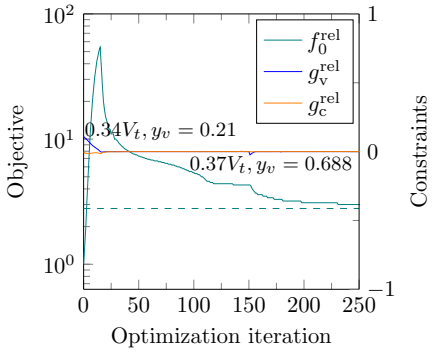


(b) Adjustement process

Figure 4.8: Convergence curve for the plate-based compliant mechanism tracing a normal line. (a) Main optimization process. Optimization starting from the initial solid design with $\overline{C}$ and $\overline{V}$ defined in Tab. 4.3. The objective value is relative to the initial solid design (b) Adjustment optimization process starting from the converged design in (a). The objective value is relative to the converged design in (a). The dashed line shows the predicted objective. From 0 to 150 iterations, $\overline{V} = 0.34V_t$ where $V_t$ is the volume of the design domain. From 150 to 250 iterations, $\overline{V} = 0.37V_t$. Here $V_t$ is the volume of the fully solid design. For the calculation of the volume upper limit, details can be seen in Algorithm 2

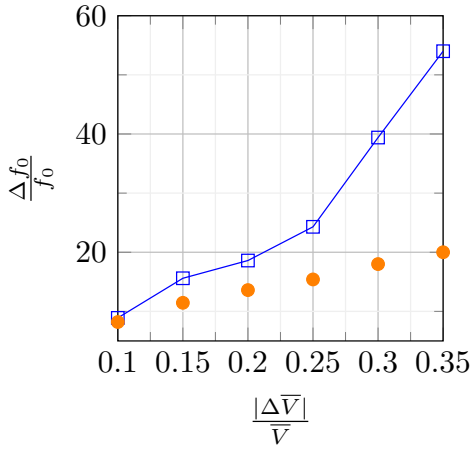


Figure 4.9: Predicted (orange) and actual (blue) relative objective change $\frac{\Delta f_0}{f_0}$ as a function of $\frac{|\Delta \overline{V}|}{\overline{V}}$. The start point of this step is the design shown in b) of Tab. 4.4 where $f_0 = 5.88 \times 10^{-3}$, $\overline{V} = 0.45 V_t$, and $y_v = 0.21$. Predicted values are derived using Eq. (4.7), and actual values are obtained from optimization.

4

### 4.4.3. A CYLINDER MOVING BACK AND FORTH

This example presents a shell mechanism, with its design domain 70% of a cylinder surface shown in Fig. 5.9. The structure bottom is fully clamped. The center node of the top side is designed to move along the displacement path shown by the blue line. The displacement in $z$ direction is prescribed as the input. The displacement along the $x$ direction is regarded as the output. In this case, we constrain both the stiffness along $x$ and $y$ directions. So two separate linear load cases are applied. In one load case, the structure is loaded by $F_x^{\mathrm{L}}$ and in the other, is loaded by $F_z^{\mathrm{L}}$ at the top center node. According to allowable $u_x^{\mathrm{L}}$ and $u_z^{\mathrm{L}}$, upper limits of compliance constraints are calculated. Next $\overline{V}$ is defined by the predictive optimization process. The mentioned parameters are shown in Tab. 4.5

Topology results are detailed in Tab. 4.6. Involving both compliance and volume constraints, the topology result is shown in (a). Although the connectivity is established, the design is preferable to be improved since gray areas are visible. We assume that relative objective error $\mu_{\mathrm{error}}^{\mathrm{obj}}$ can be increased by 5%, i.e. from current 6.4% to around 11.4%. Then, a clear final topology is shown in row (b) with $\mu_{\mathrm{error}}^{\mathrm{obj}} = 11.7\%$. The relevant deformation configurations and curves can be found in Fig. 4.11. It is seen that the final design can achieve the desired behavior, i.e., moving back and forth (see Fig. 4.11).

The convergence history in Fig. 4.12 provides information on how the volume upper limit $\overline{V}$ varies during the whole optimization process. Fig. 4.12(a) shows the process from scratch to the converged design shown in (a) of Tab. 4.6. Here, $\overline{V}$ maintains the value defined in Tab. 4.5 as a constant. Although oscillations are encountered due to constraint violation, the objective and constraint values become relatively stable after 250 iteration steps and converge at 300 iteration. Then, starting from the converged design, $\overline{V}$ is reduced based on the allowable objective error and current Lagrange multiplier. After another 100 iterations, optimization converges to a value larger than the prediction indicated by the dashed line. Then, $\overline{V}$ is adjusted based on the new $y_v$, and after another 50 iterations, the objective value finally converges to the predicted value. The aforementioned adjustment is consistent with Algorithm 2.

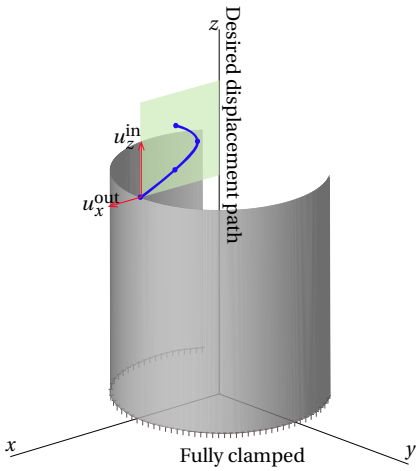


Figure 4.10: A cylinder shell fully clamped at the bottom. Radius is 5 cm, height 20 cm, and thickness 0.3 cm. The desired displacement of the output point is shown by the blue line. The path is approximated by three precision points. The positions of these points are described in the local coordinate system defined by the red arrows. Poisson's ratio is 0.3

| | |
|---|---|
| $u_{z,j}^{\text{in}}$ | $1, 2, 4$ cm |
| $u_{x,j}^{*}$ | $-2, -4, -2$ cm |
| $E$ | 100 MPa |

Table 4.5: The specification of constraints' upper bounds for the shell mechanism moving back and forth. Here, $\overline{C}$ is set by specific stiffness requirements. $\overline{V}$ is defined by the prediction process shown in Algorithm 1 with 20 optimization iterations shown in the figure. Here, only $r_{\text{v}}$ is depicted since $y_{\text{c}} = 0$. Thus, the minimum $r_{\text{v}}$ is used for calculating $\overline{V}$.

| Symbols | Values | Comments |
|---|---|---|
| $F_x^{\text{L}}$ | 1 N | Prescribed |
| $u_x^{\text{L}}$ | 0.5 cm | Prescribed |
| $\overline{C_x}$ | 0.5 N cm | $F_x^{\text{L}} \times u_x^{\text{L}}$ |
| $F_z^{\text{L}}$ | 1 N | Prescribed |
| $u_z^{\text{L}}$ | 0.15 cm | Prescribed |
| $\overline{C}$ | 0.15 N cm | $F_z^{\text{L}} \times u_z^{\text{L}}$ |
| $r_{\text{v}}^{\min}$ | 0.3 | 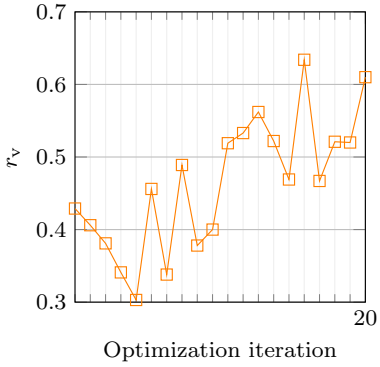 |
| $\overline{V}$ | $0.3V_t$ | $r_c^{\min} \times V_t$ |

Table 4.6: Topology results of the shell mechanism moving back and forth. (a) is the output of main optimization starting from the scratch. (b) is the output of adjustment process starting from (a). Here, $\overline{C}$ and $\overline{V}$ are upper limits for compliance and volume constraints. For $\overline{V}$, specifically, $0.3V_t$ is from the predictive process (Algorithm 1), and $0.236V_t$ is the upper limit at the end of the adjustment process (Algorithm 2). $f_0$ is the real objective. $\mu^{\text{obj}}_{\text{error}} = \frac{\sqrt{f_0}}{|u_{\max}|}$ denotes the relative objective error where $u_{\max}$ presents the maximum displacement.

| Index | Topology | $\overline{C}$ (N cm) | $\overline{V}$ | $f_0$ (cm × cm) | $\mu^{\text{obj}}_{\text{error}}$ |
|---|---|---|---|---|---|
| (a) | 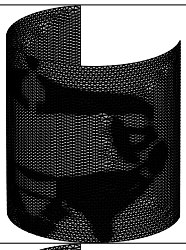 | $\overline{C}_x = 0.5, \overline{C}_y = 0.15$ | $0.3V_t$ | 0.0645 | 6.4% |
| (b) | 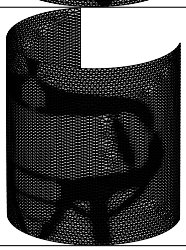 | $\overline{C}_x = 0.5, \overline{C}_y = 0.15$ | $0.236V_t$ | 0.2201 | 11.7% |

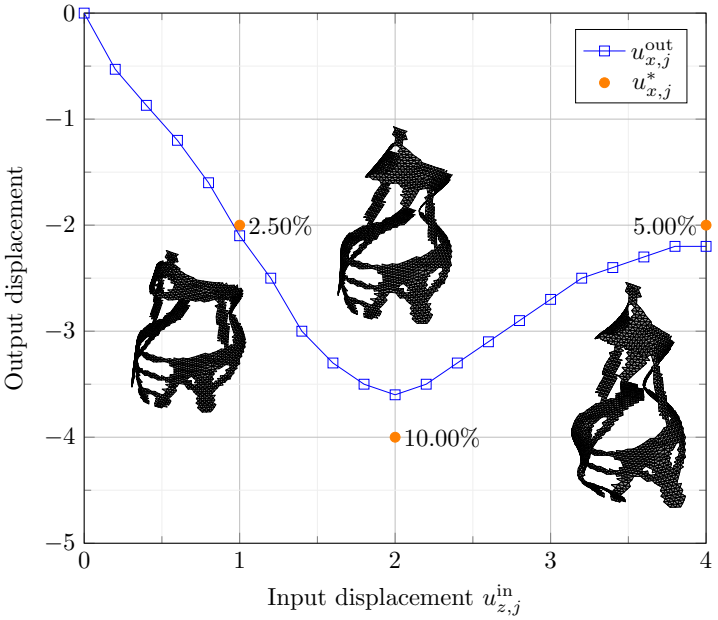


Figure 4.11: Deflection curves and configurations for the topology shown in the first row of Tab. 4.6. Here, the deformation figures are coupled to three precision points. The percentage values denote the relative displacement error $\mu^{\text{d}}_{\text{error}} = \frac{|u^{\text{out}}_{l,j} - u^{*}_{l,j}|}{|u_{\max}|}$.

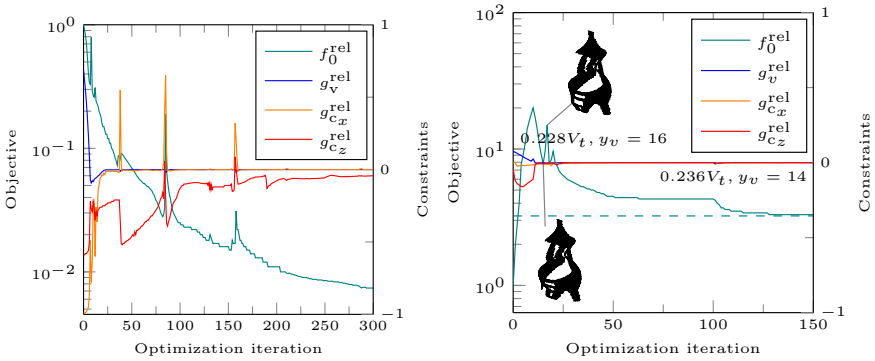


(a) Main optimization process (b) Adjustment optimization process

Figure 4.12: Optimization process for the shell mechanism moving back and forth. $g_{c_z}^{\text{rel}}$ presents compliance constraint relative to $\overline{C}_z$ and $g_{c_x}^{\text{rel}}$ that to $\overline{C}_x$. (a) Optimization starting from the fully solid design with $\overline{C}$ and $\overline{V}$ defined in 4.5. The objective value is relative to the initial solid design. (b) Adjustment optimization begins from the final design in (a), with the objective value relative to that of the final design. The dashed line indicates the predicted objective value. In (b), from 0 to 100 iteration, $\overline{V} = 0.228V_t$. From 100 to 150 iteration, $\overline{V} = 0.236V_t$. Here $V_t$ is the volume of the fully solid design. For calculation of the upper limits, details can be seen in Algorithm 2.

4

### 4.4.4. A GRIPPER STRUCTURE

This example depicts a gripper shell mechanism with independent input and output point locations. The design is derived from a half-cylinder surface shown in Fig.4.13, which is fully clamped on the right side. The input point is the center node of the structure, and the output points are the structural upper and lower left corners. The output points are designed to move through the blue line. Due to symmetry, the top half cylinder is taken as the design domain. To involve the compliance constraint, we load the top left corner by $F_x^{\text{L}}$ in a separate linear load case. Then, the upper limit $\overline{C}$ is calculated assuming that the allowable maximum displacement $u_x^{\text{L}}$ is prescribed. Then $\overline{V}$ is defined by the predictive process. The parameters mentioned above are shown in Tab. 4.7. Then, the optimization restarts with defined $\overline{V}$ and $\overline{C}$, finally a connected topology obtained in Fig.4.14 and no adjustment process is needed.

The corresponding deformed configurations and the deflection curves are presented in Fig.4.15. It is seen that the mechanism follows the prescribed path well with relative displacement errors $\mu_{\text{error}}^{\text{d}} < 3\%$. The history of optimization iterations is shown in Fig.4.16. It is seen that oscillation occurs for balancing between reducing compliance and minimizing the objective. Then after 300 iterations, the curves become stable and gradually converge.

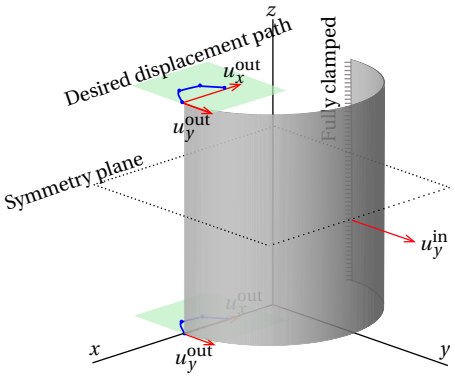


Figure 4.13: A cylinder shell fully clamped on the right side. The Radius is 5 cm, height is 20 cm, and the thickness 0.3 cm. The desired displacement of the output point is shown by the blue line. The path is approximated by three precision points. The positions of these points are described in the local coordinate system defined by the red arrows. Poisson's ratio is 0.3

| | |
|---|---|
| $u_{y,j}^{in}$ | $1, 1.6, 2$ cm |
| $\left(u_{x,j}^*, u_{y,j}^*\right)$ | $(-0.5, -0.15), (-0.8, -0.1), (-1, 0.001)$ cm |
| $E$ | 1000 MPa |

Table 4.7: The specification of constraints' upper bounds for the gripper-like shell mechanism. Here, $\overline{C}$ is set by specific stiffness requirements. $\overline{V}$ is defined by the prediction process (Algorithm 1) with 20 optimization iterations shown in the figure, where $y_c$ and the ratio $r_v$ is depicted. The average value of $r_v$ for $y_c > 0$ is used to define $\overline{V}$

| Symbols | Values | Comments |
|---|---|---|
| $F_x^L$ | 1 N | Prescribed |
| $u_x^L$ | 0.05 cm | Prescribed |
| $\overline{C_x}$ | 0.05 N cm | $F_z^L \times u_z^L$ |
| $\overline{r_v}$ | 0.628 | 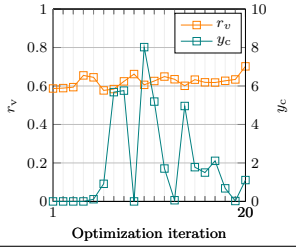 |
| $\overline{V}$ | $0.628V_t$ | $r_v \times V_t$ |



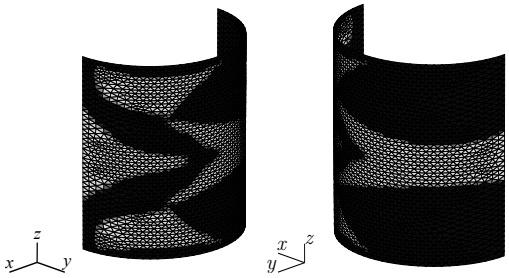


Figure 4.14: Topology optimization result of the gripper mechanism. Objective value $f_0 = 9.38 \times 10^{-3}$ and relative objective error $\mu_{\text{error}}^{\text{obj}}$=4.8%

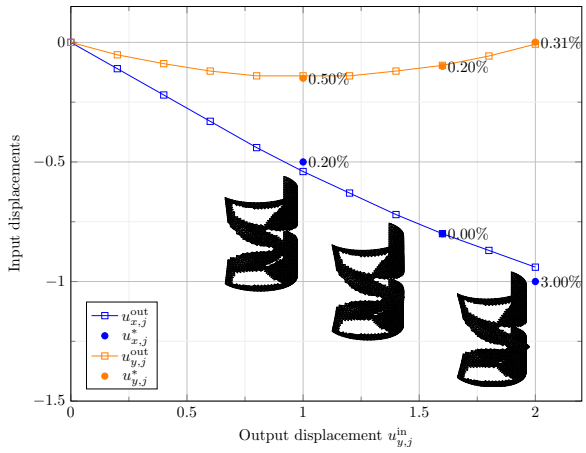


Figure 4.15: Deflection curves and deformed configurations. The percentage values denote the relative displacement error $\mu^{\text{d}}_{\text{error}} = \frac{|u^{\text{out}}_{l,j} - u^{*}_{l,j}|}{|u_{\max}|}$

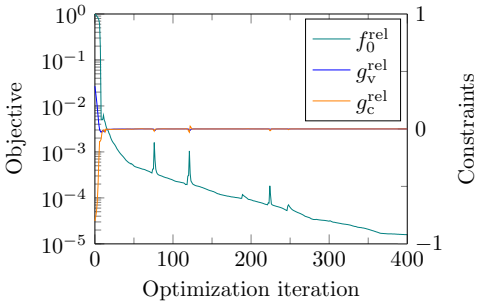


Figure 4.16: Optimization convergence curve of the gripper shell mechanism. Objective $f_0^{\text{rel}}$ is relative to the initial solid design. Here, the upper limits of volume and compliance constraints are consistent with those depicted in Tab. 4.7.

## 4.5. SUMMARY AND CONCLUSIONS

A formulation involving commonly used volume and compliance constraints is proposed to establish the connectivity among input, output, and if necessary fixture supporting the mechanism. An optimization scheme including 1) predictive step for defining the upper limits of volume, 2) main optimization step, and 3) adjustment step for further suppressing gray elements is proposed.

Numerical examples show that with the volume upper limit defined in the predictive step, a connectivity is typically promoted in the topology after the main optimization step. If gray elements appear, we can further suppress them by reducing the volume's upper limit. The influence of reducing volume upper limits on objective errors can be predicted by the value of Lagrange multipliers. The prediction is only effective within a small range around the optimum points. If the change is beyond the scope, one can adjust the upper limits again after optimization reaching a new stationary point.

Given the fact that stiffness of the structure is usually prescribed, the proposed method only considers adjusting volume upper limits to improve the obtained topology. If stiffness is also allowed to change, then adjusting upper limits of compliance or even both constraints can also take effect.

## REFERENCES

[1] M. P. Bendsøe and O. Sigmund, *Material interpolation schemes in topology optimization,* Archive of applied mechanics **69**, 635 (1999).

[2] T. Buhl, C. B. Pedersen, and O. Sigmund, *Stiffness design of geometrically nonlinear structures using topology optimization,* Structural and Multidisciplinary Optimization **19**, 93 (2000).

[3] F. Dirksen, T. Berg, R. Lammering, and T. I. Zohdi, *Topology synthesis of large-displacement compliant mechanisms with specific output motion paths,* Pamm **12**, 801 (2012).

[4] M. Otomori, T. Yamada, K. Izui, S. Nishiwaki, and J. Andkjær, *A topology optimization method based on the level set method for the design of negative permeability dielectric metamaterials,* Computer Methods in Applied Mechanics and Engineering **237**, 192 (2012).

[5] L. Lu, T. Yamamoto, M. Otomori, T. Yamada, K. Izui, and S. Nishiwaki, *Topology optimization of an acoustic metamaterial with negative bulk modulus using local resonance,* Finite Elements in Analysis and Design **72**, 1 (2013).

[6] W. Wang, D. Munro, C. C. Wang, F. van Keulen, and J. Wu, *Space-time topology optimization for additive manufacturing,* Structural and Multidisciplinary Optimization **61**, 1 (2020).

[7] C. B. Pedersen, T. Buhl, and O. Sigmund, *Topology synthesis of large-displacement compliant mechanisms,* International Journal for numerical methods in engineering **50**, 2683 (2001).

[8] O. Sigmund, *On the design of compliant mechanisms using topology optimization,* Journal of Structural Mechanics **25**, 493 (1997).

[9] T. Bruns and O. Sigmund, *Toward the topology design of mechanisms that exhibit snap-through behavior,* Computer Methods in Applied Mechanics and Engineering **193**, 3973 (2004).

[10] Y. K. Yong, S. S. Aphale, and S. R. Moheimani, *Design, identification, and control of a flexure-based xy stage for fast nanoscale positioning,* IEEE Transactions on Nanotechnology **8**, 46 (2008).

[11] L.-J. Lai, G.-Y. Gu, and L.-M. Zhu, *Design and control of a decoupled two degree of freedom translational parallel micro-positioning stage,* Review of Scientific Instruments **83**, 045105 (2012).

[12] S. Awtar and G. Parmar, *Design of a large range xy nanopositioning system,* Journal of Mechanisms and Robotics **5**, 021008 (2013).

[13] M. Olfatnia, S. Sood, J. J. Gorman, and S. Awtar, *Large stroke electrostatic comb-drive actuators enabled by a novel flexure mechanism,* Journal of Microelectromechanical Systems **22**, 483 (2012).

[14] S. Huang, K. K. Tan, and T. H. Lee, *Adaptive sliding-mode control of piezoelectric actuators,* IEEE Transactions on Industrial Electronics **56**, 3514 (2009).

[15] I. Weingrod, C. Y. Chou, B. Holmes, C. Hom, J. W. Irwin, O. Lindstrom, F. Lopez, D. M. Stubbs, and J.-P. Wüelser, *Design of bipod flexure mounts for the IRIS spectrometer,* in *Optomechanical Engineering 2013*, Vol. 8836, edited by A. E. Hatheway, International Society for Optics and Photonics (SPIE, 2013) pp. 202 – 210.

[16] N. F. Wang and K. Tai, *Design of Grip-and-Move Manipulators Using Symmetric Path Generating Compliant Mechanisms,* Journal of Mechanical Design **130** (2008), 112305.

[17] K. Tai, G. Y. Cui, and T. Ray, *Design synthesis of path generating compliant mechanisms by evolutionary optimization of topology and shape,* Journal of Mechanical Design **124**, 492 (2002).

[18] K.-J. Lu and S. Kota, *Topology and Dimensional Synthesis of Compliant Mechanisms Using Discrete Optimization,* Journal of Mechanical Design **128**, 1080 (2005).

[19] H. Zhou and K.-L. Ting, *Topological Synthesis of Compliant Mechanisms Using Spanning Tree Theory,* Journal of Mechanical Design **127**, 753 (2004).

[20] A. Saxena, *Synthesis of Compliant Mechanisms for Path Generation using Genetic Algorithm,* Journal of Mechanical Design **127**, 745 (2004).

[21] A. K. Rai, A. Saxena, and N. D. Mankame, *Synthesis of Path Generating Compliant Mechanisms Using Initially Curved Frame Elements,* Journal of Mechanical Design **129**, 1056 (2006).

[22] A. K. Rai, A. Saxena, and N. D. Mankame, *Unified synthesis of compact planar path-generating linkages with rigid and deformable members,* in *International Design Engineering Technical Conferences and Computers and Information in Engineering Conference*, Vol. 49040 (2009) pp. 223–232.

[23] A. Rai, A. Saxena, N. D. Mankame, and C. S. Upadhyay, *On optimal design of compliant mechanisms for specified nonlinear path using curved frame elements and genetic algorithm,* in *International Design Engineering Technical Conferences and Computers and Information in Engineering Conference*, Vol. 42568 (2006) pp. 91–100.

[24] S. V. Naik, A. Saxena, and A. K. Rai, *On the criteria for choice of the best solution from a generated set of partially compliant linkages,* in *International Design Engineering Technical Conferences and Computers and Information in Engineering Conference*, Vol. 44106 (2010) pp. 685–694.

[25] A. K. Rai and A. Saxena, *Optimal continuum synthesis of partially compliant mechanisms for prescribed non-smooth paths,* in *13th National Conference on Mechanisms and Machines (NaCoMM07)* (2007).

[26] B. V. S. Nagendra Reddy, S. V. Naik, and A. Saxena, *Systematic Synthesis of Large Displacement Contact-Aided Monolithic Compliant Mechanisms,* Journal of Mechanical Design **134**, 011007 (2012).

[27] S. V. Naik, A. Saxena, A. K. Rai, and B. V. S. N. Reddy, *How to Choose From a Synthesized Set of Path-Generating Mechanisms,* Journal of Mechanical Design **133**, 091009 (2011).

[28] A. Saxena, *A Material-Mask Overlay Strategy for Continuum Topology Optimization of Compliant Mechanisms Using Honeycomb Discretization,* Journal of Mechanical Design **130**, 082304 (2008).

[29] A. Saxena, *Topology design with negative masks using gradient search,* Structural and Multidisciplinary Optimization **44**, 629 (2011).

[30] P. Kumar and A. Saxena, *An improved material mask overlay strategy for the desired discreteness of pressure-loaded optimized topologies,* Structural and Multidisciplinary Optimization **65**, 304 (2022).

[31] P. Kumar and A. Saxena, *On topology optimization with embedded boundary resolution and smoothing,* Structural and Multidisciplinary Optimization **52**, 1135 (2015).

[32] N. Singh, P. Kumar, and A. Saxena, *On topology optimization with elliptical masks and honeycomb tessellation with explicit length scale constraints,* Structural and Multidisciplinary Optimization **62**, 1227 (2020).

[33] P. Kumar, R. A. Sauer, and A. Saxena, *Synthesis of c0 path-generating contact-aided compliant mechanisms using the material mask overlay method,* Journal of Mechanical Design **138**, 062301 (2016).

[34] P. Kumar, A. Saxena, and R. A. Sauer, *Computational synthesis of large deformation compliant mechanisms undergoing self and mutual contact,* Journal of Mechanical Design **141**, 012302 (2019).

[35] P. Kumar, R. A. Sauer, and A. Saxena, *On topology optimization of large deformation contact-aided shape morphing compliant mechanisms,* Mechanism and Machine Theory **156**, 104135 (2021).

[36] P. Kumar, A. Saxena, and R. A. Sauer, *Implementation of self contact in path generating compliant mechanisms,* in *Microactuators and Micromechanisms: Proceedings of MAMM-2016, Ilmenau, Germany, October 5-7, 2016* (Springer, 2017) pp. 251–261.

[37] A. Saxena and G. Ananthasuresh, *Topology synthesis of compliant mechanisms for nonlinear force-deflection and curved path specifications,* Journal of Mechanical Design **123**, 33 (2001).

[38] J. Reinisch, E. Wehrle, and J. Achleitner, *Multiresolution topology optimization of large-deformation path-generation compliant mechanisms with stress constraints,* Applied Sciences **11**, 2479 (2021).

[39] G. D. Cheng and X. Guo, *$\varepsilon$-relaxed approach in structural topology optimization,* Structural optimization **13**, 258 (1997).

[40] S. Koppen, M. Langelaar, and F. van Keulen, *A simple and versatile topology optimization formulation for flexure synthesis,* Mechanism and Machine Theory **172**, 104743 (2022).

[41] R. De Borst, M. A. Crisfield, J. J. Remmers, and C. V. Verhoosel, *Nonlinear finite element analysis of solids and structures* (John Wiley & Sons, 2012).

[42] F. Van Keulen and J. Booij, *Refined consistent formulation of a curved triangular finite rotation shell element,* International journal for numerical methods in engineering **39**, 2803 (1996).

# 5

# LARGE-STROKE HIGH-PRECISION POSITIONING DESIGN VIA TOPOLOGY OPTIMIZATION STRATEGIES

*In high-precision positioning systems, accurately tracing user-defined motion paths is essential, but large strokes often require a large footprint, which is undesirable in space-limited environments. Therefore, compact designs are preferred, measured by the displacement-to-size ratio (DSR), with higher values indicating more compact designs. However, surpassing a ratio of 10% typically leads to finite deflections and rotations, which poses challenges for experience-based analytical methods. To simplify the design process and achieve accurate path tracing, this study adopts topology optimization (TO) with geometrically nonlinear finite element analysis to directly design monolithic compliant mechanisms exhibiting large DSRs.*

*Previous studies on TO for designing compliant mechanisms tracing user-defined motion paths, typically utilize 2D in-plane stress/strain elements. These elements may become "inside-out" under compression when large input displacements are applied, causing nonlinear analysis to fail even at the first optimization step. This makes achieving a high DSR, particularly above 50% challenging, as it may demand large input displacements. To avoid the analysis failure, an input continuation approach is proposed, where input displacements are increased step-by-step during the optimization process to allow the design to gradually gain nonlinearity. Alternatively, to avoid "inside-out" elements and achieve even larger DSRs, shell- or plate-based design domains are explored. These use the bending behavior of thin structures, with out-of-plane deflections as output displacements. The resulting designs are 3D printed and validated through experiments.*

This chapter will be submitted as a journal paper.

## 5.1. INTRODUCTION

Compliant mechanisms are increasingly drawing increasing attention in high-precision positioning systems, mainly due to their almost deterministic performance achieved by the absence of backlash and friction. Given that positioning systems, such as electrostatic actuators [1] and micro-manipulators [2], favor a broad working range with a restricted placement area. A desirable compliant mechanism should exactly follow a user-defined path with high compactness. This compactness is measured by the ratio of the user-defined motion path length relative to a characterized structural dimension, i.e., displacement-to-size ratio (DSR). Typically, producing accurate large output displacements requires a large footprint [3]; consequently, the DSR, in real practice, is usually around 0.1 [4–9], and achieving a larger ratio, without compromising the accuracy is a challenging.

Such challenge is especially difficult when utilize traditional analytical modeling and component assembly techniques: First, based on traditional methods, designs are realized on integrating readily accessible flexible components. For instance, Awtar and Parmar [3] combined leaf flexures and developed a decoupled $x$-$y$ stage, achieving a DSR of up to 4%, with a position deviation at the end of the path of 0.6% compared to the path length. Xu [10] adopted two stacked actuated stages for a nanopositioning system exhibiting one-axis relatively large strokes. He attained a ratio of up to 10% almost without position deviations. Olfatnia *et al.* [1] combined clamped double parallelograms to create a one-axis large-stroke actuator, achieving a DSR of up to 12%, with a position deviation at the end of the path of less than 1% compared to the path length. Given that the available components usually come with fixed DSRs, the combination is unlikely to significantly exceed these ratios. Second, various assumptions need to be made to simplify complex analytical models. These assumptions may include neglecting the compliance of certain components [10] and ignoring interactions between different components [11]. However, when the path length is relatively large, these assumptions could be invalidated, or the analytical modeling becomes much more complex, hindering obtaining large DSRs.

One strategy to facilitate nonlinear analysis and potentially enhance mechanism performance is by means of numerical methods, such as finite element analysis, combined with optimization techniques. Rommers *et al.* [12] developed a linear guide by integrating two zig-zag-shaped springs. The mechanism's performance was further improved by adjusting the shape parameters of the springs using optimization algorithms, resulting in a DSR of up to 100%, while maintaining sufficient stiffness in the direction perpendicular to the moving direction. In the design process outlined by Rommers *et al.* [12], an initial design serves as an input to the optimization process. Typically, creating this initial design can be challenging, and the resulting mechanism performance may heavily rely on it. To simplify the design process and potentially achieve superior performance, topology optimization (TO) can be utilized.

TO [13–15], a computational design method widely used in engineering, seeks to optimize material distribution within a specified design space, to achieve optimized performance within given constraints. This technique has been used extensively in various structural designs [16–20], and more recently, on compliant mechanisms for tracing user-defined motion paths. For the latter, a user-defined motion path is specified via sev-

eral precision points, corresponding to incremental steps in the nonlinear finite element analysis (FEA). Then, by minimizing the distance between the desired precision points and those obtained via FEA, TO can achieve relatively large displacement-to-size-ratio designs with high accuracy. Examples include the 2D linear guide devised by Pedersen *et al.* with a DSR of 12% [21], Saxena's linear guide achieving a ratio of up to 33% [22], Sharma *et al.*'s 2D mechanism tracing a slightly curved path with a ratio of up to 17% [23], Wang and Tai's 2D grip-and-move manipulator reaching a ratio of up to 25% [24], Tai *et al.*'s mechanism tracing curved paths with a ratio of around 40% [25],Rai *et al.*'s design tracing a quarter circle based on an initial curved frame with a ratio of 42% [26], and Kumar *et al.*'s contact-aided shape morphing compliant mechanism traveling a straight line with a ratio of up to 25% [27]. These designs meet accuracy requirements, exhibiting average position deviations among all precision points of not more than 10% compared to the motion path length. The adoption of TO has therefore led to a substantial increase in DSRs.

The above studies are based on 2D in-plane stress/strain elements. These elements may become "inside-out" due to compression if large input displacements are required, leading to failure of the nonlinear finite element analysis even at the first optimization step. As a result, achieving a high DSR, particularly above 50%, becomes challenging, as it may demand large input displacements. To alleviate the aforementioned failure in nonlinear analysis and potentially obtain designs with large DSRs using these 2D elements, we propose a displacement continuation approach, where input displacements are increased step-by-step during optimization process to allow the design to gradually gain nonlinearity.

Alternatively, to avoid "inside-out" elements and achieve even larger DSRs, we explore ortho-planar mechanisms. These utilize the bending behavior of shells and plates, considering the out-plane deflections as output displacements.There is little to no research regarding design of ortho-planar compliant mechanisms [28, 29]. Parise *et al.* Parise et al. used a traditional analytical method, introducing formulation simplifications due to the complexity of stretching–bending coupling [29]. Romero applies TO but focuses on relatively small deflections. [28]. Given the thin-wall nature of shells and plates, which exhibit flexible bending behaviors and can be easily manufactured (e.g., using laser cutting), we explore TO for the design of shell- and plate-based mechanisms, with DSR exceeding 100%. Finally, all of our designs are manufactured and validated through experiments.

## 5.2. TOPOLOGY OPTIMIZATION FORMULATIONS

In this section, from the aspects of design variables, objective function, and constraints, we provide details for designing compliant mechanisms with large DSRs.

*Design variables.* The material distribution is presented by scaling the element stiffness matrices using pseudo densities $\rho_e$, i.e., design variables for each element where $0 < \rho_0 \leq \rho_e \leq 1$. Here, $\rho_e = 1$ means a solid element and $\rho_e = \rho_0 > 0$ void. The lower bound $\rho_0$ is a small positive value to avoid singularity in the finite element stiffness matrices.

*Objectives.* The design objective is to create a mechanism capable of accurately traversing a relatively lengthy user-defined path (desired path), when the input displacement

or load is applied step-by-step. Typically, such paths, as shown in Fig. 5.1, can be represented by multiple precision points. The latter refers to desired displacements $u^*_{i,j}$ when input step $\lambda_j$ is applied to the structure. Here, $i$ represents the direction, $j$ the index of the precision point, and $\lambda$ incremental factor used in the incremental-iterative finite element simulations. During the optimization process, efforts are made to minimize the disparity between the desired displacements $u^*_{i,j}$ and the realized displacements $u^{\text{out}}_{i,j}$. Then, the object function can be expressed by

$$f_0 = \sum_{i=1}^{n}\sum_{j=1}^{m} \theta_{i,j}\left(u^{\text{out}}_{i,j} - u^*_{i,j}\right)^2, \tag{5.1}$$

where $\theta_{i,j}$ represents a weight factor, $m$ the number of precision points, and $n$ the number of directions considered in the precision point.

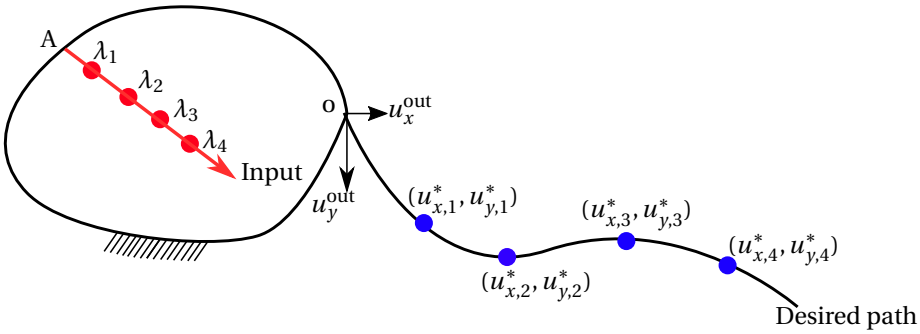


Figure 5.1: Path-generation compliant mechanism. The Point O represents the output point and Point A the input point. When the input is applied incrementally to Point A, Point O can go through the precision points (shown in blue along the black line that represents the desired path). The four precision points indicated by $u^*_{i,j}$ correspond to the four input steps $\lambda_j$ (shown in red). Here, $j$ represents the index of the precision point, and $\lambda$ incremental factor used in the incremental-iterative finite element simulations.

*Constraints.* For constraints, in practical applications, mechanisms are required to demonstrate substantial deflections and rotations to fulfill trajectory requirements. Simultaneously, they must possess sufficient stiffness to withstand loads. Consequently, the first constraint considered is stiffness or compliance.

As it is well known, in the nonlinear setting, stiffness can either increase or decrease during the loading process. For example, a stretched beam may gain stiffness perpendicular to the stretching direction while losing stiffness under compression. Therefore, it is necessary to account for changes in stiffness during loading. However, in certain situations, it may be sufficient to consider only the stiffness in the undeformed configuration: 1) If the stiffness to be constrained is expected to increase during deformation process, considering the stiffness in the undeformed configuration might be a prudent choice; 2) If the purpose of introducing compliance is to meet load transfer requirements for establishing connectivity between the input/output and the support (as discussed in Chapter 4), knowing only the stiffness in the undeformed configuration is sufficient for ensuring connectivity. Given that the designs presented in this chapter fall within these cases, we choose to exclusively consider the stiffness constraint in the undeformed configuration.

This is just a choice, definitely users can choose other options. The stiffness constraint in the undeformed configuration can be expressed by

$$g_c = C_s - \overline{C_s} \leq 0 \quad \forall s = \{1...q\}, \tag{5.2}$$

where $C_s$ is the linear compliance held by the design at the degree of freedom (DOF) $s$, $q$ the number of compliance constraints, and $\overline{C_s}$ the corresponding upper limit defined by the user. $\overline{C_s}$ can be defined in accordance with precise engineering specifications. For example, a compliant mechanism functioning as a support may be subject to a design requirement that specifies the maximum allowable displacement $(\overline{\mathbf{u}}_L)_s$ when a device with a weight load $(\mathbf{F}_L)_s$ is placed on top of it. Subsequently, $\overline{C_s}$ can be set to $(\overline{\mathbf{u}}_L^T \mathbf{F}_L)_s$. For obtaining $C_s$, a separate linear load case is solved for each design at every optimization iteration, wherein the load $(\mathbf{F}_L)_s$ is applied. Then, $C_s$ is calculated by

$$C_s = \left(\mathbf{u}_L^T \mathbf{F}_L\right)_s = \left(\mathbf{u}_L^T \mathbf{K}_L \mathbf{u}_L\right)_s, \tag{5.3}$$

where $\mathbf{K}_L$ is the linear structural stiffness matrix and $(\mathbf{u}_L)_s$ represents displacements obtained by the linear analysis for the separate load case $(\mathbf{F}_L)_s$. Besides, a volume constraint can be considered to reduce weight and save material, which can be expressed by

$$V \leq \overline{V}, \tag{5.4}$$

where $V$ represents the volume of the design and $\overline{V}$ the upper bound of volume.

Consequently, the complete optimization formulation can be written as

$$\begin{aligned} \min_{\boldsymbol{\rho}} \; & f_0(\boldsymbol{\rho}) = \sum_{i=1}^{n} \sum_{j=1}^{m} \theta_{i,j} (u_{i,j}^{\text{out}}(\boldsymbol{\rho}) - u_{i,j}^*)^2, \\ \text{s.t. } & C_s(\boldsymbol{\rho}) \leq \overline{C_s}, \quad \forall s = 1...q \\ & V \leq \overline{V}, \\ & \mathbf{0} < \boldsymbol{\rho}_0 \leq \boldsymbol{\rho} \leq \mathbf{1}. \end{aligned} \tag{5.5}$$

Next, the implementation details are presented.

## 5.3. IMPLEMENTATION

In this work, we focus on designs exhibiting geometric nonlinearity but with small strains. One 2D in-plane strain/stress design and two shell/plate-based designs are presented. For the shell- and plate-based designs, six-node, 12-DOF shell elements from [30] are used. The nonlinear finite element equations are solved by the incremental-iterative method [31]. TO method employed is SIMP [13], which can be implemented straightforwardly. Despite the simplicity of SIMP implementation, there are specific issues that need to be addressed: 1) Applying filters for achieving black-white designs; 2) Elimination of hinges in the topology, i.e., small structures consisting of two solid elements connected by a single node; 3) Avoiding failure in nonlinear analysis of 2D plane strain/stress structures caused by large input displacements. In this section the three aspects will be discussed.

### 5.3.1. FILTER FOR BLACK-WHITE DESIGNS

In TO, a filter is a mathematical operation applied to the density or material distribution field during the optimization process. One purpose of filtering is to control the spatial distribution of material within the design domain, e.g., to prompt smoother and more gradual changes in material density. The filter used in this work is density-based [32, 33], the main idea of which is to define the physical element density to be a weighted average of the neighboring design variables. The filter is popular due to its mesh-independent characteristic. However, it has disadvantage of creating gray transition zones between solid and void areas, which do not represent solid material nor void and which are therefore not preferable in manufacturing. One solution to suppress gray transition zones and get a black-and-white design is the use of the Heaviside projection to the density-filtered pseudo densities [34–36]. An element pseudo density can therefore be expressed by

$$\hat{\rho}_e = \frac{\tanh(\beta\alpha) + \tanh\beta(\overline{\rho_e} - \alpha)}{\tanh(\beta\alpha) + \tanh\beta(1-\alpha)}, \tag{5.6}$$

where $\overline{\rho_e}$ is density-filtered element pseudo density, and $\alpha$ and $\beta$ are user-defined parameters of the Heaviside function. Here $\alpha$ works as a threshold, i.e., when $\overline{\rho_e} > \alpha$, the projected pseudo density $\hat{\rho}_e$ approach the upper bound 1, and when $\overline{\rho_e} < \alpha$, $\hat{\rho}_e$ would approach the lower bound $\rho_0$. $\beta$ represents the slope of the function determining the speed of $\hat{\rho}_e$ approaching 1 or $\rho_0$. By pushing the pseudo densities to the upper and lower limits, the topology becomes more "black-and-white".

### 5.3.2. HINGE-FREE DESIGNS BY USING ROBUST FORMULATION

Although the Heaviside function discussed in the previous section yields more "black-and-white" designs, hinges, defined as two elements connected by a single node, which may lead to undesired behavior in the manufactured prototype, cannot be simply removed using this filter. To obtain hinge-free designs, robust formulations [37] are proposed based on the Heaviside projection technique.

The robustness can be ensured by considering intermediate, eroded, and dilated designs in the formulation. The three designs are typically achieved by applying Heaviside projection with different values of $\alpha$. The intermediate design refers to $\alpha = 0.5$, the eroded one to $\alpha > 0.5$, and the dilated one to $\alpha < 0.5$. By pushing all three designs to satisfy the same optimization objective and constraints, the topology length scale in both solid and void areas can be ensured, i.e., no hinges [37]. Next, formulations incorporating robustness to objective Eq. (5.1), compliance constraint Eq. (5.2), and volume constraint Eq. (5.4) are presented.

*Objective.* In the robust formulation, the resulting objective function can be expressed by

$$f_0 = \max(f^e, f^{inter}, f^d). \tag{5.7}$$

Here $f^e, f^{inter}, f^d$ are objective values derived from eroded, intermediate and dilated designs, respectively. By minimizing $f_0$, all the three designs will finally converge to similar solutions.

*Compliance constraint.* The compliance constraint at DOF $s$ in the robust formulation can be expressed by

$$C_s^e \leq \overline{C}_s^*, \tag{5.8}$$

where $C_s^{\mathrm{e}}$ represents linear compliance obtained from the eroded design, which means constraints are imposed on the design that holds the maximum compliance values to ensure that all three designs satisfy the constraints. For the upper limit $\overline{C}_s^*$, the actual engineer requirements, i.e., $\overline{C}_s$, could be excessively strict for the eroded design in the early optimization stages. Therefore, we recommend starting the optimization with $\overline{C}_s^* = \overline{C}_s$ for a few iterations; if the optimization is progressing too slowly, $\overline{C}_s^*$ can then be adjusted following the recommendations proposed by [37]. The process is as follows: 1) Use $\overline{C}_s^* = \overline{C}_s$ for the first 10 iterations; 2) At the 10th iteration, calculate the compliance of the intermediate design $C_s^{\mathrm{inter}}$ and that of the eroded design $C_s^{\mathrm{e}}$; 3) Replace $\overline{C}_s^*$ by setting $\overline{C}_s^* = \frac{C_s^{\mathrm{e}}}{C_s^{\mathrm{inter}}}\overline{C}_s$; and 4) Every 10 iterations, repeat steps 2) and 3) until $\frac{C_s^{\mathrm{e}}}{C_s^{\mathrm{inter}}}$ approaches 1.

*Volume constraint.* In the robust formulations, the volume constraints can be expressed by

$$V^{\mathrm{d}} \leq \overline{V}^*, \tag{5.9}$$

where $V^{\mathrm{d}}$ represents the volume constraint determined by the dilated design. For the upper limit $\overline{V}^*$, the same strategy employed for $\overline{C}_s^*$ is applied to gradually reach the engineer-specified value $\overline{V}$. The process is as follows: 1) Use $\overline{V}^* = \overline{V}$ for the first 10 iterations; 2) At the 10th iteration, calculate the volume of the intermediate design $V^{\mathrm{inter}}$ and the dilated design $V^{\mathrm{d}}$; 3) Replace $\overline{V}^*$ by setting $\overline{V}^* = \frac{V^{\mathrm{d}}}{V^{\mathrm{inter}}}\overline{V}$; and 4) Every 10 iterations, repeat steps 2) and 3) until $\frac{V^{\mathrm{d}}}{V^{\mathrm{inter}}}$ approaches 1.

### 5.3.3. INPUT DISPLACEMENT CONTINUATION METHOD

When using TO to design mechanisms based on 2D plane stress/strain domains, applying a relatively large input displacement to the simply-shaped initial solid design could cause divergence of the nonlinear analysis even at the start of TO due to abnormal deformations. To avoid this divergence, we propose a displacement continuation approach, whereby the input displacements are increased step-by-step during the optimization process to progressively introduce nonlinearity into structures.

In the continuation, we avoid loading the structure with the entire input at the beginning of the optimization. Instead, only a portion of the input displacement is applied. Then, typically after 20 optimization iterations, a design prototype that can approximately meet the design requirements can be created. Next, every 20 optimization iterations, the input displacement is increased by another portion until the entire input is reached. During the process, the structure will gain more and more geometric nonlinearity and finally meet the optimal requirement. Details can be found in Section 5.4.1 where a 2D expansion structure is designed.

## 5.4. TO-BASED DESIGNS

In this section, TO is used to produce three designs, including one planar and two orthoplanar path-generation mechanisms. The initial example involves a 2D expansion structure, demonstrating the failure of analysis under a relatively large input displacement, along with the effectiveness of the proposed continuation method in resolving the issue. The second example shows a shell-based linear guide, which demonstrates the com-

pactness of shell mechanisms. Additionally, the example emphasizes the hinge issue shown in the topology and compares the differences between the numerical design and the experimental prototype. The third case demonstrates a shell-based mechanism that follows a relatively complex user-defined path. Robust formulations are applied, and the impact of robustness on the final numerical and experimental designs is investigated.

### 5.4.1. A 2D EXPANSION STRUCTURE

The first design is a 2D expansion mechanism. The design is prompted by a concept to develop an adjustable spinal implant structure, whose design domain can be simplified to a rectangle structure as shown in Fig. 5.2. The desired design needs to satisfy three requirements: First, it can expand to double its thickness when the left and right edges are compressed; second, throughout the deforming process, the top and bottom layers should remain flat; third, the structure should have sufficient stiffness in $y$-direction to bear small loads.

According to the design requirements, four input Points P, Q, R, and S are selected from the left and right edges. Output Points a, b, c, d, e, and f at the top and bottom sides are considered. Due to symmetry, only a quarter of the structure is taken as the design domain. The objective function is

$$f_0 = (u_{y,20}^{\text{out,b}} - 4)^2 + (u_{y,20}^{\text{out,c}} - 4)^2, \tag{5.10}$$

where $u_{y,20}^{\text{out,b}}$ and $u_{y,20}^{\text{out,c}}$ represent displacements of Points b and c in $y$-direction at the last incremental step (in total 20 incremental steps are applied).

Then, two constraints are imposed to ensure the flatness of the top layer during the loading process. One constraint ensures displacements in $y$-direction at Points b and c are the same. The constraint involves all 20 incremental steps and is formulated as

$$\sum_{j=1}^{20} (u_{y,j}^{\text{out,b}} - u_{y,j}^{\text{out,c}})^2 \leq 0.01, \tag{5.11}$$

where $u_{y,j}^{\text{out,b}}$ and $u_{y,j}^{\text{out,c}}$ represent displacements of Points b and c in $y$-direction at incremental Step $j$. For the other constraint, the displacement of output Point c in $x$-direction is restricted by

$$\sum_{j=1}^{3} (u_{x,j}^{\text{out,c}})^2 \leq 0.1. \tag{5.12}$$

Here $u_{x,j}^{\text{out,c}}$ is the displacement of Point c in $x$-direction at incremental Step $j$, where incremental factors, $\lambda_j = \{0.2, 0.5, 1.0\}$.

Furthermore, to satisfy the stiffness requirement, we constrain the compliance in $y$-direction in undeformed configuration. The corresponding constraint is

$$g_c = C_y - \overline{C_y} \leq 0, \tag{5.13}$$

where $C_y$ is the compliance calculated in a separate linear load case, where two concentrated forces $f_y^{\text{L,b}} = 10\,\text{N}$ and $f_y^{\text{L,c}} = 10\,\text{N}$ are applied at Points b and c of the quarter of the structure. The compliance upper limit $\overline{C}$ is calculated by multiplying the forces with the

latter, where the allowable displacements are $u_y^{\mathrm{L,b}} = 0.01\,\mathrm{mm}$ and $u_y^{\mathrm{L,c}} = 0.01\,\mathrm{mm}$. Then, $\overline{C} = 0.2\,\mathrm{N\,mm}$, The volume is limited to 40% of the design domain.

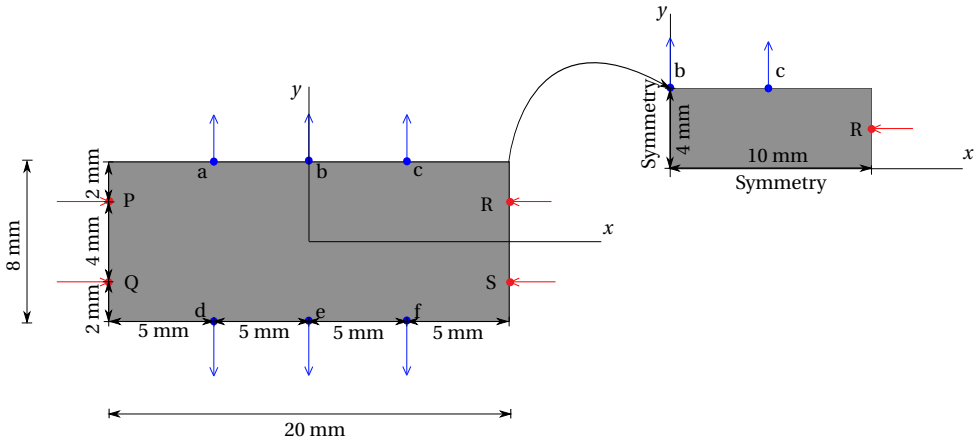


Figure 5.2: Geometry of the design domain for the 2D expansion structure. Young's modulus $E = 300\,\mathrm{GPa}$ and Poisson's ratio 0.3. Input displacements are applied at Points P, Q, R, S shown by red arrows. Output points are a, b, c, d shown by blue arrows. Due to symmetry, only a quarter of the structure is taken as the design domain.

We start the optimization from a fully solid design, as shown in Fig. 5.3(a), with the input displacement at the last incremental step equal to $u_{\mathrm{end}}^{\mathrm{in}} = 3\,\mathrm{mm}$. The corresponding deformed configuration is shown in Fig. 5.3(b).

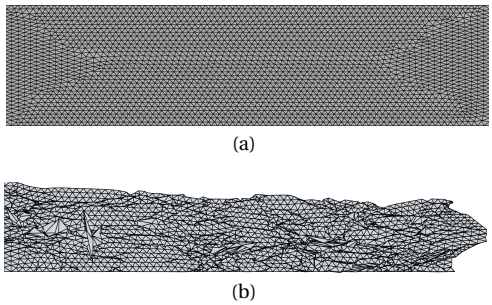


Figure 5.3: Starting from the initial fully solid design shown in (a), with input displacement $u_{\mathrm{end}}^{\mathrm{in}} = 3\,\mathrm{mm}$ at the final incremental step, the corresponding deformed configuration is shown in (b). As noticed, abnormal deformation resulting from large stresses lead to complete failure of the analysis.

As noticed, the solid elements become "inside-out" leading to complete divergence of the analysis. To mitigate this issue, we use the proposed input displacement continuation, where instead of applying $u_{\mathrm{end}}^{\mathrm{in}} = 3\,\mathrm{mm}$ at the early stage of optimization, we apply $u_{\mathrm{end}}^{\mathrm{in}^*} = 0.5\,\mathrm{mm}$. Next, $u_{\mathrm{end}}^{\mathrm{in}^*}$ is increased every 20 optimization iterations until it reaches $u_{\mathrm{end}}^{\mathrm{in}} = 3\,\mathrm{mm}$. The corresponding $u_{\mathrm{end}}^{\mathrm{in}^*}$ and obtained topology are shown in Tab. 5.1.

Observing the results in Tab. 5.1, the utilization of a small $u_{\mathrm{end}}^{\mathrm{in}^*}$ facilitates the creation

of a topology with balanced stiffness and flexibility. Building upon this, increasing the input displacements gradually introduces more flexibility to the design. Ultimately, the objective value is reduced to $1.23 \times 10^{-3}$ when $u_{\text{end}}^{\text{in}^*} = u_{\text{end}}^{\text{in}} = 3\,\text{mm}$, and the corresponding topology is shown in (5) of Tab. 5.1. However, in the topology, a few gray elements are still noticeable. To achieve a black-and-white design suitable for manufacturing, the optimization process was continued with more aggressive Heaviside parameters, where $\alpha = 0.6$ and $\beta$ doubled every 20 iterations until $\beta = 128$. The final result in the complete design domain presents a black-and-white design in (6) of Tab. 5.1. Judging from the objective and error values shown in the table, the design satisfactorily meets the specified requirements.

To validate the optimized design, the topology result is extruded in the third dimension and manufactured using 3D printing. The obtained prototype is placed between two rigid smooth panels, as seen in Fig. 5.4. The prototype is compressed when the top panel is moved down. The loading process is recorded by photographs. The experiment and simulation results are compared in Fig. 5.5, where both input and output displacements are relative to the input displacement at the last incremental step. The simulation results indicate that when the top and bottom edges of the mechanism are compressed, the structure expands to nearly double its width, while the left and right layers remain almost flat during the deformation process. Experimental results exhibit similar behavior as seen in the deformation pictures. Additionally, the deflection curves show that the 3D-printed prototype undergoes a deformation process nearly identical to that of the simulation. In conclusion, using TO, a design that demonstrates the desired expansion behavior while meeting the flatness requirement was successfully generated. The close alignment between the deformation of the 3D-printed prototype and the simulation results confirms the reliability of the TO-based design.



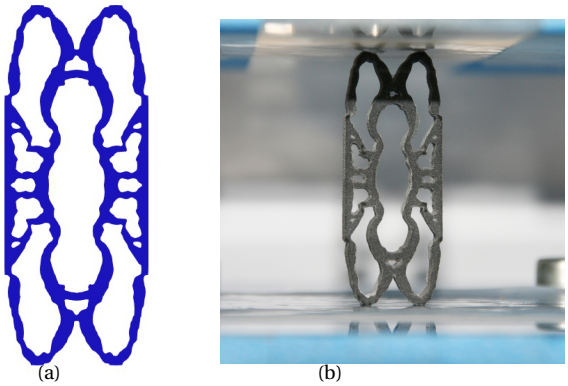

(a) (b)

Figure 5.4: (a) Final topology without void elements. (b) 3D-printed prototype and experimental set-up. Here, the mechanism is positioned between two smooth panels. When the top panel moves downward, the mechanism is compressed. The top and bottom of the mechanism are permitted to slide along the panels, while the left and right boundaries are allowed to expand in opposite directions. The left and right edges in (a) or (b) correspond to the top and bottom edges of the topology shown in (6) of Tab. 5.1.

Table 5.1: Topology optimization results for the expansion structure with input displacement continuation. Here $\alpha$ and $\beta$ are the threshold and slope of the Heaviside projection. $u_{\text{end}}^{\text{in}^*}$ represents the input displacement at the last incremental step of each continuation step. $u_{\text{end}}^{\text{in}^*}$ is set to 0.5 mm during the first continuation step, covering the initial 20 iterations, with the resulting topology shown in (1). Next, $u_{\text{end}}^{\text{in}^*}$ increases to 1 mm. After another 20 iterations, the resulting topology shown in (2). Following the same rule, $u_{\text{end}}^{\text{in}^*}$ finally increases to 3 mm, and the resulting topology is shown in (5). Then, to achieve a black-and-white design suitable for manufacturing, the optimization process continued with more aggressive Heaviside parameters, where $\alpha = 0.6$ and $\beta$ starts from 8, and it is doubled every 20 iterations until $\beta = 128$. The final topology is shown in (6). Designs shown in (1)–(5) depict a quarter of the overall design, while (6) illustrates the complete structure. $f_0$ is objective value shown in Eq. (5.10). The error related to constraint Eq. (5.11) is $\epsilon_{\text{bcy}} = \sum_{j=1}^{20} \sqrt{(u_{y,j}^{\text{out,b}} - u_{y,j}^{\text{out,c}})^2} / (20 d_{\text{len}})$. The error related to constraint Eq. (5.12) is $\epsilon_{\text{cx}} = \sum_{j=1}^{3} \sqrt{(u_{x,j}^{\text{out,c}} - 0)^2} / (3 d_{\text{len}})$. The error related to $f_0$ is defined by $\epsilon_{\text{y}} = \sqrt{(u_y^{\text{out,b}} - 4)^2} + \sqrt{(u_y^{\text{out,c}} - 4)^2} / (2 d_{\text{len}})$. The path length is $d_{\text{len}} = 4$ mm

| | Topology | $u_{\text{end}}^{\text{in}^*}$ (mm) | $\frac{u_{\text{end}}^{\text{in}^*}}{u_{\text{end}}^{\text{in}}}$ | $\alpha\&\beta$ | $f_0$ | comments |
|---|---|---|---|---|---|---|
| (1) | 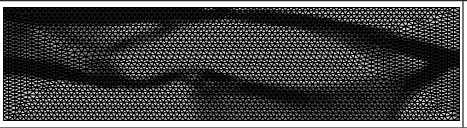 | 0.5 | 16.7% | 0.5&4 | 19.5 | Start from a fully solid design. |
| (2) | 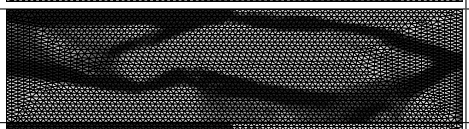 | 1 | 33.3% | 0.5&4 | 9.26 | Start from (1) |
| (3) |  | 1.5 | 50% | 0.5&8 | 3.73 | Start from (2) |
| (4) |  | 2.5 | 83.3% | 0.5&8 | 0.407 | Start from (3) |
| (5) |  | 3 | 100% | 0.5&8 | $1.23\times 10^{-3}$ | Start from (4) |
| (6) |  | 3 | 100% | 0.6&128 | $4.3\times 10^{-3}$ | Start from (5) $\epsilon_{\text{bcy}} = 0.08\%$. $\epsilon_{\text{cx}} = 1.8\%$. $\epsilon_{\text{y}} = 1\%$. |

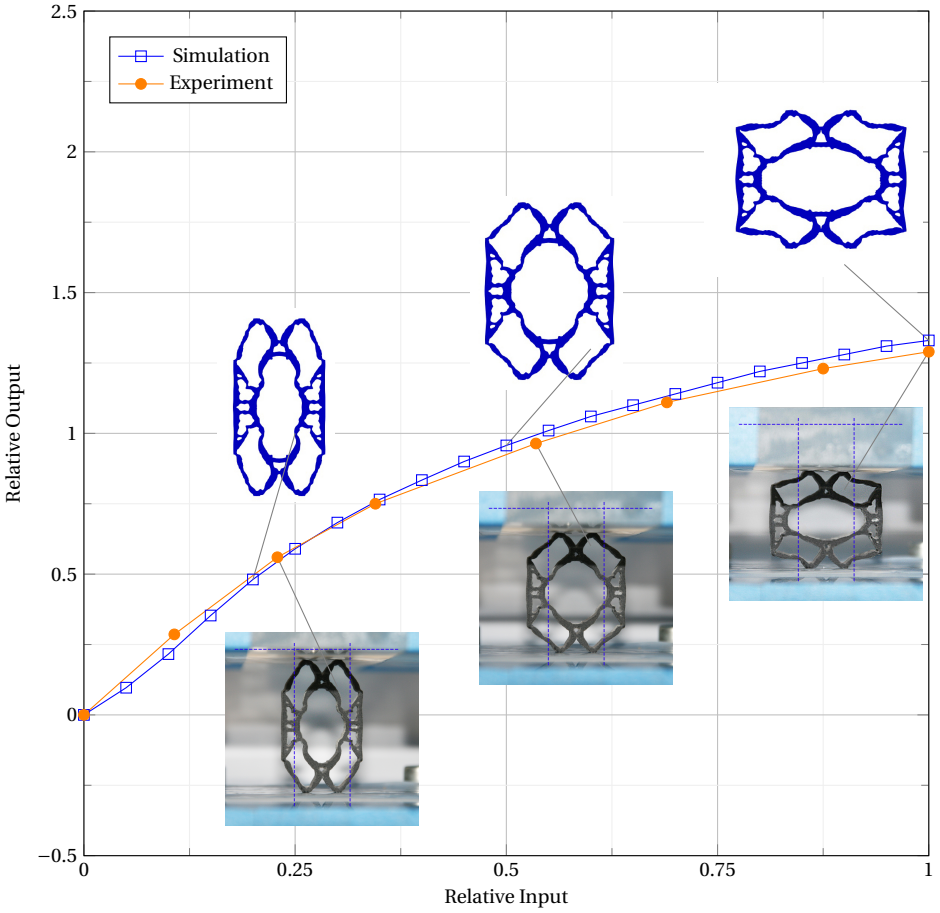


Figure 5.5: Deflection path comparison between simulation and experiments. Both the input and output are relative to the final input displacements $u_{\text{end}}^{\text{in}} = 3\,\text{mm}$. In this context, the simulation results are generated using finite element analysis. For the experiments, input displacements are determined by measuring the position changes of the top panel in the photos, while output displacements are measured by tracking the position changes of the left and right edges of the mechanism in the photos.

### 5.4.2. A PLATE-BASED LINEAR GUIDE

In this section, we design a linear guide based on plate elements. The design domain is a cantilever plate as shown in Fig. 5.6. The black area in the middle represents a non-design area. The central node is designed to move along $z$-direction with no motion in $y$-direction. To satisfy this requirement, displacement in $z$-direction is specified as input, while displacement in $y$-direction is included in the objective function:

$$f_0 = (u_{y,1}^{\text{out}})^2 + (u_{y,2}^{\text{out}})^2 + (u_{y,3}^{\text{out}})^2. \tag{5.14}$$

To ensure the stiffness in $z$-direction, we constrain the $z$-direction compliance in the undeformed configuration. The corresponding constraint is

$$g_c = C_z - \overline{C_z} \leq 0, \tag{5.15}$$

where $C_z$ represents the compliance calculated for a separate linear load case where $f_z^L = 0.01\,\text{N}$ is applied at the top center in $z$-direction. $\overline{C_z}$ represents the upper limit can be calculated by multiplying the forces with the allowable displacements, where the allowable displacement is $u_z^L = 0.3 \times 10^{-3}$ cm. Then, $\overline{C_z} = 3 \times 10^{-6}$ N cm. The volume is limited to 60% of the design domain. TO results are shown in Tab. 5.2. The first row shows the result without the Heaviside projection, where transition areas between the solid and void areas can be observed, consisting of elements with intermediate pseudo-density values. To avoid the unmanufacturable transition areas, the Heaviside projection is applied. With the Heaviside projection, the final topology is shown in the second row of Tab. 5.2. As observed, most of the gray transition areas are eliminated; however, those along the fixed boundary are replaced with single-element hinges. Given that the number of hinges is quite limited, we decide to remove these hinges in the post-processing for 3D printing and investigate the impact posed by neglecting the hinges in the experiments.

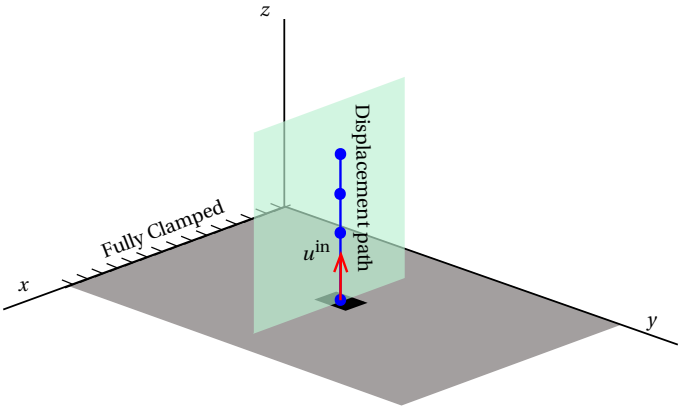


Figure 5.6: A cantilever plate model. The length is 3 cm, the width 2 cm, and the thickness 0.08 cm. Here, $u_{end}^{in}$ denotes the final input displacement whose direction is presented by the red arrow. The displacement path is shown by the blue line, where 3 precision points, i.e., incremental steps are selected. The corresponding incremental parameter $\lambda_j$ and the desired output displacements $u_{x,j}^*$ are shown in the table. Young's modulus is $E = 300\,\text{GPa}$ and Poisson's ration is 0.3.

| | |
|---|---|
| $u_{end}^{in}$ | 2 cm |
| $\lambda_j$ | 0.5, 0.75, 1 |
| $u_{y,j}^*$ | 0, 0, 0 cm |

The 3D prototype is shown in Fig. 5.7(b). Then, with the prototype, an experiment is conducted using a tensile machine. As seen in Fig. 5.7(b), the left edge of the prototype is fully clamped. Regarding the input, a rope with a blocker on one end passes through a small hole near the center point of the structure. The other end of the rope is attached to the movable top of the tensile machine. When the machine pulling the rope up, the structure gains inputs. The experiment is recorded by photographs. The experiment and simulation results are compared in Fig. 5.8.

As shown by the simulation results, the inner and outer strips of the design rotate in opposite directions, which counteracts the in-plane movement of the center point. Due to symmetry, the center can both move up and down, consequently, tracing a relatively long distance. The deformations observed in the experiments matches the simulations. However, when we look at the deflections curves closely, there are some differences. When the input is less than half of the final input displacement, the experimental results closely match the simulation. As the input increases beyond this point, the experimental results gradually deviate, leading to increased error. This error is mostly attributable to the removal of the two hinges connected to the boundary. In conclusion, the simulation and manufactured designs generally exhibit the same behavior, while the performance of the manufactured design is influenced by the removal of boundary-connected hinges, when the input displacements are relatively large.

Table 5.2: Topology optimization results for the plate-based linear guide. Here $u_{\text{end}}^{\text{in}}$ represents the input displacement at the last incremental step. $\alpha$ and $\beta$ are the threshold and slope of the Heaviside projection. $f_0$ is objective value calculated in Eq. (5.14). The errors $\epsilon_y$ below is measured by $\left(\sqrt{(u_{y,1}^{\text{out}})^2}+\sqrt{(u_{y,2}^{\text{out}})^2}+\sqrt{(u_{y,3}^{\text{out}})^2}\right)/\left(3d_{\text{len}}\right)$.The path length is $d_{\text{len}}=2\,\text{cm}$.

| Topology | $u_{\text{end}}^{\text{in}}$ (cm) | $\alpha\&\beta$ | $f_0$ | comments |
|---|---|---|---|---|
| 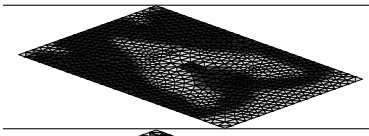 | 2 | - | $5.91\times10^{-3}$ | Without Heaviside projection. $\epsilon_y=2\%$ |
| 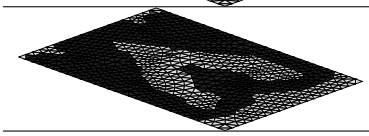 | 2 | 0.4&64 | $7.91\times10^{-3}$ | With Heaviside projection. $\beta$ is initially set to 2, doubled every 20 iterations, and finally 64. $\epsilon_y=2\%$ |

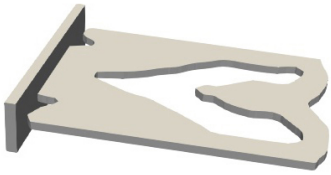

(a)

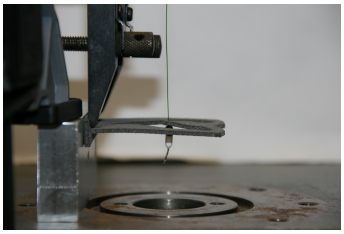

(b)

Figure 5.7: (a) Final design. (b) 3D-printed prototype and experimental set up. Here, the left is fully clamped, while a rope passes through a hole at the center and is connected to the movable top of the tensile machine.

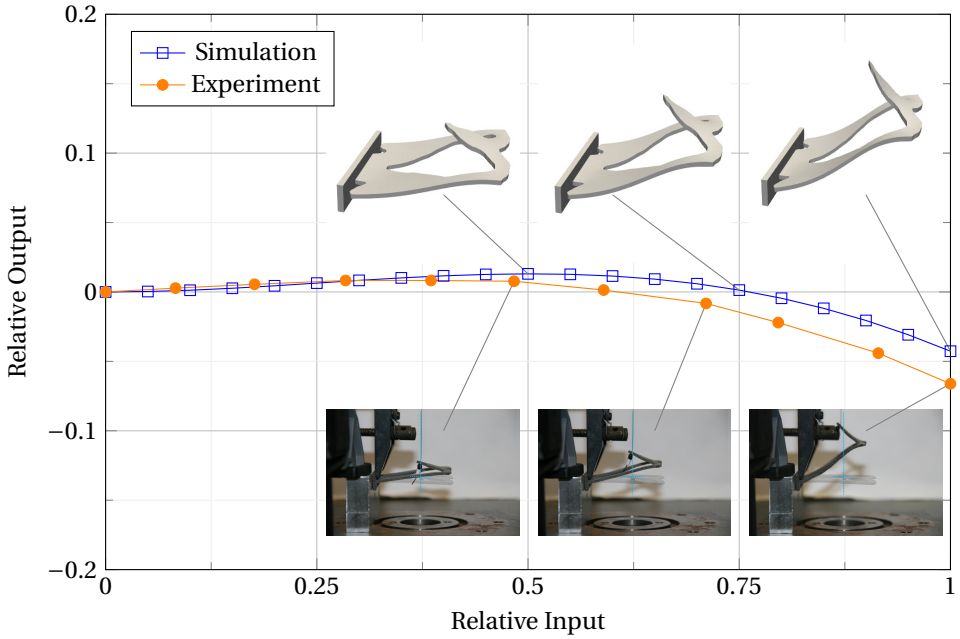


Figure 5.8: Deflection path comparison between simulation and experiment. Here the simulation results are generated using finite element analysis and the experimental results are obtained by measuring the position change of the input point. Both the input and output are relative to the final input displacement of 2 cm. When the input is less than half of the final input displacement, the experimental results closely match the simulation. As the input increases beyond this point, the experimental results gradually deviate, leading to increased error, which we attribute to the removal of the two hinges connected to the boundary.

### 5.4.3. A CYLINDER MOVING BACK AND FORTH

Given that shell mechanisms may exhibit complex trajectory behaviors owing to the nature of their motion coupling, a design that can move back and forth is generated based on shells. A cylinder design domain is shown in Fig. 5.9, where the bottom is fully clamped. The top center is designed to first move in the negative $x$-direction and then in the positive $x$-direction, following the displacement path indicated by the blue line as shown in Fig. 5.9.

Here, $u_z$ is regarded as the input and $u_x$ is considered in the objective function:

$$f_0 = (u_{x,1}^{\text{out}} + 2)^2 + (u_{x,2}^{\text{out}} + 4)^2 + (u_{x,3}^{\text{out}} + 2)^2. \tag{5.16}$$

To ensure stiffness in $z$-direction, we constrain the compliance in $z$-direction in the undeformed configuration. The corresponding constraint is

$$g_{\text{c}} = C_z - \overline{C_z} \leq 0, \tag{5.17}$$

where $C_z$ represents the compliance calculated for a separate linear load case, where $f_z^{\text{L}} = 1\,\text{N}$ is applied at the top center in $z$-direction. $\overline{C_z}$ represents the upper limit calculated by multiplying the forces with the allowable displacements. Here, the allowable

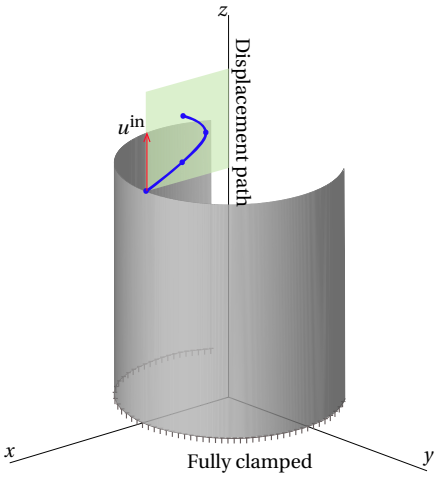


Figure 5.9: A fully clamped cylinder structures. The Radius is 5 cm, height 20 cm, and thickness 0.3 cm. Here, $u^{\text{in}}_{\text{end}}$ denotes the final input displacement whose direction is presented by the red arrow. The displacement path is shown by the blue line, where 3 prediction points, i.e., incremental steps are selected. The corresponding incremental parameter $\lambda_j$ and the output displacements $u^*_{x,j}$ are seen in the table. Young's modulus $E = 100$ MPa and Poisson's ration is 0.3.

| | |
|---|---|
| $u^{\text{in}}_{\text{end}}$ | 4 cm |
| $\lambda_j$ | 0.25, 0.5, 1 |
| $u^*_{x,j}$ | -2, -4, -2 cm |

displacement is $u^{\text{L}}_z = 0.15$ cm then, $\overline{C} = 0.15$ N cm. The volume is limited to 45% of the design domain.

Topology results are shown in Tab. 5.3. Firstly, a coarse mesh is used for efficiency, whose final design is shown in the first row of Tab. 5.3. Regarding the objective, the design meets the requirement, but it cannot be manufactured due to the presence of many hinges. To eliminate those hinges, a finer mesh and robust formulations are applied. Due to symmetry, only half of the domain is modeled. Finally, a hinge-free design is obtained shown in the second row of Tab. 5.3. In comparison to the topology without the robust formulation, this design comes at the expense of a six-fold increase in the objective function value $f_0$. According to the deflection curves shown in Fig. 5.10, the largest difference between the results with and without the robust formulation appears at the stationary point, i.e., $\lambda_j = 0.5$. The robust design produces a smaller deflection than the non-robust one. Despite this reduction in the output displacement, the result still effectively demonstrates the intended back-and-forth movement.

The robust design is then manufactured via 3D printing shown in Fig. 5.11. with the prototype, an experiment is conducted using the tensile machine. In Fig. 5.11(b), the bottom of the prototype is fixed. Regarding the input, a rope with a blocker at one end goes through a small hole just below the top center. The other end is attached to the movable top of the tensile machine. By pulling up the rope, the input is applied to the structure. To eliminate the influence induced by rope's rotation, The length of the rope is 10 times that of the height of the prototype. The deformation process is photographed. To avoid splitting caused by stress concentration around the hole, loading is terminated before the input displacement reaches its prescribed maximum.

Table 5.3: Topology optimization results for the cylinder mechanism. Here the final input displacement is denoted by $u^{\text{in}}_{\text{end}}$. $\alpha$ and $\beta$ are the threshold and slope of the Heaviside projection. $f_0$ is objective value calculated in Eq. (5.16). The path length is approximately equal to $d_{\text{len}} = 2 * \sqrt{2^2+1} + \sqrt{2^2+2^2}$=7.3 cm. The errors $\epsilon_z$ below are measured by $\left(\sqrt{(u^{\text{out}}_{x,1}+2)^2} + \sqrt{(u^{\text{out}}_{x,2}+4)^2} + \sqrt{(u^{\text{out}}_{x,3}+2)^2}\right) / \left(3d_{\text{len}}\right)$.

| Topology | $u^{\text{in}}_{\text{end}}$ (cm) | $\alpha$&$\beta$ | $f_0$ | comments |
|---|---|---|---|---|
| 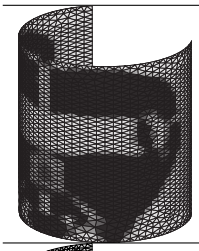 | 4 | - | 0.091 | Without robust formulations. $\epsilon_z = 2.1\%$ |
| 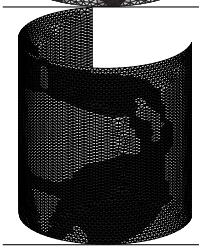 | 4 | 0.5&64 | 0.58 | With robust formulations. $\epsilon_z = 5.6\%$. $\beta$ is initially set to 2, doubled every 20 iterations, and finally 64. |

The experiment and simulation curves are compared in Fig. 5.12(a). Both simulation and experimental results show the back-forth movement: When the input is small, the top of the structure is allowed to move back, whereas the bottom of the structure acts as a support; when the input becomes larger than half of the final input displacement, the bottom part of the structure is pushed forward, resulting in the whole structure moving forward. However, it can be observed that the experimental deflection curve deviates from the simulation result at the early stage, and that the displacement at the stationary point is largely reduced. There are two reasons behind this inconsistency. Firstly, the thickness of the prototype is slightly larger than that specified in the simulation due to the limitations of the 3D-printing technique employed. Secondly, the input point is not precisely positioned at the top. We can validate the two reasons using simulations. First, we increase the thickness of the shell in the simulation model from 0.3 cm to 0.45 cm, to yield the corresponding deflection curve in Fig. 5.12(b). As observed, the deflection at the stationary point generally aligns with the simulation results, though differences persist during the early stages of deflection. Next, with the adjusted thickness 0.45 cm, the input point position in the simulation is aligned with that of the experiment, i.e., 0.07 cm away from the top center. As shown in Fig. 5.12(c), the deflection at the early stages also matches. As observed, the thickness has a significant impact on the results, indicating that shell-based mechanisms are highly sensitive to variations in thickness. Therefore, precise manufacturing techniques are crucial for achieving accurate performance in shell mechanisms. In conclusion, the simulation and manufactured designs generally exhibit the same behavior, while the performance of the manufactured design is influenced by the thickness and the position of the input point.

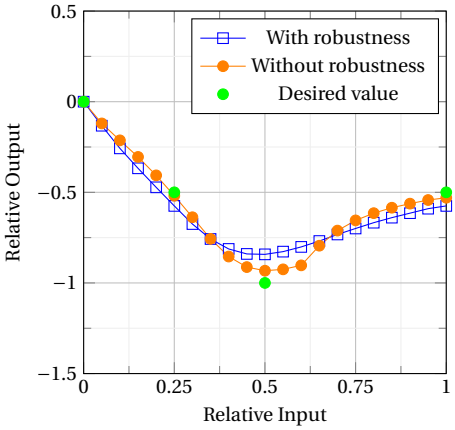


Figure 5.10: Deflection path comparison between with and without robust formulations. Both the input and output displacements are relative to the final input displacement of 4 cm. Introducing of robust formulation reduces the maximum output at the stationary point.



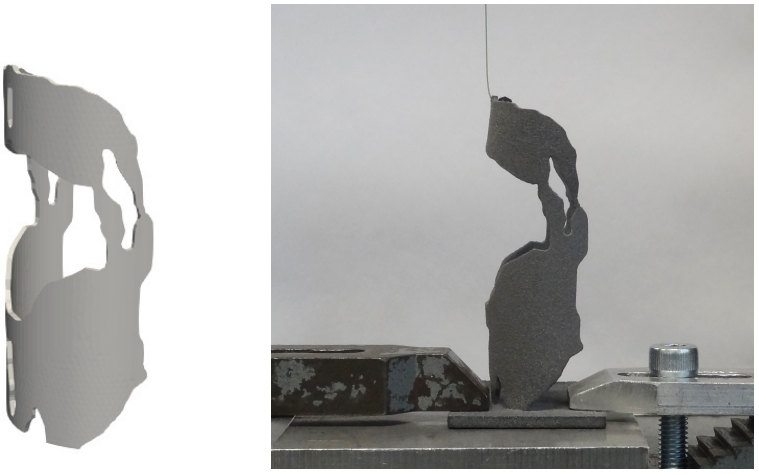

(a) (b)

Figure 5.11: (a) Final design obtained by TO; and (b) 3D-printed prototype and experimental set up. The bottom is fully clamped, while a rope passes through a hole just below the top center and is connected to the movable top of a tensile machine.

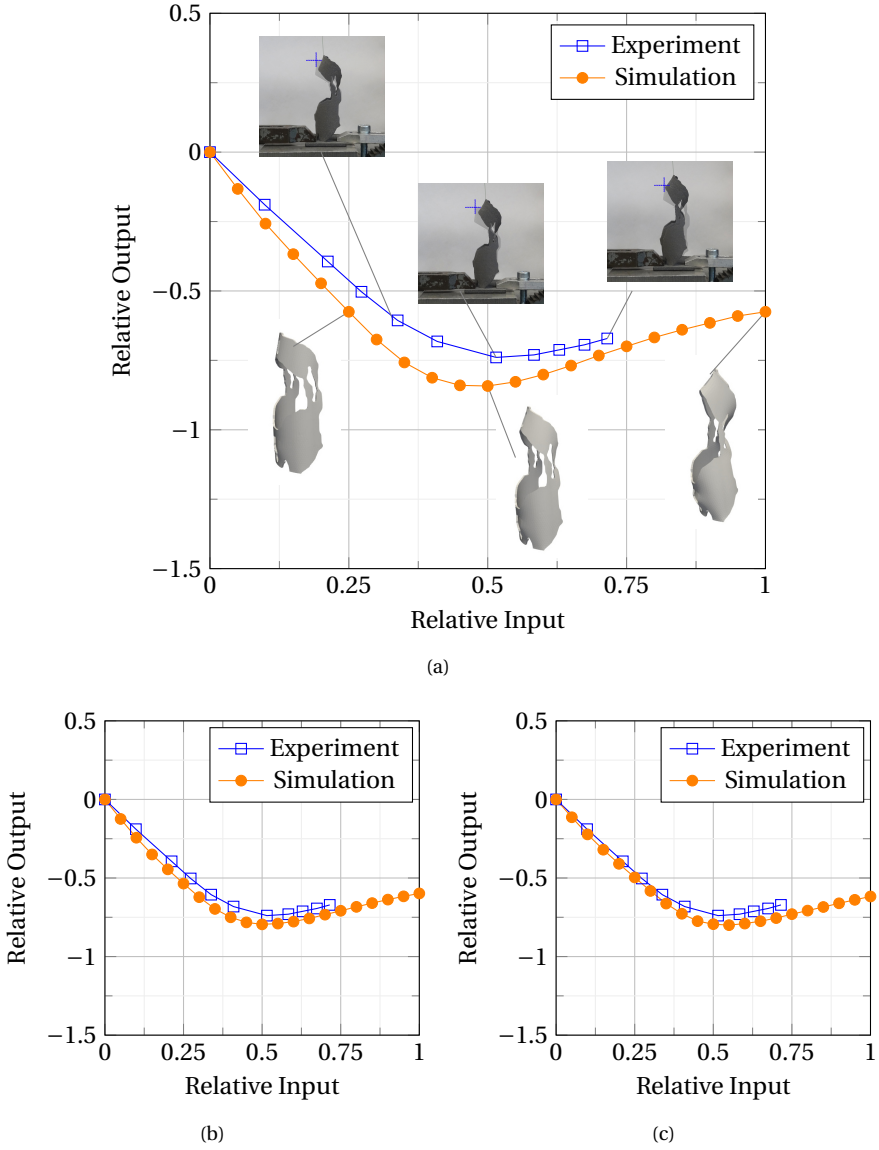


Figure 5.12: Deflection path comparison between simulation and experiments. Both the input and output displacements are relative to the final input displacement of 4 cm. In (a), the simulation results are based on settings with a thickness of 0.3 cm and an input applied at the top center. In (b), the simulation used a thickness of 0.45 cm and the input is placed at the top center. In (c), the simulation is based on settings with a thickness of 0.45 cm and the input is placed 0.07cm away from the top center. Simulation results are generated using finite element analysis and the experiment results are obtained by measuring position changes of the input point, i.e., the rope attachment in the photos.

## 5.5. SUMMARY AND CONCLUSIONS

This work focuses on the design of path-generation mechanisms capable of delivering relatively large strokes. Topology optimization was employed with a least-squared-error objective, linear compliance constraints, and a volume constraint. Three representative designs were presented: one planar mechanism and two ortho-planar mechanisms, all validated through experiments.

Based on the 2D expansion mechanism example, the proposed input continuation method is verified to be effective to prevent solid 2D plane stress/strain elements from inverting ("inside-out") at the early stage of the optimization. This ensures stable analysis resulting in a design that achieves a displacement of up to 100% of its structural size along the motion direction.

The use of plate and shell design domains demonstrates the potential of ortho-planar mechanisms in achieving even larger DSRs. For instance, the plate-based linear guide can reach a displacement of up to 130% of its size if considering its symmetric configuration. Additionally, these design domains enable the generation of mechanisms with more complex motion paths, as shown by the cylindrical design capable of moving back and forth.



Experimental results show that the optimized designs perform as intended, and that extending 2D designs into the third dimension does not affect their mechanical behavior. However, performance can be strongly affected by manufacturing details, such as material thickness and the removal of hinges.

## REFERENCES

[1] M. Olfatnia, S. Sood, J. J. Gorman, and S. Awtar, *Large stroke electrostatic comb-drive actuators enabled by a novel flexure mechanism,* Journal of Microelectromechanical Systems **22**, 483 (2012).

[2] S. Xiao and Y. Li, *Visual servo feedback control of a novel large working range micro manipulation system for microassembly,* Journal of Microelectromechanical Systems **23**, 181 (2013).

[3] S. Awtar and G. Parmar, *Design of a large range xy nanopositioning system,* Journal of Mechanisms and Robotics **5**, 021008 (2013).

[4] K.-B. Choi and D.-H. Kim, *Monolithic parallel linear compliant mechanism for two axes ultraprecision linear motion,* Review of scientific instruments **77**, 065106 (2006).

[5] Y. K. Yong, S. S. Aphale, and S. R. Moheimani, *Design, identification, and control of a flexure-based xy stage for fast nanoscale positioning,* IEEE Transactions on Nanotechnology **8**, 46 (2008).

[6] L.-J. Lai, G.-Y. Gu, and L.-M. Zhu, *Design and control of a decoupled two degree of freedom translational parallel micro-positioning stage,* Review of Scientific Instruments **83**, 045105 (2012).

[7] S. Huang, K. K. Tan, and T. H. Lee, *Adaptive sliding-mode control of piezoelectric actuators,* IEEE Transactions on Industrial Electronics **56**, 3514 (2009).

[8] P.-K. Wong, Q. Xu, C.-M. Vong, and H.-C. Wong, *Rate-dependent hysteresis modeling and control of a piezostage using online support vector machine and relevance vector machine,* IEEE Transactions on Industrial Electronics **59**, 1988 (2011).

[9] U. Bhagat, B. Shirinzadeh, L. Clark, P. Chea, Y. Qin, Y. Tian, and D. Zhang, *Design and analysis of a novel flexure-based 3-dof mechanism,* Mechanism and Machine Theory **74**, 173 (2014).

[10] Q. Xu, *Design and development of a flexure-based dual-stage nanopositioning system with minimum interference behavior,* IEEE Transactions on Automation Science and Engineering **9**, 554 (2012).

[11] Y. Song, J. Wang, K. Yang, W. Yin, and Y. Zhu, *A dual-stage control system for high-speed, ultra-precise linear motion,* The international journal of advanced manufacturing technology **48**, 633 (2010).

[12] J. Rommers, M. Naves, D. Brouwer, and J. Herder, *A large range spatial linear guide with torsion reinforcement structures,* in *International Design Engineering Technical Conferences and Computers and Information in Engineering Conference*, Vol. 51807 (American Society of Mechanical Engineers, 2018) p. V05AT07A025.

[13] M. P. Bendsøe and O. Sigmund, *Material interpolation schemes in topology optimization,* Archive of applied mechanics **69**, 635 (1999).

[14] M. P. Bendsoe and O. Sigmund, *Topology optimization: theory, methods, and applications* (Springer Science & Business Media, 2003).

[15] O. Sigmund and K. Maute, *Topology optimization approaches,* Structural and Multidisciplinary Optimization **48**, 1031 (2013).

[16] F. Niu, S. Xu, and G. Cheng, *A general formulation of structural topology optimization for maximizing structural stiffness,* Structural and Multidisciplinary Optimization **43**, 561 (2011).

[17] Y. Li, J. Zhu, F. Wang, W. Zhang, and O. Sigmund, *Shape preserving design of geometrically nonlinear structures using topology optimization,* Structural and Multidisciplinary Optimization **59**, 1033 (2019).

[18] A. Saxena, *Topology design of large displacement compliant mechanisms with multiple materials and multiple output ports,* Structural and Multidisciplinary Optimization **30**, 477 (2005).

[19] T. Bruns and O. Sigmund, *Toward the topology design of mechanisms that exhibit snap-through behavior,* Computer Methods in Applied Mechanics and Engineering **193**, 3973 (2004).

[20] H. Deng, L. Cheng, X. Liang, D. Hayduke, and A. C. To, *Topology optimization for energy dissipation design of lattice structures through snap-through behavior,* Computer Methods in Applied Mechanics and Engineering **358**, 112641 (2020).

[21] C. B. Pedersen, T. Buhl, and O. Sigmund, *Topology synthesis of large-displacement compliant mechanisms,* International Journal for numerical methods in engineering **50**, 2683 (2001).

[22] A. Saxena, *Synthesis of Compliant Mechanisms for Path Generation using Genetic Algorithm,* Journal of Mechanical Design **127**, 745 (2004).

[23] D. Sharma, K. Deb, and N. N. Kishore, *Towards generating diverse topologies of path tracing compliant mechanisms using a local search based multi-objective genetic algorithm procedure,* in *2008 IEEE Congress on Evolutionary Computation (IEEE World Congress on Computational Intelligence)* (IEEE, 2008) pp. 2004–2011.

[24] N. F. Wang and K. Tai, *Design of Grip-and-Move Manipulators Using Symmetric Path Generating Compliant Mechanisms,* Journal of Mechanical Design **130** (2008), 112305.

[25] K. Tai, G. Y. Cui, and T. Ray, *Design synthesis of path generating compliant mechanisms by evolutionary optimization of topology and shape,* J. Mech. Des. **124**, 492 (2002).

[26] A. K. Rai, A. Saxena, and N. D. Mankame, *Synthesis of Path Generating Compliant Mechanisms Using Initially Curved Frame Elements,* Journal of Mechanical Design **129**, 1056 (2006).

[27] P. Kumar, R. A. Sauer, and A. Saxena, *On topology optimization of large deformation contact-aided shape morphing compliant mechanisms,* Mechanism and Machine Theory **156**, 104135 (2021).

[28] A. Romero, *Optimum design of two-material bending plate compliant devices,* Engineering Computations **39**, 395 (2021).

[29] J. J. Parise, L. L. Howell, and S. P. Magleby, *Ortho-planar linear-motion springs,* Mechanism and Machine Theory **36**, 1281 (2001).

[30] F. Van Keulen and J. Booij, *Refined consistent formulation of a curved triangular finite rotation shell element,* International journal for numerical methods in engineering **39**, 2803 (1996).

[31] R. De Borst, M. A. Crisfield, J. J. Remmers, and C. V. Verhoosel, *Nonlinear finite element analysis of solids and structures* (John Wiley & Sons, 2012).

[32] T. E. Bruns and D. A. Tortorelli, *Topology optimization of non-linear elastic structures and compliant mechanisms,* Computer methods in applied mechanics and engineering **190**, 3443 (2001).

[33] B. Bourdin, *Filters in topology optimization,* International journal for numerical methods in engineering **50**, 2143 (2001).

[34] J. K. Guest, J. H. Prévost, and T. Belytschko, *Achieving minimum length scale in topology optimization using nodal design variables and projection functions,* International journal for numerical methods in engineering **61**, 238 (2004).

[35] O. Sigmund, *Morphology-based black and white filters for topology optimization,* Structural and Multidisciplinary Optimization **33**, 401 (2007).

[36] S. Xu, Y. Cai, and G. Cheng, *Volume preserving nonlinear density filter based on heaviside functions,* Structural and Multidisciplinary Optimization **41**, 495 (2010).

[37] F. Wang, B. S. Lazarov, and O. Sigmund, *On projection methods, convergence and robust formulations in topology optimization,* Structural and multidisciplinary optimization **43**, 767 (2011).

# 6

# CONCLUSIONS AND RECOMMENDATIONS

## 6.1. SUMMARY AND CONCLUSIONS

This dissertation focuses on topology optimization for geometrically nonlinear structures and explores strategies to address the challenges of computational burden and convergence difficulties caused by spurious buckling modes. Furthermore, to facilitate the practical application of topology optimization in industrial design, a simple formulation for path-generation mechanism design is proposed, with the resulting designs validated through experiments.

To improve computational efficiency, Chapter 2 introduces reduced-order models (ROMs) based on the Ritz method, aiming to reduce the scale of nonlinear finite element analysis and sensitivity evaluation. The results show that augmenting the ROM basis with full-order model (FOM) solutions from previous designs significantly improves ROM accuracy. For problems involving nearly inextensional bending, incorporating path-derivative information into the ROM basis is essential. With respect to sensitivity analysis, although the use of approximate sensitivities may lead to slightly different final topologies for highly flexible structures, the achieved objective values remain close to those obtained using FOM-based analyses.

However, ROMs are less efficient when convergence issues arise from low-density regions compressed by stiffer neighboring regions. This setting leads to “inside-out" elements in 2D or spurious local buckling in shells. Such instabilities are often embedded in the ROM basis, reducing its convergence performance. Chapter 3 addresses this challenge by investigating four strategies from two perspectives: The first focuses on refining the ROM basis; and the second targets the physical cause of spurious buckling. For the former, they may fail to capture newly emerging spurious modes during optimization, temporarily increasing the need for FOM-based corrections. For the latter, based on findings, although introducing scaling factors to displacement field is effective in eliminating spurious buckling, it introduces artificial stiffness in flexible shells, leading to in-

correct representation of displacements. To avoid artificial stiffness, flexible support can be introduced for low-density elements. In particular, a complementary structure connected through spring elements can effectively stabilize these regions. Although large deformations may occur in the transition zones between solid and void elements, they do not appear to adversely affect convergence. Despite doubling the number of degrees of freedom, this approach can remain computationally efficient when combined with reduced-order modeling techniques.

To go beyond algorithmic improvements, Chapter 4 applies geometrically nonlinear topology optimization to design of path-generation compliant mechanisms. A key challenge, i.e. ensuring connectivity among input, output, and supporting fixtures, is addressed through a formulation that incorporates compliance and volume constraints. Analytical and numerical studies confirm that these constraints are effective when their upper limits are properly defined: the compliance limit is set according to design requirements, while the volume limit is determined and refined through a three-step optimization scheme. With a fixed compliance limit, adjusting the volume limit helps suppress non-functional low-density elements. In addition, instead of applying the adjustment step proposed in the optimization scheme, robust formulations can be combined with our proposed formulations in the main optimization process to ensure a low-density-element-free design. Given low-density elements may not appear at the convergence of the main optimization step, neither the robust formulation nor the adjustment step may be necessary.



Next, the formulation proposed in Chapter 4 is applied in Chapter 5 to design path-generation large-stroke compliant mechanisms, with experimental validation conducted on one mechanism based on 2D in-plane elements and two based on shell and plate elements. In 2D domains, large input displacements can cause solid elements to flip ("inside-out"), leading to failure of the finite element analysis at the initial optimization step. For this, the proposed input continuation method proves to be effective in ensuring stability by gradually increasing the input displacement during the optimization process. Alternatively, to avoid “inside-out" elements, shell or plate-based design domains may be used. Based on the latter, obtained designs highlight the advantages of flexible shells and plates, which due to their thin and compliant nature, can achieve larger displacement-to-size ratios. Experiments confirm the effectiveness of the topology design, but reveal that manufacturing details, particularly thickness and the removal of hinges in shell and plate structures, can significantly affect performance.

## 6.2. RECOMMENDATIONS

Here, we provide some possible directions and the corresponding recommendations to extend the work in this thesis.

- Currently, the proposed ROMs are limited to static displacement analysis. It is recommended to extend them to more computationally demanding problems, such as buckling and dynamic analysis. This would require incorporating and updating vibration or buckling modes during the optimization process to maintain the accuracy and efficiency of the ROM basis under such conditions.

- Inertial effects could be critical in the design of mechanisms for high-precision

positioning systems, when high-speed operation is required. The current study focuses on the static performance of path-generation mechanisms. It is recommended to incorporate dynamic constraints into the proposed formulation for designing path-generation mechanisms, so that the resulting designs can satisfy both static and dynamic performance requirements.

- Path-generation compliant mechanisms in this work are single-input and single-output. Many practical applications would be multi-input and multi-output. We would recommend extending the proposed formulation to multi-input and multi-output cases by combining multiple independent load cases for broader applicability in complex design scenarios.
- Complementary structures are introduced to stabilize low-density regions. Currently, only translational displacements are coupled between the original and complementary structures, while ignoring rotations. We would recommend coupling all, to allow pseudo densities to reach zero without introducing singularity issues.
- Due to limitations of the 3D printing method we used, thickness could not be precisely controlled. Since thickness is critical in the performance of shell and plate mechanisms, manufacturing methods, e.g., laser cutting, could be explored and validated in future work to ensure better accuracy. Besides, manufacturing uncertainties of thickness would be considered in the optimization process to help further mitigate this issue.

# ACKNOWLEDGMENTS

Completing this thesis has been anything but easy. While the research itself was finished on time, writing it down in a clear and proper manner proved far more challenging than I initially expected. The process was further delayed by various unforeseen circumstances, ranging from the global lockdown during the COVID-19 pandemic to the sudden promotion of my promotor to Dean. Fortunately, I was never alone in this journey. Many people offered their support, and my promotor also did his utmost to see this work through with me. Despite the unexpected obstacles, this journey has been filled with valuable experiences and many happy memories.

First of all, I would like to express my sincere gratitude to my promotor, Prof. Fred van Keulen. Working with him has always been both inspiring and productive. His valuable suggestions, broad expertise in nonlinear structures and optimization, and his patience have provided me with excellent guidance throughout my research. Beyond academic matters, I have also learned much from him in real life—how to build professional networks, how to balance work and life, how to face challenges with resilience, and how to express complex ideas in a simple and clear way. I am deeply grateful for all this wisdom, both in research and in life. At the same time, my heartfelt thanks go to Dr. Alejandro M. Aragón. He has provided me with valuable suggestions in writing papers, and I greatly appreciate all the training he offered in this regard, which proved extremely helpful. Beyond academic writing, he has consistently encouraged me to improve how I present myself, communicate my research, and build professional networks—skills that are essential for any researcher to develop.

I would also like to acknowledge people I worked with during my master's studies in Dalian, especially Prof. Gengdong Cheng and Prof. Biaosong Chen. They offered me numerous opportunities to grow, provided profound academic support, and helped pave the way toward pursuing my PhD. I am particularly grateful that they gave me the opportunity to meet and present my work to my current promotor during his visit to Dalian, which strengthened my determination to undertake PhD studies abroad and to pursue the topic of geometrically nonlinear structures. I sincerely thank the China Scholarship Council (CSC) for their generous support, which made this PhD research and thesis possible.

I would like to express my heartfelt appreciation to my colleagues at TU Delft for their support in both work and life. My special thanks go to Dr. Stijn Koppen, for his inspiring ideas on compliant mechanism design and for his patience in improving the figures and language of my papers; Dr. Vibhas Mishra, for his invaluable collaboration when we served together as teaching assistants for the course Nonlinear Mechanics; Prof. Matthijs Langelaar, Dr. Hans Goosen, Dr. Can Ayas, and Dr. Arnoud Delissen, for their valuable input during team meetings that greatly enriched my research; Patrick van Holst, for his assistance with experiments; and the lab technician team, for their help in recovering my laptop storage. I am especially thankful to Dr. Jian Zhang, who help me in getting

started in the Netherlands and at TU Delft; and to Xiliang Yang , who generously provided me with accommodation, shared many enjoyable conversations during breaks, and, together with Dr. Kai Wu and Jingyi Liu, offered invaluable help in preparing for my wedding. Finally, I would like to thank Ran Xue, Dr. Jiayu Li, Yuheng Yan, Yang Yang, Dr. Xianfeng Chen, Dr. Yong Zhang, and Dr. Qi Wang for the many pleasant conversations and good times we shared. I also extend my appreciation to all my other colleagues whom I have not mentioned by name for their contributions and encouragement over the years.

Besides, my heartfelt thanks go to my good friends. Many thanks to Jos van Gerwen and Josien Groenendijk, for organizing wonderful board games and parties, and for their dedication in helping prepare my wedding. I am also grateful to Ye Zhou and Peng He, who always welcome me in Germany with delicious food and dessert. My appreciation goes to Xiangli Su, for her many suggestions in daily life and for her help with translations during the wedding. I am thankful to Dr. Fan Zhang, for his nice suggestions on research and for flying from Norway to the Netherlands to attend my wedding. I would also like to thank Yan Cheng and Dr. Zhou Lu for their excellent taste and skill in Chinese cooking, as well as their inspiring ideas on how to enjoy life. Jia Zhang and Mengfei Yi, for their thoughtful gifts and food preparations; and Ning Ma, Tingting Liang, Di Sun, and Dr. Zhe Song, for their generous help with photography during my wedding. I will not forget my good friends in China. Special thanks go to Zijun Song and her husband Dr. Boyang Shi, for always giving me a warm welcome in Beijing and for the many joyful times we shared together. I am also thankful to Dr. Dawei Zhou, with whom I enjoyed delicious desserts and engaging conversations, especially during the WCSMO conference. My gratitude also goes to Peng Zhang, who organized wonderful gatherings with other friends in Beijing; Huan Wang and Xin Xu, who made the effort to travel from different cities to spend time with me; and I am also deeply appreciative of the warm words and kind care from Yuting Li during the COVID-19 pandemic. Furthermore, I would like to thank Dong Gao and Yu Fu for the happy memories and the nice meals we shared together.

Last but not least, I would like to thank my parents and my husband, for their endless love and encouragement. They are always trying to offer me a better life, and their support has given me the confidence to face challenges and overcome setbacks.

# A

# APPENDIX

## A.1. ORTHONORMALIZATION

Gram-Schmidt orthogonalization is applied to obtain a well-conditioned ROM basis once a new base vector is introduced to the ROM basis. To illustrate the normalization progress, we start from an empty ROM basis $\mathbf{R} = []$. First, the bootstrapping process generates the FOM-based linear solution $\overline{\boldsymbol{\Phi}}_1$. Then we introduce it to $\mathbf{R}$. Since $\overline{\boldsymbol{\Phi}}_1$ is the only one in the basis, orthogonalization is not required. Then, $\boldsymbol{\Phi}_1 = \overline{\boldsymbol{\Phi}}_1$ and $\mathbf{R} = [\boldsymbol{\Phi}_1]$ . Here we use $\boldsymbol{\Phi}$ to represent the base vector after orthogonalization.

Second, after the convergence of the FOM-based analysis, we introduce the FOM-based solution, i.e. $\overline{\boldsymbol{\Phi}}_2$, to the basis. Here we consider the ROMs without path derivatives for simple illustration. Now, the basis is not empty, we need to apply the orthogonalization. Since $\overline{\boldsymbol{\Phi}}_2$ is the latest vector, the corresponding deformation mode is closest to the current and the next load step. Given this, the vector is regarded as the start point of normalization, and the mode is completely maintained. Next, we remove $\overline{\boldsymbol{\Phi}}_2$ from $\overline{\boldsymbol{\Phi}}_1$, which means only the components orthogonal to $\overline{\boldsymbol{\Phi}}_1$ in $\overline{\boldsymbol{\Phi}}_2$ are attained. The orthogonalization can be explained by formulations

$$\begin{aligned} \boldsymbol{\Phi}_2 &= \overline{\boldsymbol{\Phi}}_2, \\ \boldsymbol{\Phi}_1 &= \overline{\boldsymbol{\Phi}}_1 - \frac{< \overline{\boldsymbol{\Phi}}_1, \boldsymbol{\Phi}_2 >}{< \boldsymbol{\Phi}_2, \boldsymbol{\Phi}_2 >} \boldsymbol{\Phi}_2, \end{aligned} \tag{A.1}$$

where $< \mathbf{a}, \mathbf{b} >$ denotes the inner product of vectors $\mathbf{a}$ and $\mathbf{b}$. Then $\mathbf{R} = [\boldsymbol{\Phi}_1, \boldsymbol{\Phi}_2]$. Next, the $\mathbf{R}$ can be used for the ROM-based analysis. If FOM-based error correction is required, then we need to add a new FOM-based solution to the basis, i.e. base vector $\overline{\boldsymbol{\Phi}}_3$. Follow-

A

ing the same rules, we can get

$$\begin{aligned}
\boldsymbol{\Phi}_3 &= \overline{\boldsymbol{\Phi}}_3, \\
\boldsymbol{\Phi}_2 &= \overline{\boldsymbol{\Phi}}_2 - \frac{<\overline{\boldsymbol{\Phi}}_2, \boldsymbol{\Phi}_3>}{<\boldsymbol{\Phi}_3, \boldsymbol{\Phi}_3>}\boldsymbol{\Phi}_3, \\
\boldsymbol{\Phi}_1 &= \overline{\boldsymbol{\Phi}}_1 - \frac{<\overline{\boldsymbol{\Phi}}_1, \boldsymbol{\Phi}_2>}{<\boldsymbol{\Phi}_2, \boldsymbol{\Phi}_2>}\boldsymbol{\Phi}_2 - \frac{<\overline{\boldsymbol{\Phi}}_2, \boldsymbol{\Phi}_3>}{<\boldsymbol{\Phi}_3, \boldsymbol{\Phi}_3>}\boldsymbol{\Phi}_3,
\end{aligned} \tag{A.2}$$

Then $\mathbf{R} = [\boldsymbol{\Phi}_\mathbf{1}, \boldsymbol{\Phi}_\mathbf{2}, \boldsymbol{\Phi}_\mathbf{3}]$. For each new base vector, we apply the same rule. Generally, if we assume at a specific load step, the corresponding ROM basis $\mathbf{R}$ before normalization with base vectors $[\overline{\boldsymbol{\Phi}}_1 ... \overline{\boldsymbol{\Phi}}_m]$, where $\overline{\boldsymbol{\Phi}}_1$ is the first vector added to $\mathbf{R}$ and $\overline{\boldsymbol{\Phi}}_m$ is the vector just added to $\mathbf{R}$. The Gram-Schmidt orthogonalization starts from $\overline{\boldsymbol{\Phi}}_m$ and ends at $\overline{\boldsymbol{\Phi}}_1$. The orthogonalized progress is shown by

$$\begin{aligned}
\boldsymbol{\Phi}_m &= \overline{\boldsymbol{\Phi}}_m, \\
\boldsymbol{\Phi}_{m-1} &= \overline{\boldsymbol{\Phi}}_{m-1} - \frac{<\overline{\boldsymbol{\Phi}}_{m-1}, \boldsymbol{\Phi}_m>}{<\boldsymbol{\Phi}_m, \boldsymbol{\Phi}_m>}\boldsymbol{\Phi}_m, \\
&\vdots \\
\boldsymbol{\Phi}_1 &= \overline{\boldsymbol{\Phi}}_1 - \frac{<\overline{\boldsymbol{\Phi}}_1, \boldsymbol{\Phi}_m>}{<\boldsymbol{\Phi}_m, \boldsymbol{\Phi}_m>}\boldsymbol{\Phi}_m - \frac{<\overline{\boldsymbol{\Phi}}_1, \boldsymbol{\Phi}_{m-1}>}{<\boldsymbol{\Phi}_{m-1}, \boldsymbol{\Phi}_{m-1}>}\boldsymbol{\Phi}_{m-1} - \cdots - \frac{<\overline{\boldsymbol{\Phi}}_1, \boldsymbol{\Phi}_2>}{<\boldsymbol{\Phi}_2, \boldsymbol{\Phi}_2>}\boldsymbol{\Phi}_2,
\end{aligned} \tag{A.3}$$

In this way, a well-defined base vector is obtained and $\mathbf{R} = [\boldsymbol{\Phi}_\mathbf{1}, \boldsymbol{\Phi}_\mathbf{2}, ..., \boldsymbol{\Phi}_\mathbf{m}]$.

## A.2. ROMS FOR INEXTENSIONAL-BENDING STRUCTURES

In order to accurately simulate structures subjected to nearly inextensional bending, path derivatives are taken into consideration for the ROM basis. In this section, the necessity of considering path derivatives for inextensional-bending structures is illustrated analytically. Next, the validity of path derivatives is highlighted by a numerical model.

### A.2.1. A PURE BENDING CANTILEVER STRIPE MODEL

In this section, we describe a cantilever plate, which is bent to a cylinder shell by the moment at the tip. The model is shown in Fig. A.1, where 100 load steps are involved in the analysis. At first, the normal FOM-based method is applied to the analysis and the deformed configuration at the last load step ($\lambda$=1) is shown in Fig. A.2(a). The number of FOM iterations is 199. Then, ROMs without path derivatives are applied to the analysis. We observe that after the ROM-based analysis converges, FOM-based error correction is involved and convergence difficulties appear during progress. The reason for the latter is that the corresponding ROM-based result provides a bad start for FOM-based correction updates, and causes instabilities, shown in Fig. A.2(b), in the FOM-based correction progress. The bad start provided by ROMs is mainly because of artificial in-plane stiffness introduced by ROMs. In the next section, an analytical example is studied to better understand the problem.

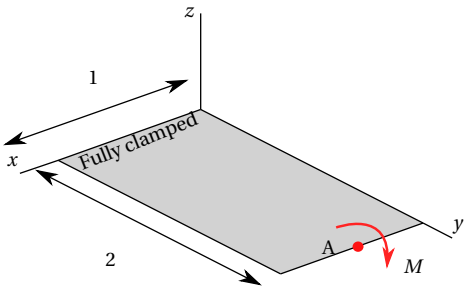


$E$=3 × $10^{11}$ $t$=0.01
$\nu$=0.3
$M$=30
$\lambda$=1
$\Delta\lambda$=0.01
$\epsilon_r = 1 \times 10^{-8}$
$\epsilon_f = 1 \times 10^{-5}$
$\delta_{\text{rej}} = 1 \times 10^{-8}$
$\delta_s = 0.5$

Figure A.1: The pure-bending cantilever stripe. Here, $E$ is Young's modulus, $M$ a moment, $t$ thickness, $\lambda$ load factor, $\Delta\lambda$ increment of $\lambda$, $\epsilon_r$ the convergence tolerance of FOMs, $\epsilon_r$ the convergence tolerance of ROMs, $\delta_{rej}$ the rejection tolerance, and $\delta_s$ the error tolerance of ROM-based results.

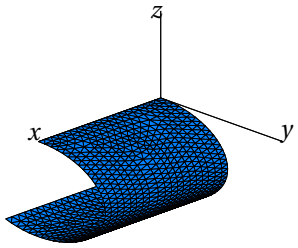


(a) FOM based result

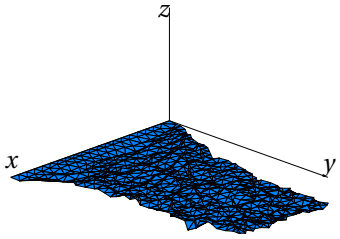


(b) ROM-based result

Figure A.2: Final FOM-based and ROM-based deformed configurations of the cantilever stripe

### A.2.2. ERRORS OF ROMS IN INEXTENSIONAL-BENDING STRUCTURES

In order to understand artificial in-plane stiffness introduced by ROMs, a simple pure-bending problem for a cantilever beam is illustrated in Fig. A.3. For pure-bending condition, the curvature is a constant along the length :

$$\frac{1}{R} = \frac{M}{EI}, \tag{A.4}$$

where $\frac{1}{R}$ is curvature, $M$ is the moment, and $EI$ is the bending stiffness. Thus, the shape of the deformed configuration is a part of a circle with a radius of $R$. The displacement $u$ along the x-axis and the displacement $v$ along the y-axis at arbitrary points of the beam can be defined by Eq. (A.5).

$$\begin{bmatrix} u \\ v \end{bmatrix} = \begin{bmatrix} R \cdot \sin\theta - x \\ R - R \cdot \cos\theta \end{bmatrix}, \tag{A.5}$$

with

$$\theta = \frac{x}{R}. \tag{A.6}$$

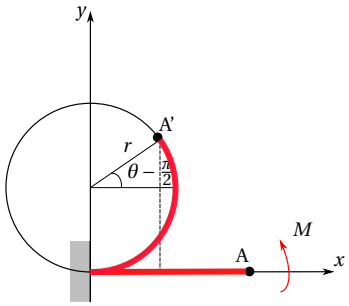


Figure A.3: A pure-bending cantilever beam subjected to the moment $M$. The Point A moves to Point A' after bending. Here, $R$ is the radius of curvature.

If we introduce non-dimension variables $\eta = \frac{x}{L}$ and $\alpha = \frac{L}{R}$, the Eq. (A.5) can be expressed by:

$$\begin{bmatrix} \frac{u}{L} \\ \frac{v}{L} \end{bmatrix} = \begin{bmatrix} -\eta(1 - \frac{\sin[\eta\alpha]}{\eta\alpha}) \\ \frac{1}{\alpha}(1 - \cos[\eta\alpha]) \end{bmatrix}. \tag{A.7}$$

Then, taking the solution Eq. (A.7) as the only base vector, we can construct a ROM basis $\mathbf{R} = \begin{bmatrix} \frac{u}{L} \\ \frac{v}{L} \end{bmatrix}$. Then a ROM-based solution based on the basis $\mathbf{R}$ can be described as

$$\begin{bmatrix} \frac{u}{L} \\ \frac{v}{L} \end{bmatrix}_{ROM} = C \begin{bmatrix} -\eta(1 - \frac{\sin[\eta\alpha]}{\eta\alpha}) \\ \frac{1}{\alpha}(1 - \cos[\eta\alpha]) \end{bmatrix}, \tag{A.8}$$

where $C$ represents the generalized DOF. Next, we use the ratio between stretching energy and bending energy as the error measurement, since analytically, the stretching energy should be exactly zero for pure bending, and numerically, the stretching energy should be very small compared to the bending energy. If the ratio is relatively large, then errors should exist in our solutions. Thus, the error measurement can be defined by

$$\text{error} = \frac{W_{\text{stretching}}}{W_{\text{bending}}}. \tag{A.9}$$

Here, $W_{\text{stretching}}$ represents stretching energy and $W_{\text{bending}}$ bending energy.

In the pure bending problem, $W_{\text{bending}}$ can be obtained directly by

$$W_{\text{bending}} = \frac{1}{2} M\alpha = (\frac{1}{2}) \frac{EI\alpha^2}{L}. \tag{A.10}$$

The stretching energy can be evaluated using the integration related to the bending stress $\sigma_{11}$ and strain $\epsilon_{11}$:

$$W_{\text{stretching}} = (\frac{1}{2}) \int_V \sigma_{11}\epsilon_{11} dV = (\frac{1}{2}) \int_{x=0}^{x=L} \sigma_{11}\epsilon_{11} A dx = (\frac{A}{2}) \int_{\eta=0}^{\eta=1} \sigma_{11}\epsilon_{11} d\eta = (\frac{AE}{2}) \int_{\eta=0}^{\eta=1} {\epsilon_{11}}^2 d\eta. \tag{A.11}$$

Thus, the error can be illustrated by

$$\text{error} = \frac{W_{\text{stretching}}}{W_{\text{bending}}} = (12\frac{L^2}{h^2})(\frac{1}{\alpha^2})\int_{\eta=0}^{\eta=1} {\epsilon_{11}}^2 d\eta. \tag{A.12}$$

Since

$$\epsilon_{11} = \frac{\partial u}{\partial x} + \frac{1}{2}(\frac{\partial u}{\partial x})^2 + (\frac{\partial v}{\partial x})^2, \tag{A.13}$$

the integration in the Eq. (A.11) can be described by:

$$\int_{\eta=0}^{\eta=1} {\epsilon_{11}}^2 d\eta = \int_{\eta=0}^{\eta=1} (\cos(\alpha\eta)-1)^2 (C-C^2)^2 d\eta = (\frac{1}{4\alpha}\sin(2\alpha) - \frac{2}{\alpha}\sin\alpha + \frac{3}{2})(C-C^2)^2. \tag{A.14}$$

Stretching energy should be zero for pure bending. However, according to Eq. (A.14), the stretching energy is a function of the generalized coordinate $C$ when the ROM is applied. The relationship between $C$, $\alpha$, and strain energy error is illustrated in Fig. A.4 where $L/h = 100$. Here, $C = 1$ means we use the base vector Eq. (A.7) to represent itself, and consequently, there are no errors. When $C \neq 1$, we intend to use the base vector Eq. (A.7) to represent nearby solutions, which is exactly the usual case in the ROM-based analysis. From the result, a subtle perturbation of $C$ will substantially increase error, i.e. stretching energy. With a fixed $C \neq 1$, the error will reach the peak when the structure is bent to a half-circle, where $\alpha$ is between 3 and 4. The reason for the large stretching energy is that inextensional mode cannot be described by the base vector Eq. (A.7). The problem can be solved by introducing the 2nd order of path derivative in the ROM basis, which can give ROMs more information associated with the in-plane deformation.

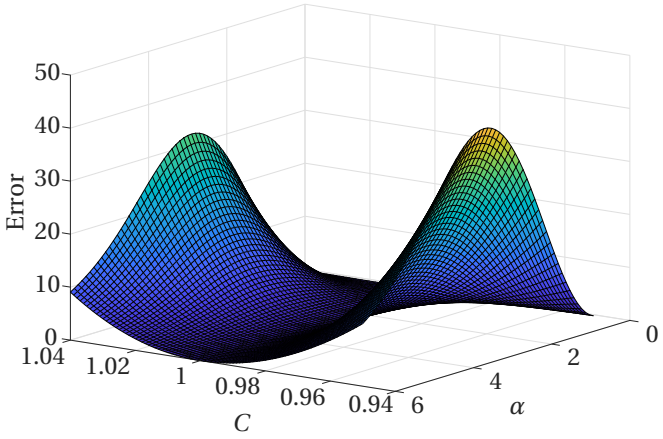


Figure A.4: Strain energy error encountered by ROMs. $C$ is generalized coordinates and $\alpha$ is curvature

A

### A.2.3. FEA OF THE PURE BENDING PLATE WITH PATH DERIVATIVES

The pure bending plate is tested again using ROMs with path derivatives. The maximum number of base vectors is 20. The analysis result is shown in Fig. A.5. The ROM-based analysis can converge with path derivatives, and the deformed configuration is the same as the FOM-based one. In the ROM-based method, the number of FOM solves is only 93, and the number of ROM solves is 299. Compared to the FOM-based method, where the number of FOM solves is 199, ROMs' efficiency is dramatically enhanced.

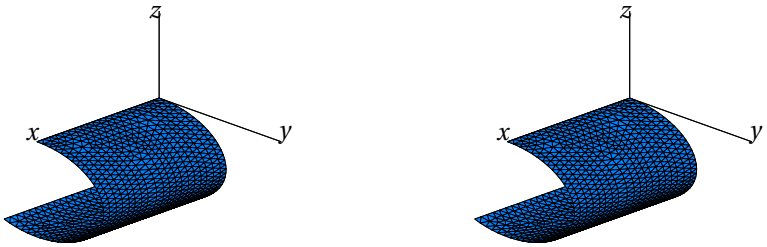


(a) FOM-based deformed configuration

(b) ROM-based deformed configuration with path derivatives

Figure A.5: Final FOM-based and ROM-based deformed configurations of the pure bending stripe

Concerning this model, we will discuss the feasibility of replacing the full Newton method with the modified Newton for path derivatives. At first, we analyze the plate model using ROMs involving the full Newton method. The corresponding number of ROM-based and FOM-based correction updates are illustrated in Tab. A.1. Here, we try different perturbation steps $\Delta\lambda^* = \Delta\lambda \times \epsilon$ by changing the perturbation parameter $\epsilon$, where $\Delta\lambda$ is the load incremental step. We also consider different convergence tolerances $\epsilon_p$ in the perturbed displacement generation progress for path derivatives. The purpose is to define suitable $\epsilon$ and $\epsilon_p$ for the calculation. It can be seen in Tab. A.1, when $\epsilon = 1 \times 10^{-3}$ or $1 \times 10^{-4}$, we can obtain relative good results. Besides, similar to the finite difference method, too small a perturbation parameter $\epsilon$ cannot lead to better results. Moreover, we can see that a smaller $\epsilon_p$ can contribute to a better result.

Table A.1: The number of Newton iterations involving ROMs, where path derivatives are calculated by full Newton method. In the table, $\epsilon$ is the perturbation, and $\epsilon_p$ is the convergence tolerance in the path-derivative calculation loop. The tolerance $\epsilon_f$ in the error correction loop is $1 * 10^{-5}$

| $\epsilon$ | $\epsilon_p$ | FOM | ROM |
|---|---|---|---|
| 1e-3 | 1e-5 | 105 | 322 |
| 1e-3 | 1e-8 | 98 | 310 |
| 1e-4 | 1e-5 | 103 | 311 |
| 1e-4 | 1e-8 | 94 | 302 |
| 1e-6 | 1e-5 | 148 | 303 |
| 1e-6 | 1e-8 | 113 | 564 |

Then, the same test is conducted with the modified Newton method and the results are shown in Tab. A.2. It can be seen that similar to full Newton, good results can be ob-

tained by modified Newton when $\epsilon = 1 \times 10^{-3}$ or $1 \times 10^{-4}$. Considering the latter, when $\epsilon_p = 1 \times 10^{-8}$, the number of FOM-based correction updates involving the modified Newton is nearly the same as the full Newton. Thus, modified Newton is feasible to replace the full Newton method when a small tolerance $\epsilon_p$ is used for calculating perturbed displacements.

Table A.2: The number of Newton iterations involving ROMs, where path derivatives are calculated by modified Newton method. In the table, $\epsilon$ is the perturbation, and $\epsilon_p$ is the convergence tolerance in the path-derivative calculation loop. The tolerance $\epsilon_f$ in the error correction loop is $1 * 10^{-5}$

| $\epsilon$ | $\epsilon_p$ | FOM | ROM |
|---|---|---|---|
| 1e-3 | 1e-5 | 136 | 253 |
| 1e-3 | 1e-8 | 97 | 268 |
| 1e-4 | 1e-5 | 131 | 262 |
| 1e-4 | 1e-8 | 93 | 299 |
| 1e-6 | 1e-5 | 157 | 396 |
| 1e-6 | 1e-8 | 106 | 565 |

## A.3. EXPLANATION OF THE ARTIFICIAL STIFFNESS

To understand the extra stiffness introduced to the inextensional bending shell by the strain interpolation method, in this section, we analytically investigate the pure bending of a cantilever beam, which is shown in Fig. A.6(a). The corresponding nonlinear membrane strain in $x$-direction $\epsilon_{xx}$ and the nonlinear curvature $\kappa$ can be expressed by:

$$\epsilon_{xx} = u_{,x} + 0.5(u^2{}_{,x} + v^2{}_{,x}) = 0 \tag{A.15}$$

and

$$\kappa = \frac{v_{,xx}(1 + u_{,x}) - v_{,x}\, u_{,xx}}{1 + 2\epsilon_{xx}} = \frac{M}{EI}. \tag{A.16}$$

Here $u$ denotes the displacement in $x$-direction, $v$ in $y$-direction, $M$ the bending moment, $EI$ bending stiffness, and $(,x)$ and $(,xx)$ denote the first-order and second-order derivatives related to $x$. By solving the equations above and introducing non-dimensional variables $w = \frac{x}{L}$ and $\alpha = \frac{\kappa}{L}$, where $L$ is the length of the beam, analytical solutions can be expressed as

$$\frac{u}{L} = \frac{\sin[w\alpha]}{\alpha} - w, \tag{A.17}$$

$$\frac{v}{L} = \frac{1}{\alpha} - \frac{1}{\alpha}\cos[w\alpha]. \tag{A.18}$$

The above are solutions without interpolation. Next, to obtain solutions with interpolation, we introduce the scaling parameter $\gamma$ to the membrane strain and obtain

$$\epsilon_{xx} = u_{,x} + 0.5\gamma^2(u^2_{,x} + v^2_{,x}) = 0. \tag{A.19}$$

By reducing $\gamma$ to 0 and combining with Eq. (A.16), analytical solutions with interpolation can be easily obtained:

$$\frac{u}{L} = 0, \tag{A.20}$$

A

$$\frac{v}{L} = 0.5w^2\alpha. \tag{A.21}$$

It is observed that after scaling, the displacement in x-direction completely vanishes, indicating that artificial in-plane stiffness has been introduced to the structure. Due to this extra stiffness, the beam is unable to bend into a circular shape as it does without scaling, as illustrated by the vertical displacement comparison in Fig. A.6(b). Notably, when the rotation angle $\alpha$ is relatively small, the vertical displacements with and without scaling remain nearly identical. However, as the rotation increases, significant differences emerge.

To validate the analytical solutions, nonlinear finite element analyses with and without strain interpolation are conducted on a cantilever shell structure, as shown in Fig. A.7. The threshold in the Heaviside function is set to $\eta = 0.01$.

First, we examine a relatively small element pseudo-density of $\rho_e = 1 \times 10^{-3}$. Since $\rho_e \ll \eta$, the elements completely lose their nonlinearity. The deformed configurations with and without interpolation are compared in Fig. A.8, and the corresponding displacements are presented in Tab. A.3. As observed, the numerical results fully align with the analytical solutions. With strain interpolation, artificial in-plane stiffness is introduced, preventing the cantilever shell from bending into a circular shape as it does without scaling.

Secondly, we consider a relatively large pseudo-density of $\rho_e = 0.2$. Since $\rho_e > \eta$, the elements partially retain their nonlinearity. The deformation results are shown in Fig. A.9, and the displacement comparisons are provided in Tab. A.3. Although more nonlinearity is preserved compared to $\rho_e = 1 \times 10^{-3}$, in-plane deformations are still minimal. This indicates that when the nonlinear term of strains, consequently the rigid body motions, are scaled down, even if not completely eliminated, in-plane hardening behavior can still be observed.

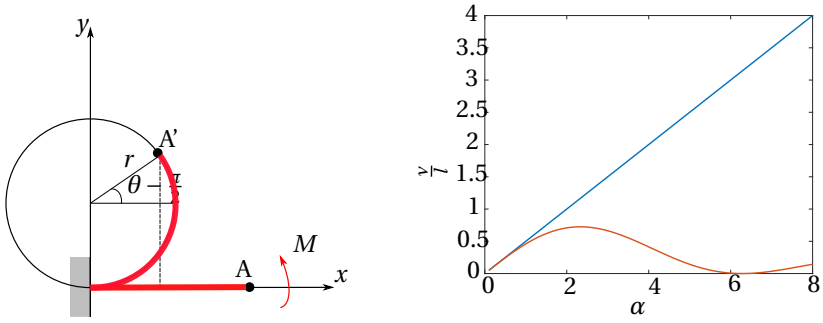


(a) (b)

Figure A.6: Pure bending cantilever beam and analytical analysis results with membrane strain interpolation. (a) The cantilever beam model. $M$ denotes the bending moment at the tip, $r$ bending radius, and $\theta$ rotations. (b) Comparison of vertical displacements between with and without membrane strain interpolation. The blue line shows the result with interpolation and the red without. Here $\alpha$ is non-dimensional curvature, $\frac{v}{l}$ non-dimensional displacement in y-direction.

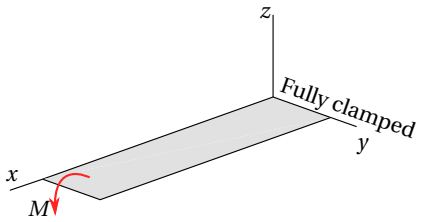


Figure A.7: A cantilever shell, subjected to pure bending $M$, with length 2, width 0.5, thickness 0.01, $E = 3\times10^{11}$. All quantities have consistent dimensions

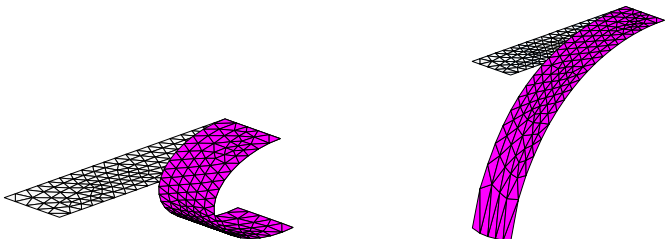

(a) (b)

Figure A.8: FOM-based final deformed configurations of the pure-bending shell shown in Fig. A.7 with $M = 5\times10^{-7}$, $\rho_e = 1\times10^{-3}$, and $\eta = 0.01$. (a) without strain interpolation and (b) with strain interpolation.

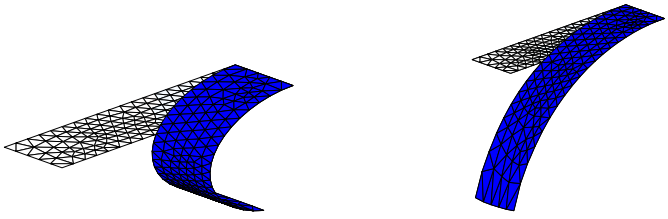

(a) (b)

Figure A.9: FOM-based final deformed configurations of the pure-bending shell shown in Fig. A.7 with $M = 3\times10^{2}$, $\rho_e = 0.2$, and $\eta = 0.01$. (a) without strain interpolation and (b) with strain interpolation.

Table A.3: FOM-based results of the pure-bending cantilever shell. Here, $n_{\mathrm{f}}$ is the number of FOM updates, $u_x$ and $u_z$ the displacements in x-direction and y-direction at $(x, y, z) = (2, 0.25, 0)$. $\eta = 0.01$. Here method "Normal FOM" means FOM without interpolation and "Scaled FOM" means with interpolation. The number of incremental steps is 10 and for each incremental step, the maximum number of Newton iterations is 50.

| $\rho_{\mathrm{e}}$ | method | $n_{\mathbf{f}}$ | $u_x$ | $u_z$ |
|---|---|---|---|---|
| $1 \times 10^{-3}$ | Normal FOM | 71 | -2.289 | -0.9967 |
| | Scaled FOM | 49 | $-4.111 \times 10^{-2}$ | -2.5443 |
| 0.2 | Normal FOM | 94 | -1.747 | -1.393 |
| | Scaled FOM | 44 | $-4.762 \times 10^{-2}$ | -3.040 |

# CURRICULUM VITÆ

## Lidan ZHANG

09-04-1992 Born in Jinzhou, China.

## EDUCATION

since 2018 Ph.D. candidate in Mechanical Engineering
Department of Precision and Microsystems Engineering
Delft University of Technology

2015–2018 M.Sc. in Computational Mechanics
Department of Engineering Mechanics
Dalian University of Technology

2012–2015 B.Sc. in Port, Waterway and Coastal Engineering
Department of Civil Engineering
Dalian Ocean University

2011–2012 Undergraduate in English Language and Literature
Department of Foreign Languages
Dalian Ocean University

# LIST OF PUBLICATIONS

5. **Lidan Zhang**,, Stijn Koppen, and Fred van Keulen *Connectivity-driven topology optimization for path-following compliant mechanism: a formulation with predictive volume constraints and adaptive strategies for gray element suppression*, Structural and Multidisciplinary Optimization, **68(2)**, Article 36. (2025).

4. **Lidan Zhang**, Yi Zhang, Fred Van Keulen, *Topology optimization of geometrically nonlinear structures using reduced-order modeling*, Computer Methods in Applied Mechanics and Engineering **416**, 116371 (2023).

3. **Lidan Zhang**, Stijn Koppen, Fred van Keulen *Enhancing Compactness in High-Precision Positioning Systems: A Journey through Topology Optimization and Ortho-Planar Bending*, to be submitted.

2. **Lidan Zhang**, Fred van Keulen *Elimination of spurious modes in ROM-based topology optimization of geometrically nonlinear structures*, to be submitted.

1. Coen Bakker, **Lidan Zhang**, Kristie Higginson, and Fred van Keulen *Simultaneous optimization of topology and layout of modular stiffeners on shells and plates*, Structural and Multidisciplinary Optimization **64**, 3147–3161 (2021) .


TU Delft